

**Collimation System
for the VUV Free-Electron Laser
at the TESLA Test Facility**

Dissertation

zur Erlangung des Doktorgrades
des Fachbereichs Physik
der Universität Hamburg

vorgelegt von

HOLGER SCHLARB
aus Frankfurt am Main

Hamburg

2001

Gutachter der Dissertation

Prof. Dr. P. Schmüser
Priv. Doz. Dr. J. Rossbach

Gutachter der Disputation

Prof. Dr. P. Schmüser
Dr. R. Brinkmann

Datum der Disputation

1. November 2001

Dekan des Fachbereichs Physik und

Vorsitzender des Promotionsausschusses

Prof. Dr. F.-W. Büßer

Abstract

To perform a proof-of-principle experiment for a Free Electron Laser operating at VUV wavelengths an undulator has been installed in the TESLA Test Facility linac phase I. To meet the requirements on the magnetic field quality in the undulator, a hybrid type structure with NdFeB permanent magnets has been chosen. The permanent magnets are sensitive to radiation by high energy particles. In order to perform the various experiments planned at the TESLA Test Facility linac, a collimator section has been installed to protect the undulator from radiation. In this thesis the design, performance and required steps for commissioning the collimator system are presented.

To identify potential difficulties for the linac operation, the beam halo and the dark current transport through the entire linac is discussed. Losses of primary electrons caused by technical failures, component misalignments, and operation errors are investigated by tracking simulations, in order to derive a complete understanding of the absorbed dose in the permanent magnets of the undulator.

Various topics related to a collimator system such as the removal of secondary particles produced at the collimators, generation and shielding of neutrons, excitation of wake fields, and beam based alignment concepts are important subjects of this thesis.

Zusammenfassung

Zur Demonstration eines Freien-Elektronen Lasers, der im VUV-Wellenlängenbereich hochintensive Strahlungspulse erzeugt, wurde in Phase I der TESLA Testbeschleunigeranlage (TTF) ein Undulator installiert. Um die geforderten magnetischen Feldstärken und Feldqualitäten im Undulator zu erreichen, ist eine mit NdFeB Permanentmagneten bestückte Hybridstruktur gewählt worden. Bei Bestrahlung von Permanentmagneten mit hochenergetischen Teilchen können bereits nach kleinen Dosen erhebliche Schädigungen der Magnete auftreten. Damit das an der TTF geplante experimentelle Programm keine Eingeschränkungen erfährt, wurde zum Schutz des Undulators ein Kollimationssystem von mir entwickelt. Diese Arbeit behandelt das Design, die Konstruktion, die Realisierung und die Inbetriebnahme der Kollimatorsektion.

Gefährliche Quellen für hochenergetische Teilchen können die Elektronen des Strahlhalos sein und die sogenannten Dunkelströme im Beschleuniger sowie jegliche Sekundärstrahlung, die durch diese beiden Quellen erzeugt wird. Um mögliche Probleme für den Strahlbetrieb bei TTF zu identifizieren, sind Strahlhalo und Dunkelstrom in der Maschine untersucht worden sowie deren Auswirkungen auf die Permanentmagnete.

Bei der Auslegung eines Kollimatorsystems sind Fragen wie die Erzeugung von elektromagnetischen Störwellenfeldern (wake fields) und deren Auswirkungen auf den Elektronenstrahl, Methoden zur Korrektur von fehlaufgestellten Komponenten, die Emission und Absorption von Sekundärstrahlung sowie die Neutronenbelastung hinter Tunnelabschirmungen zu untersuchen. All diese komplexen Themen werden in dieser Arbeit ausführlich diskutiert.

Contents

1 TESLA Test Facility Linac	11
1.1 Implication due to the Installation of the Undulator	12
1.2 Basic Layout of the Collimator Section	18
1.2.1 Transformation of apertures	18
1.2.2 Description of the acceptances by Twiss parameters	21
1.2.3 Two stage collimator system	25
1.2.4 Layout of the two stage spoiler-absorber system	31
1.2.5 Description of the collimator beamline	34
1.2.6 Beam steering concept	36
1.2.7 Using the collimator section as a beam dump	36
1.2.8 Radiation shielding	38
1.2.9 Energy dependence of the collimation	39
1.2.10 Consequences of the energy dependence and the radiological shield .	43
2 Development of Beam and Dark Current in the Linac	45
2.1 RF Photo-Injector	45
2.1.1 Injector beamline and performance status	47
2.1.2 Beam dynamics at the injector	49
2.1.3 Simulation of the injector for FEL operation	51
2.1.4 Emission of dark current	53
2.2 Bunch Compressor BC2	57
2.2.1 Components in the bunch compressor 2 section	59
2.2.2 rms-Bunch length after compression	61
2.2.3 Longitudinal bunch shape	61
2.2.4 Phase scan of acceleration module 1	62
2.2.5 Higher-order dispersion	63
2.2.6 Tracking of dark current through bunch compressor 2	65
2.2.7 Coherent synchrotron radiation	69
2.3 Dark current transport through ACC3 and collimator section	72
2.4 Undulator	74
2.4.1 The FEL principle	74
2.4.2 Undulator section	76
2.4.3 Influence of higher harmonics of the dipole field	79
2.4.4 Hard-edge model of undulator magnets	82
2.4.5 Hard-edge model of the undulator modules	84
2.4.6 Periodic solution for a the FODO-cell and instability limit	86
2.4.7 Linear beam optics of the undulator	88

2.4.8	Octupoles	89
2.4.9	Dark current transport through undulator	90
2.4.10	Demagnetization of NdFeB permanent magnets	95
3	Collimator Section	106
3.1	Geometry of the collimator section	107
3.2	Removal efficiency of the collimator for primary electrons	108
3.2.1	Energy bandwidth of the collimator for different beam energies	114
3.2.2	Clearance of the collimated beam to the undulator vacuum chamber	116
3.2.3	Loss distribution along the undulator caused by energy deviation .	117
3.2.4	Collimator quadrupole gradient errors	118
3.2.5	Collimator quadrupole displacements	120
3.2.6	Loss distribution along the undulator caused by quadrupole dis- placements	122
3.2.7	Comparison of different spoiler apertures	124
3.2.8	Summary of collimator efficiency for primary electrons	125
3.3	Energy deposition due to primary electrons in the undulator	127
3.3.1	Parameters for the Monte Carlo simulation	127
3.3.2	Energy deposition in the undulator for point-like losses	130
3.3.3	Doses in permanent magnets for loss distributions	140
3.3.4	Absorbed dose in magnets caused by dark current	142
3.4	Propagation of secondary particles from the spoilers	145
3.4.1	Clearances of the collimated beam to the absorbers	145
3.4.2	Energy deposition in the collimator section	146
3.4.3	Energy deposition of secondary particles in the undulator	149
3.5	Limits for beam losses preventing damages of the undulator	152
3.6	Spoiler protection	154
3.7	Orbit Correction	157
3.7.1	Shift of the beam orbit due to quadrupole displacements	157
3.7.2	Beam based alignment by using the SASE photon beam	158
3.8	Wake fields induced at the Collimator	163
3.8.1	Short range wake fields	164
3.8.2	Long range wake fields	174
4	Summary	176
A	Beam Dynamics	178
A.1	Linear Beam Transfer Matrices	178
B	Energy Measurement	182
B.1	Layout of the spectrometer	182
B.2	Orbit independent energy measurement	183
B.2.1	Calibration of the beam position monitors	184
B.2.2	First test of the orbit corrected energy measurement	186
B.3	First long macropulses with $800\mu\text{s}$ pulse duration.	188
B.4	Influence of quadrupoles Q4 and Q5 on the energy measurement	191

C Safety of the Exit Window	193
C.1 Beam optics for long macropulse operation	195

List of Figures

1.1	Scheme of the TESLA Test Facility linac.	13
1.2	Beam envelopes for TTF phase I	15
1.3	Scheme of an aperture at phase space	18
1.4	Scheme of an aperture in phase space after transformation.	19
1.5	Phase space area defined by two apertures	20
1.6	Transformation of the undulator vacuum chamber.	21
1.7	Phase ellipse of a particle beam.	22
1.8	Phase ellipse surrounding the acceptance of apertures.	23
1.9	Inner acceptance phase ellipse at apertures.	24
1.10	FODO-cell optic at first undulator module.	26
1.11	Image of the collimator and undulator acceptances.	27
1.12	Acceptance for rectangular and cylindrical collimator cross-sections.	28
1.13	Clearances for cylindrical and rectangular collimator cross-section.	29
1.14	Variation of the β -functions with beam energy in the undulator.	30
1.15	Scheme of the collimator section.	33
1.16	Variation of the collimator quadrupole gradients with beam energy.	34
1.17	Optics from ACC3 to undulator	35
1.18	Overview of the collimator section.	37
1.19	Scheme of beam steering through the collimator section.	38
1.20	Radiological dose due to beam losses at the collimator section.	40
1.21	Beat of collimator acceptance β -function.	42
1.22	Energy bandwidth of the collimator.	43
2.1	Drawing of the rf gun.	46
2.2	Schematic overview of the photo-injector laser system.	47
2.3	Pulse train and pulse width of rf photo-injector laser.	48
2.4	Schematic overview of the injector.	48
2.5	Transverse phase space showing the emittance growth and reduction.	50
2.6	Simulation of beam transport from rf gun to exit of acceleration module 1.	52
2.7	Example of transverse phase space distribution at exit of acceleration module 1.	53
2.8	Emission of dark current versus rf phase.	54
2.9	Dark current distribution at the exit of acceleration module 1.	56
2.10	Beam orbit, transverse and horizontal dispersion at BC2.	58
2.11	Overview of bunch compressor 2 at TTF.	60
2.12	Simulation of longitudinal phase space before and after BC2.	62
2.13	Simulation of the longitudinal profile for different module phase.	62
2.14	Phase scans of module 1	63

2.15	Offset and path length at bunch compressor 2 versus energy deviation.	65
2.16	Transverse position of the energy collimators at BC2.	66
2.17	Dark current distribution at the exit of acceleration module 2.	68
2.18	Scheme of coherent synchrotron emission.	70
2.19	Energy loss due to coherent synchrotron radiation.	71
2.20	Dark current transport through ACC3 and collimator section	73
2.21	Dark current measured at the injector and the collimator section.	73
2.22	Side view of the undulator section.	76
2.23	Scheme of cross-section of a planar undulator.	77
2.24	Magnetic field B_y of an undulator module.	77
2.25	Beam trajectory in an undulator module.	78
2.26	Side-view of the diagnostic station.	79
2.27	Hard-edge model for half an undulator magnet period.	84
2.28	Scheme of the transverse undulator cross-section.	84
2.29	Integrated gradients of the undulator quadrupoles.	85
2.30	Scheme of the undulator model by hard-edge magnets.	86
2.31	β -functions and phase advances of undulator FODO-cell.	87
2.32	Phase advances per FODO-cell versus beam energy.	87
2.33	Beat of the β -function along the undulator.	88
2.34	Measurement of vertical magnetic field at a quadrupole versus x	90
2.35	Longitudinal distribution of dark current deposited in the undulator modules	93
2.36	Transverse distribution of dark current deposited in the undulator modules	94
2.37	Experimental setup used at ESRF.	96
2.38	Results on demagnetization of permanent magnets at ESRF.	98
2.39	Particle energy spectrum of exposure at ESRF.	99
2.40	Experimental setup used for magnet exposure in POSTECH	101
2.41	Irradiation of NdFeB permanent magnets at 2 GeV.	102
2.42	Magnetic field loss per absorbed dose at 2 GeV electron exposure.	104
2.43	Radiation hardness of various types of NdFeB magnets (2 GeV)	105
3.1	Side-view of the collimator section.	107
3.2	Cross-section of spoilers and absorbers.	109
3.3	Transverse beam distributions at collimator screen.	111
3.4	Sketch of time averaged charge distribution.	112
3.5	Transmission probability through the collimator.	113
3.6	Transmission probability through the undulator at 200 MeV.	114
3.7	Transmission probability through the undulator for different beam energies.	115
3.8	Energy bandwidth for different beam energies.	115
3.9	Clearance of a mono-energetic beam at 230 MeV	116
3.10	Clearance of a mono-energetic beam for different energy deviations	117
3.11	Distribution of lost electrons along the undulator	118
3.12	Distribution of lost electrons along the module 1 and module 2	119
3.13	Undulator length in which losses caused by energy deviation appear.	119
3.14	Influence of quadrupole gradient errors on the transmission probability.	120
3.15	Energy bandwidth of the collimation for 1% rms gradient errors.	121
3.16	Influence of a quadrupole displacement on the transmission.	121
3.17	Influence of random quadrupole displacements on the transmission.	122

3.18 Energy bandwidth of the collimation for $50\mu\text{m}$ rms quadrupole displacements.	122
3.19 Loss distribution along the undulator caused by quadrupole offsets.	124
3.20 Undulator length in which losses caused by quadrupole displacements appear.	125
3.21 Energy bandwidth for different spoiler radius	126
3.22 Cross-section of the undulator as used for Monte Carlo simulations.	127
3.23 Side-view of undulator used for Monte Carlo simulations	129
3.24 Magnetic field in the undulator as used for Monte Carlo simulations.	129
3.25 Electromagnetic shower for vertical incidence in the undulator.	130
3.26 Electromagnetic shower after 1, 2, 3, and 4 undulator periods (vertical incidence)	131
3.27 Absorbed dose in permanent magnets for incidence in vertical direction	133
3.28 Transverse shower development for vertical incidence.	134
3.29 Energy spectrum of charged particles for vertical incidence.	135
3.30 Absorbed dose ($E > 20\text{ MeV}$) for incidence in vertical direction	135
3.31 Electromagnetic shower for horizontal incidence in the undulator.	136
3.32 Absorbed dose in permanent magnets for incidence in horizontal direction	137
3.33 Transverse shower development for horizontal incidence.	138
3.34 Energy spectrum of charged particles for horizontal incidence.	139
3.35 Absorbed dose ($E > 20\text{ MeV}$) for incidence in horizontal direction	139
3.36 Absorbed dose in magnets for losses caused by energy deviation.	141
3.37 Absorbed dose for horizontal quadrupole displacements.	143
3.38 Absorbed dose in magnets for dark current losses.	144
3.39 Clearance to absorber 2 and absorber 3	145
3.40 Geometry of the collimator used in EGS4	146
3.41 Electromagnetic shower initiated at spoiler 1.	147
3.42 Electromagnetic shower initiated at spoiler 2.	148
3.43 Spectrum of secondary particles reaching the undulator.	150
3.44 Secondary particles at the entrance of undulator modules	151
3.45 Absorbed dose in magnets caused by secondary particles from the collimator.	152
3.46 Absorbed dose caused by charged particles above 20 MeV	153
3.47 Temperature rise for a head on collision.	155
3.48 Beam centroids at entrance of undulator due to quadrupole displacements	158
3.49 FEL-radiation versus beam positions in the collimator section.	159
3.50 Injection condition into the undulator yielding SASE.	161
3.51 Most likely quadrupole displacements in the collimator section.	162
3.52 Coordinates used for calculating the wake functions	163
3.53 Geometric wake potentials caused by collimator tapers	166
3.54 Numerical simulation of a wake potential for an iris structure	167
3.55 Geometric wake potentials caused by steps in the beam pipe	168
3.56 Geometric wake potentials caused by gaps in the beam pipe	169
3.57 Resistive wall wake potentials	171
3.58 Surface roughness of spoilers	172
3.59 Surface roughness wake potentials for $\sigma_z = 250\mu\text{m}$	173
3.60 Surface roughness wake potentials for $\sigma_z = 40\mu\text{m}$	174
3.61 Geometry of pump-port in collimator section.	175

A.1	Scheme of wedge magnet.	180
B.1	Beam line close to the spectrometer dipole.	182
B.2	Beam energy from SASE-spectrum versus spectrometer dipole current.	183
B.3	Response function of BPMs in EXP1 and EXP3.	186
B.4	Setup for resolution measurements of stripline BPM electronics.	187
B.5	Resolution measurement of stripline BPMs at EXP1 & EXP3	187
B.6	First test for an orbit independent energy measurement.	189
B.7	Energy distribution of one of the first macro pulse with full beam loading. .	190
B.8	Orbit correction of energy measurement including Q4 and Q5.	192
C.1	Equilibrium temperature at the exit window.	194
C.2	Goodman stress diagram for the CuCo0.5Be exit window	196
C.3	Optics design at experimental area.	199
C.4	Phase space acceptance at the exit window.	200
C.5	Regular and minimum beam at the exit window.	201
C.6	Sensitivity of optics designed for long pulse operation.	202

Introduction

Accelerators have become a key tool for the understanding of the fundamental forces of nature in particle physics and to study the structure and electronic properties of matter. To open new research possibilities the TESLA project (TeV-Energy Superconducting Linear Accelerator), a superconducting electron-positron collider of 500 GeV total energy and an integrated X-ray laser laboratory has been developed. The result of eight years work in an international collaboration effort has recently been presented in a technical design report [1].

The Standard Model of particle physics has been developed through decades of intensive dialogue between theory and experiments at both hadron and electron accelerators. Leptons and quarks have been discovered as the fundamental constituents of matter, while the photon, the W and Z bosons, and the gluons have been identified as the carriers of the electromagnetic, weak, and strong forces. Many aspects of the Standard Model have been stringently tested with e^+e^- , ep and $p\bar{p}$ colliders making complementary contributions to the determination of the electroweak and strong interaction parameters. Combining the results, the experimental analysis is in excellent agreement with the Standard Model. Despite these great successes there are many gaps in understanding. As an example, there is no direct evidence of the Higgs boson, the corner particle in the Standard Model for the generation of masses of gauge bosons and fermions. Experiments on the largest electron-positron collider LEP at CERN have reported weak hints of a signal at a Higgs mass of $M_h \simeq 115$ MeV. If the electroweak sector of the Standard Model is an accurate description of nature, then with 95% confidence level the limit on the mass of the Higgs boson is just above 200 GeV. The final state with the lowest center-of-mass energy for the production of a Higgs boson requires in addition a Z -boson (mass 91 GeV).

The electron-positron collider LEP is a storage ring. Caused by synchrotron radiation losses emitted in the arcs of the storage ring, that increase with the fourth power of the beam energy, but decrease only inversely proportional to the arc radius, the operational cost would become prohibitive above 200 GeV. To go beyond this energy limit a future electron-positron collider has to follow the concept of two linear accelerators in collision [2]. The TESLA baseline design has a 2.5 times larger center-of-mass energy compared to LEP. The high luminosity of $3.4 \cdot 10^{34} \text{ cm}^{-2}\text{s}^{-1}$ and the well defined initial state originating from a e^+e^- annihilation opens up the possibility for precision measurements of the Higgs particle and the top quark.

At synchrotron radiation sources based on storage rings a gain in brilliance by more than ten orders of magnitude has been achieved over the last thirty years. With each generation, the synchrotron radiation facilities opened new applications for physics, chemistry and material science, for structural biology, environmental and geo-sciences. Modern third-generation synchrotron radiation facilities provide polarized photon beams of high brilliance, with cross-sections in the sub-millimeter range having a significant degree of coherence.

Making use of the principle of Self Amplified Spontaneous Emission (SASE) [3, 4] together with the high quality electron beams of TESLA and a careful design of undulator-magnets allows the production of laser-like X-ray beams with wavelength in the Ångstrom regime. The X-ray free-electron lasers (FELs) will provide radiation of the proper wavelength and time structure to investigate fast chemical reactions and dynamical processes in biomolecules at atomic resolution.

The TESLA collaboration proposes a superconducting linear accelerator with a center-of-mass energy of 500 GeV in first stage. In total, TESLA will be 33 km long. The acceleration structures will consist of 9-cell superconducting rf-cavities, made of niobium and cooled by superfluid helium to 2 K. The operation frequency is 1.3 GHz. The accelerating field of the cavities has to be 23.4 MV/m to reach the design center-of-mass energy. The superconducting radio frequency (rf) technology has important advantages compared to normal conducting cavities and is extremely well suited to drive an X-ray FEL:

1. The power dissipated in the cavity walls is very small. Thus the power transfer efficiency from the radio frequency source to the particles is very high. It results in an acceptable electric power consumption for the operation of the linear collider at 500 GeV and simultaneously provides a high luminosity.
2. When a beam is accelerated in a cavity, the charged particles induce electromagnetic fields (so-called wakefields), which act back on the beam. The wakefields can spoil the beam quality by increasing the energy spread and the emittance. The effect decreases strongly with the distance between the electron beam and the cavity walls. It is much weaker in the large superconducting cavities working at low rf-frequencies than in smaller room temperature cavities operating at higher frequencies.
3. Because of the small power dissipated in the cavities, superconducting accelerators permit large rf-pulse durations (\sim ms) and thus large spacing between individual electron bunches (\sim μ s). Due to the large bunch spacing, orbit and rf-feedback systems can control and correct the bunch positions and the bunch energies based on measurements within the 1 ms long marcopulse. Thus the technology is well suited to operate a linac with high stability.

The challenges of the superconducting technology are the production of multicell cavities with gradients above 25 MV/m and at same time, to achieve a cost reduction to about 2000 EUR per MV of acceleration. In parallel, the technical components required to operate the cavities at high gradients in an accelerator have to be investigated to identify difficulties and to optimize the design of the various components. In order to demonstrate the technical feasibility of high gradients in superconducting cavities, the TESLA collaboration began in 1992 to set up the TESLA Test Facility (TTF) at DESY [5].

The experimental program for the TTF linac has been extended in 1995 by a proof of principle experiment of a SASE based Free Electron Laser operating at wavelength between 70-160 nm. For that purpose, an undulator has been installed at TTF in spring 1999. The magnetic field of the undulator is produced by permanent magnets. The type of magnets used (NdFeB) is known to be sensitive to radiation damage if exposed to high energy electrons. A protection systems for the undulator turned out to be a challenging topic. Already beam losses in the order of 10^{-6} of the nominal beam current are critical for the undulator since they may cause an irreversible damage of its magnets after a few months of operation. The design of the protection system foresees a passive element, realized by a collimator section installed upstream of the undulator and an active beam loss detection system integrated to the TTF technical interlock. The basic concepts, the performance and the experimental experience with the protection system are reported and discussed in this thesis.

Chapter 1

TESLA Test Facility Linac

The TESLA Test Facility linac is a superconducting linear accelerator whose purpose it is to demonstrate that a linear collider based on superconducting cavities can be built and operated reliably. The TTF linac is constructed from 12 m long acceleration modules, each is comprised of a string of eight 9-cell cavities. The commissioning and operation of the linac also provides valuable experiences on the design of sub-systems like the electron source, the bunch compressors or the diagnostic components required for analyzing the beam properties. The following list contains the issues which can be investigated at the TTF linac [5]:

- maximum gradient achievable
- cavity construction and processing technique
- power input coupler and higher-order mode coupler design
- radio frequency control of multi-cavity system
- Lorentz detuning effects and control
- cryostat design
- cryogenic operation and heat load
- dark current
- energy and position beam feedback and control
- alignment and its stability
- beam position monitor systems
- TESLA 500 bunch charge (or similar to it)
- estimate on projected system costs.

Initially, in TTF phase 0, sketched in Fig. 1.1, an injector based on a thermionic gun was used to provide the TESLA design current, but not the TESLA large bunch spacing and intense bunches. The 250 keV beam from the thermionic gun was accelerated in a single superconducting cavity (capture cavity) followed by a 10 MeV beam analysis area before injection into a single acceleration module.

In TTF phase I the thermionic gun has been replaced by a laser driven photocathode within a radio frequency (rf) resonator, which provides the TESLA 500 large bunch spacing ($\approx \mu\text{s}$) and high bunch charge (few nC). The low emittance beam produced in such

a gun opened up the possibility to drive a Free-Electron Laser (FEL). The experimental program of the TTF linac has been extended by the following tasks related to the FEL:

- Extended studies on injector design (optimized for FEL operation)
- Studies on bunch compressor 2 (coherent synchrotron radiation)
- Undulator design
- Proof of principle for a SASE-FEL (wavelength ≈ 100 nm)
- Regenerative Amplifier FEL (RAFEL)
- Photon diagnostic design
- Feedback for orbit stability.

To compress the electron bunch longitudinally, the bunch compressors I at the injector and bunch compressor II behind the first acceleration module have been implemented. A second acceleration module raises the beam energy up to about 340 MeV. In summer 1999 the installation work on TTF phase I was completed, with the installation of an undulator and a collimator section.

Finally, in TTF phase II, it is planned to extend the linac to energies beyond 1 GeV. Such an electron beam can drive a Free Electron Laser at wavelengths below 10 nm. The extension of the linac will be built in a tunnel equal to the TESLA tunnel. Important experience concerning the design of the infra structure required to operate the linac housed in the tunnel and experience concerning the life time of linac components will complete the experimental program of TTF. In 2004 the TESLA test facility is planned to become an user facility. The FEL beam will be transported to the photon experimental hall located at the exit of the tunnel and provides the possibility for permanent scientific investigations.

1.1 Implication due to the Installation of the Undulator

In this section the implication due to the installation of the undulator are presented. For a better understanding, the TTF linac phase I is described in more detail and the important beam dynamical properties and issues are summarized.

Sections of TTF linac phase I

The TTF linac phase I consists of 10 sections.

INJ: At the injector, the low emittance, high bunch charge beam is generated in a 1.3 GHz rf photo-gun. Electron bunches are produced by the photo-electric interaction of an UV laser pulse impinging on a Cs_2Te photo cathode which is installed at the backplane of the cavity. The first superconducting acceleration structure, called booster cavity, accelerates the beam to about 16 MeV. The design average beam current within the rf-pulse is 8 mA with $1\ \mu\text{s}$ bunch spacing for the collider mode and 9 mA with $0.111\ \mu\text{s}$ bunch spacing in case of the FEL mode. With a maximum beam pulse train duration of 0.8 ms and a repetition rate of 10 Hz the duty cycle of the linac amounts to 0.8%. The injector is equipped with diagnostic components to analyze the beam properties. With focusing

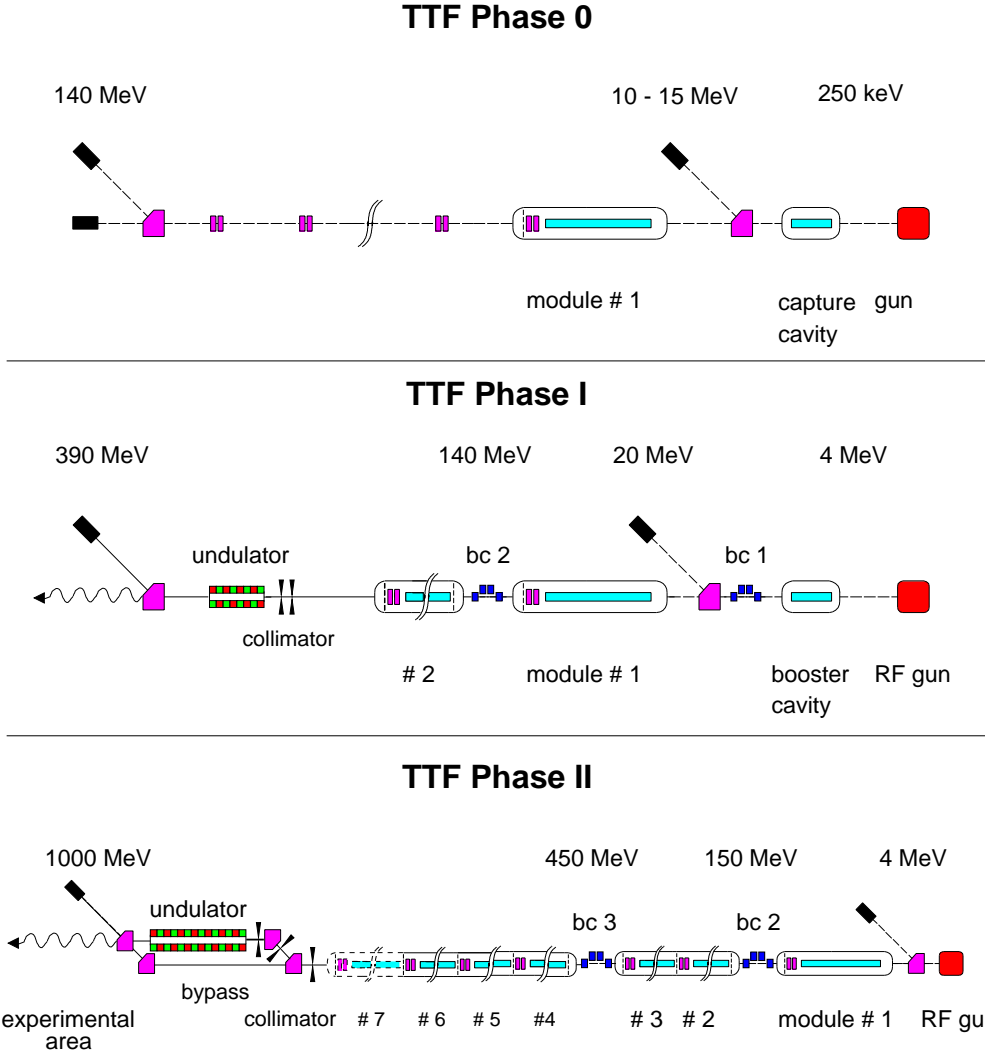


Figure 1.1: Schematic drawing of the TESLA Test Facility linac layout for phase 0, phase I and phase II.

lenses (magnetic quadrupoles) the beam is matched to the downstream superconducting acceleration module 1 (section ACC 1).

ACC 1: The energy behind the first acceleration module can be varied between 30 MeV and 200 MeV. For most experiments, cavity gradients of 15 MV/m have been chosen, resulting in a beam energy of 136 MeV. The rf power is delivered by a 10 MW klystron which is controlled by a digital feedback system. A wave-guide system distributes the rf power to each cavity in the modules. Both modules are connected to the same klystron.

BC 2: The beam leaving the section ACC 1 enters the bunch compressor 2. A magnetic chicane of four dipoles is used to compress the beam longitudinally. This increases the peak current of the beam to values in the kA range which is required for FEL operation.

ACC 2: In section ACC 2 the beam is accelerated to the final energy (up to 340 MeV). At the downstream end of both acceleration modules, superconducting quadrupole doublets are installed. During the run of phase I, a short circuit in the quadrupoles of ACC 2 required the installation of additional warm quadrupoles at the entrance of the following section ACC 3.

ACC 3: The section is equipped with two quadrupole doublets, two fast orbit feedback

kickers and diagnostic components for bunch length measurements.

COL 1: The collimator section is located in front of the undulator. Several collimators of fixed aperture protect the undulator from radiation damage. Correction dipole magnets and focusing quadrupoles are installed to match the beam from the collimator to the undulator.

UND 1-3: The undulator consists of three 4.5 m long undulator modules separated by diagnostic stations. In the undulator modules an alternating vertical magnetic field is produced by permanent magnets. The magnetic field causes a sine-like motion of the electron beam in the horizontal plane. The transverse deflection of the electrons produces synchrotron radiation which is, within the bandwidth of the FEL, amplified exponentially while the beam propagates along the undulator.

EXP 1 & EXP 3: The electron beam can be analyzed in the high energy experimental areas EXP 1 (not dispersive) and EXP 3 (dispersive). A spectrometer dipole between EXP 1 and EXP 3 allows to separate the electron and the photon beam. At the end of the EXP 3 the beam transmits through an exit window and its energy is absorbed in a beam dump.

EXP 2: The photon beam can be examined at a photon diagnostic area (EXP 2) downstream of EXP 1 (straight). A spectrometer (1 meter normal incidence) equipped with a spherical grating is used to determine the wavelength spectrum of the FEL pulses. The intensity and the angular distribution can be measured with a platinum silicide photodiode.

Important beam dynamic properties

The horizontal and vertical beam envelopes along the TTF linac phase I are plotted in Fig. 1.2. The operation of a FEL requires a tightly focused beam inside the undulator. The focusing is achieved by strong quadrupoles superimposed to the dipole field. A FODO-cell structure (focusing quadrupole, drift space, defocusing quadrupole, drift space) with a period length of 0.96 m has been chosen. The quadrupole fields are generated by additional permanent magnets embedded between the undulator poles. The quadrupole gradients are fixed. This determines the injection conditions for the beam into the undulator, aiming at the smallest beam cross-section the optimum FEL operation.

The cross-sections σ_x and σ_y at the undulator and partially along the collimator are 3 to 15 times smaller compared to the other beamline sections of the TTF linac. Due to the fixed quadrupole gradients in the undulator, the initial conditions on the beam size and the beam divergence at the entrance of the undulator depend on the beam energy. The adaption of the beam from the linac to the undulator requires a demanification which varies with energy.

The beam quality is dominantly determined by the rf and magnet settings in the injector. Due to space charge forces the beam dynamics at low beam energies is fairly complicated. An optimization has to take into account also the beam properties at higher energies (approximately behind ACC 1) and cannot be restricted to the injector area.

In section BC 2, coherent synchrotron radiation emitted in the bending dipoles of the magnetic chicane can decrease the beam quality. The amount of degradation depends on the beam optics along the chicane. Various constraints at the first 40 m of the linac suggest to decouple the optics considerations of this sections from the downstream linac. Their focusing devices are not suited to adapt the optics to the undulator, but the choice

of magnet settings have a large impact on the beam size at the collimator-undulator section.

For adapting the beam from the linac to the undulator, the collimator section plays the key role. Its design allows for a simple beam matching. The diagnostic components for measuring the transverse beam profiles have been foreseen. In addition, at the collimator section, nominal beam positions and angles are defined which can be monitored with high precision. This determines the beam orbit along the undulator independent of the orbit at the upstream linac. The collimator section has the functionality of a junction between the undulator and the upstream linac sections.

The beam optics behind the undulator at the experimental areas 1 and 3 is adapted either to the needs of the specific beam experiments (emittance or energy spread) or to the requirements on the beam cross-section at the exit window in case of long bunch trains.

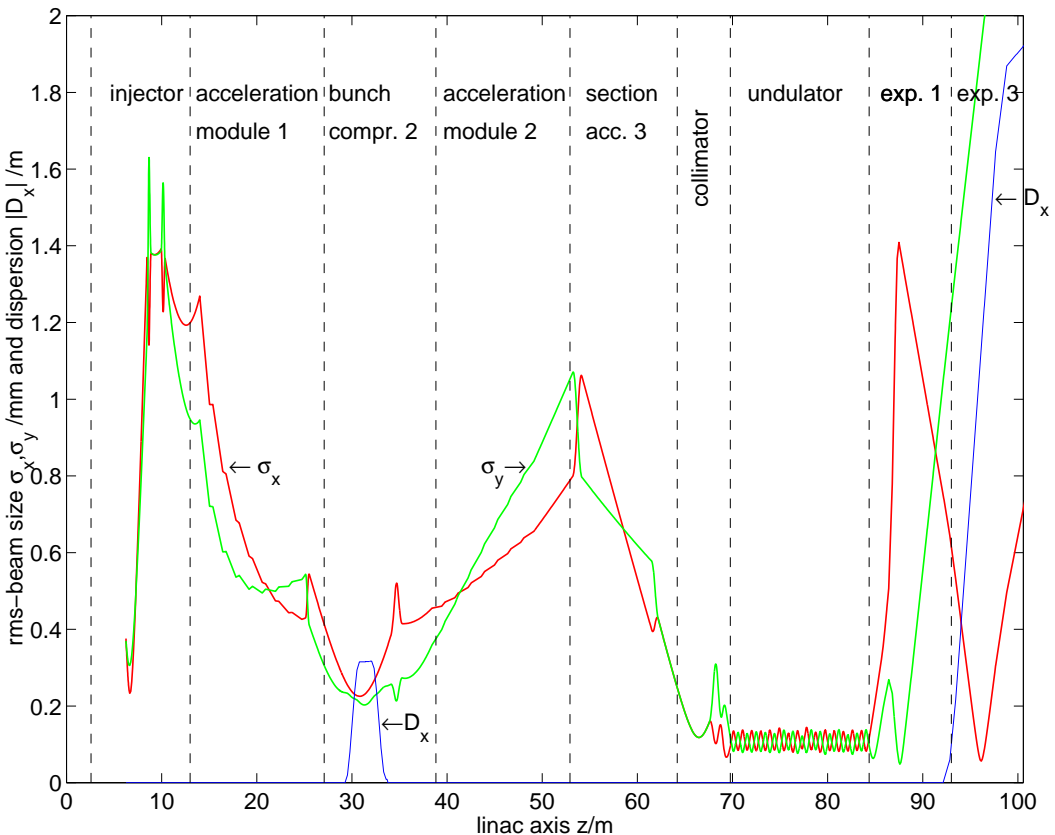


Figure 1.2: Example of computed horizontal and vertical beam envelopes along the TTF linac in phase I. The initial beam parameters for the computation have been determined at the injector by experiment [6]. The horizontal dispersion function D_x is also shown. The contribution of the dispersion D_x to the horizontal beam size is not included in this figure.

Need for a protection system for the undulator

When a high-energy electron or photon is incident on material, it initiates an electromagnetic cascade as pair production and bremsstrahlung generate more electrons and photons with lower energy. At energies below the critical energy, the electrons dominantly dissipate their energy by ionization and excitation rather than by the generation

of more shower particles. Due to the ionization process, energy is deposited in the material. This energy deposition can cause a degradation of the material performance e.g. a demagnetization of the permanent magnets installed at the undulator modules. The goal of the collimator is to protect the undulator from irradiation by the high-energy electron beam generated in the linac.

Along the undulator, more than a thousand NdFeB magnet blocks have been installed. The type of magnet is known to be sensitive to irradiation. At absorbed dose rates of 100 kGy a demagnetization in the percent range is expected (see Sec. 2.4.10). To relate this dose level to the design beam parameter of the TTF linac, a rough estimation is given:

Typically, the electromagnetic shower generated by an electron of a few 100 MeV extends longitudinally to about 6 radiation length ($6X_0$) and radially to about the Molière radius R_M of the specific material [7]. Within this volume, about 75% of the electron energy is deposited. The radiation length of the compound NdFeB is $X_0 = 1.7$ cm and the Molière radius is $R_M = 1.5$ cm. With the density of the permanent magnets $\rho = 7.6$ g/cm³ the mass of this volume yields 0.54 kg. The average beam power at 300 MeV and design beam current is 19 kW. Thus, the dose level of 0.1 MGy is collected within 3.7 s if the entire electron beam hits the magnets directly. Obviously, this is not a very realistic situation. But a local beam loss of 0.1% within $6X_0$ during beam operation might be realistic. Then the dose level of 0.1 MGy is collected in about 1 hour. On the other side, the protection system based on current monitors can detect beam losses of a few percent. This is totally insufficient for the protection of the undulator.

Already these values demonstrate that for TTF phase I a high performance protection concept had to be developed. The concept foresees a passive and an active protection system. The passive protection system is realized by collimators which remove electrons with large orbit deviation. In parallel, the active protection system monitors the remaining beam losses. The active system is integrated to the technical interlock system at TTF and restricts or inhibits the beam operation in cases of unacceptable beam losses in the undulator. Both systems together can provide sufficient safety for the permanent magnets of the undulator.

Additional requirements on the protection system due to beam cross-sections

The rms beam-size at the collimator section is 0.1 mm or even less. The energy density carried by the electron beam is sufficient to damage the vacuum tubes, if the beam hits the beam pipe walls directly. At energies of a few hundred MeV, the highest risk occurs where the well focused electron beam enters the material. Caused by ionization, the energy deposition per unit volume is largest in the first few millimeters of the material. Multiple scattering leads to a rapid growth of the beam cross-section and to a reduction of the energy deposition at greater depth in spite of the larger number of secondary particles (see section 3.6).

The deposited energy causes a rapid heating of the material and the transverse distribution of the electrons causes a temperature gradient. The material expands non-uniformly and the induced stress can cause a crack in the material before it starts to melt or to vaporize. At beam cross-sections of about 0.01 mm² and design current of 8 mA, most materials are damaged within a few μ s.

Thus, the choice of the materials at the collimator section and the protection of the col-

limitor itself is a serious issue. The active protection system described above needs not only to be very sensitive, it also has to be very fast. The required reaction time of the active protection system is inversely proportional to the bunch repetition rate.

1.2 Basic Layout of the Collimator Section

In this section the basic layout and the purpose of the collimator section is described. Details about the collimation efficiency, alignment tolerances and the additional protection system for the collimator are given in chapter 3.

1.2.1 Transformation of apertures

The simplest way to remove electrons with a large orbit offset is to install devices with sufficiently small aperture at different locations along the beamline. First, consider the situation of two parallel plates separated by a distance $2b$ in the horizontal plane. It is assumed that the plates have perfect absorption properties, hence an electron hitting the plate is immediately stopped and no secondary particles emerge. In the horizontal phase space (x, x') , with $x' = dx/dz$ the angle of the electron trajectory versus the design orbit, the plates can be represented as shown in Fig. 1.3. Obviously, there is no restriction on

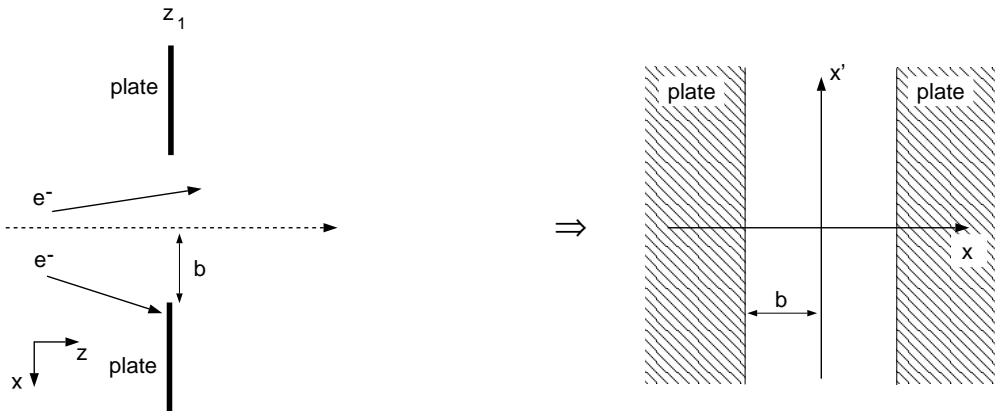


Figure 1.3: Scheme of a horizontal aperture in a beamline (left) and at the phase space (right).

the electron angles x' . Thus, the possible offset x before or behind the aperture is not fully determined by the distance $2b$ of the plates.

To image the aperture to a downstream point z of the beamline, the points $(x, x')_{z_1}$ of the phase space at z_1 have to be mapped to points $(x, x')_z$ of the phase space at z :

$$\begin{pmatrix} x \\ x' \end{pmatrix}_{z_1} \xrightarrow{\mathcal{M}} \begin{pmatrix} x \\ x' \end{pmatrix}_z. \quad (1.1)$$

If electromagnetic fields are present the map \mathcal{M} depends on the electron energy and might also be a function of time (e.g. in presence of acceleration sections). To yield a map which depends only on (x, x') , consider the case of static electromagnetic fields and mono-energetic electrons with an energy E_0 ¹. For linear optics elements (drifts, bending dipoles, quadrupoles) the map \mathcal{M} can be expressed by transfer matrices $M(z, z_1)$ as described in App. A. The Eq. 1.1 simplifies to

$$\begin{pmatrix} x \\ x' \end{pmatrix}_z = \begin{pmatrix} M_{11} & M_{12} \\ M_{21} & M_{22} \end{pmatrix} \begin{pmatrix} x \\ x' \end{pmatrix}_{z_1}. \quad (1.2)$$

¹It is also assumed that the motions of the electrons in horizontal and vertical direction can be treated independently. The coupling between both is studied with tracking calculations.

The surface of the plates at z_1 can be parameterized by

$$x = \pm(b + \chi), \quad \chi \in [0, \infty) \quad \text{and} \quad x' = \chi', \quad \chi' \in (-\infty, \infty), \quad (1.3)$$

with the upper sign for the right plate and the lower sign for the left plate. The edge of the plates are described by $\chi = 0$ and $\chi' \in (-\infty, \infty)$. After the transformation the area of the plates can be written as

$$\begin{pmatrix} x \\ x' \end{pmatrix}_z = \pm \mathbf{M}_1 b \pm \mathbf{M}_1 \chi + \mathbf{M}_2 \chi', \quad \mathbf{M}_1 = \begin{pmatrix} M_{11} \\ M_{21} \end{pmatrix} \quad \text{and} \quad \mathbf{M}_2 = \begin{pmatrix} M_{12} \\ M_{22} \end{pmatrix}. \quad (1.4)$$

The edges of the plates are transformed into parallel lines along the vector \mathbf{M}_2 starting at $\pm \mathbf{M}_1 b$. Since the determinant of the transfer matrix M equals unity ($\det(M) = 1$) the two vectors \mathbf{M}_1 and \mathbf{M}_2 are linearly independent. Thus, the distance between the two transformed plates in the phase space can never vanish.

In case of a drift space with length d the transformation matrix is

$$\mathbf{M}_d = \begin{pmatrix} 1 & d \\ 0 & 1 \end{pmatrix}. \quad (1.5)$$

The image of the aperture in the phase space behind the drift is sketched Fig. 1.4.

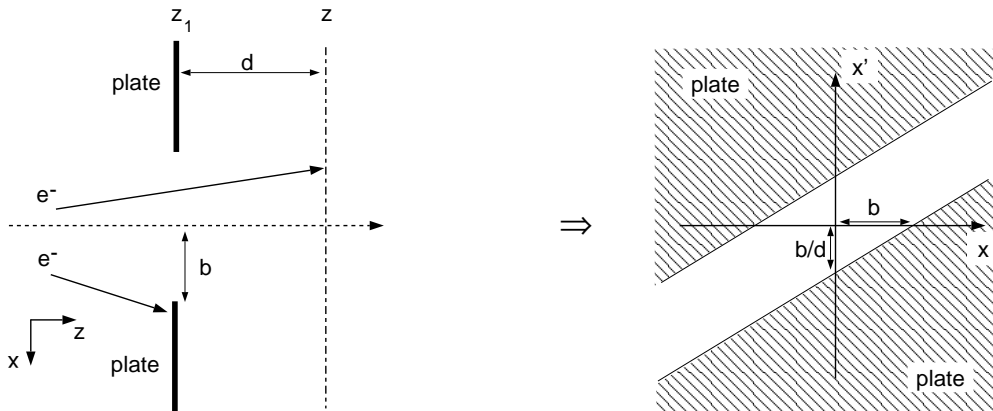


Figure 1.4: Scheme of a horizontal aperture followed by a drift space in a beamline (left) and the image of the aperture in the phase space at the position z (right).

Next, introduce a second aperture at the longitudinal position $z_2 = z_1 + 2d$. The geometry is chosen equal to the first aperture. Instead of transforming the first aperture to the position z_2 , the second aperture is transformed backwards to the upstream point z . In this case the transformation matrix is

$$\mathbf{M}_d^{-1} = \begin{pmatrix} 1 & -d \\ 0 & 1 \end{pmatrix}. \quad (1.6)$$

The image obtained for both apertures in the phase space located at z is plotted in Fig. 1.5. Because of the second aperture, the electron angles are now restricted to the maximum value of $|b'| = b/d$. The area A enclosed by the edges of the plates is a parallelogram (of finite area). The area A is referred in this thesis the acceptance of the aperture system, here given by the four plates. Electrons with the properties $(x, x') \in A$ pass through the

aperture system while electrons with $(x, x') \notin A$ are removed by one of the plates. Due to the specific choice of the position z (symmetry point) the parallelogram is rhombic. This often simplifies the analysis of acceptances, particularly if different aperture systems are studied. More generally, if ones the aperture systems are imaged in a phase space at an arbitrary point in the beamline, it can be further transformed by matrices with $\det(M) = 1$ to an arbitrary phase space (“virtual” phase space not existing in the beamline), where for instance the rhombus is mapped to a square. Properties like points of connections of the apertures or the area of the acceptances are preserved.

If n thin apertures are considered, the enclosed acceptance phase space is given by a

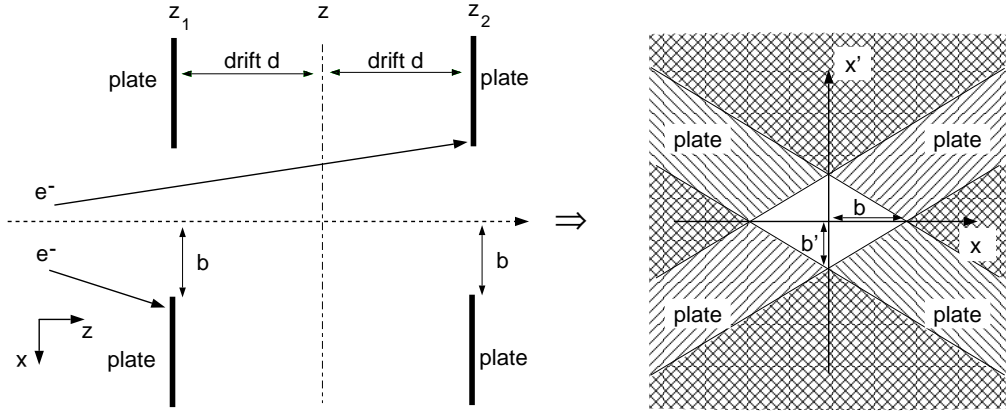


Figure 1.5: Scheme of two horizontal apertures separated by the drift $2d$ in a beamline (left) and in the phase space at the position z (right).

polygon with at most $2n$ edges. In linac optics the acceptance phase space of an aperture system is always convex.

The most relevant example of such a multiple aperture system is the vacuum chamber of the undulator. Using the formalism derived above, the back-transformed vacuum chamber, subdivided longitudinally into thin apertures of constant distance is shown in Fig. 1.6. The phase spaces (a) horizontal and (b) vertical are located at the symmetry point of the collimator system.

The passive protection system for the undulator is a set of apertures installed upstream of the undulator. The apertures have to be chosen such that no electrons can be lost in the undulator. To meet this goal, the acceptance phase space of the collimator defined by e.g. two apertures (rhombus) has to be inside the acceptance phase space of the undulator (polygon).

So far, nothing has been said about the cross-section of the undulator vacuum chamber. Generally, in case of rectangular apertures the above treatment can be applied on the horizontal and the vertical phase space separately. To protect the undulator it is sufficient to meet the requirements on the collimator for both phase spaces simultaneously.

The cross-section of the undulator vacuum chamber, however, is cylindrical. At given longitudinal position in the undulator the horizontal aperture size depends on the vertical offset of the electron and vice versa. Hence the (x, x') and (y, y') phase spaces are not independent and the 4-dimensional phase space (x, x', y, y') has to be considered. For designing the collimator apertures the 4-dimensional acceptance of the undulator has to be compared to that of the collimator. The enclosed areas plotted in Fig. 1.6 show the 2-dimensional cuts of the 4-dimensional undulator acceptance phase space, which are valid

for electron motions restricted either to the horizontal plane, $(y, y') \equiv 0$ or to the vertical plane, $(x, x') \equiv 0$. In all other cases, the 3-dimensional trajectories (x, y, z) of the electrons are not confined to a plane e.g. (x, z) for $(y, y') \equiv 0$, and the transformations of the apertures are much more complicated.

In section 1.2.3 (p. 27) it will be shown, that due to the choice of the collimator cross-sections the most critical electron trajectory can be determined by analyzing the horizontal and vertical acceptances only.

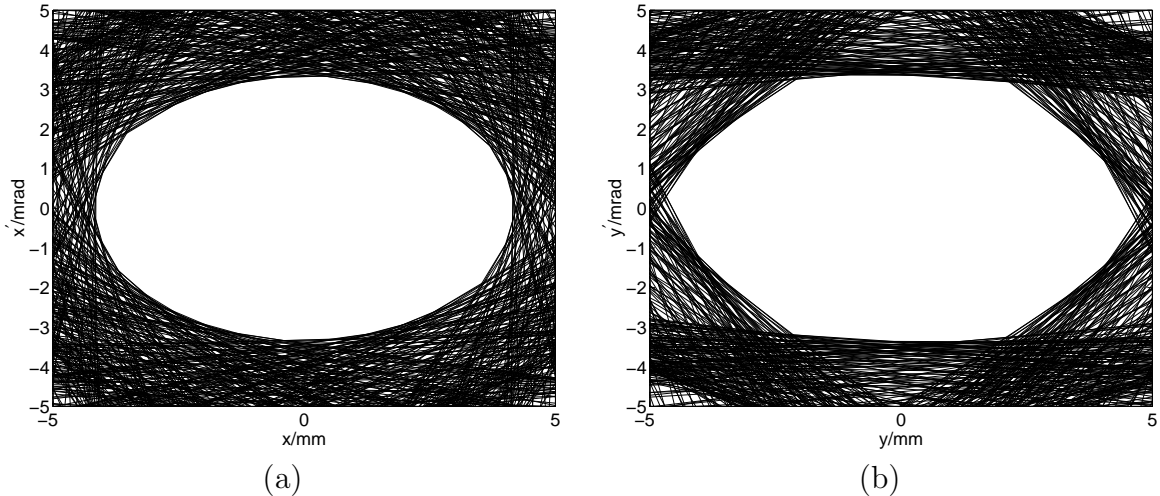


Figure 1.6: (a) Image of the undulator vacuum chamber in the horizontal phase space for $(y, y') \equiv 0$ and (b) in the vertical phase space for $(x, x') \equiv 0$ for an energy of 230 MeV. The beam Twiss parameters are $\beta_{x,y} = 1.25$ m and $\alpha_{x,y} = 0$ (see Sec. 1.2.2).

1.2.2 Description of the acceptances by Twiss parameters

In this section, the acceptance phase space of a two aperture system is related to phase ellipses. Transforming the phase ellipse along the beamline allows to derive important properties of the collimation system.

For any particle with known initial coordinates in phase space (x, x', y, y') it is possible to calculate the trajectory along a beamline made up of drift spaces, dipoles and quadrupole magnets. Since a large number of particles forms a particle beam, it is impractical, to concentrate on individual particle trajectories, specifically when the initial coordinates for each particle in phase space are totally unknown. Because it is easy to describe analytically an ellipse in phase space, it has become customary in accelerator physics to surround the particles of a beam in phase space by an ellipse called the phase ellipse. To determine the shape and the orientation of the ellipse in the horizontal phase space three parameters are required, i.e. the three second order moments $(\sigma_{xx}, \sigma_{xx'}, \sigma_{x'x'})$ or alternatively the Twiss parameters $(\beta_x, \alpha_x, \gamma_x)$ related by $\beta_x \gamma_x - \alpha_x^2 = 1$ together with the beam emittance ϵ_x . The relation between the phase space ellipse and the second order moments of the beam is shown in Fig. 1.7. For electron beams with gaussian density distribution usually the 1σ phase space ellipse is used.

To derive the properties of a collimator, the relevant formulas describing the particle and beam motion through a transfer beamline are summarized in the following. The equation

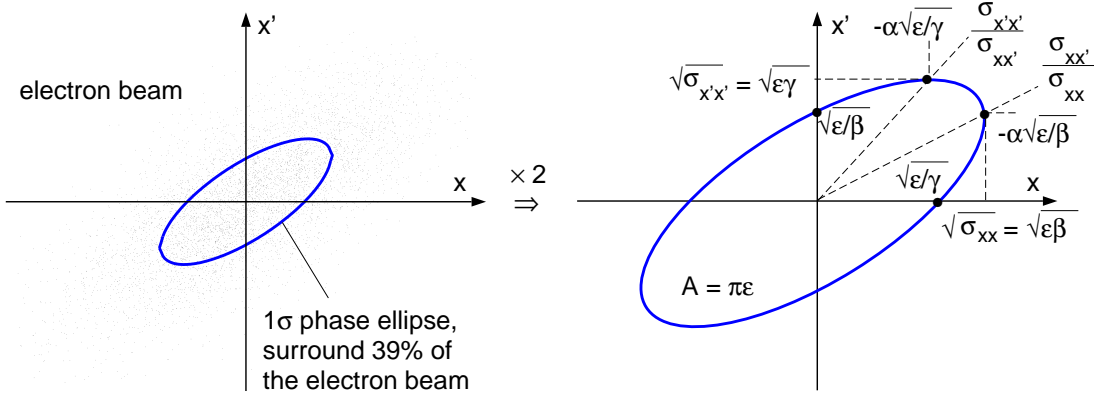


Figure 1.7: 1σ phase ellipse of a particle beam (left) and the description by Twiss parameters (right).

(Courant-Snyder invariant)

$$\gamma_x(z_0)x^2 + 2\alpha_x(z_0)xx' + \beta_x(z_0)x'^2 = \epsilon_x \quad (1.7)$$

describes the phase ellipse at the position z_0 in the beamlne. The beam matrix is defined by [8]

$$\boldsymbol{\sigma}_x(z_0) = \begin{pmatrix} \sigma_{xx} & \sigma_{xx'} \\ \sigma_{x'x} & \sigma_{x'x'} \end{pmatrix}_{z_0} = \epsilon_x \begin{pmatrix} \beta_x & -\alpha_x \\ -\alpha_x & \gamma_x \end{pmatrix}_{z_0} \quad (1.8)$$

and transforms to the position z like

$$\boldsymbol{\sigma}_x(z) = \mathbf{M} \cdot \boldsymbol{\sigma}_x(z_0) \cdot \mathbf{M}^T. \quad (1.9)$$

The rms-beam envelope is proportional to the square root of the β -function

$$\sigma_x(z) = \sqrt{\epsilon_x \beta_x(z)} \quad (1.10)$$

and increases with larger rms-beam emittance

$$\epsilon_x = \sqrt{\sigma_{xx}\sigma_{x'x'} - \sigma_{xx'}^2} \quad (\text{statistical definition}). \quad (1.11)$$

For mono-energetic beams, the beam emittances ϵ_x and ϵ_y are preserved along beam transfer lines build up by linear optic elements². Since the above definitions use the angular divergence of particles instead of the canonical momenta p_x and p_y , the emittance decreases when the beam gains energy. Therefore, usually the normalized emittances $\epsilon_{x,y}^N = \gamma \epsilon_{x,y}$ with $\gamma = E/m_0 c^2$ (m_0 is the mass of the electron) are used to describe the properties of the transverse beam distribution.

Finally, a point on the phase ellipse is determined by its initial phase $\Psi_{x,0}$ and transforms as

$$x(z, \Psi_{x,0}) = \sqrt{\epsilon_x} \sqrt{\beta_x(z)} \cos(\Psi_x(z) - \Psi_{x,0}), \quad (1.12)$$

$$x'(z, \Psi_{x,0}) = -\frac{\sqrt{\epsilon_x}}{\sqrt{\beta_x(z)}} [\alpha_x(z) \cos(\Psi_x(z) - \Psi_{x,0}) + \sin(\Psi_x(z) - \Psi_{x,0})], \quad (1.13)$$

²If skew quadrupoles are installed the value of the determinant $\det < (X \cdot X^T) >$ with $X^T = (x, x', y, y')$ is conserved

where the relation $\alpha = -\beta'/2$ has been used to derive Eq. 1.13 from Eq. 1.12. The phase function Ψ_x can be computed from the β -function by

$$\Psi_x(z) = \int_{z_0}^z \frac{1}{\beta_x(\tilde{z})} d\tilde{z}. \quad (1.14)$$

Properties of a two-aperture system

Now, consider a two-aperture system which in general yields a parallelogram in phase space. The smallest ellipse enclosing the parallelogram is called the outer acceptance ellipse of the aperture system. Similar to that, the inner acceptance ellipse is defined to be the largest ellipse that fits into the parallelogram. The outer acceptance ellipse is the smallest ellipse encloses all possible electrons passing the apertures, while the inner acceptance ellipse is the largest phase space ellipse enclosing electrons which definitely pass the apertures. For these ellipses, the acceptance a^{app} and the Twiss parameters $(\beta^{acc}, \alpha^{acc}, \gamma^{acc})$ can be calculated. If the parallelogram is transformed to a square, as

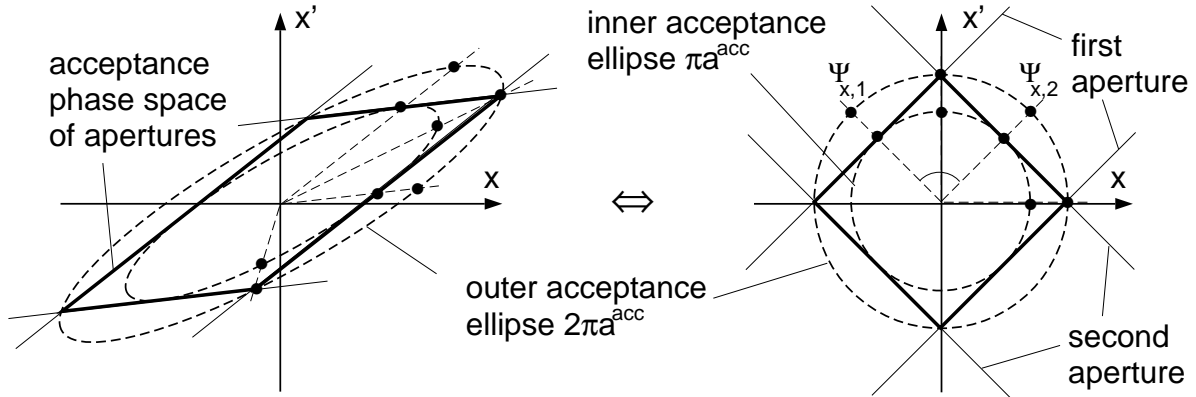


Figure 1.8: The inner and outer phase ellipse surrounding the acceptance of a two aperture system, left at a point in the beamlime, right in “virtual” phase space.

sketched in Fig. 1.8, the following properties become obvious (vertical correspondingly):

1. The orientation of the inner and outer acceptance ellipse is equal and can be described by a single set of Twiss parameters $(\beta_x^{acc}, \alpha_x^{acc}, \gamma_x^{acc})$.
2. The enclosed areas are:

$$\begin{aligned} \text{outer ellipse } A^{out} &= 2\pi a_x^{acc}, \\ \text{two apertures } A^{aper} &= 4a_x^{acc}, \\ \text{inner ellipse } A^{in} &= \pi a_x^{acc}, \end{aligned}$$

where a_x^{acc} is the acceptance, similar to the definition of the beam emittance, calculated for the inner acceptance ellipse .

3. Let denote z_1 and z_2 the position of the first and the second aperture in the beamlime. The point of connection of the first (second) aperture to the inner acceptance phase ellipse fulfills the equation (see Fig. 1.9)

$$\cos(\Psi_x^{acc}(z_i) - \Psi_{x,i}^{acc}) = \pm 1 \quad \Rightarrow \quad \Psi_x^{acc}(z_i) = \Psi_{x,i}^{acc} + n_i \pi, \quad i = 1, 2 \quad \text{with} \quad n_i \in \mathbb{N}.$$

The difference of the initial phases $\Psi_{x,i}^{acc}$ is given by $\Delta\Psi^{acc} = \Psi_{x,2}^{acc} - \Psi_{x,1}^{acc} = \pi/2$. Thus, the phase advance $\Delta\Psi$ of the acceptance ellipse between the two apertures obeys the equation

$$\Delta\Psi_x^{acc} = \frac{\pi}{2} + n\pi, \quad n \in \mathbb{Z}. \quad (1.15)$$

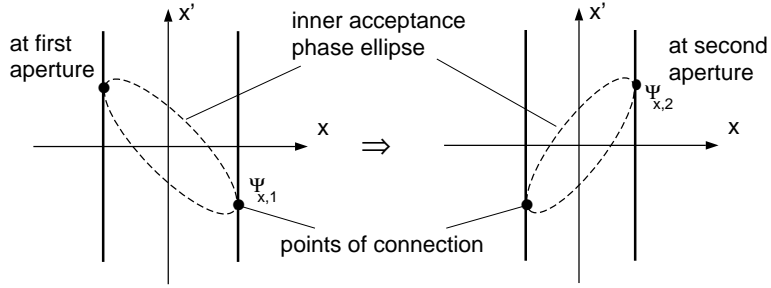


Figure 1.9: Inner acceptance phase ellipse at apertures.

4. Let denotes $2X_1$ ($2X_2$) the gap of the first (second) aperture. The inner acceptance is determined by

$$a_x^{acc} = \frac{X_1^2}{\beta_x^{acc}(z_1)} = \frac{X_2^2}{\beta_x^{acc}(z_2)}, \quad (1.16)$$

and πa^{acc} its area.

5. The particle amplitude behind the aperture system is limited to

$$|x| \leq \sqrt{2a_x^{acc}\beta_x^{acc}(z)}. \quad (1.17)$$

The factor $\sqrt{2}$ takes into account the corners of the parallelogram.

6. The corners of the parallelogram are mapped to the x-axis at phase advances of $\Psi^{acc} = \Psi_x^{acc}(z_2) + (n + 1/2)\pi/2$, $n \in \mathbb{N}$.
7. The highest transmission probability for a beam with a 2-dimensional gaussian distribution in phase space is achieved if the Twiss parameters describing the beam are equivalent to the Twiss parameters of the acceptance phase ellipse of the aperture (β^{acc} , α^{acc} , γ^{acc}). To achieve beam losses of less than 1% at the two apertures the emittance has to be smaller than $1/9$ of the acceptance of the inner acceptance ellipse

$$9\epsilon_x^{beam} \leq a_x^{acc}, \quad \text{for beam losses less than 1\%.} \quad (1.18)$$

1.2.3 Two stage collimator system

An ideal collimator should remove only those electrons which would hit the undulator. The undulator acceptance phase space, being a multiple aperture system, is well described by an ellipse (see Fig. 1.6). Thus, the ideal collimator system should have an ellipsoidal shape for its acceptance phase space. Such an collimator requires several stages. Due to space limitations (5.5 m total length) only a two stage collimator system was possible for TTF. In two dimensions (x, x'), the area of the acceptance A^{aper} of a two aperture system is reduced to $\pi/2 = 64\%$ compared to the area A^{out} of the outer phase ellipse. Therefore, a non-negligible amount of additional electrons might be removed by the two stage collimator, additional to an ideal collimator system.

Matching of the collimator to the undulator

Let denote $(\beta^{col}, \alpha^{col}, \gamma^{col}; a^{col})$ the Twiss parameters and acceptance defined by the inner acceptance ellipse of the two stage collimator and $(\beta^{und}, \alpha^{und}, \gamma^{und}; a^{und})$ the parameters defined by the inner acceptance ellipse of the undulator aperture system. To guarantee that no electrons are lost in the undulator two conditions have to be fulfilled:

1. The outer acceptance phase ellipse of the collimator has to be smaller than the inner acceptance phase ellipse of the undulator a^{und} .

$$2a^{col} < a^{und}. \quad (1.19)$$

2. The orientation of both ellipses to each other at a given phase space have to be adapted such that no point of connection occur.

The orientation of the inner acceptance ellipse of the undulator requires the knowledge of Twiss parameters $(\beta^{und}, \alpha^{und}, \gamma^{und})$. The orientation of the collimator and the undulator phase ellipse is then determined by the transfer function between the collimator and the undulator.

To yield the highest transmission probability through the collimator section, a^{col} equals $a^{und}/2$, which requires an equal orientation of both acceptance ellipses. In this case, the Twiss parameters of the collimator and the undulator acceptance ellipses are identical. In a real machine, several effects like alignment errors and energy spread of the beam, leads to the choice of smaller acceptance for the collimator than in the limit $a^{col} \approx a^{und}/2$. The choice of a^{col} depends on the orientation of the ellipses, but also on the collimator cross-sections. First, the optimum orientation between the acceptance phase ellipse of the collimator section and the undulator for a given a^{col} is discussed. For that, the undulator optics has to be investigated in detail. According to Eq. 1.17, the possible electron offsets along the undulator are bounded by the square root of the collimator acceptance function $\beta^{col}(z)$. In other words, $\beta^{col}(z)$ describes how the aperture of the collimator propagates through the undulator. Since the undulator vacuum chamber is of constant diameter, the smallest possible distance of an electron to the beam pipe walls occurs at the peak values of $\beta^{col}(z)$. Thus, the most efficient adaption from the collimator section to the undulator is given when the maximum value of $\beta^{col}(z)$ along the undulator is minimized. For a FODO channel, as installed in the undulator, this goal is achieved if $\beta^{col}(z) = \beta^{col}(z + L)$ is a periodic function with L the length of a FODO-cell [8]. For this solution the largest

clearance for the electron beam is achieved. In Fig. 1.10 the periodic solution of a FODO channel in horizontal and vertical plane along the first undulator module is plotted.

Next it will be shown, that this solution is identical to the undulator acceptance function

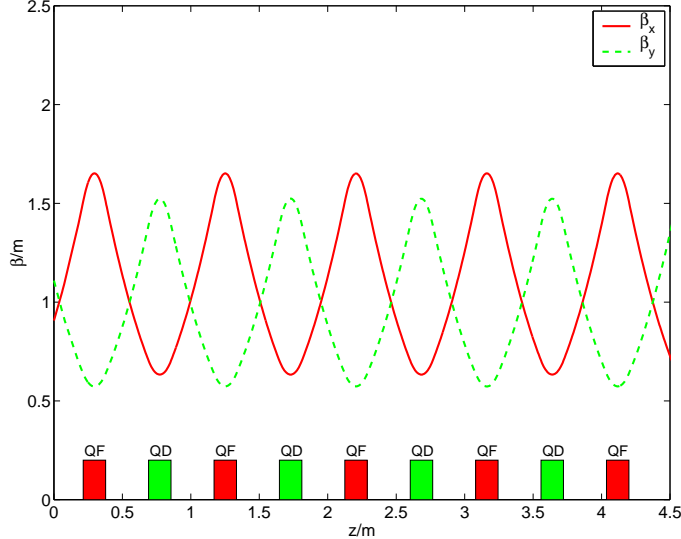


Figure 1.10: Periodic solution for the β -function of the FODO-channel (first undulator module) at an energy of 230 MeV.

β^{und} . According to the definition of the inner acceptance phase ellipse being the largest ellipse enclosed by an aperture system, the equation

$$R(z) \geq \sqrt{a^{mul} \beta^{mul}(z)} \cos(\Psi^{mul}(z) - \Psi^{mul}) . \quad (1.20)$$

has to be fulfilled for all positions z from the entrance to the exit of the system. The index mul is used to indicate a multi aperture system with an aperture size given by $R(z)$. The points of connection between the apertures and the ellipse have the phases

$$\Psi^{mul,i} = \Psi^{mul}(z_i) , \quad i \geq 2 \quad (1.21)$$

and Eq. 1.20 can be rewritten as

$$a^{mul} = R^2(z_i) / \beta^{mul}(z_i) . \quad (1.22)$$

The radius of the undulator vacuum chamber is constant. To achieve the largest possible phase ellipse the function $\beta^{und}(z)$ have to be minimized. The solution is again given by the periodic solution for a FODO channel. Therefore, the optimized collimator operation requires an equal orientation between the outer collimator acceptance ellipse and the inner undulator acceptance ellipse if observed at the same longitudinal position z .

Matching of the beam into the collimator

The periodic solution for a FODO channel is also the best solution for the FEL operation where a minimum beam cross-section along the undulator is achieved. The largest transmission probability of a gaussian distributed beam through the collimator apertures is obtained if the electron beam matches with the inner collimator acceptance phase ellipse. The inner and the outer acceptance ellipse of the collimator are equally oriented.

Therefore, the optimum conditions for operating the collimator and simultaneously for operating the FEL is achieved, if the beam phase ellipse, the collimator acceptance phase ellipse and the undulator acceptance phase ellipse are equally oriented to each other, hence if

$$\beta^{beam} = \beta^{col} = \beta^{und}. \quad (1.23)$$

Figure 1.11 shows the horizontal phase space at the symmetry point of the collimator for the optimized operation.

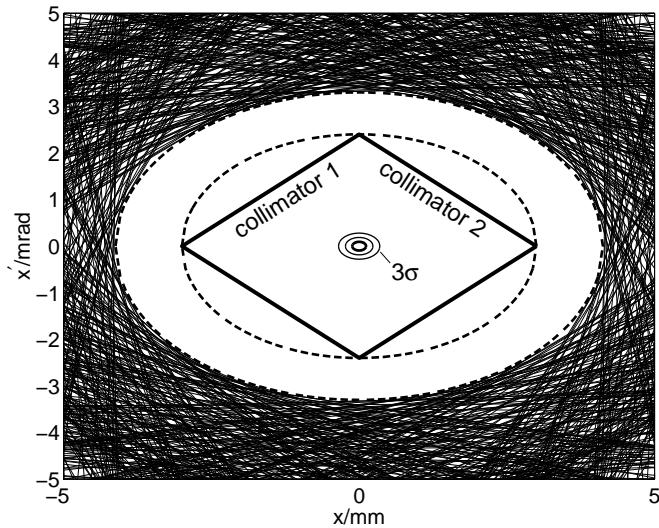


Figure 1.11: Image of collimator and (ideal) undulator acceptances in phase space at optimum operation conditions. The 1σ , 2σ and 3σ ellipse of a matched electron beam with normalized emittance of $5\ \mu\text{m}$ is also plotted. The calculations are performed at a beam energy of $230\ \text{MeV}$. The minimum distance between the collimator acceptance phase space and the wall of the undulator vacuum chamber is $1.4\ \text{mm}$. The Twiss parameters are $\beta_x = 1.25\ \text{m}$ and $\alpha_x = 0$.

Choice of the aperture cross-section for the collimators

For the rest of this section it is assumed that the β -function of the beam, of the collimator acceptance and of the undulator acceptance are identical. They are simply denoted by β without an index.

The undulator vacuum chamber is a cylinder with a radius of $R_{und} = 4.75\ \text{mm}$. An electron hits the vacuum wall if

$$x^2 + y^2 = \beta_x(z) e_{x,0} \cos^2(\Psi_x(z) - \Psi_{x,0}) + \beta_y(z) e_{y,0} \cos^2(\Psi_y(z) - \Psi_{y,0}) \geq R_{und}^2 \quad (1.24)$$

where $(e_{x,0}, \Psi_{x,0}, e_{y,0}, \Psi_{y,0})$ defines the initial conditions of the electron. The electron motion has to be investigated in x and y to avoid irradiation of permanent magnets in the undulator. The collimator puts constraints on the initial conditions.

Consider first the case of collimators with rectangular cross-sections. The constraints

for the horizontal plane is independent from that of the vertical plane. Using the outer acceptance ellipse as an upper estimated for the electron motion behind the two stage collimator system

$$e_{x,0} \leq 2a_x^{col}, \quad e_{y,0} \leq 2a_y^{col} \quad \text{and} \quad \Psi_{x,0}, \Psi_{y,0} \in [0, 2\pi] \quad (1.25)$$

the electron radius r is bounded to

$$r \leq \sqrt{2} \sqrt{\beta_x(z) a_x^{col} + \beta_y(z) a_y^{col}} \quad (\text{rectangular}). \quad (1.26)$$

For equal acceptances in x and y the largest electron radius is determined by the sum of the β -functions. Thus, for a cylindrical undulator beam pipe the allowable acceptance a^{col} is always smaller than the calculated ones from the horizontal and the vertical analysis alone. The collimator acceptance cross-section for rectangular collimators is sketched in Fig. 1.12(a).

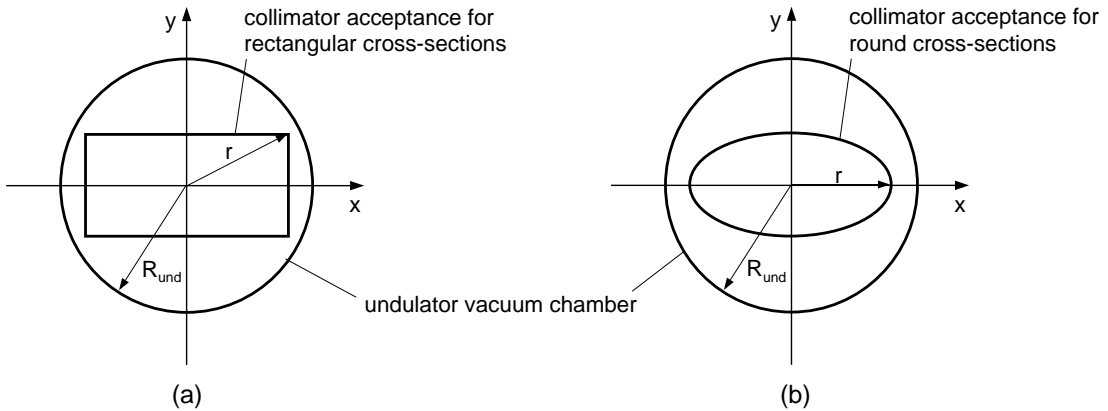


Figure 1.12: Scheme of the collimator acceptance cross-section at a focusing quadrupole of the undulator for rectangular (left) and cylindrical (right) collimator cross-sections

Now, consider cylindrical collimators with an equal acceptance in horizontal and vertical plane ($a_x^{col} = a_y^{col}$). From Eq. 1.16 it follows that the β -function at the position of the collimators have to be equal in both planes, $\beta_x(z_i) = \beta_y(z_i)$, $i = 1, 2$. Let denote R_i the radii of the two collimators. The restrictions on the initial conditions of an electron passing the collimator system are

$$\begin{aligned} x_i^2 + y_i^2 &= \beta_x(z_i) e_{x,0} \cos^2(\Psi_x(z_i) - \Psi_{x,0}) + \beta_y(z_i) e_{y,0} \cos^2(\Psi_y(z_i) - \Psi_{y,0}) \leq R_i^2 \\ &\Rightarrow e_{x,0} \cos^2(\Psi_x(z_i) - \Psi_{x,0}) + e_{y,0} \cos^2(\Psi_y(z_i) - \Psi_{y,0}) \leq a^{col} \end{aligned} \quad (1.27)$$

If the Eqs. 1.27 for $i = 1$ and $i = 2$ are added, the initial conditions on $e_{x,0}$ and $e_{y,0}$ are related by

$$e_{x,0} + e_{y,0} \leq 2a^{col} \quad (1.28)$$

and cannot be chosen independently. The two Eqs. 1.27 for $i = 1, 2$ put additional constrains on the electron phases $\Psi_{x,0}$ and $\Psi_{y,0}$. Both phases are coupled which is a consequence of the cylindrical cross-section of the collimator, even when the initial conditions $e_{x,0}$ and $e_{y,0}$ of the electron fulfills Eq. 1.28. If this constrains are ignored and any initial

electron phases in the interval $[0, 2\pi]$ are considered, one obtains a 4-dimensional phase space which encloses the acceptance of the collimator. This enlarged phase space can be used to yield an upper estimate for the possible electron offset r along the undulator. By Eq. 1.24, after some simple manipulations, one finds

$$r \leq \sqrt{2} \sqrt{a^{col} \max [\beta_x(z), \beta_y(z)]} \quad (\text{circular}). \quad (1.29)$$

For $\beta_x(z) > \beta_y(z)$ the largest transverse offset appears in the horizontal direction ($r \mathbf{e}_x$) while for $\beta_x(z) < \beta_y(z)$ it appears in the vertical direction ($r \mathbf{e}_y$). Thus, to design the collimator it is sufficient to analyze the two special cases of the horizontal and the vertical phase space acceptance where the motion of the electrons are bound to a plane. A scheme of the collimator acceptance cross-section in case of cylindrical collimators is shown in Fig. 1.12(b).

The development of electron offset r along the undulator according to Eq. 1.26 and Eq. 1.29 for a given a^{col} is plotted in Fig. 1.13. The peak values for the electron off-

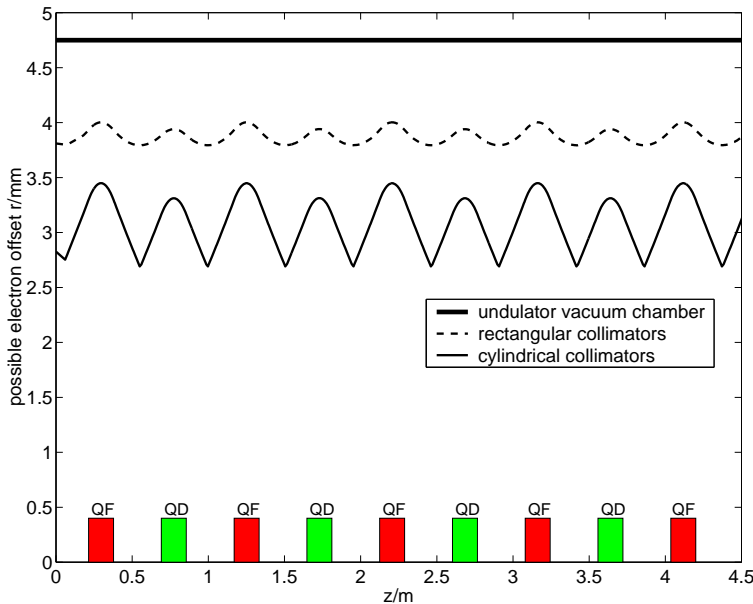


Figure 1.13: Development of the electron radius along the undulator for given a^{col} in case of cylindrical and quadratical collimator cross-sections. The beam energy is 230 MeV.

set appear in both cases at the quadrupoles of the FODO-channel. For given clearances between the largest possible electron offset and the vacuum chamber walls of the undulator, the half gap X of quadratical collimators have to be chosen smaller than the radius R of cylindrical collimators. For increasing electron beam energies the variation of the horizontal and the vertical β -functions along the undulator decreases. For high beam energy the required half gap X approach the value

$$X = \frac{R}{\sqrt{2}}, \quad (1.30)$$

to achieve the same clearances for cylindrical and rectangular cross-sections. Because of this, the apertures defining the acceptance of the collimator have been chosen cylindrically symmetric.

Choice of the collimator acceptance a^{col}

Originally, the experimental program of TTF has foreseen beam studies at bunch charges between 1 nC and 8 nC, with normalized emittances of $2 \mu\text{m}$ and $20 \mu\text{m}$ at beam energy from 150 to 500 MeV. Because of the permanent magnet quadrupoles in the undulator the focusing strength of the quadrupoles decreases inversely proportional with the beam energy. The peak values of the β -functions, β_x^{peak} and β_y^{peak} , are plotted in Fig. 1.14. Caused by the natural focusing of the undulator dipole field, the peak value of the verti-

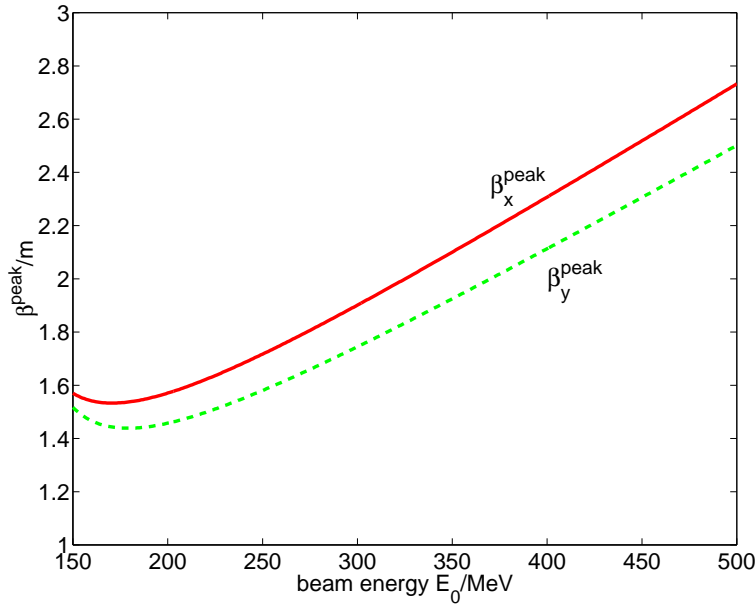


Figure 1.14: Variation of the peak values β_x^{peak} and β_y^{peak} of a periodic FODO-cell structure in the undulator with beam energy E_0 .

cal β -function is always smaller than the one of horizontal β -function. Above 250 MeV the β -functions grow approximately linearly with the beam energy. Since the peak values of the β -function define the area of the inner acceptance ellipse of the undulator, the acceptance a^{und} drops inversely with beam energy. It is smaller in the horizontal plane x than in the vertical plane y ($a_x^{und} < a_y^{und}$). The highest expected beam energy at TTF phase I is 500 MeV. The horizontal β -function has a peak value β_x^{peak} of 2.73 m at 500 MeV. Thus the smallest acceptance of the undulator is calculated to be

$$a^{und} = \frac{R_{und}^2}{\beta_x^{peak}} = 8.27 \mu\text{m} \quad (1.31)$$

With a minimum distance Δx_{clear} of $300 \mu\text{m}$ between the undulator vacuum chamber walls and the electron beam the collimator acceptance must be less than

$$a^{col} \leq \frac{(R_{und} - \Delta x_{clear})^2}{2\beta_x^{peak}} = 3.83 \mu\text{m} \quad (1.32)$$

At 150 MeV and a bunch charge of 8 nC the normalized design beam emittance $\epsilon_{x,y}^N$ of 20 μm sets a the lower limit on the collimator acceptance

$$a^{col} \geq \frac{3^2 \epsilon_{x,y}^N}{\gamma} = 0.6 \mu\text{m}, \quad (1.33)$$

where the 3σ rms-beam emittance has been used to ensure full transmission through the collimator section. This limit would not allow any beam orbit variation at the collimators. It has been decided to choose the upper limit given in Eq. 1.32 for the acceptance of the collimator. The decision was motivated by the following arguments:

1. It is very challenging to achieve the design beam emittance of 20 μm for high bunch charges. Thus the beam transport through the collimator might get difficult at low energies.
2. In the presence of large non-gaussian beam tails, the losses at the collimator section might reach unacceptable values concerning the radiological dose levels outside the tunnel shielding. In this cases, the beam operation has to be interrupted.
3. The absorbed electrons cause an electromagnetic shower of secondary particles which cannot be fully stopped at the collimator. A fraction of secondary particles irradiate the undulator and contributes to the dose budged.
4. The required operation time to perfectly match the beam from the linac to the collimator increases significantly for smaller collimator apertures. It requires full knowledge of the 4-dimensional phase space distribution delivered by the linac which is difficult to determine experimentally at TTF phase 1.
5. Most time of linac operation in TTF phase I is dedicated to experiments at beam energies between 200 MeV and 300 MeV. In this energy regime the clearances between electrons of the beam and the wall of the vacuum chamber is always larger than 1 mm which should be sufficient to guarantee a safe beam operation.

1.2.4 Layout of the two stage spoiler-absorber system

In the previous section, the optimum conditions for the beam matching from the linac into the collimator and the adaption of the collimator phase space acceptance to the undulator has been derived. In this section the realization of the collimator concept and the basic layout of the collimator section are presented.

The heart of the collimator are the two apertures that restrict the four dimensional phase space such that no electrons of a mono-energetic beam can hit the undulator vacuum pipe. Previously, it has been assumed that the collimators are perfect absorber, hence an electron would deposit its whole energy in the collimator. In reality, due to the finite thickness and the edges of a collimator, a substantial amount of energy of the incident electrons which is carried by a large number of secondary particles can damage the undulator permanent magnets. Additional collimators are required to remove the secondary particles from the beamline. It is useful to distinguish two types of collimators. The collimators that limits the acceptance phase space of the beamline are called spoilers, while the collimators which remove the secondary particles created at the spoilers, are

called absorbers. The requirements on the spoilers are different from that of the absorbers. The spoilers of the collimator system can directly be hit by the electron beam. Due to the small beam cross-sections the spoilers might be destroyed if a too large number of bunches within a bunch train penetrates through the spoiler walls. Their design are optimized to withstand as many electron bunches as possible to gain time for a fast protection system to inhibit the beam operation in case of an accidental beam loss. The length of the spoilers are chosen such, that the intercepted electrons are sufficiently perturbed to allow the removal by a downstream absorber system without spoiling the nominal beam. For that, two different techniques can be used:

1. Due to the emission of bremsstrahlung the primary electrons traveling a distance x through the spoilers loose in average the energy

$$\langle E(z) \rangle = E_0 \cdot \exp\left(-\frac{z}{X_0}\right) \quad (1.34)$$

where X_0 is the radiation length of the spoilers. For sufficient thick spoilers (typically 1-2 X_0) most of the electrons loose enough energy to achieve in a dispersive section a transverse separation from the proper beam where absorbers can be placed for removal of the secondary particles.

2. Due to multiple scattering in the material the primary electron receives a large angle. The electron angle is transformed after a proper phase advance to an offset which then allows the removal by an absorber.

Because of space limitations in TTF phase I a dispersive section could not be incorporate into the beamline. Thus, only the second mechanism allows to remove the degraded primary electrons and the additionally produced secondary particles.

The absorber system is located in the shadow region of the spoiler acceptance. It cannot be hit by the beam directly. The electromagnetic shower in the absorber is mainly produced by lower energy particles leaving the spoilers and to a small fraction by degraded electrons scattered from the spoiler edges. The fraction of energy leaving the absorber through its edges is usually small and not anymore critical for the undulator safety. To dissipate the energy of the secondary particles within a reasonable absorber length (typically 10-30 X_0) a material with short radiation length X_0 is chosen.

In Fig. 1.15, a scheme of the collimator section shows the two spoilers defining the acceptance phase space of the collimator. The spoilers are separated by a drift space L of 2.5 m length. The choice of the β -function along the drift space defines the nominal beam cross-section at the spoilers and the radius of the spoilers. The nominal beam cross-section at the spoilers determines the time until the beam can destroy the spoilers. The radius of the spoilers determines the strength of the wakefields exited at the spoilers. The optimum choice for the β -function is achieved if the values of $\beta(z)$ at both spoilers are maximized. The β -function and the phase advance Ψ along a drift space can be expressed by

$$\beta(z) = \beta^* + \frac{(z - z_*)^2}{\beta^*} \quad (1.35)$$

$$\Delta\Psi(z_1, z_2) = \int_{z_1}^{z_2} \frac{dz}{\beta(z)} = \arctan\left(\frac{z_2 - z_*}{\beta^*}\right) - \arctan\left(\frac{z_1 - z_*}{\beta^*}\right), \quad (1.36)$$

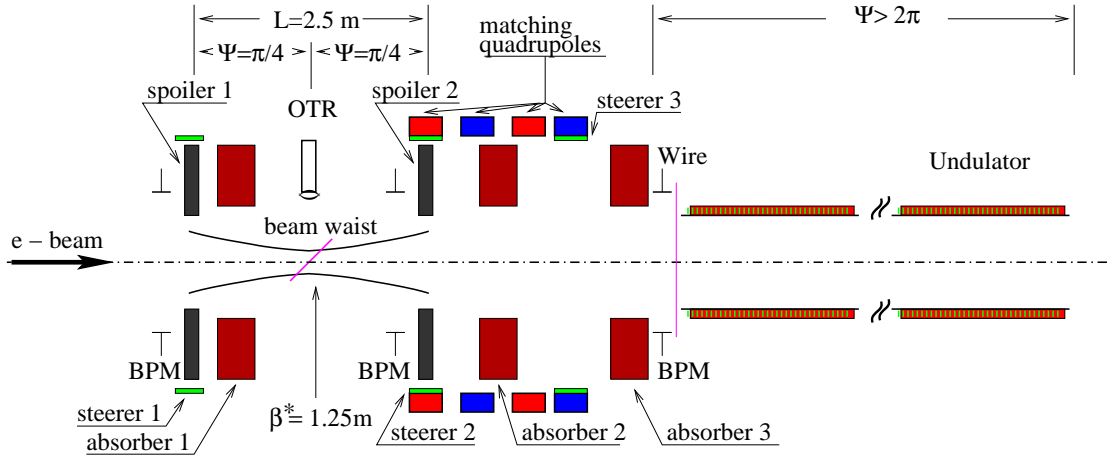


Figure 1.15: Scheme of the collimator section.

where β^* is the value of the β -function at the waist located at z_* . Let z_1 and $z_2 = z_1 + L$ denote the longitudinal positions of the two spoilers in the beamline. The condition $\beta(z_1) = \beta(z_2)$ can only be fulfilled if the waist is located at the center between the two spoilers ($z_* = z_1 + L/2$). $\beta(z)$ describes the acceptance β -function of a two aperture system β^{col} only if the phase advance $\Delta\Psi$ between the two spoilers is equal to 90° . By Eq. 1.36, the value of the β -function at the waist is determined to be $\beta^* = L/2$. Thus, at the design optics the envelope of the electron beam is symmetrically with respect to the center point between the spoilers. The point z_* has previously been called the symmetry point of the collimator. The map of the spoiler edges in phase space at the symmetry point yields a rhombus and is shown in Fig. 1.11 together with the vacuum chamber of the undulator in case of matched conditions.

Finally, the spoiler radius R_{sp} for an acceptance of $a^{col} = 3.83 \mu\text{m}$ (see Eq. 1.32) and with the values of the β -function at the spoilers $\beta(z_0 \pm L/2) = L$ yields (see Eq. 1.16)

$$R_{sp} = \sqrt{a^{col} \cdot L} \approx 3 \text{ mm}. \quad (1.37)$$

The spoilers are made of aluminum.

The largest fraction of the collimated beam is lost at spoiler 1. The absorber 1 protects the diagnostic equipment in the collimator section, but has little influence on the radiation background in the undulator. Two more absorbers (#2 and #3 in Fig. 1.15) are needed to remove the secondary particles produced at spoiler 2. All absorber blocks are made from copper. The geometry of the spoilers and the absorbers are discussed in chapter 3. The matching of the optics from the collimator to the undulator requires the adaption of four independent parameters $(\beta_x, \alpha_x, \beta_y, \alpha_y)$. For given beam matrices σ_x and σ_y in the collimator at $z = z_*$ and the undulator at $z = z_{und}$ the transfer matrices \mathbf{M}_x and \mathbf{M}_y have to fulfill the equations

$$\sigma_x(z_{und}) = \mathbf{M}_x \cdot \sigma_x(z_*) \cdot \mathbf{M}_x^T \quad \text{and} \quad \sigma_y(z_{und}) = \mathbf{M}_y \cdot \sigma_y(z_*) \cdot \mathbf{M}_y^T. \quad (1.38)$$

The four degrees of freedom are obtained by the four matching quadrupoles of the collimator section (see Fig. 1.15). The Twiss parameters at the symmetry point of the collimator

z_0 are

$$\beta_x = 1.25 \text{ m}, \quad \alpha_x = 0, \quad \text{and} \quad \beta_y = 1.25 \text{ m}, \quad \alpha_y = 0, \quad (1.39)$$

and independent of beam energy. The Twiss-parameters at a given point in the undulator depend on the beam energy (see Fig 1.14). Therefore, the four matching quadrupole gradients have to be adjusted if the energy in the linac is changed. In Fig. 1.16 the required variation of the four matching quadrupole gradients g with the energy is plotted.

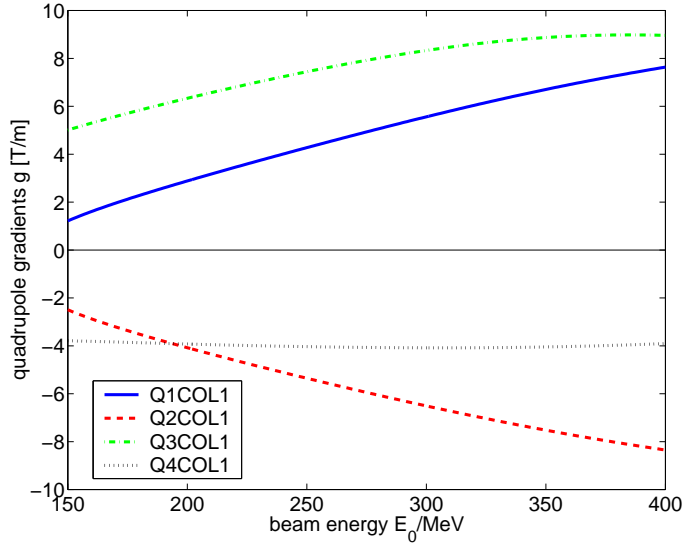


Figure 1.16: Variation of the matching quadrupole gradients at the collimator section with beam energy E_0 .

For matching the beam from the linac to the collimator section another set of four quadrupoles at the upstream section ACC3 are foreseen. The optics from the beginning of ACC3 to the end of the first undulator module is plotted in Fig. 1.17.

1.2.5 Description of the collimator beamline

The collimator section is shown in Fig. 1.18. The overall length is 5.6 m. The first spoiler and the first absorber are surround by 10 cm lead shielding. The second spoiler is installed inside the first matching quadrupole Q1COL1. The second absorber is 1.2 m long and mounted inside the matching quadrupoles Q2-Q4COL1. The third absorber is directly in front of the undulator. It is the last barrier for secondary particles. To reduce the background for wire scanner measurements at the undulator the absorber 3 is additionally surrounded by a lead shield of 30 cm diameter and 20 cm length. To operate the collimator section various diagnostic components are required.

The beam current can be measured before and behind spoiler 1 by the toroids T5 and T6. At short macropulse lengths ($\leq 10 \mu\text{s}$) the toroids can measure the beam current with an accuracy of about 1-2%. To monitor the beam losses at spoiler 1 with higher accuracy additional photomultipliers (PM1 and PM2) are located behind absorber 1. The radiation level at the collimator section is too large to use scintillators. The photomultipliers are

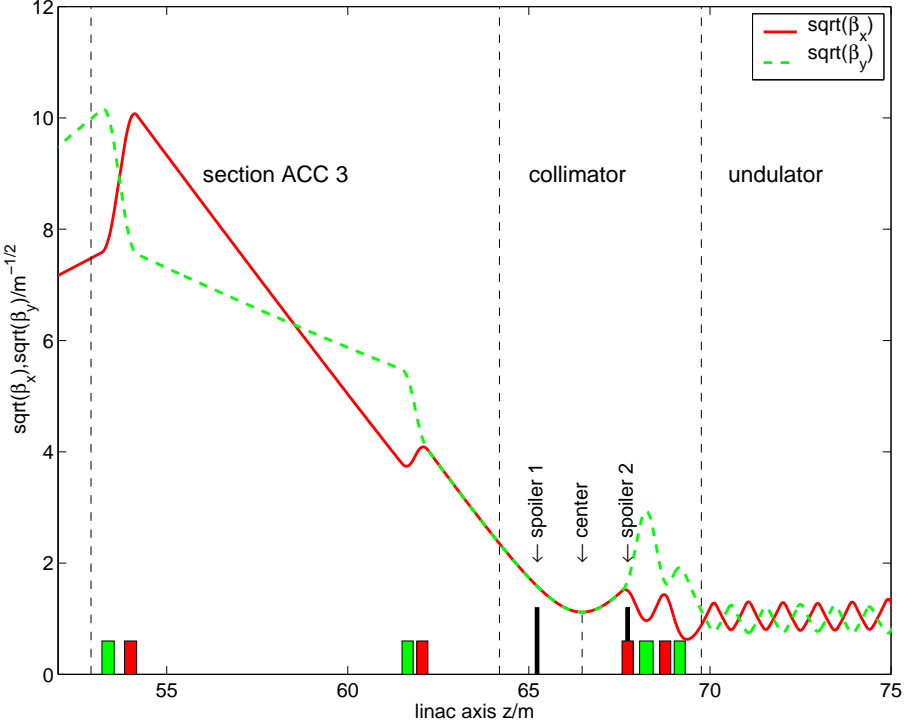


Figure 1.17: Optics from the exit of the second acceleration module to the end of the first undulator module. The first four quadrupoles in section ACC3 are used to adapt the beam from the exit of section ACC2 to the center of the collimator. The second four quadrupoles connect the center of the collimator to the entrance of the undulator. The gradients of the matching quadrupoles are determined by the choice of the beam energy (here 230 MeV). The location of the two spoilers are also shown.

equipped with an aluminum cathode and are sensitive to photon energies above 100 keV. The beam losses at spoiler 2 are measured with PM3, while PM4 is used to monitor the production of secondary particles in the second spoiler. To localize the beam losses two additional lead walls placed behind the spoiler-absorber system 1 and between the quadrupoles Q2 and Q3 are mounted.

To adjust the beam orbit properly to the center line of the two spoilers, two beam position monitors (BPM) are installed directly upstream of the spoilers. The beam position monitors are reentrant broad-band cavities with a resolution less than 20 μm . The electrical axis agrees within 300 μm with the mechanical symmetry axis which is aligned with respect to the axes of the spoilers.

The transverse charge distribution of the bunches can be measured by inserting a thin mylar foil coated with aluminum. When the electrons of the beam transmit the foil transition radiation is emitted in backward and forward direction. The optical transition radiation is proportional to the transverse charge density and is recorded with a CCD camera. For standard beam operation the foil is not inserted. Beside the OTR target, a cromox screen made of 0.5 mm thick aluminum can be inserted. The sensitivity of the cromox screen is much higher than of the OTR-screen but its response is non-linear and less suitable for beam profile measurements. The screen station is located at the symmetry point of the collimator where the electron beam has a waist with an equal rms-size in horizontal and vertical direction.

To achieve the ultra-high vacuum (typically 10^{-10} mbar) required for the superconducting

acceleration modules the collimator section is equipped with five vacuum pump stations. Each station consists of a titan sublimation and an ion getter pump. A fast shutter at the entrance of the collimator section allows to separate the downstream beamline from the cold sections upstream within a shutter time of 40 ms.

1.2.6 Beam steering concept

A total number of eight dipole correctors are installed for horizontal and vertical orbit correction. To locate the beam to the center of the two spoilers the steerers H1ACC3, H1COL1 and V1ACC3, V1COL1 are used. The beam positions are measured with the beam position monitors BPM1COL1 and BPM2COL1. Both BPM's have been aligned to the center of the spoilers and thus can be used to steer the beam properly into the collimator.

A quadrupole with a transverse offset induces an angle to the beam. Due to misalignments of the matching quadrupoles Q1-Q4COL1 the beam can receive an angle and an offset when it leaves the collimator section. The main purpose of the steerers H2-H3COL1 and V2-V3COL1 is to correct for quadrupole misalignments and for an offsets between the collimator section and the first undulator module. Like the gradients of the matching quadrupoles, the dipole field of the steerers are determined by the choice of the beam energy. The steerer settings have a large impact on the collimation properties of the collimator section. Due to space limitations the correctors are implemented as additional yoke coils at the first and last matching quadrupole (Q1COL1 and Q4COL1). For that reason their field quality is poor, but adequate for the purpose. The beam steering concept for the collimator is sketched in Fig. 1.19. Details concerning orbit corrections caused by quadrupole displacements are discussed in Sec. 3.7.

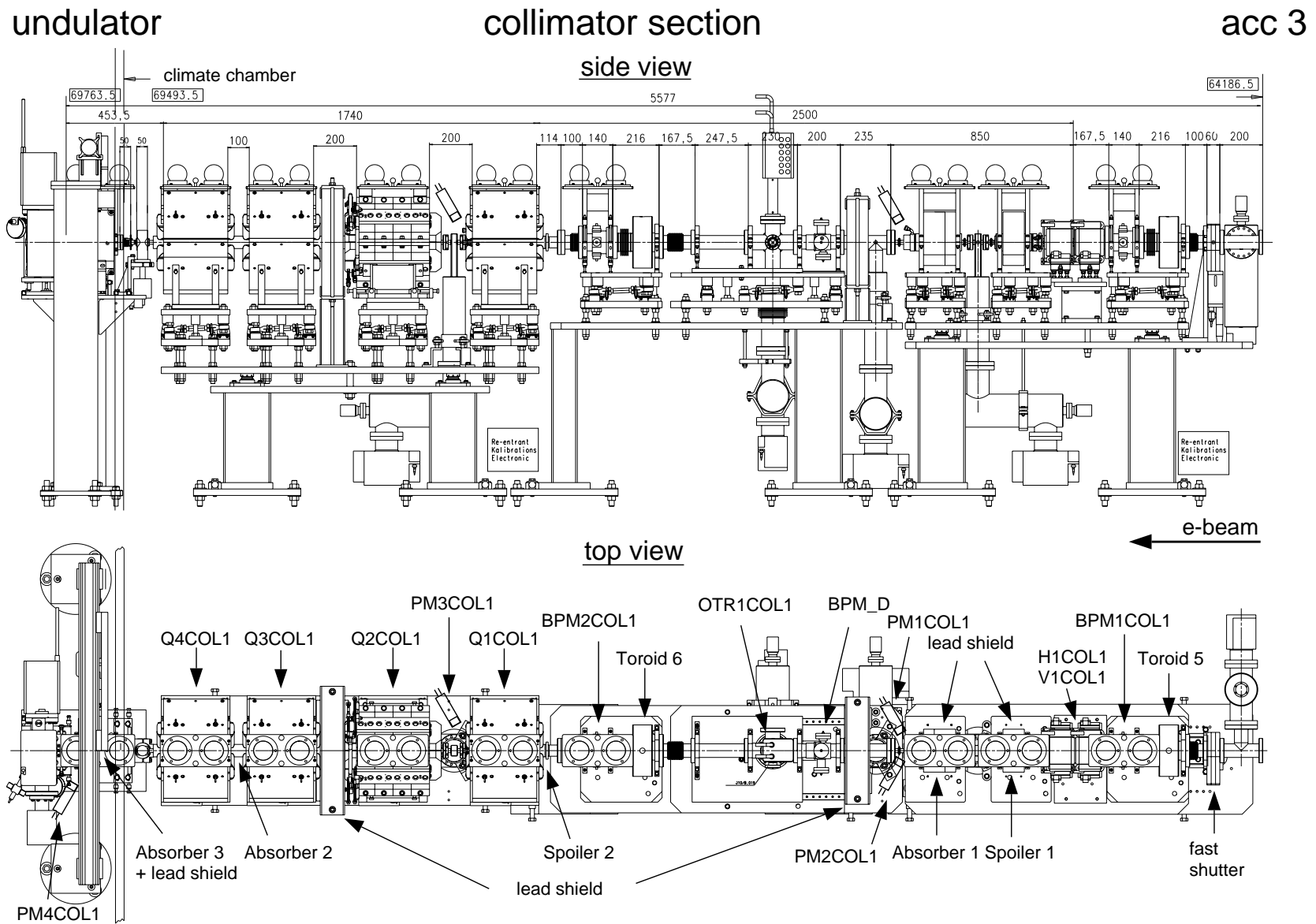
1.2.7 Using the collimator section as a beam dump

For certain experiments it is required to disturb the beam orbit or the transverse beam size by such an amount that a transport through the undulator becomes impossible. In such cases the collimator section can be used as a beam dump provided that the total beam power is restricted to less than 250 W. This application is possible because of the following features:

- additional shielding (lead and concrete shields)
- low activation rate of the material (aluminum)
- water cooling system for the collimators
- temperature control of the collimators
- current measurements available
- steerers for dumping the beam available.

Beam stop at high energy: In the short pulse mode (macropulse length $\leq 10 \mu\text{s}$) and for sufficiently large beam sizes the beam can be stopped at the collimator without any difficulties. At beam energies above 150 MeV the steerers H1ACC3 and V1ACC3 can

Figure 1.18: Overview of the collimator section.



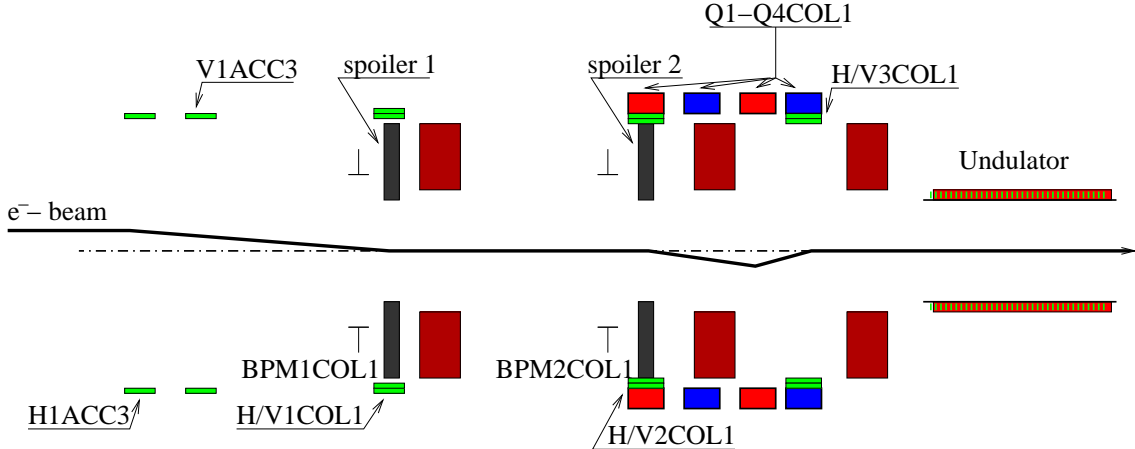


Figure 1.19: Scheme of beam steering through the collimator section.

be used to move the beam onto the first spoiler (≈ 1.0 cm displacement from beamline center). The steerers H1COL1 and V1COL1 are chosen such that the electrons passing the first spoiler are bent onto the second spoiler. Using this procedure, the yield of secondary particles reaching the undulator is small.

Beam stop at low energy: For higher-order mode experiments the collimator has also been used as a beam dump at low energy (≤ 40 MeV), but with a long macro pulse duration of 0.5 ms. The total beam power at 1 Hz repetition rate is about 160 W. To stay below the material stress limitation for aluminum a rms-beam size of at least 5-6 mm at the spoilers is required. A simple way for monitoring the rms-beam size is obtained by centering the beam at the first spoiler and monitoring with toroid T6 the fraction of the charge that passes through the spoiler. Since the aperture of the collimator has a diameter of 6 mm the ratio of the charge measured before and behind the spoiler 1 depends on the rms-beam size. A safe operation is achieved if the charge at T6 does not exceed 15% of the charge measured at the toroid T5. At beam energies below 40 MeV nearly all energy of the incident electrons is absorbed in the spoiler itself and the yield of secondary particles is corresponding low.

1.2.8 Radiation shielding

The beam reaches its final energy after acceleration module 2. Electrons with an improper orbit are removed in the collimator section. Because of radiological safety, the radiation produced in the collimators requires additional concrete shielding, which has been added to the standard shielding of the linac tunnel.

The parameters with the largest relevance for the radiological safety are the electron beam energy E_0 and the average beam power P . The electron beam energy decides which physical mechanisms are responsible for the production of secondary radiation while the beam power determines the intensity of radiation. The interaction of a primary electron with the collimator starts the development of an electromagnetic cascade, so the dominant radiation consists of photon, electrons and positrons. The threshold for neutron production is in the range of 6-13 MeV for most of the materials [9]. Thus, in the collimator section, neutrons produced by photons in the energy region of the giant-resonances must be considered. At beam energies above 150 MeV, neutrons produced in photonuclear reactions

via the quasi-deuteron effect and in processes involving the π meson production become important [9]. The peaks of the photopion cross-section are only a fraction of the ones for the giant resonances, but the liberated neutrons have higher energies (>25 MeV) and are much more penetrating than the neutrons produced by giant resonance with comparable small energies (mainly at ≈ 1 MeV). The neutrons, mainly high-energy neutrons, make the dominated contribution to the dose rates outside of the massive concrete shields, while inside the tunnel the electromagnetic part (γ, e^\pm) dominates completely. The first peak of the photopion production cross-section is centered at photon energies of about 300 MeV with a resonance width of about 110 MeV [9]. Therefore, the yield of high-energy neutrons increases strongly with the electron beam energy in the range between 200 MeV, the onset of the production mechanism, and 1 GeV, where the yield approximately scales proportional to the beam power.

The neutron dose equivalent produced by an electron beam incident on an aluminum target³ at 230 MeV and 460 MeV beam energy is reported in [10]. For the numerical simulations the Monte Carlo code FLUKA is used [11, 12]. The geometry of the tunnel shielding is shown in Fig. 1.20. Figure 1.20(a) shows the spatial distribution of the dose equivalent (Sv/h) for a beam loss of 10^{15} electrons per hour and a beam energy of 230 MeV. The largest dose rate of $1\text{-}10 \mu\text{Sv}/\text{h}$ outside the tunnel is calculated perpendicular to the incident beam direction z . At a beam energy of 460 MeV the equivalent dose rate increase to $10\text{-}100 \mu\text{Sv}/\text{h}$ shown in Fig. 1.20(b). The additional heavy concrete shield at the collimator section is shown in Fig. 1.20(c). The blocks with 80 cm thickness in x -direction are positioned at the first and second spoiler. The pictures show the irradiation of the first spoiler. With the additional shielding blocks the equivalent dose rate related to neutrons at 90° is reduced to $1\text{-}10 \mu\text{Sv}/\text{h}$. The results are summarized in Table 1.1. The number of electrons ($10^{15} e^-/\text{h}$) corresponds to an average beam loss of

	tunnel shield only	+ concrete blocks
230 MeV	$10 \mu\text{Sv}/\text{h}$	$1 \mu\text{Sv}/\text{h}$
460 MeV	$100 \mu\text{Sv}/\text{h}$	$10 \mu\text{Sv}/\text{h}$

Table 1.1: Dose equivalent due to neutrons for a beam loss of $10^{15} e^-/\text{h}$. At design beam current and design duty cycle (8 mA, 0.8%) the loss of $10^{15} e^-/\text{h}$ corresponds to $6\cdot 10^{-4}$ losses of the beam current.

0.06% at TTF design parameters (beam current 8 mA, duty cycle 0.8%). The tolerable dose equivalent outside the tunnel should stay below $10 \mu\text{Sv}/\text{h}$. The beam losses at the collimator which produce $10 \mu\text{Sv}/\text{h}$ outside the tunnel amounts to 0.6% at 230 MeV and 0.06% at 460 MeV.

The neutron doses outside the tunnel shield has been measured at 230 MeV beam energy [10]. For beam losses of $10^{15} e^-/\text{h}$ at section ACC3 (only tunnel shield) and at the collimator section (+ concrete blocks) the measured data are in good agreement with the simulated ones.

1.2.9 Energy dependence of the collimation

The permanent-magnet quadrupoles in the undulator cause an energy dependence of the optics. The transfer matrix through the undulator as well as the optimum Twiss-

³Geometry of aluminum target: cylinder with 1 cm inner radius, 3.4 cm outer radius and 40 cm length.

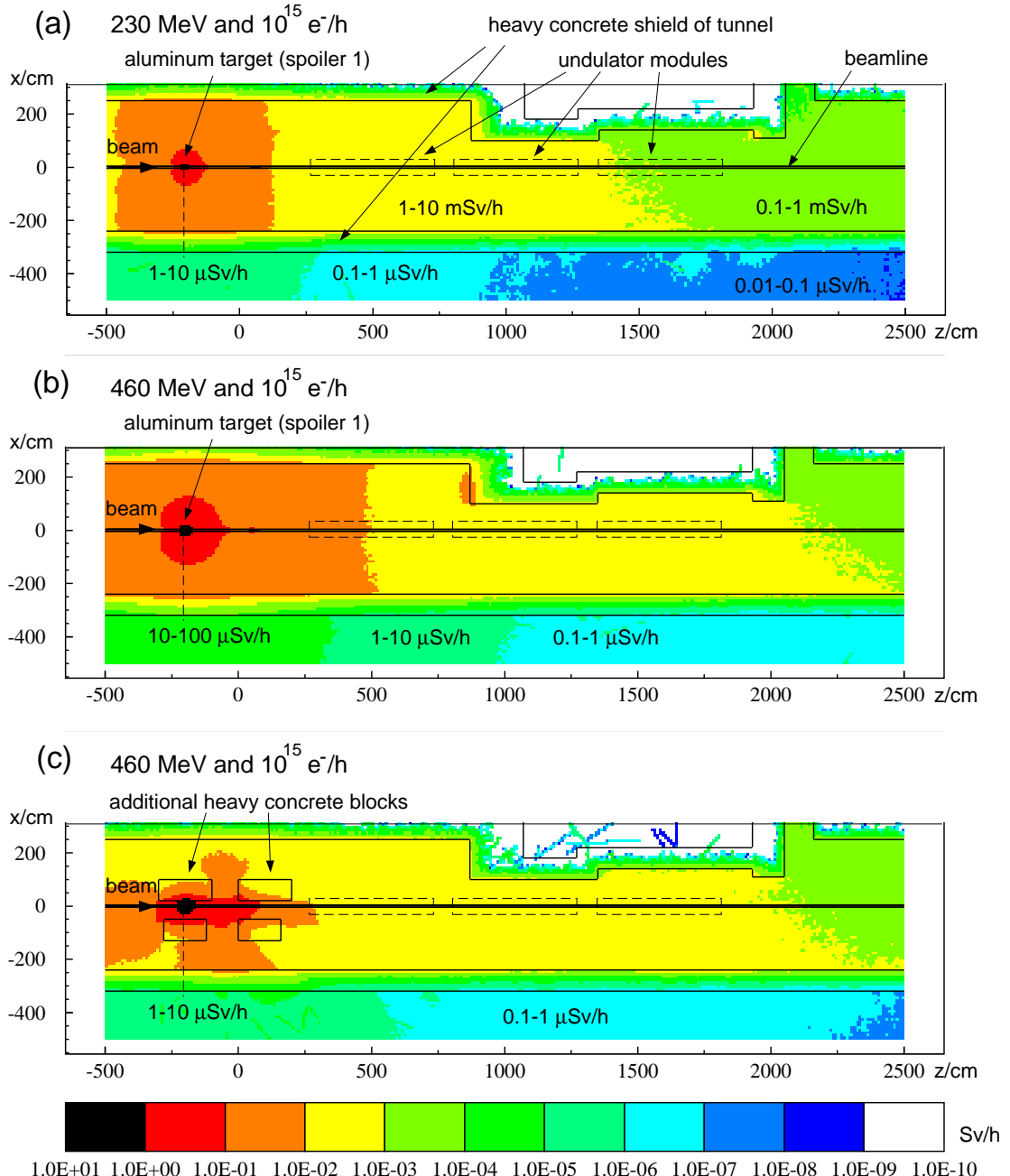


Figure 1.20: Dose equivalent caused by neutrons calculated with FLUKA for beam losses at the collimator section. (a) beam loss of 10^{15} electrons per hour at a beam energy of 230 MeV incident on a thick aluminum target. (b) the beam energy is increased to 460 MeV. (c) with additional heavy concrete blocks as used to shield the collimator section. The dose rates due to bremsstrahlung is not shown. Those rates are inside the tunnel typically 2 orders of magnitude larger than the ones due to neutrons.

parameters at the entrance of the undulator vary with the beam energy. This is corrected by a proper choice of the gradients in the collimator matching quadrupoles (see Fig. 1.16). For a sudden change of the beam energy i.e. by a change of the rf-phase in the acceleration module, the quadrupoles have improper values resulting in an improper adaption of the collimator acceptance phase space to the undulator acceptance phase space. Let denote

E_0 the energy for which the beam is properly matching into the undulator by the actually adjusted quadrupoles gradients. For increasing energy deviations $\Delta E/E_0$, the minimum distance between the possible electron offsets and the undulator vacuum chamber begins to shrink. For too large $\Delta E/E_0$, electrons can be lost in the undulator.

The acceptance β -function of the collimator, β^{col} , describes the possible electron offsets along the undulator. In section 1.2.4 the initial conditions for β^{col} at the symmetry point of the collimator has been derived. Because the beamline between the two spoilers is a drift space, the volume of the acceptance phase space of the collimator remains unchanged and no chromatic corrections have to be applied on the initial conditions. The development of β^{col} through the collimator matching quadrupoles and the undulator FODO-channel, however, strongly depends on the energy E . For $E_0 = 230$ MeV, in Fig. 1.21 is plotted the variation of β^{col} for three different energies E in horizontal and vertical plane. For $E \neq E_0$ a beat of β -functions is observed which causes at the focusing quadrupoles in the undulator larger peak values than the periodic solution for the FODO-channel at $E = E_0$. The energy dependence of β^{col} is caused by chromatic aberrations in the focusing quadrupoles [13].

Due to the large values of the vertical β -function at the second matching quadrupole (Q2COL1) the beat along the undulator is stronger in vertical direction than in horizontal direction. The energy bandwidth of the collimator δ_{col} can be defined by the smallest deviation $\Delta E/E_0$ required to create an overlap between the outer collimator acceptance phase ellipse and the inner undulator acceptance phase ellipse. The energy bandwidth might be asymmetrical with respect to E_0 . Using Eq. 1.29, p. 29, one can write ($\delta = \Delta E/E_0$)

$$\delta_{col,\pm}(E_0) = \max_{\delta} \left\{ \delta \quad \text{with} \quad \sqrt{\max_{i=x,y} \left[\beta_i^{peak}(\pm\delta, E_0) \right]} \leq \frac{R_{und}}{\sqrt{2} \epsilon^{col}} \right\} \quad (1.40)$$

where $\beta_{x,y}^{peak}$ are the peak values of $\beta_{x,y}^{col}$ along the undulator. For $E_0 = 230$ MeV the variation of $(\beta_{x,y}^{peak})^{1/2}$ with δ is plotted in Fig. 1.22.

So far, it has been assumed that the beam as a whole has an energy E different from E_0 , but the beam has been assumed to be mono-energetic. In a real machine the electron beam has an energy distribution which depends on the operation mode of the linac. In most cases, the rms-energy spread $\sigma_E = dE/E$ is small compared to the energy bandwidth of the collimator. This might change, if the linac operation includes the longitudinal compression of the electron bunches in magnetic chicanes. To yield a compression of the bunch in a magnetic chicane a time-energy correlation by an off-crest acceleration in the cavities is imposed to the bunch. In case of initially long bunches the off-crest acceleration causes a non-gaussian energy tail. Together with the asymmetric behavior of the β -beat the optimum operation condition might differ from the simple mono-energetic considerations as developed before.

Furthermore, for deriving the results in the last sections, several effects concerning alignment of the components, influence of higher order magnetic field errors have not been taken into account. Most of these effects reduce the energy bandwidth of the collimator. The following list summarises the relevant topics:

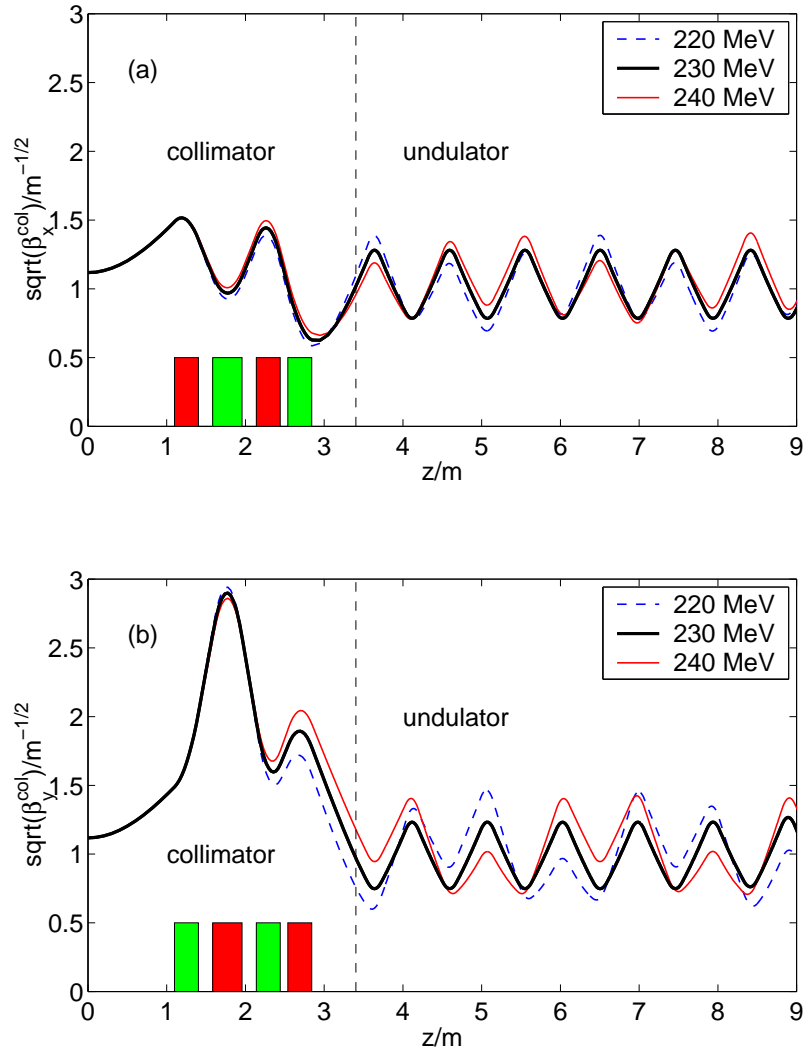


Figure 1.21: Beat of collimator acceptance β -function due to an energy variation by ± 10 MeV. The plot (a) shows the horizontal plane and plot (b) the vertical plane.

- misalignments of quadrupoles (collimator and undulator)
- errors of the matching quadrupole gradients of the collimator
- non-linear field-errors of the undulator
- mismatch between the undulator modules
- difference in gradients between the undulator modules
- octupole field components in the undulator quadrupoles
- displacement of spoilers
- displacement of undulator vacuum chamber
- influence of correction steerers.

The influence of the errors are studied by Monte Carlo calculation and is discussed in chapter 3.

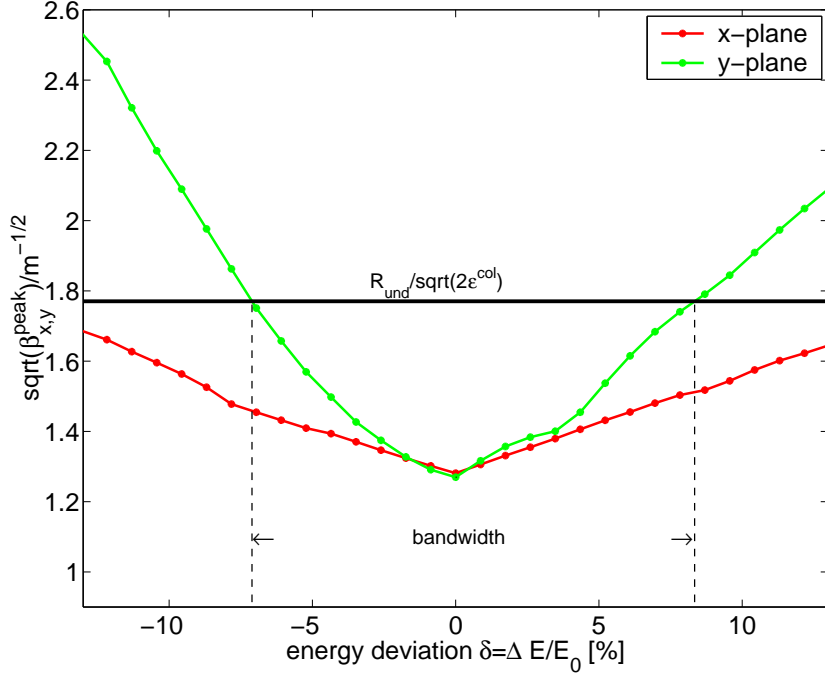


Figure 1.22: Variation of the peak values β_x^{peak} and β_y^{peak} with the energy deviation $\delta = \Delta E / E_0$ for quadrupole gradients adjusted to $E_0 = 230$ MeV. The horizontal line indicates the limit where the acceptance phase ellipse of collimator overlaps with the acceptance phase ellipse of the undulator. The energy bandwidth of the collimator at 230 MeV is $\delta_{col} = -7.1\%, +8.3\%$.

1.2.10 Consequences of the energy dependence and the radiological shield

The finite bandwidth of the collimation system puts constraints on the linac operation. The direct consequence is that the beam energy has to be within narrow bandwidth and either the collimator matching quadrupoles have to be corrected to the actual beam energy or vice versa. A method to measure the beam energy is described in App. B. In section 1.2.2 the electrons in a beam have been described by phase ellipses. The definitions of the beam phase ellipses are based on the beam rms-sizes and rms-divergences. For transverse charge distributions of gaussian shape the β -functions and the emittances are well suited to describe the propagation of the beam in the linac. For more complicate distributions, the values of β , α and ϵ reflect the properties of the beam only insufficiently. Particularly, the beam properties important for FEL operation differ significantly from that which are relevant for the protection of the undulator. For the FEL operation, the charge density at the core of the bunch determines the achievable FEL power and an optimization of the linac has to focus on this part of the bunch charge. To protect the undulator and for the radiological protection, the electrons located in the beam tails of the charge distributions (beam halo) are important and may cause interruptions of the machine operation in cases of too large beam losses.

Beside the electron beam, which is produced by the UV-laser in the rf photo-gun, additional electrons, called dark current, might be accelerated in the linac. The energy spectrum of the dark current differs significantly from the energy spectrum of the electron beam. Thus, even if the dark current is several orders of magnitudes smaller than the regular current, it can dominate the radiation losses in the undulator.

Thus, the linac parameters influencing the dark current and the dynamics for the beam halo are of interest. A better knowledge opens the possibility

1. to avoid the production of dark current and beam halo
2. to improve the collimator operation
3. to define the positions and apertures for additional collimators
4. to reduce the activation of beamline components
5. to accomplish the active protection system.

The following chapter is dedicated to describe the properties of the electron beam and the dark current at the different sections of the linac.

Chapter 2

Development of Beam and Dark Current in the Linac

2.1 RF Photo-Injector

The installation of an rf-photocathode gun capable to deliver high bunch charges (1-8 nC) with low emittances (2-20 μm) allows various experiments for the future TESLA linear collider and its integrated X-Ray FEL. One of the main goals for TTF phase 1 is the proof-of-principle experiment of a SASE-FEL operating at wavelength in the VUV (200-50 nm) [14]. In addition, experiments related to the high peak currents of several hundred amperes such as the power deposition of wake fields in the superconducting cavities or coherent synchrotron radiation emitted in the bunch compressor are of essential importance. Operation of full beam current with long rf-pulses as an integral test of all sub-systems along the linac has recently been performed where valuable experiences with the rf injector were gained.

A mandatory step for an electron beam that drives a SASE-FEL was the development of a compensation scheme counteracting the space-charge induced projected emittance growth in photoinjectors producing electron beams with low emittance and high phase space densities in all three dimensions [15, 16].

In Fig. 2.1 the side-view of the rf gun is shown [17, 18]. The electrons of a bunch are produced by the photo-electric effect using a UV-laser pulse impinging on a Cs_2Te photocathode of high quantum efficiency (0.5-1%) [19]. The electron bunch is accelerated rapidly by strong electromagnetic fields in a 1 1/2-cell room-temperature copper gun cavity. With an acceleration gradient of 35 MV/m at the cathode the electron energy at the exit of the gun reaches 3.8 MeV. The resonance frequency of the cavity is 1.3 GHz. The rf power of 2.2 MW with a pulse duration of 900 μs is fed into the full cell of the gun cavity by a side-coupled waveguide [20].

Beam focusing is provided by the primary and the secondary solenoids. The primary solenoid acting on electrons of low energy is subdivided into two coils with opposite current flow. This guarantees a very small magnetic field remaining on the cathode which can be tuned to zero by using a third small correction coil [17].

The rapid acceleration, the fringe field focusing and the helical path of the electrons in the solenoid field counteract the emittance blowup caused by space charge forces (see Sec. 2.1.2). The electron beam leaving the gun is injected into the superconducting booster cavity to increase the beam energy to 16.5 MeV.

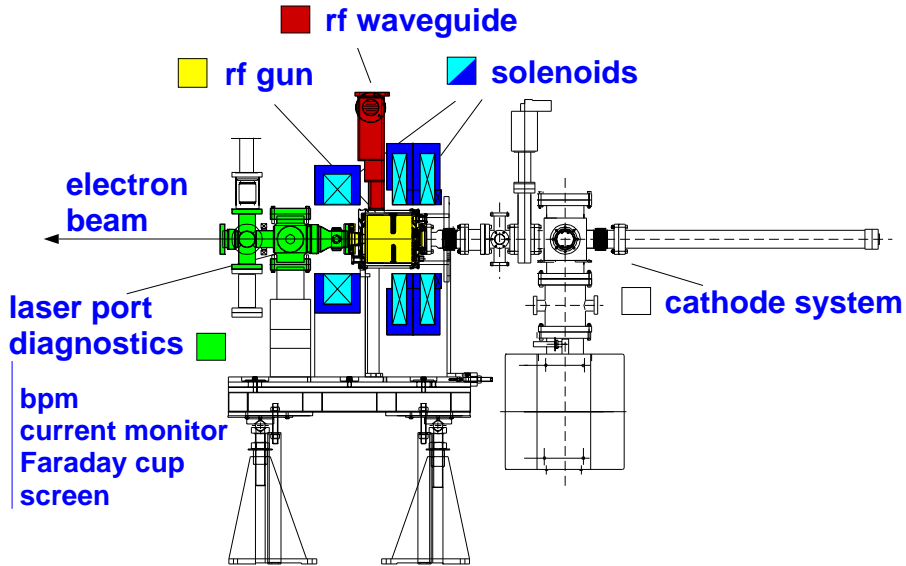


Figure 2.1: Drawing of the TTF rf gun. On the right hand side the photocathode system is shown. At the center, the gun body and the rf-input coupler, enclosed by the primary (right) and secondary solenoid (left). The laser port is placed downstream the secondary solenoid. A small mirror guides the laser beam onto the cathode at the back plane of the gun.

The design parameters of the injector for the collider mode (TTF) and the Free-Electron laser mode (FEL) are summarized in Table 2.1[21].

Parameter	units	TTF		FEL
		(a)	(b)	
rf frequency	GHz		1.3	
repetition rate	Hz		10	
pulse train length	μ s		800	
pulse train current	mA	8	9	9
bunch spacing	μ s	1	0.444	0.111
bunch charge	nC	8	4	1
rms bunch length	mm	2/1	2/1	2/0.8
normalized emittance	μ m	20	10	2
energy spread	%		0.1	

Table 2.1: Injector design parameters for the collider mode (TTF) and the Free-Electron laser mode (FEL) [21]. The design bunch length before and behind the bunch compressor I is given.

Laser system

A key element of the injector is the laser system sketched in Fig. 2.2. The laser design is demanding by the unusual requirement of providing synchronized picosecond UV pulses in 0.8 ms long pulse trains with high stability and reliability requirements [22]. An actively mode-locked pulse train oscillator (PTO) based on Nd:YLF at a wavelength of 1047 nm provides a 3 ms long output pulse train of 1 W. Mode locking is established by an acoustooptic mode locker driven by a 27 MHz rf signal which is delivered by the TTF

master oscillator [23]. Before the amplification process, the 54 MHz pulse train output (zero crossing of the 27 MHz) of the PTO is reduced to the desired train length and the number of pulses in the train using a Pockels cell together with a polarizer.

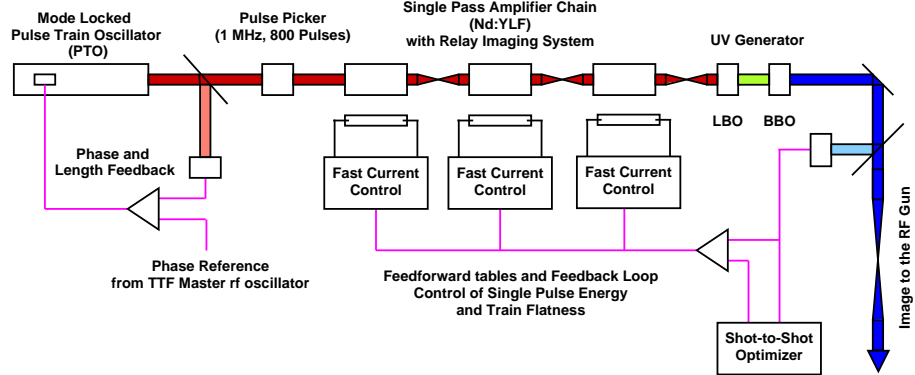


Figure 2.2: Schematic overview of the photo-injector laser system [22].

In a first phase, laser pulse rates of 0.1, 1, and 2.25 MHz have been realized, where the number of pulses are adjustable from 1 to 1800 at 2.25 MHz. The selected laser pulses are amplified in a single pass to $200\text{ }\mu\text{J}$ by a linear chain of three Nd:YLF amplifiers. The amplitude stability of the laser pulse train is controlled by the adjustable gain of the amplifiers and programmable power supplies setting the flash-lamp currents in time steps of $10\text{ }\mu\text{s}$ by predefined feed-forward tables. Since the work function of the Cs_2Te cathode reaches its maximum at about 5 eV, the fundamental wavelength is converted into UV (4.7 eV) by means of an LBO crystal (green light) and by an BBO crystal (UV). The conversion efficiency from 1047 nm to 262 nm is about 15% which is sufficient to produce electron bunches of 8 nC charge. The output of the PTO, the phase of the pulses relative to the reference and the pulse train after amplification in the green is shown Fig. 2.3(a) [24]. The laser pulse shape in the UV is one of the most critical parameters for tuning the injector and for the achievable electron bunch quality. An example of a laser pulse shape measured with a streak camera at 262 nm is plotted in Fig. 2.3(b) [24]. The laser beam is imaged onto the cathode where an aperture at the laser port defines the desired laser spot diameter. For further details on the laser system see [24].

2.1.1 Injector beamline and performance status

In Fig. 2.4 a schematic view of the injector beamline is shown. After the booster cavity the bunch compressor 1 (magnetic chicane) is installed followed by a matching section for adapting the beam to the first acceleration module. The beam energy and the beam energy spread at the injector can be determined in the analysis section using a magnetic spectrometer and a screen (OTR6) for imaging the horizontal beam profile. With 12 MV/m operation gradient of the booster cavity the beam energy has been measured to be 16.5 ± 0.1 MeV [21]. Due to rms-bunch length between 2 mm and 3 mm the time dependent rf acceleration induces a correlated energy spread which dominates the energy distribution of the beam. The uncorrelated energy spread of the beam can be determined from the core of the beam which is on-crest accelerated in the booster cavity. The core of the beam appears as a sharp peak towards high energies in the horizontal beam profile.

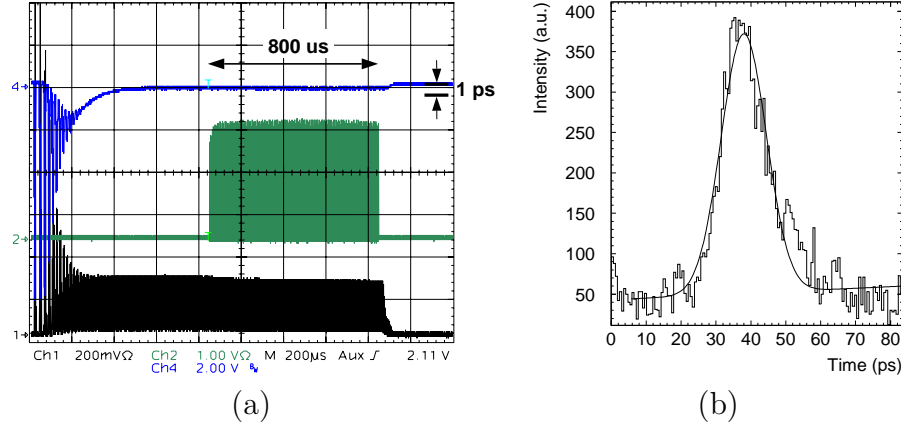


Figure 2.3: (a) Oscilloscope trace of the output of the pulse train oscillator (PTO) (trace 1), the phase of the pulses relative to the reference (trace 4), and the pulse train after amplification measured in the green with a fast photo diode (trace 2). (b) Example of a laser pulse shape measured with a streak camera at 262 nm. The pulse length determined by a fit to a gaussian profile is $\sigma_t = 8.0 \pm 0.1$ ps.

Its width is proportional to the uncorrelated energy spread. By fitting a gaussian curve on the peak, an energy spread of $\sigma_E = 22.1 \pm 2.7$ keV has been measured [21].

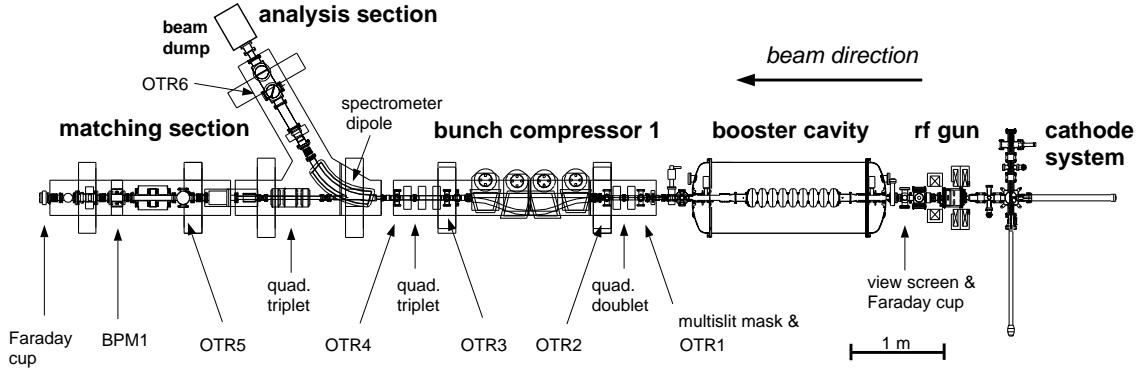


Figure 2.4: Schematic overview of the TTF injector. Beam direction is from the right to left. Various station required for beam diagnostic are labeled.

Five beam current monitors and three Faraday cups are used to measure and monitor the bunch charge.

For nominal operation the injection phase of the laser into the gun is -50° with 0° to the maximum accelerating field at the cathode ¹. The laser is injected before the acceleration field in the gun reaches its maximum.

The injection phase can be obtained with a reproducibility of $\pm 1^\circ$ from a fit to the phase acceptance of the gun. The phase acceptance of the gun is determined by measuring the charge at the gun exit as a function of the phase between the rf wave in the gun cavity and the injection time of the laser pulse. In addition, the rising edge of the phase acceptance allows to reconstruct the laser pulse length [25].

For a bunch charge of 1 nC, normalized emittances between $3 \mu\text{m}$ and $5 \mu\text{m}$ in both planes have been measured [26]. The emittance measurements were performed either by varying

¹Commonly used for the gun is a sine-like rf wave while a cosine rf wave is used for the acceleration structures. For a sine-like rf wave the injection phase of the laser is 40° .

the quadrupole current of the quadrupole doublet while monitoring the transverse beam profile at screen OTR3 or by using a multi-slit arrangement.

The dark current emitted from the gun has been measured routinely with the gun Faraday cup. During the time period December 1999 to May 2000 the dark current varied between $20\text{ }\mu\text{A}$ and 2 mA [19]. A special electronic processing of the sum signal of the beam position monitor BPM1 allows also to monitor the dark current at the exit of the injector.

Numerical simulations for FEL beam parameters predict unacceptable emittance growth due to space charge force along the dispersive sections in the bunch compressor [27]. Because of this, the magnetic chicane has not been commissioned at TTF so far. The length of the bunch is therefore larger than originally designed in TTF phase 1 (see Table 2.1). The electron bunch length has been determined by measuring the synchrotron light pulse emitted at the high energy spectrometer with a streak camera. The rms-bunch length vary between 2 mm for low rf-phases and 5 mm for -30° . Within the measurement errors the phase dependence of the bunch length is good agreement with simulations [28].

2.1.2 Beam dynamics at the injector

The electron-beam dynamics in rf guns needs to take into account several effects, such as the time variation of the rf field over the duration of the electron acceleration or the velocities of the electrons nearby the gun cathode. In addition, the high charge densities in the non-relativistic electron bunch generates a strong repulsive space-charge force that varies in time and in space [29]. This force has an influence on the projected transverse emittance of the beam. If the beam is accelerated to higher energies E the repulsive force due to space charge decrease $\propto 1/E^2$ and, for TTF, at energies above 100 MeV the influence on the beam quality can be neglected. Since the space-charge force is a collective effect, the rms-emittance at higher energies depends sensitively on the transverse and the longitudinal charge distribution along the beamline the bunch propagates at low energies. The beam reaches an energy of 100 MeV approximately at the center of the first cryo-module. Hence, the optimization of the injector parameters has to focus on the emittance measurable at the bunch compressor 2 and should not be restricted to the injector area alone.

The transverse space charge fields and the time variation of the rf focusing cause an opening of a “phase space fan”, where each longitudinal slice of the charge has rotated by a different angle in the phase space (see Fig. 2.5). The projected emittance along the bunch is hence larger than the emittance of the individual slices. The emittance growth due to time dependent linear rf focusing scales with the square of the bunch length and the square of the rms-beam size [29]. Usually, the effect is small compared to the space charge induce emittance growth at high bunch charges (1-10 nC).

A compensation scheme for the space charge induced correlated emittance growth which can decrease the rms-emittance by more than an order of magnitude has been developed by Carlson [16]. The compensation scheme is based on a proper focusing of the electron beam such that the phase space fan which initially creates a large normalized emittance growth starts to close resulting in a decreasing rms-emittance as the beam travels down the beamline. To close the phase space fan the net effect of the space charge defocusing on the motion of the electrons for different axial and radial positions has to be equal. The purpose of the focusing is to rotate the entire phase-space distribution. Using a lens

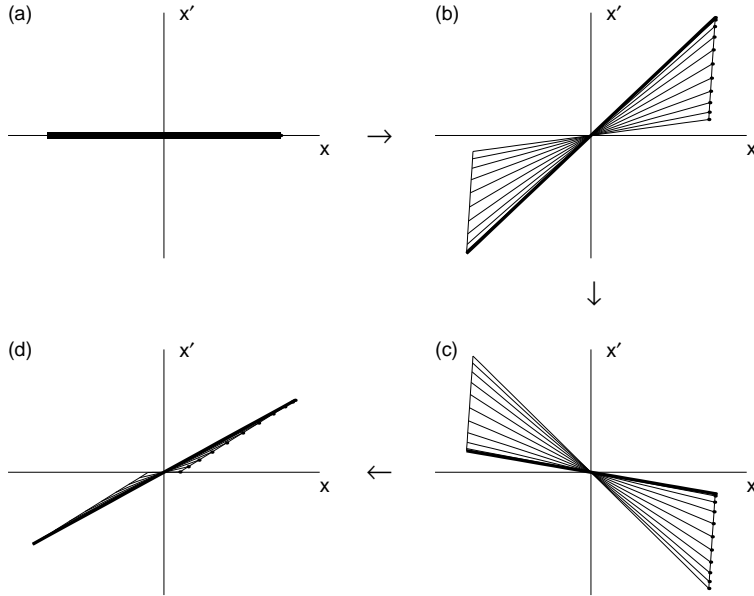


Figure 2.5: Schematic drawing of the transverse phase-space showing the emittance growth and reduction. (a) initial phase-space with very small emittance. (b) phase space after a drift space shows a correlated emittance growth due to the different expansion rate of the individual slices along the bunch. The thick line width corresponds to the center slice. (c) phase space immediately after a lens. (d) phase space plot after a drift space behind the lens. The emittance is reduced and the correlation vanishes due to the different expansion rates of the individual slices.

of appropriate strength, the head and tail slices can be made more convergent than the center slice. The space charge forces of the now converging beam compensates the difference in rotation between the individual slices of the beam. The process in phase space is sketched in Fig. 2.5.

The focusing is realized by solenoids close to the photocathode. The focusing by the acceleration field of the cavities and the quadrupoles along the injector have to be included for minimizing the final rms-emittances.

Since the axial and the radial non-linearities of the space charge force increases the complexity of the compensation scheme, the laser beam is uniformly shaped transverse direction. A longitudinal rectangular laser pulse shape is in preparation (see [30]).

Presently, the longitudinal distribution shown in Fig. 2.3(b) is of gaussian shape. For this shape it is difficult to find injector parameters for which the compensation scheme works also properly for the head and the tail slices of the bunch at the same time. Moreover, the tight focusing of the beam required for the bunch center causes a crossover of the electrons located in the tails. For the center slice the space charge force for a converging beam deflects the particles away from the beam center and the horizontal and vertical position does not change the sign at a beam waste. However, electrons that suffer weak space charge forces can crossover through the beam center. Hence, the phase space bifurcates and the transverse electron distribution splits into a bunch core with high charge density surrounded by a large tail of low charge density [31]. Due to radial non-linearities in the space charge forces the bifurcation can also appear at center slices.

In this way a beam halo is created which may have to be collimated in order to protect the undulator.

2.1.3 Simulation of the injector for FEL operation

The charge distribution produced in the injector is simulated using the particle tracking code ASTRA [32]. As an example for the present conditions at TTF phase 1, the linac settings during FEL operation in April 2000 are used for numerical calculations. The relevant parameter are listed in Table 2.2. The electrons are tracked with ASTRA from the gun to the exit of the first acceleration module. To minimize the correlated energy spread of the beam along the injector, the booster cavity is operated slightly off-crest (-9°). The rf-phase of the first acceleration module is adjusted to achieve the minimum rms-bunch length behind bunch compressor 2 (see Sec. 2.2). The results of the simulation for the transverse rms-emittances and rms-beam sizes are plotted in Fig. 2.6.

laser rms-pulse duration	8 ps
laser spot diameter at cathode	3 mm
primary solenoid peak field (220 A)	106 mT
secondary solenoid peak field (104 A)	89 mT
rf-phase gun	-50°
rf-phase booster cavity	-9°
rf-phase module	-14°
field at cathode	35 MV/m
gradient in booster cavity	12.3 MV/m
gradient in first acceleration module	13.7 MV/m
beam energy at injector	16.3 MeV
beam energy at exit of module 1	126 MeV

Table 2.2: Input parameter for the tracking simulation with ASTRA [32].

The normalized rms-emittance has a minimum of $3.7 \mu\text{m}$ after the booster cavity and grows along the remaining injector. At the middle of the acceleration module the emittance approaches constant values of $\epsilon_x^N = 10.4 \mu\text{m}$ and $\epsilon_y^N = 8.2 \mu\text{m}$.

The rms-beam sizes have a first beam waist at the end-cell of the booster cavity and increase to the first triplet at the matching section. A second waist of the rms-beam sizes occur behind the second triplet, first in the horizontal plane then in the vertical plane. The asymmetric focusing causes an elliptical beam which results in different emittances in both planes at the exit of cryo-module 1.

In Fig. 2.7 the particle distribution is examined in more detail. The upper two plots show the transverse phase space distribution in the x and y -plane. Both beam cores indicate that the phase space fan has not been closed while accelerating the beam. The tentacles of the beam halo adapted to the central distribution are created by the bunch tails. The middle plots show the transverse distributions versus longitudinal position z . The large mismatch between center and tails of the beam is due to particles crossover. Also a non-negligible part of the central slice distribution are bifurcated creating a large transverse beam halo and a dilution of the slice emittance. For a slice width of $0.5 \cdot \sigma_z$, the orientation and the size of the phase ellipse of individual slices along the bunch are plotted in the bottom pictures of Fig. 2.7. The normalized emittances of the slices are listed in Table 2.3 and vary between $2 \mu\text{m}$ and $4 \mu\text{m}$ at the core of the beam ($\pm 1\sigma_z$). Such complex non-gaussian charge distributions cause a number of difficulties:

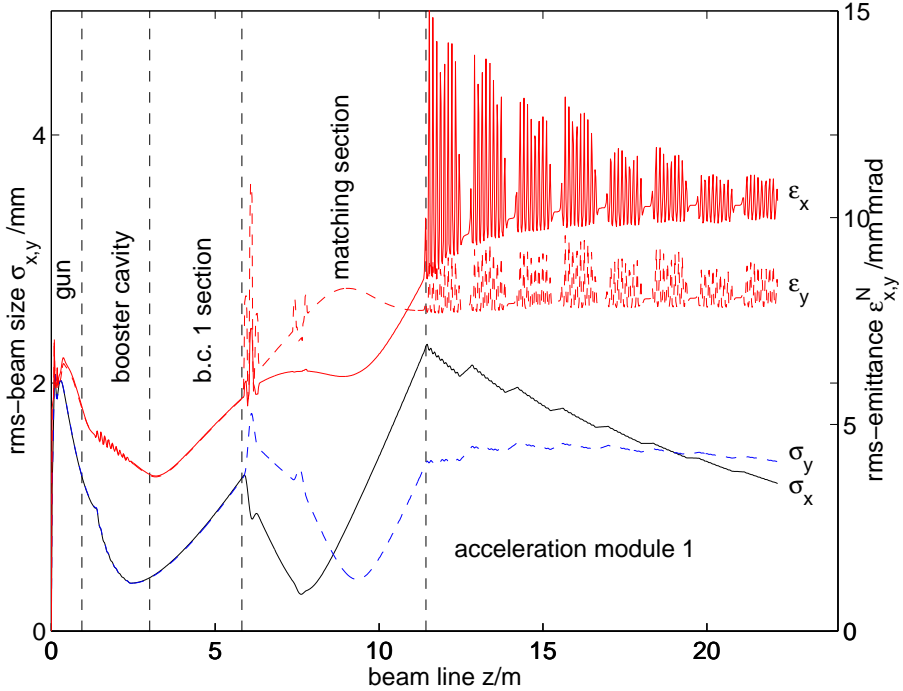


Figure 2.6: Example of a beam transport from the rf gun to exit of acceleration module 1 simulated with ASTRA [32]. The evolution of the normalized projected emittance (upper two curves) has a minimum behind the booster cavity and approaches constant values at about the center of the first acceleration module. The rms-beam sizes are shown below.

z/σ_z	-2.0	-1.5	-1.0	-0.5	0.0	0.5	1.0	1.5	2.0
ϵ_x^{slice} [μm]	5.7	7.7	3.7	1.9	3.2	3.0	2.1	2.6	7.1
ϵ_y^{slice} [μm]	5.8	5.5	2.6	3.3	3.9	4.2	3.2	1.8	5.2
charge contained %	2.1	6.8	12.8	16.1	17.1	16.4	13.7	9.5	4.3

Table 2.3: Slice emittance at various positions along the bunch after the first acceleration module. The width of the individual slice is $0.5\sigma_z$.

1. If the beam is further compressed by magnetic chicanes the mismatch of the bunch slices yields an uncorrelated emittance dilution by mixing up the individual slices.
2. A matching of the beam to a downstream design optics can only be successful for a fraction of the bunch charge. Moreover, standard technique for determining the Twiss parameters and emittances such as parabola fit analysis of quadrupole scans may fail and more complicated analysis methods have to be applied (i.e. phase space tomography) [33].
3. The successful matching of the bunch core to a desired beam optics increases the loss probability of halo electrons along the beamline. More strictly, rf photoinjectors tend to produce beam halo by the intrinsically given beam dynamical properties. The beam halo depends sensitively on the tuning of the linac. This may require to include collimators to the overall design of the linac for the halo removal.

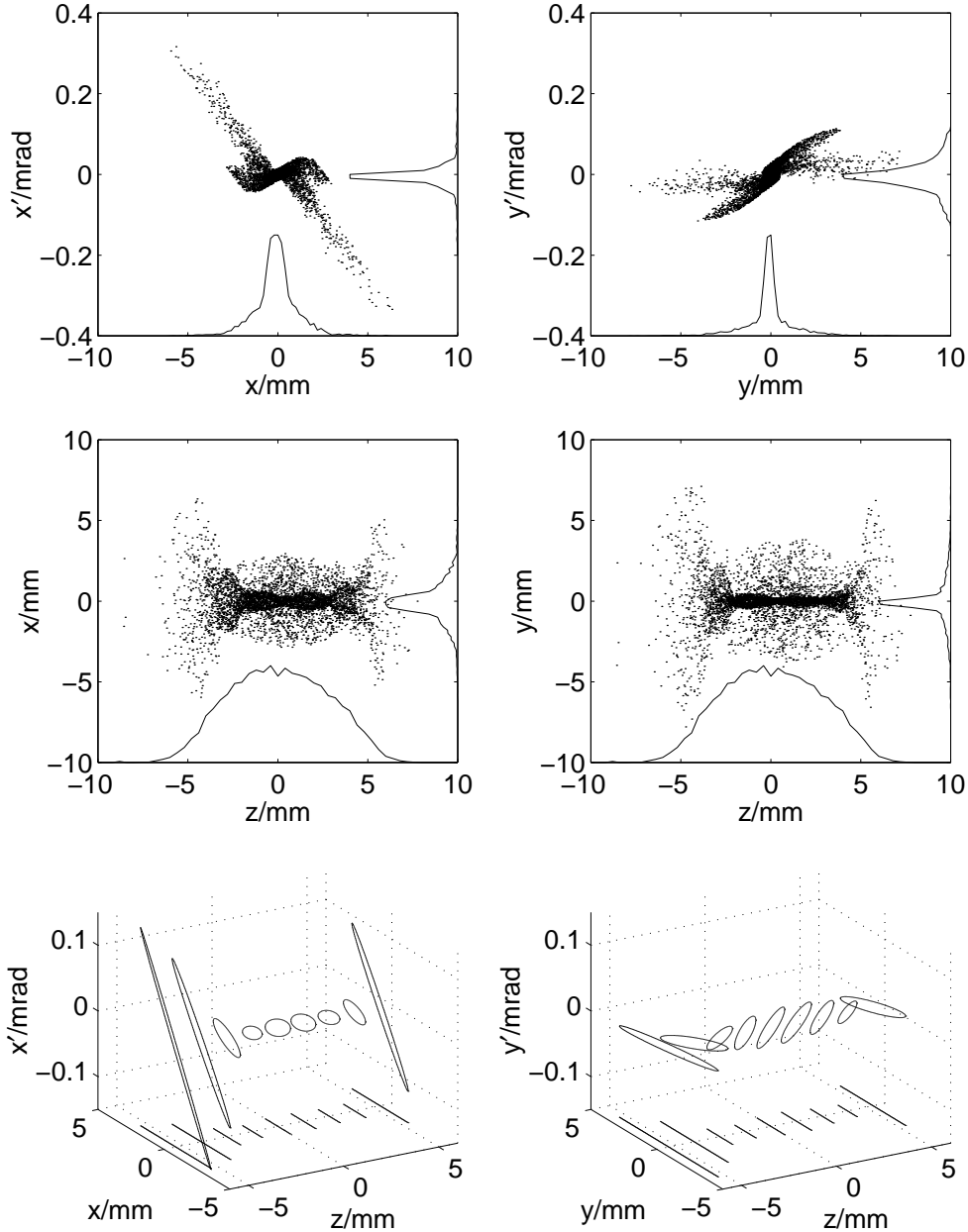


Figure 2.7: Example of transverse phase space distribution at exit of acceleration module 1 simulated by ASTRA. The upper plots show the particle distributions in x and y -plane. The spread of the particle positions versus the longitudinal position in the bunch is plotted in the middle plots while the last plots show the individual slice emittance ellipses along the bunch.

2.1.4 Emission of dark current

The high electric field gradients at the surface of the rf gun cavity enhance the emission of dark current. Due to the unfavorable ratio of the rf-pulse duration to the emission time of the beam, the dark current can have a comparable magnitude as the average beam current. Dark current accelerated through the entire linac can cause operation difficulties like the use of screen for beam diagnostics, the activation of beamline components and the radiation damage of sensitive devices i.e. electrons.

The dark current by field emission of electrons has been investigated by Fowler and

Nordheim [34]. The Fowler-Nordheim equation, adapted to the rf case reads [35]

$$I_{dark} \propto \frac{5.7 \cdot 10^{-12} \cdot 10^{4.52\psi^{-0.5}}}{\psi^{1.75}} (\beta_{en} E)^{2.5} \exp \left[-\frac{6.53 \cdot 10^9 \cdot \psi^{1.5}}{\beta_{en} E} \right] \quad (2.1)$$

where ψ is the work function in eV (for Cs_2Te $\psi = 5$ eV), E is the macroscopic surface field in V/m. To obtain agreement with the observation a large field enhancement factor $\beta_{en} \approx 100\text{-}300$ has to be applied. It has been shown in [36] that dark current induced by a radio frequency field is restricted to a narrow phase interval around the crest of the rf wave (see Fig. 2.8). In the following simulation $\sigma_\phi = 16.5^\circ$ is assumed.

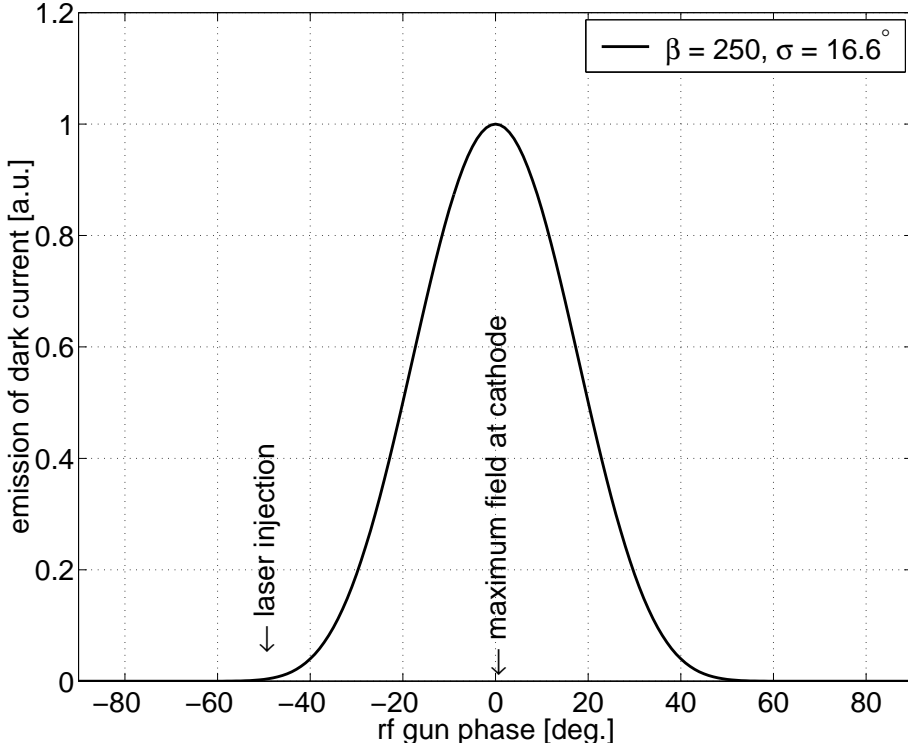


Figure 2.8: Emission of dark current versus rf phase according to the Fowler-Nordheim equation. The enhancement factor amounts to $\beta = 250$. The largest field emission occurs at maximum accelerating gradient.

A more complex subject than the emission time structure of the dark current is the location of the emitters in the gun. In [36] the trajectories of electrons emitted at the middle and the exit iris of the TTF-FEL gun has been investigated. It was shown that the transmission probability of the electrons through the exit aperture is much smaller than the transmission probability of electrons emitted from the cathode. The difference is caused by the initially large radial offset of the electron trajectories starting from the gun iris and due to the strong focusing by the solenoid fields. The simulation results are confirmed by experimental observations at the photo-injector A0 at Fermilab, where it has been shown that under normal operation conditions the transmitted dark current is emitted dominantly from the cathode [37].

For the simulation the emission time structure shown in Fig. 2.8 and an uniformly emitted dark current from the cathode of 10 mm diameter is assumed. The results of the tracking calculation for the linac settings during the FEL operation in April 2000 are shown in

Fig. 2.9.

In Fig. 2.9(c) the transmission of the dark current to the entrance of module 1 is shown. About 16% of the initially 10000 particles are accelerated backwards to the cathode plane and do not exit the gun. 3% of the particles are lost radially in the gun cavity. The transmission probability decreases rapidly by 29% along the drift space of 70 cm length between the gun exit iris and entrance of the booster cavity while only 10% of the particles are lost inside the booster cavity. Hence, the drift space between the gun and the following acceleration structure has a strong influence on the dark current transmission probability. In the present design of the beamline with the booster cavity close to the gun cavity the dark current is captured and a considerable amount of 40% of the dark current emitted at the cathode reaches the downstream sections of the injector.

Finally, 24% of dark current is reaching the first acceleration module and is accelerated to high energies. In the simulation no particle are lost inside the module. The ratio between the dark current measurable at the gun Faraday cup and the dark current monitor (BPM1) installed at the exit of the injector amount to 3 in agreement to observations.

The heat load in the booster cavity caused by the energy deposition of the dark current is 0.3 W in case of 1% rf-duty cycle and a dark current emission of 0.1 mA. At 1% repetition rate the heat load in the booster cavity reduces to 0.03 W which is below the measurement accuracy at 2 K.

The dark current distribution behind the first acceleration module in phase space is shown in Fig. 2.9(a) the horizontal plane and in Fig. 2.9(b) the vertical plane. The dark current distribution is dominantly created by the time dependent rf-focusing which opens a large phase space fan. The beam pipe diameter behind the module is 60 mm. Thus the dark current fills nearly half the entire beam pipe. For comparison the statistical emittances are computed.

Figure 2.9(d) shows the distribution of the dark current in the longitudinal phase space. The longitudinal position of the particles are plotted with respect to the rf-phase of the acceleration module (opposite sign). The energy distribution follows the cosine time dependence of the rf. The dark current is distributed in the range between -80° to $+15^\circ$ with center at -35° . The beam phase is $+11^\circ$ ahead of the dark current.

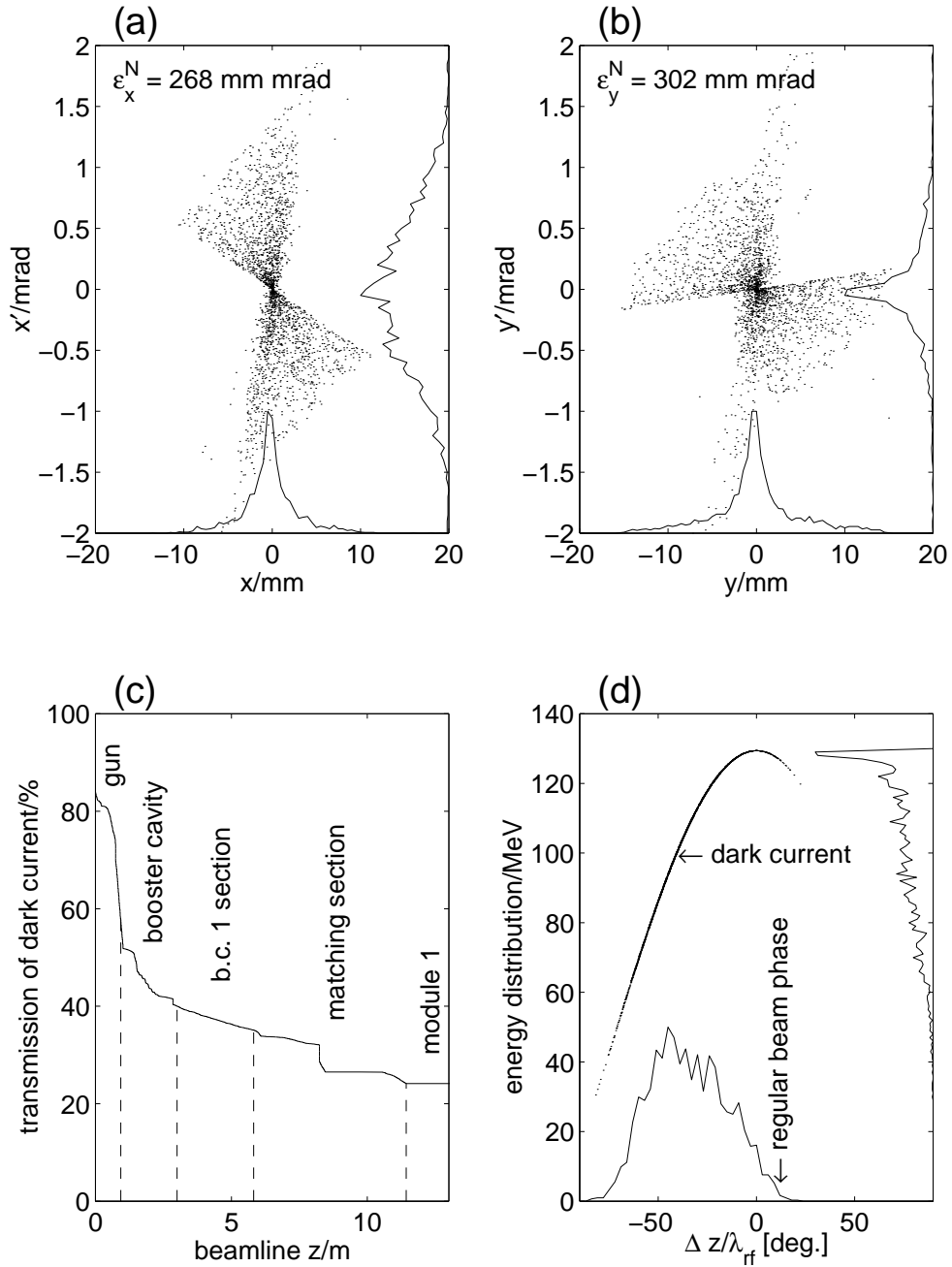


Figure 2.9: Distribution of the dark current behind acceleration module 1 simulated with ASTRA. (a) particle distribution in the horizontal phase space and (b) in the vertical phase space. (c) transmission probability of the dark current along the injector. (d) dark current distribution in the longitudinal phase space.

2.2 Bunch Compressor BC2

A longitudinal compression of the relativistic electron beam is achieved by generating a correlation between the longitudinal position and the energy along the bunch using an off-crest acceleration in an rf section, and an energy dependent path length in a dispersive beamline. The tail of the bunch travels a shorter path length than the head, and the bunch becomes shorter. For the dispersive beamline a horizontal magnetic chicane consisting of four rectangular bending magnets as sketched in Fig. 2.10 is used. Electrons with the nominal energy (p_0) follow the reference trajectory while electrons with higher energy ($p > p_0$) are less deflected by the dipoles and move with a smaller horizontal offset with respect to the linac axis \mathbf{e}_z . The overall path length through the chicane is thus shorter for electrons of higher energy. For ultra-relativistic electron beams the variation in velocity can be neglected.

The electron beam propagating through the chicane follows no longer the linac axis z and the coordinate s is used to describe the path length of the curvilinear reference trajectory in the bunch compressor. The distance of an electron to a reference particle with momentum p_0 is denoted by Δs , with $\Delta s > 0$ if the electron travels ahead and $\Delta s < 0$ behind the reference particle. The indices $i, j, k = 1 \dots 6$ are used for the coordinates $(x, x', y, y', \Delta s, \delta)$ in the six dimensional phase space, where $\delta = \Delta p/p_0 \approx \Delta E/E_0$ denotes the momentum deviation of an electron from the reference particle. In linear optics the change of the distance Δs through a dispersive beamline can be expressed as

$$\begin{pmatrix} \Delta s \\ \delta \end{pmatrix}_{s_2} = \begin{pmatrix} 1 & R_{56} \\ 0 & 1 \end{pmatrix} \begin{pmatrix} \Delta s \\ \delta \end{pmatrix}_{s_1}, \quad (2.2)$$

where s_1 and s_2 are the initial and the final position in the beamline. $R_{56}(s)$ is called the longitudinal dispersion function. An electron starting at $\Delta s = 0$ with $p > p_0$ propagates on a shorter path through the magnetic chicane than the reference particle. Hence at the exit of the chicane it is ahead ($\Delta s > 0$) and according to Eq. 2.2 the function R_{56} must be positive². The development of the longitudinal dispersion function is shown in Fig. 2.10. It can be calculated by

$$R_{56}(s) = -\frac{1}{s} \int_0^s ds' \frac{R_{16}(s')}{\rho(s')}, \quad (2.3)$$

where the integral is taken along the reference trajectory, with R_{16} the horizontal dispersion function ($D_x = R_{16}$ for linear optics). ρ is the bending radius of the dipoles in the chicane with $\rho < 0$ for the first dipole. From Eq. 2.3 the behavior of R_{56} becomes obvious: the integrand vanishes at the drift spaces ($\rho \rightarrow \infty$) and becomes large at locations of large dispersion causing a rapid variation of R_{56} at the second and third dipole. This means the compression of the electron bunch takes place at the inner two dipoles of the chicane.

The position-energy correlation r_{56} of an electron distribution describes the dependence of the momentum deviation δ (index 6) on the longitudinal position Δs inside the bunch (index 5) and is defined by

$$r_{56} = \frac{\sigma_{56}}{\sqrt{\sigma_{55}\sigma_{66}}}, \quad (2.4)$$

²In this thesis the opposite sign convention to that in storage rings for the momentum compaction α_c is used.

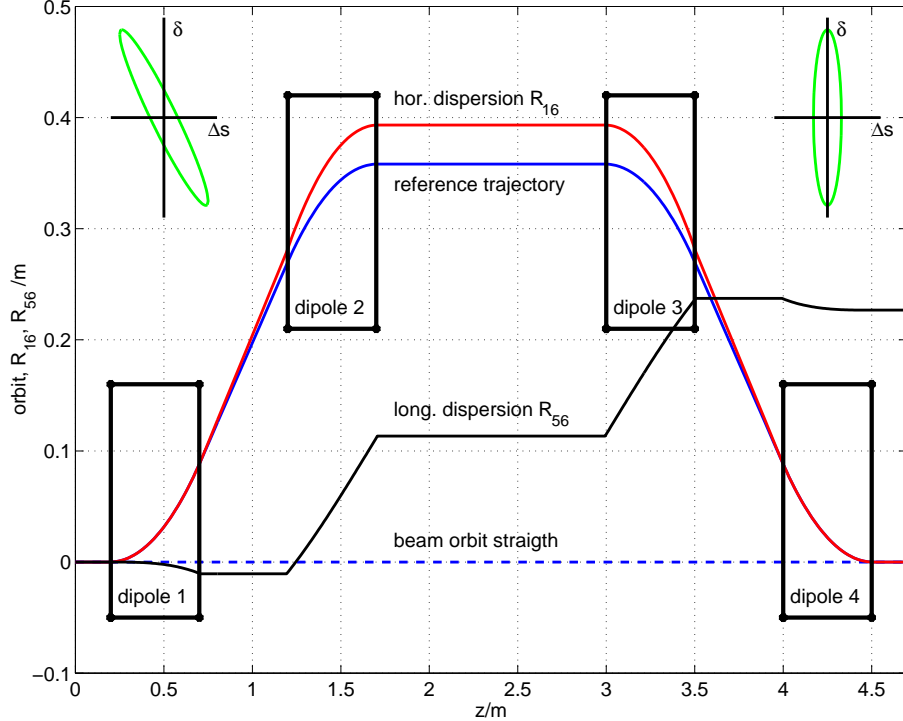


Figure 2.10: Development of the reference orbit, the linear horizontal dispersion R_{16} and the longitudinal dispersion R_{56} along the magnetic chicane compressor BC2. With a deflection angle of 20° at the dipoles the beam transmits through the center of the screen between the second and the third bending dipoles. The bunch in the longitudinal phase space represented by the phase ellipse before (left top) and after (right top) compression is also shown.

with $\sigma_{55} = \langle (\Delta s)^2 \rangle$, $\sigma_{56} = \langle \Delta s \cdot \delta \rangle$, and $\sigma_{66} = \langle \delta^2 \rangle$ the second order moments of the distribution. Compression of the bunch is obtained for negative correlation $\sigma_{56} < 0$. Then the trailing high-energy tail can catch up the leading low-energy head.

The correlation is induced by an off-crest acceleration in module 1. Let ϕ_0 denote the rf-phase of the reference particle ($\Delta s = 0$). An electron in a distance Δs to the reference particle is accelerated at a rf-phase $\phi = k_{rf}\Delta s + \phi_0$ with $k_{rf} = 2\pi/\lambda_{rf}$ the wavenumber of the acceleration field. The energy of an electron E^f after the module operating at an acceleration voltage U_{acc} is

$$E^f = E^i + eU_{acc} \cos(\phi) \quad (2.5)$$

with E^i the initial energy before acceleration. The trigonometric dependence of the final energy on Δs introduces non-linearities. Expanding Eq. 2.5 in a Taylor series up to the second order in Δs at the reference phase $\phi = \phi_0$ yields³

$$\delta_f = M_{65}\Delta s_i + M_{66}\delta_i + M_{655}\Delta s_i^2 + \dots \quad (2.6)$$

where the linear coefficients are

$$M_{66} = \frac{E_0^i}{E_0^f}, \quad M_{65} = -\frac{eU_{acc} \sin(\phi_0)}{E_0^f} k_{rf} \quad (2.7)$$

³Notation: the first index i of the coefficients $M_{ijk\dots}$ refer to the coordinate to be described, i.e. $i = 6$ for δ_f . The remaining indices j, k, \dots denote the dependence on the initial coordinates, i.e. $j = 5$ linear on Δs and $j = k = 5$ quadratical on Δs , etc.

with

$$E_0^f = E_0^i + eU_{acc} \cos(\phi_0), \quad (2.8)$$

and

$$M_{655} = -\frac{1}{2} \frac{eU_{acc} \cos(\phi_0)}{E_0^f} k_{rf}^2 \quad (2.9)$$

the second order contribution to δ . The longitudinal position of an electron in a bunch remains unchanged during acceleration $\Delta s_f = \Delta s_i$. For a small initial correlation ($\sigma_{56}^i \approx 0$) using Eq. 2.6 and Eq. 2.4 the final correlation after acceleration behaves like

$$r_{56} \propto M_{655} \sigma_{55} < 0 \quad \text{if } \phi_0 > 0 \quad (2.10)$$

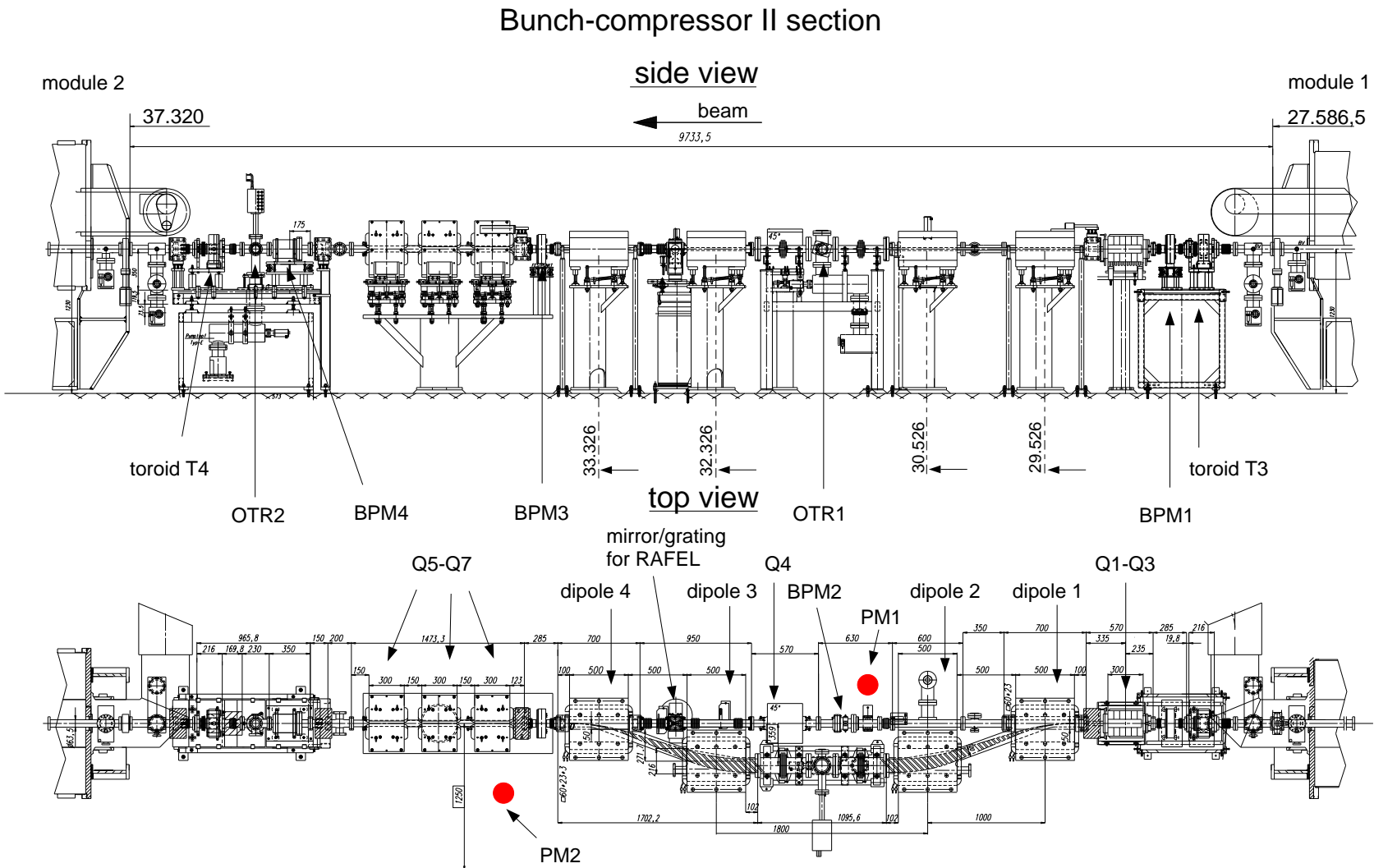
and becomes negative when the beam is injected at a positive rf-phase ϕ_0 .

2.2.1 Components in the bunch compressor 2 section

A side and a top view of the magnetic arrangement in the bunch compressor 2 section is shown in Fig. 2.11. The beam leaving the first acceleration module passes a quadrupole triplet Q1-Q3 and enters the magnetic chicane. The beam position monitors BPM1ACC1 (not drawn) and BPM1 (cavity monitor) are used to measure the beam offset and angle into the magnetic chicane. A screen, OTR1, is located in the center part of the dispersive section in the chicane. To determine the energy spread of the beam with 0.1% precision the beam has to be focused horizontally with the quadrupole triplet to a beam size below 0.4 mm. The center of the screen has a horizontal distance of 359 mm to the linac axis. The nominal bending angle of the dipoles is 20°. Behind the bunch compressor a second quadrupole triplet Q5-Q7 is used to match the beam into the acceleration module 2 and to measure the transverse beam profile at a second screen, OTR2. The proper beam transport can be controlled by monitoring the bunch charge at the toroids T3 before and T4 behind the bunch compressor. Plastic scintillator equipped with photomultipliers PM1-PM2 are used to detect small beam losses.

A straight pipe between the first and the last dipole enables the beam transport without the magnetic chicane. A skew quadrupole Q4 has been installed for correlation measurements in horizontal and vertical direction [38]. The beam position monitor BPM2 in the straight beamline is equipped with a broad band electronics for high-order mode measurements [39]. A mirror and gratings are installed in the straight section for a regenerative amplifier FEL (RAFEL) operating at wavelengths around 100 nm [40]. The difference in path length for the operation modes with and without magnetic chicane is 105 mm or 163.6° in rf-phase. Stub-tuners are used to adjust the rf-phase between module 1 and module 2.

Figure 2.11: Overview of bunch compressor 2 at TTF.



2.2.2 rms-Bunch length after compression

From Eqs. 2.2-2.6 a formula for the final rms-bunch length can be derived. Assuming that the bunch at the entrance of module 1 initially has a gaussian distribution in the longitudinal phase space with a vanishing correlation ($\sigma_{56} = 0$), then the final bunch length can be calculated by

$$\sigma_z = \sqrt{\sigma_{55} (1 + R_{56} M_{65})^2 + \sigma_{66} R_{56}^2 M_{66}^2 + 2\sigma_{55}^2 R_{56}^2 M_{655}^2}. \quad (2.11)$$

with M_{ijk} the matrix elements for the acceleration section and R_{ij} the one for the magnetic chicane. The minimum rms-bunch length is achieved if the condition

$$R_{56} M_{65} = -1 \Rightarrow R_{56} = \frac{E_0^i + eU_{acc} \cos(\phi_0)}{eU_{acc} \sin(\phi_0) k_{rf}} \quad (2.12)$$

is fulfilled. In this case, the linear part of the correlation induced by an off-crest acceleration is removed in the bunch compressor. With a nominal gradient of 15 MV/m, an initial beam energy of 16.5 MeV and a longitudinal dispersion of $R_{56} = 227$ mm at 20° bending angle the phase for maximum compression is 10.4°.

The second term in Eq. 2.11 is proportional to the initial energy spread of the beam and can only be reduced by increasing the gradient of the module. The third term is caused by the non-linearity of the rf-wave. For vanishing initial energy spread ($\sigma_{66} \rightarrow 0$) the rms-bunch length after full compression depends quadratically on the initial bunch length. In the present condition with a bunch length of $\sigma_z^i \approx 2.7$ mm and $\sigma_E^i/E^i \approx 0.13\%$ the rms-bunch length after compression is determined by the rf-wave and limited to about 0.76 mm.

2.2.3 Longitudinal bunch shape

Caused by the large initial bunch length the longitudinal beam profile after the bunch compressor is non-gaussian distributed. Fig. 2.12 shows the simulated phase space distribution before (a) and behind (b) the magnetic chicane. The acceleration phase has been set to maximum compression. The rms-bunch length after the chicane is in good agreement to the value given by the expression in Eq. 2.11. The sharp rising edge of the head of the bunch can be estimated using Eq. 2.11 for $M_{655} = 0$. It is shown in Fig. 2.12 by the dashed curve of gaussian shape. The peak current obtained from the simulation reaches 780 A for a 1 nC bunch charge. The off-crest acceleration increases the energy spread of the beam to $\sigma_E = 1.64$ MeV. The energy of the electrons at the tail of the compressed bunch is split into two branches.

The very sharp rising edge of the bunch with the high peak current can induce strong longitudinal wakefields. Since the energy widths of the branches are very small the energy modulation caused by longitudinal wakefields would appear in a magnetic spectrometer as an energy break-up of the bunch into several bunchlets. Such an energy break-up is observed whenever the beam is compressed to short bunch length [41].

The variation of the longitudinal beam profile behind the bunch compressor for various rf-phases is shown in Fig. 2.13(a). The long initial bunch length causes a sharp rising of charge distribution at the bunch head already when the beam is accelerated on-crest

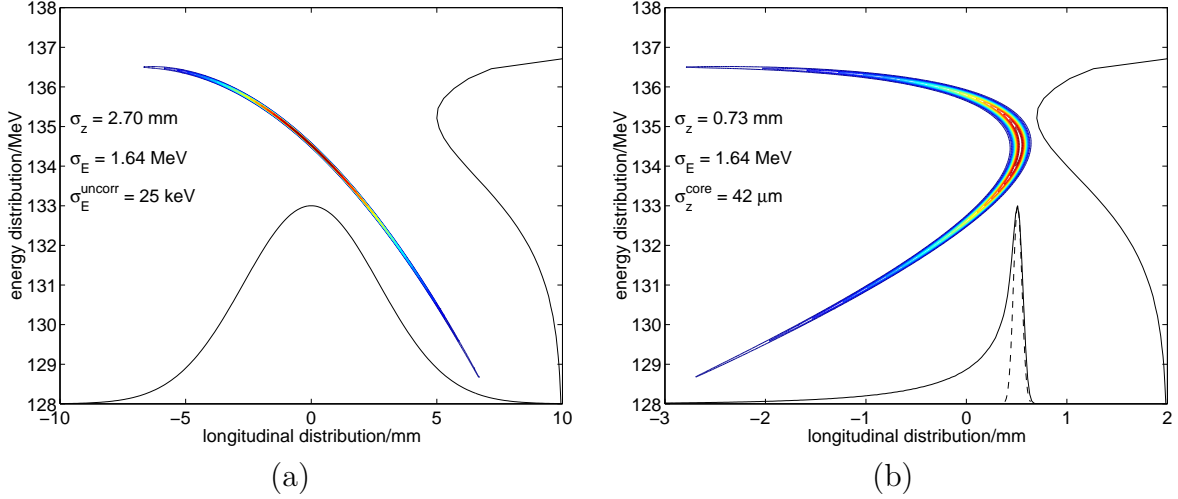


Figure 2.12: Simulation of the longitudinal phase space distribution (a) in front of the bunch compressor and (b) behind the bunch compressor. The initial energy spread of the beam is 25 keV. The dashed Gaussian curve in Figure (b) shows the minimum achievable bunch length according to Eq. 2.11.

$(\phi_0 = 0)$. The largest peak current of the beam is achieved for the shortest rms-bunch length. The variation of the beam peak current with the rf-phase is plotted in Fig. 2.13(b). It is well approximated by a gaussian function of $\sigma_\phi = 4.2^\circ$.

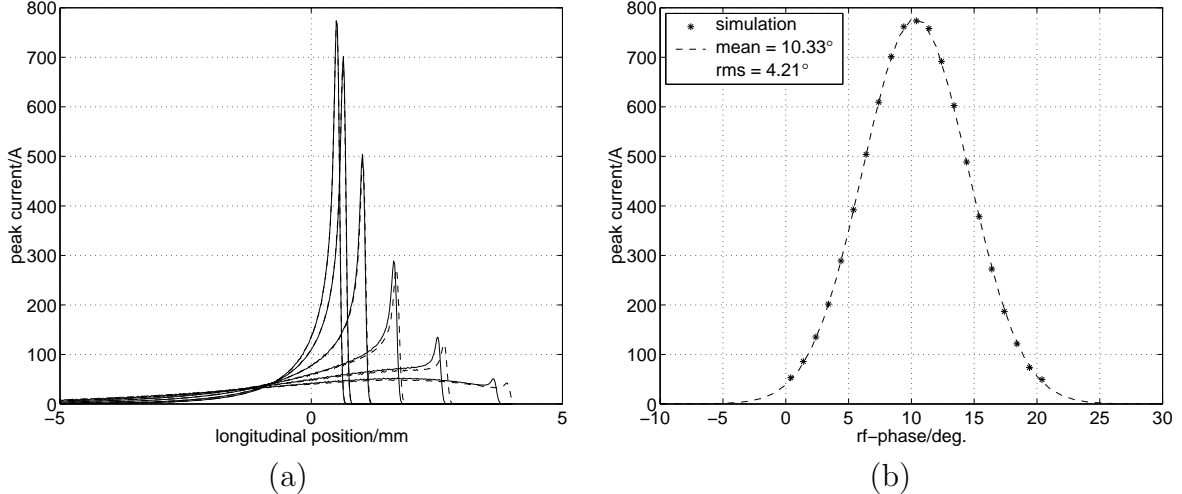


Figure 2.13: (a) Simulation of the longitudinal profile for various beam phase versus module phase. The solid curves from right to left are the profiles obtained for $0.4^\circ, 2.4^\circ, \dots, 10.4^\circ$ and the dashed curves from left to right are for $12.4^\circ, 14.4^\circ, \dots, 20.4^\circ$. (b) Peak current versus phase. The dependence is well described by a gaussian distribution of variance $\sigma_\phi = 4.2^\circ$, centered at 10.3° .

2.2.4 Phase scan of acceleration module 1

The emission of coherent transition radiation (CTR) in the far infrared regime can be used for a fast determination of the optimum rf-phase yielding the shortest rms-bunch length behind the magnetic chicane.

If a relativistic electron bunch traverses a thin aluminum foil transition radiation is emitted. The transition radiation is coherent for wavelength in the order of the bunch length.

The frequency spectrum of coherent radiation is proportional to the square of the bunch form factor $|\lambda_{\parallel}(\omega)|^2$, the Fourier transform of the longitudinal charge distribution. Thus, for shorter bunch length σ_z the emitted energy increases with $1/\sigma_z^2$. The detected energy can be written as

$$U = q^2 \int_{-\infty}^{\infty} |\lambda_{\parallel}(\omega)|^2 F(\omega) d\omega \quad (2.13)$$

with q the bunch charge and $F(\omega)$ the frequency response of the apparatus (see [38]). Due to the finite size of the foil and the finite diameter of the quartz window, diffraction reduces the frequency response at low frequencies (below 80 GHz). It is therefore difficult to measure variations of the bunch length above 2-3 mm.

During a phase scan the coherent transition radiation is monitored using a pyro-electric detector and plotted versus the rf-phase of the acceleration module. Three typical scans taken within 1 hour of beam operation are shown in Fig. 2.14(a). Each of the data points represents the mean value of the detector signal for 10 bunches. The error bars indicate the variation over the bunches which is caused by jitter in bunch charge or rf-phase. A gaussian distribution is fitted to the data points to determine the rf-phase of maximum measured coherent emission. The reproducibility of the rf-phase with this technique is better than $\pm 1^\circ$. The typical rms-width of phase-scans performed in spring 2000 was 3.6° . The histogram Fig. 2.14(b) shows the variation of the rms-width determined from 51 scans.

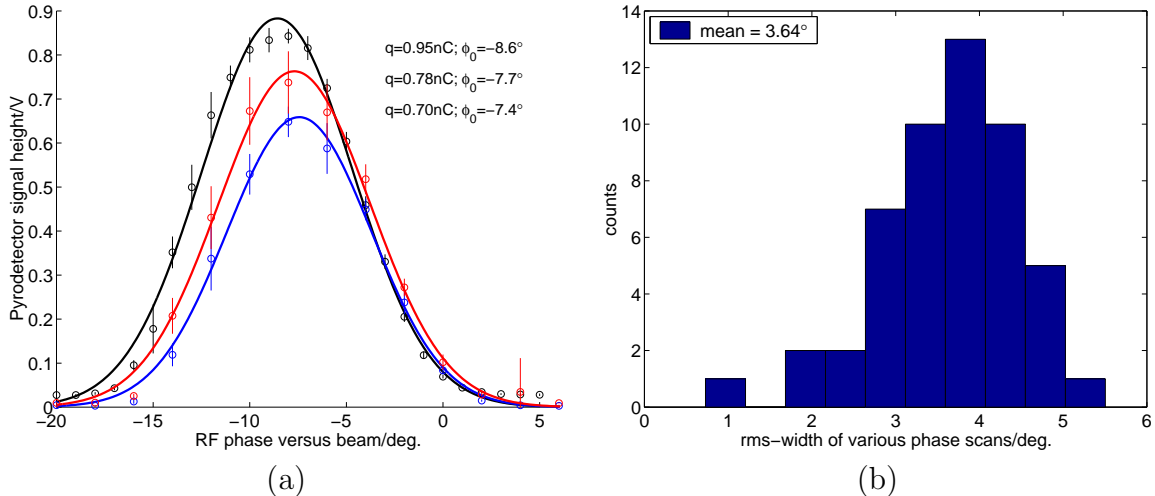


Figure 2.14: (a) Pyroelectric detector signal versus the phase of module 1. The center of the distribution is calculated from a gaussian fit. The three measured curves are collected within 1 hour. The amplitude and the phase for the maximum detector signal depend on the bunch charge. (b) Distribution of the rms-width of various phase scans performed in February to April 2000.

2.2.5 Higher-order dispersion

If the energy deviation δ gets large, higher-order dispersion influences the electron transport through the magnetic chicane. Analytical expressions for the non-linear dispersion

functions can be derived, when the bending dipoles are modeled by hard edge magnets. Let ρ_0 denote the bending radius for the bending angle α_0 . It is given by

$$\rho_0 = \frac{z_{eff}}{\sin(\alpha_0)}. \quad (2.14)$$

The effective dipole length in z-direction has been measured to $z_{eff} = 513$ mm. This determines the drift space $z_d = 487$ mm between the dipoles 1 and 2 (3 and 4). The horizontal non-linear dispersion at the OTR-screen is calculated to

$$\delta D_x^{OTR}(\delta) = X_{OTR}(1 + \delta) - X_{OTR}(1) \quad (2.15)$$

with

$$X_{OTR}(u) = -2\rho_0 \left(u - \sqrt{u^2 - \sin^2(\alpha_0)} \right) - \frac{z_d \sin(\alpha_0)}{\sqrt{u^2 - \sin^2(\alpha_0)}} \quad (2.16)$$

where $X_{OTR}(1)$ describes the horizontal distance between the reference trajectory and the linac axis. The non-linear longitudinal dispersion determines the initial rf-phase of an electron with large energy deviation in the second module. At the exit of the chicane it is given by

$$\delta D_s^{exit}(\delta) = -(s^{exit}(1 + \delta) - s^{exit}(1)) \quad (2.17)$$

with

$$s^{exit}(u) = 2u \left[2\rho_0 \arcsin(u \sin(\alpha_0)) + \frac{z_d}{\sqrt{u^2 - \sin^2(\alpha_0)}} + z_{str} \right] \quad (2.18)$$

where $s^{exit}(1)$ describes the path length through the chicane for the reference trajectory ($\delta = 0$). The drift space between the second and third dipole has been denoted by $z_{str} = 1.287$ m. In Fig. 2.15 the variation with δ of the horizontal offset x_{OTR} and the path length $\Delta z = s^{exit} - z_0$ are plotted with $z_0 = z_{str} + 2z_d + 4z_{eff}$ the length of the chicane along the z-axis. The distance $\Delta z(\delta = 0)$ describes the difference in length for beam operation with and without chicane.

The dispersion functions are usually expressed as a series expansion:

$$\delta D_x^{OTR}(\delta) = R_{16}\delta + R_{166}\delta^2 + R_{1666}\delta^3 + \dots \quad (2.19)$$

$$\delta D_s^{exit}(\delta) = R_{56}\delta + R_{566}\delta^2 + R_{5666}\delta^3 + \dots, \quad (2.20)$$

and listed in Table 2.4. The linear approximations using the dispersion function R_{16} and R_{56} are plotted in Fig. 2.15 for comparison (dashed line).

The correction due to higher-order dispersion for electrons with $\Delta p/p_0 = 5\%$ is 0.3% horizontally and 1% longitudinally. Thus, for most applications the first-order approximation is sufficient. However, it can not be neglected for larger momentum deviations δ required for dark current tracking. At $\Delta p/p_0 = 15\%$ the corrections are 2.8% for D_x^{OTR} and 9% for D_s^{exit} . Electrons with a too large deviation from the nominal energy hit the vacuum chamber. The energy range in which an electron which is injected on-axis into the bunch compressor transmits through the chicane is called the energy acceptance of the bunch compressor. Because of the non-linearity the width of the energy acceptance is

Higher order dispersion			
horizontal dispersion at OTR1BC2 screen	R_{16}	R_{166}	R_{1666}
	393 mm	-452 mm	542 mm
longitudinal dispersion at exit of BC2	R_{56}	R_{566}	R_{5666}
	227 mm	-378 mm	575 mm

Table 2.4: Higher order dispersion at BC2 derived for 20° bending angle.

asymmetrically distributed in δ from -14% to 20% (see Fig. 2.15) and not symmetrically $\pm 17\%$ as calculated in linear optics. Also, the injection phase to the downstream acceleration module 2 is significantly shifted by the high-order longitudinal dispersion. Finally it is noted, that both non-linear coefficients, M_{566} due to the rf acceleration and R_{566} due to geometrical effects in the magnetic chicane are equal in sign which enhances the lengthening of the beam tails. The chicane as designed cannot be used to remove higher-order terms.

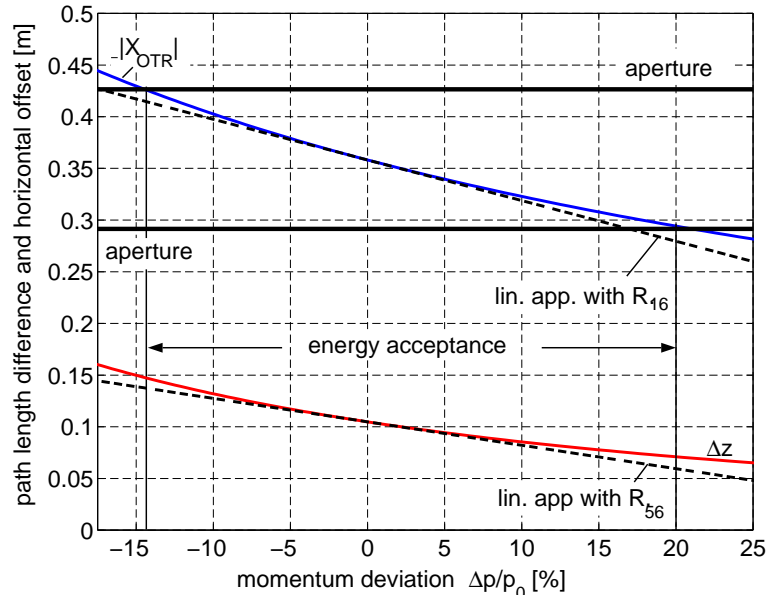


Figure 2.15: The transverse offset from the linac axis at the screen OTR1, $|X_{OTR}|$, and the additional path length through the magnetic chicane, Δz , are plotted versus the momentum deviation δ of an electron. The difference to the linear approximations using only the transfer matrix elements R_{16} and R_{56} shows the influence of higher-order dispersion. The dipole deflection angle of 20° corresponds to $\delta = 0$. The vacuum chamber is drawn by the horizontal lines labeled with “aperture”. The energy acceptance is obtained from the values for δ where the horizontal offset X_{OTR} cuts the lines of the aperture.

2.2.6 Tracking of dark current through bunch compressor 2

The transport of dark current through the bunch compressor 2 section is calculated by tracking simulation. In section 2.1.4 the origin of the dark current and its transport from the injector to the exit of acceleration module 1 has been presented. Due to the delay of 50° in the gun rf-phase of the central dark current emission with respect to the

electron beam, a substantial fraction of the dark current is distributed at low energies. In the magnetic chicane the low-energy tail of the dark current will be removed to a large extent. The energy acceptance of the magnetic chicane is defined by the vacuum chamber shown in Fig. 2.15. To reduce the dark current in a controlled way it is planned to install a scraper in the magnetic bypass. In the present simulations, various scenarios are studied: no scraper, only a low-energy scraper and both high and low-energy scrapers.

Obviously, a scraper should be located at the position of maximum dispersion, hence between the second and the third bending magnet. The minimum distance from the edge of the scraper to the design orbit of the beam has been chosen such that only 1% of the high or low energy tails of the proper beam is removed. The beam distribution at the screen OTR1 for a bending angle of 20° and a rf-phase set for maximum compression is

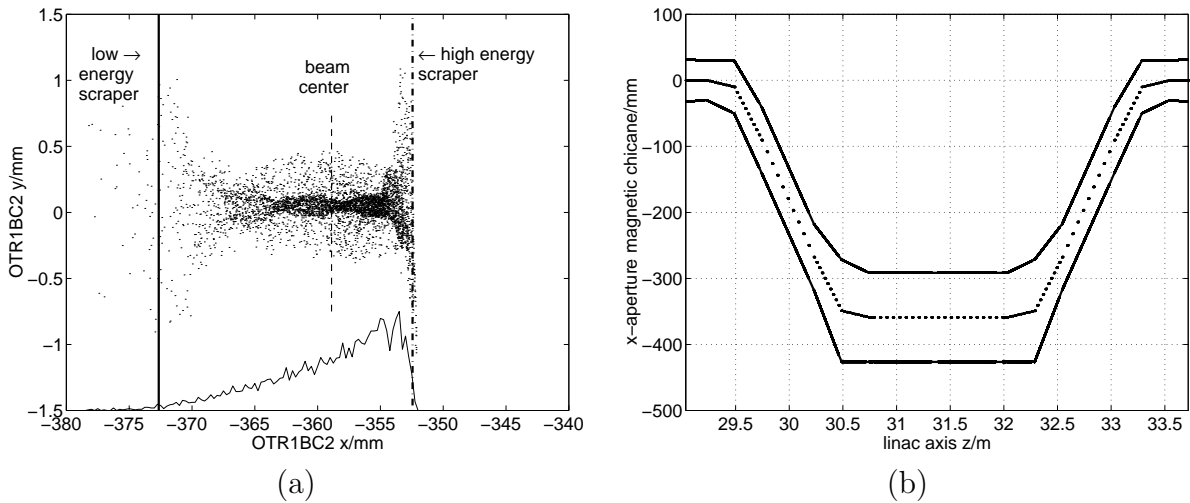


Figure 2.16: (a) The transverse charge distribution and the horizontal beam profile at the screen OTR1 is shown. The positions of the scraper are chosen such that less than 1% of the beam tails are removed (solid: low-energy scraper, dashed-dotted: high-energy scraper). (b) The vacuum chamber as used in the tracking code. The dotted points show the center of the chamber.

shown in Fig. 2.16(a).

The gap between the two scrapers is about 20 mm. The high-energy scraper is closer to the beam center (6.4 mm). In case of small energy jitter ($\approx 1\text{-}2\%$) it is hit by the beam. Due to the long low-energy tail of the beam, the low-energy scraper has a distance of 13.8 mm to the beam center.

The vacuum chamber as used in the tracking code is shown in Fig. 2.16(b). The currents of the magnets in BC2 correspond to typical FEL runs in April 2000. The rf-phase of the second acceleration module is set for maximum energy gain of the electron beam. The results of the dark current tracking calculation to the exit of the last cavity in acceleration module 2 are summarized in Fig. 2.17.

The transmission of dark current from the cathode amounts to 24% in ACC1. In the warm beamline section to the entrance of the magnetic chicane it is reduced to 23% (see Fig. 2.17(e)). The small aperture of 35 mm at the quadrupole triplet Q1-Q3 causes a minor effect. Between the first and the second dipole the dark current drops to 10.4%. The energy deposition along this 70 cm long part of the beamline is approximately 1.4 W for a dark current of $100\text{ }\mu\text{A}$ (measured at the gun Faraday cup), an rf-pulse length of 0.8 ms and 1 Hz repetition rate. In this area, typically, a dose rate of several $100\text{ }\mu\text{Sv/h}$

due to activation of the beamline components has been measured. A 5 cm lead shield has been installed to reduce the high energy photon leakage to the experimental hall 3.

According to the simulation a low-energy scraper reduces the dark current transmission from 10.4% to about 5.1%. An additional high-energy scraper has a negligible effect (-0.3%). The dark current reaching the third dipole is transported to the exit of the second acceleration module. Activation of beamline components behind the chicane are most likely caused by dark current from field emission in the second module which may be accelerated upstream.

The electron distribution in the transverse phase space are shown in Fig. 2.17(a) and (b). Caused by the enormous energy spread and the time structure of the dark current the transverse phase space occupied by electrons grows rapidly, even though 2/3 has been lost. The phase space is filamented due to chromatic aberration. The spread in time causes different focusing strength during acceleration in the module. For comparison the statistical “emittance” of the dark currents is computed. The transverse distribution fills nearly the entire beam pipe of 70 mm diameter as shown in Fig. 2.17(c). The vertical spot size is larger than the horizontal. The edge focusing of the bending magnets causes a small waist in the vertical plane behind the magnetic compressor section. The dark current has thus a stronger divergence in the vertical than in the horizontal plane when it enters the second acceleration module.

The energy distribution of the dark current versus the rf-phase is plotted in Fig. 2.17(d). Due to the large R_{56} of the bunch compressor dark current electrons enter the second acceleration module between -100° and 0° with an energy range between 100 MeV to 240 MeV. Note that a fraction of the dark current is decelerated (rf-phase $< -90^\circ$) in ACC2 while the dark current at an rf-phase of -7° has a slightly higher energy (≈ 3 MeV) than the beam at 0° .

This kind of behavior is a general difficulty, if bunch compressors and off-crest acceleration in rf-section are involved in the particle transport. An efficient collimation scheme has to take into account the particle collimation in time and energy, since both are mixed in the bunch compressor stages. The incorporation of an energy collimator at BC2 has two main advantages. First, the phase space is less populated as shown by the dashed curves showing the profiles of the dark current in Fig. 2.17(a)-(c). Second, the lower energy limit of the dark current moves from about 90 MeV to 215 MeV (proper beam energy 237 MeV). This restricted energy range is within the energy bandwidth of the collimator, see Fig. 1.22, and far above the minimum energy of 114 MeV for a stable transport through the undulator FODO-channel (see 2.4.6).

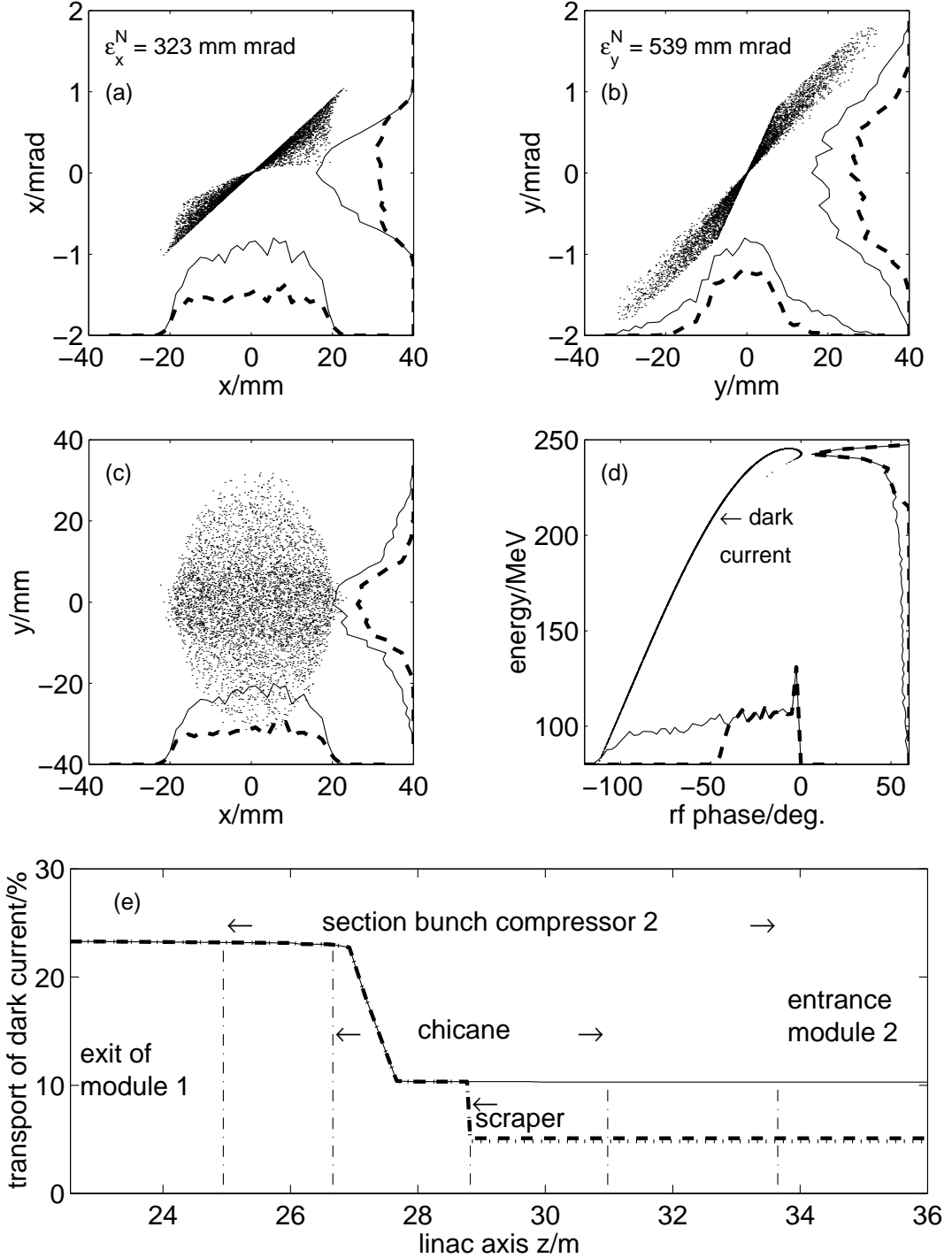


Figure 2.17: Simulation of dark current through BC2 to the exit of acceleration module 2. The plots (a) and (b) show the horizontal and vertical phase space distribution. Plot (c) shows the transverse cross-section and (d) the energy distribution versus the rf acceleration phase of module 2. The projections are added to the plots (solid: no scraper, thick-dashed: low-energy scraper). In (d) the transport of dark current through the bunch compressor is shown where 100% corresponds to the emitted electrons at the cathode area. The solid, dashed and dotted curves are for no scraper, with low-energy scraper, and with high and low-energy scraper.

2.2.7 Coherent synchrotron radiation

An relativistic electron bunch moving in a transverse magnetic field radiates electromagnetic energy in a wide frequency spectrum. The radiation is coherent in the wavelength range of $\lambda \gg \sigma_s$ where σ_s is the bunch length. This frequency range is much below the characteristic frequency $\omega_c \propto \gamma^3/\rho$ of synchrotron radiation, where γ is the relativistic Lorentz factor. Therefore, the spectral coherent radiation intensity, $dI/d\omega$, of a bunch with charge $q = Ne$ behaves like

$$\frac{dI}{d\omega} \propto \frac{q^2}{\rho} \left(\frac{\omega}{\omega_c} \right)^{1/3}, \quad (2.21)$$

and the energy loss of the bunch scales like

$$\frac{d\mathcal{E}_{coh,tot}}{cdt} \approx \int_0^{c/\sigma_s} d\omega \frac{dI}{cd\omega} \propto \frac{q^2}{\rho^{2/3} \sigma_s^{4/3}}. \quad (2.22)$$

The energy loss of a bunch is strongly enhanced for short bunch length and high bunch charge. Because the charge of the dark current in a rf-period is about 4 orders of magnitude smaller than the bunch charge, coherent synchrotron radiation is negligible for the dark current transport.

The coherent synchrotron radiation (CSR) emitted by highly charged micro-bunched beams in the arcs of bending magnets can increase the energy spread and the emittance of a beam. In the past 10 years, the influence of CSR on the beam quality has been studied intensively [42, 43, 44, 45, 46, 47]. Several investigations concern the expected emittance dilution in TTF bunch compressor 2 [48, 49, 50]. The influence of the optics and the optimum choice for beam parameters along the magnetic chicane is discussed in [50]. From the experimental result on the longitudinal beam profile and the observation of an energy modulation within the bunch [41], the electron distribution in the longitudinal phase space is fragmented into almost isolated bunchlets. This observation is so far not fully understood, but the emission of CSR in the bunch compressor 2 has been shown to be responsible for parts of this observations [51].

The energy loss along the bunch is not uniformly distributed and causes an additional energy spread. The way the radiation losses occur along the bunch is a geometrical effect, sketched in Fig. 2.18. It is due to the difference in path length between the electron bunch propagating on a curved trajectory and the emitted electromagnetic field that travels on a straight line. Unlike to wakefields, where a given slice of the bunch acts only on the slices in the back, the radiation field generated at slices in the back overtakes the front slices of the bunch. These fields are called the “overtaking” fields [44].

If an electron at the tail of a bunch radiates at the point *A*, then the electromagnetic field can overtake an other electron at the distance Δs ahead of the source electron, at the point *B*. The distance Δs satisfies the following condition:

$$\Delta s = arc(AB) - |AB| = \rho\theta - 2\rho\sin(\theta/2) \approx \frac{1}{24}\theta^3\rho \quad \text{if } \theta \ll 1. \quad (2.23)$$

The distance $|AB|$ which the electromagnetic field travels, is called the overtaking distance $L_0 = |AB| \approx \rho\theta = (24\Delta s\rho^2)^{1/3}$. The time $\tau = L_0/c$ describes the retardation between

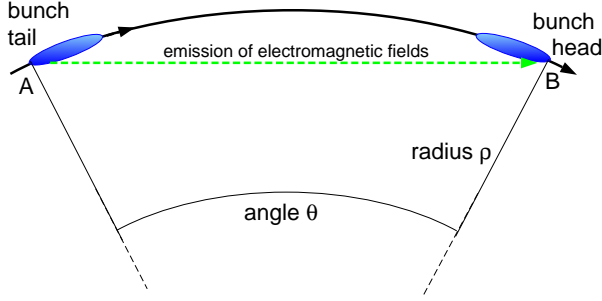


Figure 2.18: Geometrical scheme of the synchrotron radiation from the tail of the bunch to its head along a curved trajectory.

the emission and the interaction of the radiated field with the bunch. The dependence on the coordinate Δs is reflected in the longitudinal overtaking-function $\mathcal{W}'_0(\Delta s)$ which describes the acceleration of an unit charge due to the radiated field by a trailing unit charge (1-dimensional theory) [44]:

$$\mathcal{W}'_0(\Delta s) = -\frac{1}{2\pi\epsilon_0} \frac{1}{3^{1/3}\rho^{2/3}(\Delta s)^{1/3}} \frac{\partial}{\partial(\Delta s)} \quad (\text{steady state solution}). \quad (2.24)$$

The derivative $\partial/\partial(\Delta s)$ is taken with respect to the longitudinal coordinate Δs with $\Delta s < 0$ the bunch tail. To calculate the energy loss per unit length at a position Δs in a bunch the overtaking-function \mathcal{W}'_0 has to be convolved with longitudinal charge distribution of the bunch λ (here as a line-charge distribution):

$$\begin{aligned} \frac{d\mathcal{E}}{cdt} &= Ne^2 \int_{-\infty}^{\Delta s} d(\Delta s)' \mathcal{W}'_0(\Delta s - \Delta s') \lambda(\Delta s') \\ &= -\frac{qe}{2\pi\epsilon_0 3^{1/3} \rho^{2/3}} \int_{-\infty}^{\Delta s} \frac{d(\Delta s)'}{(\Delta s - \Delta s')^{1/3}} \frac{\partial \lambda(\Delta s')}{\partial(\Delta s')} \end{aligned} \quad (2.25)$$

where λ is normalized to unity ($\int d(\Delta s) \lambda(\Delta s) = 1$). For a gaussian charge distribution with a bunch charge of 1 nC and a bunch length of $\sigma_s = 1$ mm the energy loss with the position in the bunch is shown in Fig. 2.19. The coherent synchrotron radiation fields in a bend redistribute the radiative energy losses along the bunch. The electrons at the head of the bunch are accelerated by the fields radiated by the electrons in the tail. The total energy change, however, is always negative. Due to the derivative with respect to the longitudinal coordinate Δs in the overtaking-function Eq. 2.24, the effect of CSR is strongly enhanced in charge distributions with large gradients.

The maximum energy loss of the electron per unit length calculated for 1 mm bunch length is 42 keV/m for 1 nC of charge. The bunch length of 1 mm is the rms-bunch length at the center of the third dipole. The path length through a dipole is 0.52 m. The correlated energy spread induced by CSR in the third bending magnet is in the order of the uncorrelated energy spread of the incoming beam ($\sigma_E = 25$ keV). An effect on the bunch compression and the longitudinal bunch distribution at the exit of the chicane can be expected. The effect is enhanced by the non-gaussian shape of the bunch in the chicane induced by the rf non-linearities (see Fig. 2.12).

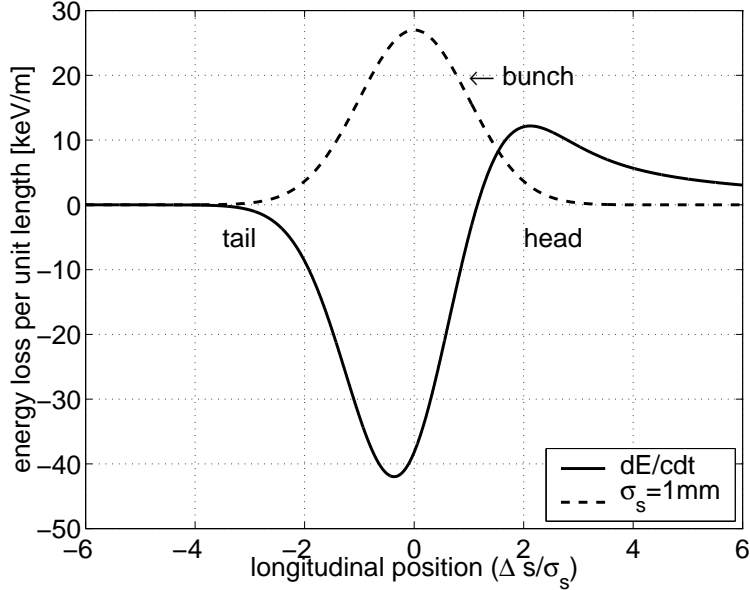


Figure 2.19: Energy loss along the bunch per unit length due to coherent synchrotron radiation calculated by the steady state solution Eq. 2.24 and Eq. 2.25 (solid curve). The longitudinal charge distribution is shown by the dashed curve. Parameters: bending radius $\rho = 1.5$ m, bunch length $\sigma_s = 1$ mm, and charge $q = 1$ nC.

The overtaking distance L_0 for $\Delta s = 1$ mm is $L_0 = 0.19$ m and in the order of the path length through a dipole. If the bunch enters or leaves a dipole, the overtaking-function differs due to the different geometry of the beam trajectory (see [46, 52]). Thus, the longitudinal fields inside the dipole will not reach a steady state over the full length of the bend, and beam dynamics in the chicane are influenced by transient effects. To determine the retarded fields, the history of the beam has to be stored for computation. If the influence of the CSR is strong enough to change the compression process, then perturbative tracking can not longer be applied and more sophisticated methods are required (see [52]). This is the case if the bunch collects a correlated longitudinal energy spread by CSR of the same order of magnitude as the one which is induced in the preceding acceleration section.

The CSR induces an energy gain or loss along the bunch in a region with non-vanishing dispersion. The influenced electrons thus follow a non-vanishing dispersion trajectory when they leave the dispersive section. The dispersion mismatch causes a projected emittance growth. Since the energy change of the electron is a function of the longitudinal coordinate Δs in the bunch, the process adds along the dispersive beamline [53]. If the energy change due to CSR is not too strong along the compressor section, then the projected emittance growth can be removed by a proper beamline design [53]. In the present beamline, the dispersion is always positive and the effect due to CSR adds up, while in the design for phase 2 with an S-shape, the effects cancel partially [54].

The emittance growth due to dispersion mismatch will also influence the halo of the bunch. Since the core of the bunch loses more energy than its tails, the dispersion causes a horizontal shift of the bunch center to the bunch tails. The head of the incoming bunch becomes the low-energy tail after compression, as shown in Fig. 2.12(b). It transmits through the center of the bunch while traveling through the chicane and the distribution will differ from the high-energy tail which is only weakly influenced.

2.3 Dark current transport through ACC3 and collimator section

The transport of the dark current after passing the bunch compressor BC2 and being accelerated in the second cryo-module has been continued through the sections ACC3 and COL1. The simulations show that the amount of dark current which is lost at the first fast feedback kicker depends sensitively on the focusing properties at the upstream linac. For further discussion the transport of dark current has been simulated using two different setting that frequently have been used during SASE runs in April 2000. Both magnet setting vary only by 15% focusing currents of the quadrupole triplet Q5-Q7BC2 for run 2 compared to run 1 while the remaining magnet values are equal.

Beside the two matching doublets Q1-2ACC2 and Q1-2ACC3 the section ACC3 is equipped with two ceramic fast feedback kickers. The kickers with an inner diameter of 36 mm are located in a distance of 0.4 m of Q1-Q2ACC2 and 1.4 m downstream of Q1-Q2ACC3, respectively. With typical focal length $f = 2$ m of the quadrupole doublets it can be expected that the first kicker is potentially irradiated by dark current while at the second kicker the transverse particle distribution will be sufficiently small.

The transmission of the dark current simulated for the two magnet setting is plotted in Fig. 2.20. The solid curve describes the case of a weak focusing by Q5-Q7BC2 at the entrance of the module 2 as shown in Fig. 2.17. The cross-section of the dark current fills nearly the entire beam pipe. At the kicker 1 about 4% of the dark current is scraped off while 0.2% is lost at the kicker 2 only. The total amount of dark current reaching the collimator section is 5.3%.

The dashed curve shows the behavior if a stronger focusing at the end of BC2 is applied. At both kickers only 0.3% of the simulated particles are scraped off and about 0.9% of the particles are lost along the remaining sections of ACC3. In this case, the dark current reaching the collimator section gets 9% of the initially started particles from the cathode. Note that the dark current measured at the monitor BPM1COL1 varies by about a factor of 2 for the two magnet settings.

In Fig. 2.21 a measurement of the dark current at the exit of the injector and the entrance of the collimator is shown. The dark current of $30 \mu\text{A}$ at BPM2INJ2 was 3 times larger than the one of about $10 \mu\text{A}$ measured at BPM1COL1. The magnet setting was similar to the settings used for the simulations. The simulations predict a ratio between BPM2INJ2 and BPM1COL1 of 4.6 in case of the weak focusing and of 2.7 in case of the somewhat strong focusing, in agreement to the measurement.

During this period the dark current measured at the gun Faraday cup was in the range between $185 \mu\text{A}$ and $240 \mu\text{A}$ [55]. From the simulation a dark current at the position BPM1COL1 is expected to be in the range between $11 \mu\text{A}$ and $14 \mu\text{A}$ for the weaker focusing case and in the range between $19.5 \mu\text{A}$ and $25.4 \mu\text{A}$ for stronger focusing case. Thus, the amount of dark current is slightly overestimated by the simulation.

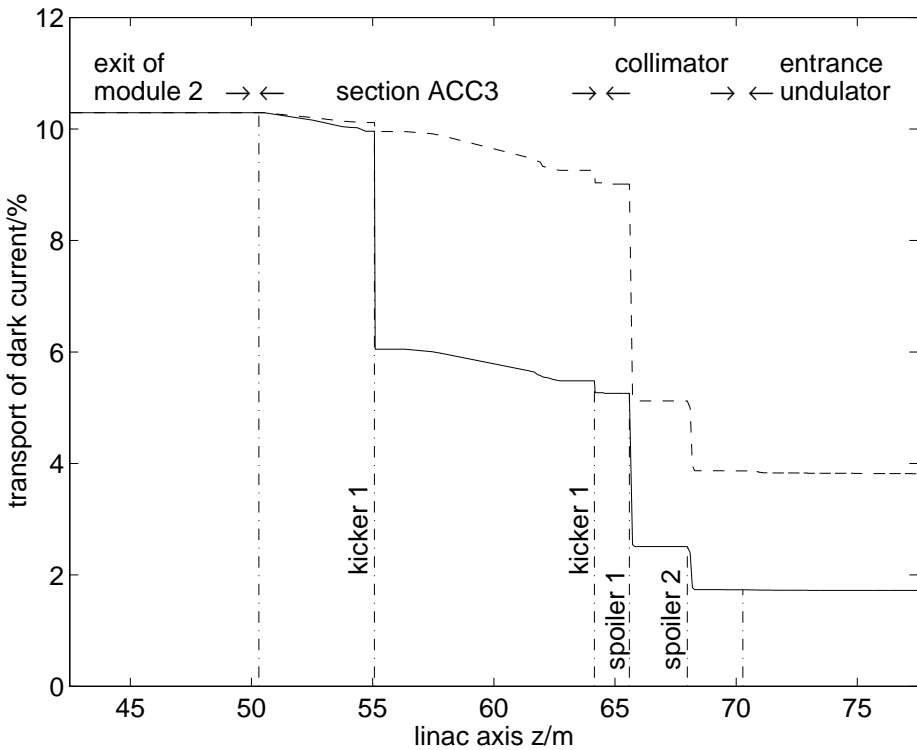


Figure 2.20: Simulation of dark current transmission through section ACC3 and the collimator section to the entrance of undulator. Two settings for the triplet Q5-Q7BC2 frequently used for the SASE runs are shown by the solid and the dashed curve. The focusing strength between the settings vary by 15% only, while the transportation of the dark current differs significantly.

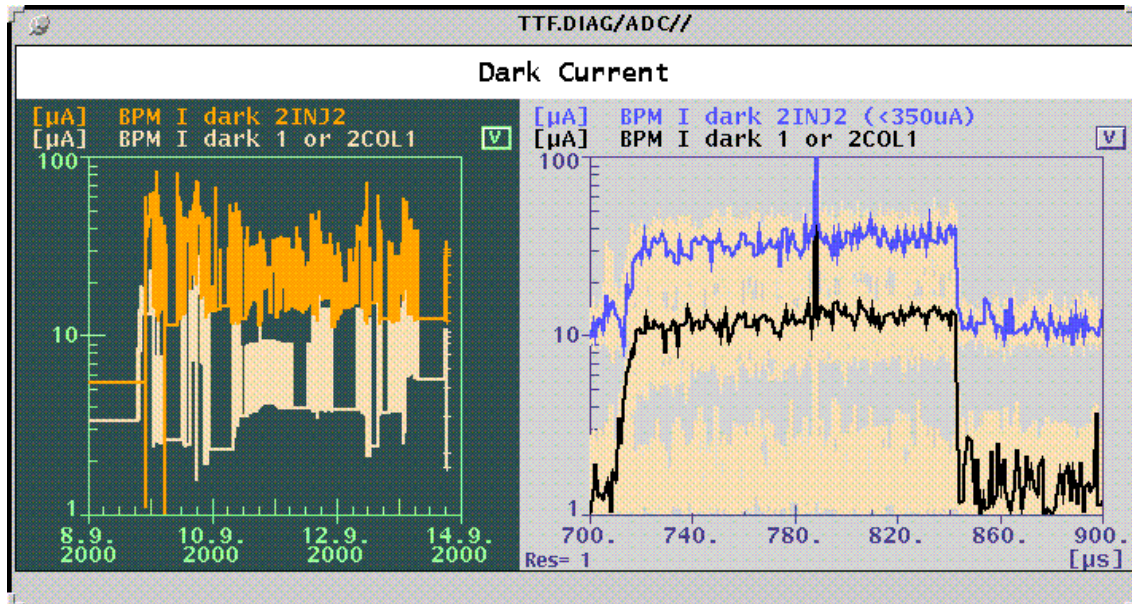


Figure 2.21: Measurement of dark current at the exit of the injector (BPM2INJ2) and at the entrance of the collimator section (BPM1COL1). Typically a ratio of 3-5 between the two dark current monitors has been observed. The magnet settings are similar to the setting used for the simulations. In this example the rf-pulse length of the gun was $150\ \mu\text{s}$.

2.4 Undulator

A precise knowledge of the magnetic field inside the undulator is mandatory for the understanding of the performance and the limits of the collimator. The linear beam optics, mainly determined by the focusing quadrupoles of the FODO-channel together with the weak vertical focusing of the undulator dipole field has been used to define the allowable phase space acceptance of the collimator. It has been assumed, that non-linear effects can be treated as perturbations of the electron motion calculated by linear optics. Due to chromatic aberration in the collimator matching quadrupoles, the electrons with a momentum deviation are not properly matched into the undulator. These electrons follow trajectories with much smaller clearance to the vacuum chamber walls than the regular beam. Hence, to calculate the performance of the collimator the magnetic field in the entire volume of the vacuum chamber has been taken into account. The magnetic field pattern far away from the undulator axis, however, deviates considerably from the field pattern relevant for the electron motion close to the central axis.

The design of the undulator is optimized for operating the FEL. The relevant part of the electron beam contributing to the FEL process propagates within a “tube” of about $200\text{ }\mu\text{m}$ diameter close to and ideally on the undulator axis. The magnet adjustments as well as the magnetic field measurements were focused on this small cylindrical volume to guarantee the high field quality and field strength required. Unfortunately, no direct measurements exist on the magnetic field profiles at large transverse positions. This magnetic field will be reconstructed by theoretical considerations of the undulator magnetic field and the available data. From the reconstructed field, the effects of the higher undulator harmonics on the electron trajectories will be estimated and the strength of the non-linear multipoles are calculated. For fast computation the undulator field is modeled by hard-edge magnets. The geometry and the input parameter for the hard-edge magnets will be derived.

The energy spectrum of the dark current is much larger than the energy bandwidth of the collimator. It is thus unavoidable that a fraction of the dark current is lost inside the undulator. The higher-order magnetic fields influence the position where electrons of the dark current hit the undulator chamber walls. For the life time of the undulator it is essential whether the distribution of the lost electrons is smeared out and covers the whole undulator, or if it is localized. The distribution of the lost electrons is obtained by tracking calculations taking the non-linear magnetic fields into account. For the dark current the results are discussed in section 2.4.9. The calculated distributions will be used in chapter 3 to estimate the radiation doses collected by the permanent magnets by Monte Carlo simulations.

In section 2.4.10, the sensitivity of NdFeB permanent magnets to irradiation is discussed. Several reports from other laboratories are compared and analyzed in detail to estimate the damage threshold for the permanent magnets.

But first of all a short introduction of the FEL principle is given.

2.4.1 The FEL principle

The radiation from a Free Electron Laser (FEL) has much in common with conventional laser radiation, such as high power, narrow bandwidth and diffraction limited beam propagation. The main difference of the two laser types is the gain medium: In a conventional

laser the amplification comes from the stimulated emission of electrons bound in atoms, molecules, or solids, whereas the amplification medium of the FEL are free relativistic electrons interacting with a radiation field.

In a FEL the electrons are propagating through a long periodic magnetic dipole array, the undulator, where the interaction with an electromagnetic radiation field leads to an exponential growth of the radiation emitted by the electrons. The amplification of radiation is initiated by an increasingly pronounced longitudinal density modulation of the electron bunch at the radiation wavelength. The free electron laser is called Self Amplified Spontaneous Emission (SASE) FEL when the initial radiation field is the spontaneous emission of the undulator, and when the full radiation power builds up from spontaneous emission within a single pass through the undulator. To achieve the full radiation power in a single pass the electron beam must have a high phase space density. The wavelength of the FEL is tunable over a wide range depending on the acceleration energy and the undulator parameter. The single pass principle makes it possible to produce laser beams with wavelengths well below the UV, where an optical cavity with normal incident mirrors can no longer be used due to the low reflectivity at short wavelengths.

The basic principle of the free electron laser can be described within the standard picture for the generation of synchrotron radiation. The relativistic electrons are accelerated in the direction transverse to their propagation due to the Lorentz force caused by the magnetic field of the undulator. They propagate along a sinusoidal path and emit synchrotron radiation in a narrow cone in the forward direction with typical opening angle $\propto 1/\gamma$. The deflection of the electrons from the forward direction is comparable to the opening angle of the synchrotron radiation. Thus the radiation produced by electrons along the individual magnetic periods overlaps. Because of the transverse oscillation of the electrons the longitudinal velocity is less than βc . This causes a slippage of the electrons with respect to the faster electromagnetic field propagating on a straight line. The resonance condition for the wavelength λ_{ph} of the first harmonic of the on-axis undulator spontaneous emission

$$\lambda_{ph} = \frac{\lambda_u}{2\gamma^2} (1 + K_{rms}^2) \quad (2.26)$$

with λ_u the magnetic period length of the undulator reflects the electrons slippage by one radiation length λ_{ph} while traveling along one period of the undulator. The value K_{rms} is the “averaged” undulator parameter

$$K_{rms} = \frac{eB_{rms}\lambda_u}{2\pi m_0 c}, \quad (2.27)$$

where B_{rms} denotes the rms magnetic field of the undulator. For a planar undulator and a purely sinusoidal magnetic field, the commonly used undulator parameter K is related to K_{rms} by $K = \sqrt{2}K_{rms}$ and Eq. 2.27 can be used for K instead of K_{rms} if B_{rms} is replaced by the peak magnetic field B_0 .

To achieve an exponential amplification of the spontaneous emission one needs a low emittance, low energy spread electron beam with extremely high charge density and a sufficient overlap between the radiation pulse and the electron bunch along the undulator. Then the electron bunch oscillating through the undulator interacts with its own electromagnetic field created via spontaneous emission. Depending on the relative phase between the radiation and electron oscillation, electrons are either decelerated or accelerated. The

modulation of the electron beam energy causes different longitudinal velocities where the faster electrons catch up with the slower ones. The beam tends to bunch periodically (so called micro-bunching) with the wavelength λ_{ph} of the emitted radiation which causes the energy modulation. In the micro-bunched beam, more and more electrons begin to radiate in phase, which results in an increasingly coherent superposition of the emitted radiation. The stronger the radiation field forces get, the faster the pronunciation of the longitudinal density modulation so that the radiation field amplitude increases exponentially. The exponential growth of the radiation power is obtained until the electron beam is completely bunched (saturation) after which electrons start to extract energy from the radiation field.

2.4.2 Undulator section

Figure 2.22 shows the side view of the 14.4 m long undulator section. The planar undulator is subdivided into three modules, separated by diagnostic stations. Each of the undulator modules consists of more than 600 permanent magnets. Large girders are used to support the magnets. The modules can be adjusted in transverse and longitudinal position. The undulator is temperature stabilized and housed in a climatized chamber.

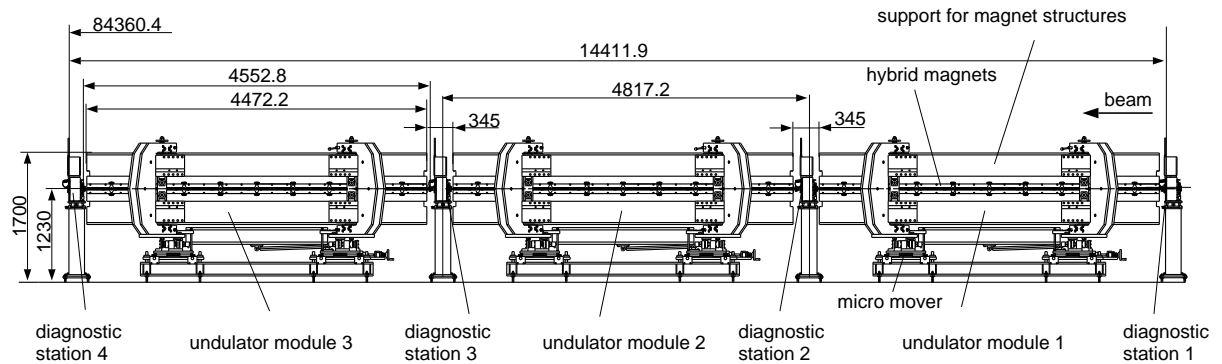


Figure 2.22: Side view of the undulator section.

The magnetic field strength is achieved by hybrid magnets, where iron poles with high permeability are placed between permanent magnets. Figure 2.23 shows a schematic cross-section of a planar undulator based on hybrid magnets. The magnetic field of the permanent magnets points either in positive or negative z -direction. The flux of two adjoining magnets is bent into the transverse direction by the iron pole. The cross section of the iron pole face is smaller than that of a permanent magnets. Therefore, the magnetic field is increased by compressing the magnetic flux. Additional permanent magnets placed between the undulator poles are used to produce the focusing quadrupoles (see Section 2.4.5). The vertical magnetic field of the undulator is periodic and follows approximately a sinusoidal curve. Since the undulator is subdivided into modules with field free regions along the diagnostic blocks a transition of about 2-3 undulator periods occurs at the entrance and the exit of each module. The vertical magnetic field at the center and the transition region of an undulator module is shown in Fig. 2.24.

To achieve the required field quality in the undulator the permanent magnets are sorted such that the resulting field errors are minimized. Then techniques as height adjustment or shimming are used to tune the x and y component of the magnetic field to the required

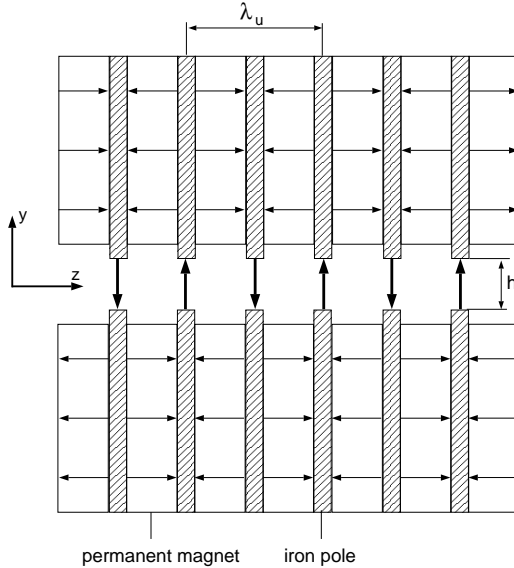


Figure 2.23: Scheme of cross-section of a planar undulator with gap g and a periodicity λ_u . The direction of the magnetic field is indicated by arrows.

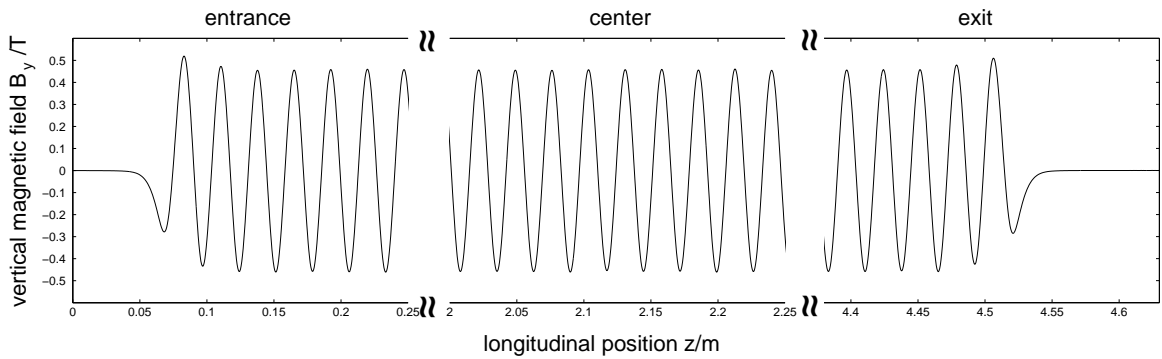


Figure 2.24: Magnetic field B_y at the entrance, the center and the exit of a undulator module.

specification [56].

The electron beam trajectory calculated for an on-axis injection at a beam energy of 230 MeV is plotted in Fig. 2.25. The fast wiggling of the beam is removed by averaging over one undulator period. Due to the transition fields at the entrance and the exit of the undulator the beam is shifted by about $80 \mu\text{m}$ in horizontal direction. Inside the undulator module the rms variation of the horizontal beam trajectory in the regime indicated by stars is smaller than $1.4 \mu\text{m}$. The field data represents only the dipole magnetic field and does not include the focusing quadrupoles.

The important parameters of the undulator are listed in Table 2.5. The magnetic peak field B_0 and the rms magnetic field B_{rms} are calculated in section 2.4.3 from the field measurement of one module shown in Fig. 2.24 excluding the matching field at the entrance and the exit.

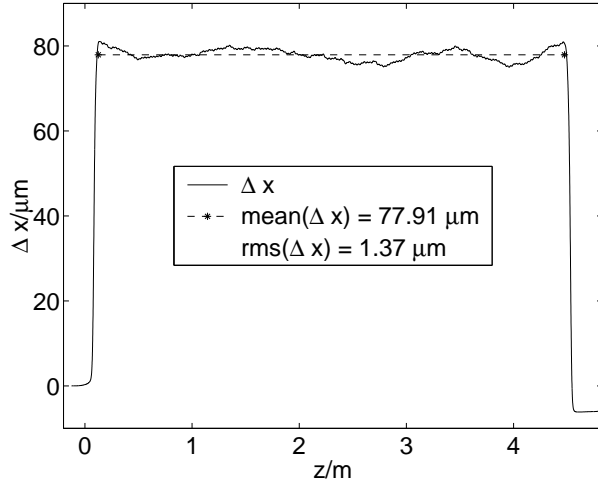


Figure 2.25: Beam trajectory along a undulator module. The calculation have been performed at 230 MeV. The wiggling of the trajectory has been removed by averaging the trajectory over one undulator period.

number of segments		3
period length	λ_u	27.3 mm
number of poles		327
undulator peak field	B_0	0.4582 T
undulator rms field	B_{rms}	0.3210 T
average K-value of undulator	K_{rms}	0.8184
average quadrupole gradient	g_{mean}	10.497 T/m
length of quadrupole	l_q	163.8 mm
length of FODO-cell	λ_{FODO}	955.5 mm
undulator gap height	h	12 mm
vacuum chamber radius	R_{und}	4.75 mm

Table 2.5: Parameters of the undulator [57].

Diagnostic station

The diagnostic station is equipped with horizontal and vertical wire scanners for transverse beam profile measurements [58, 59, 60]. For that, a thin wire is moved transversely across the electron beam. The electrons intercepted by the wire are scattered and generate bremsstrahlung photons. The scattered electrons or photons can be detected downstream the scanner by large scintillators equipped with photomultipliers. The resolution of the wire scanners is limited by the wire diameter and the accuracy of the wire movement. On each fork of the scanners are mounted two carbon wires with $5 \mu\text{m}$ diameter and one tungsten wire with $20 \mu\text{m}$ diameter [61]. The position of the wires is measured by optical encoders with a resolution better than $1 \mu\text{m}$. The wires have been aligned with an accuracy of $20 \mu\text{m}$ vertically and $50 \mu\text{m}$ horizontally to reference marks on the diagnostic station blocks [61].

In addition to the scanners, two cavity BPM's, one for each direction, are installed at the entrance of the diagnostic station.

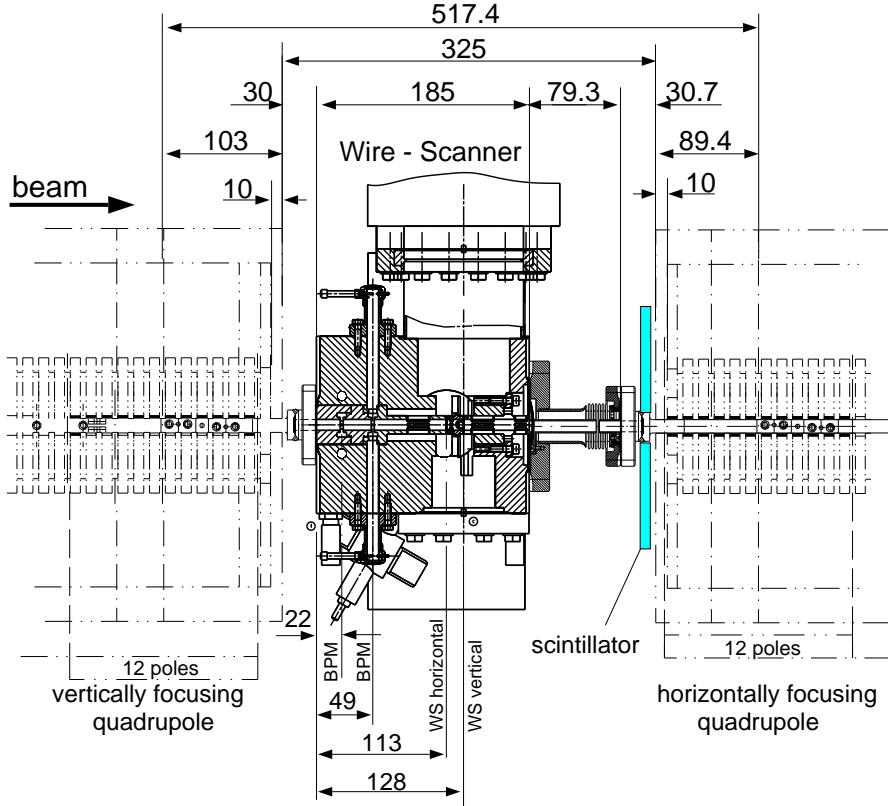


Figure 2.26: Side-view of the diagnostic station.

2.4.3 Influence of higher harmonics of the dipole field

The periodic magnetic field of the undulator can be described by a magnetic potential of the form

$$\Phi(x, y, z) = \sum_{n \geq 0} \phi_{2n+1}(x, y) \cos [(2n + 1)k_u z] \quad \text{and} \quad \mathbf{B} = \nabla \cdot \Phi \quad (2.28)$$

with $k_u = 2\pi/\lambda_u$ the wavenumber of the undulator. The aperture of the vacuum chamber is much smaller than the horizontal width of the undulator poles. Therefore, x dependence of the magnetic field can be neglected ($\phi_{2n+1}(x, y) = \phi_{2n+1}(y)$). From $\Delta\Phi = 0$ the functions $\phi_{2n+1}(y)$ obey the ordinary differential equation

$$\partial_y^2 \phi_{2n+1}(y) - [(2n + 1)k_u]^2 \phi_{2n+1}(y) = 0 \quad (2.29)$$

with the solution

$$\phi_{2n+1}(y) = a_{2n+1} \sinh [(2n + 1)k_u y] + c_{2n+1} \cosh [(2n + 1)k_u y]. \quad (2.30)$$

Since B_y is symmetric with respect to the plane $y = 0$ ($B_y(y) = B_y(-y)$), the coefficients c_{2n+1} vanish identically. Let denote B_0 the on-axis magnetic peak field of the undulator. From Eq. 2.28 and Eq. 2.30 the magnetic field components are calculated to

$$B_x = 0, \quad (2.31)$$

$$B_y = B_0 \sum_{n \geq 0} b_{2n+1} \cosh [(2n + 1)k_u y] \cos [(2n + 1)k_u z], \quad (2.32)$$

$$B_z = -B_0 \sum_{n \geq 0} b_{2n+1} \sinh [(2n + 1)k_u y] \sin [(2n + 1)k_u z], \quad (2.33)$$

with

$$\sum_{n=0}^{\infty} b_{2n+1} = 1. \quad (2.34)$$

To calculate the contribution of the higher harmonics of the undulator the measured magnetic field of 156 undulator periods has been analyzed. The transition at the entrance and the exit of the undulator is not taken into account (13 poles at each side of the undulator module). The result for the parameters b_{2n+1} is listed in Table 2.6 up to the fifth harmonic. Caused by the fairly large ratio between the gap length and period length

first harmonic	$B_0 b_1$	454.0 mT	b_1	0.9908
third harmonic	$B_0 b_3$	4.455 mT	b_3	0.0097
fifth harmonic	$B_0 b_5$	-0.248 mT	b_5	-0.0005

Table 2.6: Coefficients of the higher undulator harmonics.

of $h/\lambda_u = 0.44$, compared to other undulator designs, the third harmonic is less than 1% [62]. The rms-magnetic field B_{rms} for $y = 0$, using Eq. 2.32, is given by

$$B_{rms} = \left(\frac{1}{\lambda_u} \int_0^{\lambda_u} dz B_y^2(z) \right)^{1/2} = \frac{B_0}{\sqrt{2}} \sqrt{\sum_{n \geq 0} b_{2n+1}^2}. \quad (2.35)$$

The values listed in Table 2.5 for the average peak field B_0 and the rms magnetic field B_{rms} are calculated taking the contribution from the first to the fifth harmonic into account. Note that, the ratio B_0/B_{rms} between the undulator peak field B_0 and rms-magnetic field B_{rms} differs from $\sqrt{2}$ if higher undulator harmonics are present.

Maximum deflection angle

The orbit distortion from a straight line, caused by the undulator dipole field can be determined following the reference trajectory through one quarter period starting at the middle of a pole, e.g. at $z = 0$. Using Eq. 2.32 the deflection angle θ at a downstream point z is given by

$$\begin{aligned} \theta(z) &= -\frac{e}{p_0} \int_0^z dz' B_y(z') \\ &= \frac{e}{p_0} B_0 \left[\sum_{n \geq 0} b_{2n+1} \frac{\cosh((2n+1)k_u y) \sin((2n+1)k_u z)}{(2n+1)k_u} \right], \end{aligned} \quad (2.36)$$

with p_0 the nominal momentum of the electron. The maximum deflection angle is equal to the deflection angle for half an undulator pole and yields for $y = 0$ and $k_u z = \pi/2$

$$\theta_{1/2} = \frac{e}{p_0} \frac{B_0}{k_u} \left[\sum_{n \geq 0} (-1)^n \frac{b_{2n+1}}{(2n+1)} \right]. \quad (2.37)$$

At a beam energy of 230 MeV the maximum deflection angle is 2.6 mrad. The correction due to the third undulator harmonic is approximately 0.3%.

Modification of the resonance condition due to field harmonics

The electrons propagating on a curved trajectory always slip with respect to the radiation wave traveling on a straight line. If the electron slippage after one undulator period λ_u is equal to λ_{ph} then the motion is periodical synchronized with a phase front of the electromagnetic field and the emission of the radiation is resonant. Thus, the time $\Delta l/v$ the electrons need to pass the length Δl of their curved trajectory along one undulator period must be

$$\frac{\Delta l}{v} = \frac{\lambda_u + \lambda_{ph}}{c}. \quad (2.38)$$

For small deflection angles θ and at $y = 0$ one can write ($dl = dz/\cos(\theta)$)

$$\begin{aligned} \lambda_{ph} &= \frac{1}{\beta} \int_0^{\lambda_u} \frac{dz}{\cos(\theta(z))} - \lambda_u \approx \frac{\lambda_u}{2\gamma^2} + \frac{1}{2} \int_0^{\lambda_u} dz \theta^2(z) \\ &= \frac{\lambda_u}{2\gamma^2} \left\{ 1 + \frac{1}{2} \left(\frac{eB_0\lambda_u}{2\pi m_0 c} \right)^2 \left[\sum_{n \geq 0} \frac{b_{2n+1}^2}{(2n+1)^2} \right] \right\}. \end{aligned} \quad (2.39)$$

with $\beta = v/c$ the normalized velocity of the electrons. For $b_1 = 1$ and $b_{2n+1} \equiv 0, n > 0$ the formula in Eq. 2.39 reduces to the resonance condition for a sinusoidal motion given in Eq. 2.26. The relative correction of the wavelength by the coefficient of the third harmonic b_3 is 10^{-5} and can be neglected.

Focusing in an undulator

The beam path in an undulator is a nearly harmonic wave along the z -direction. The longitudinal field component B_z appears to the particle partially as a transverse field $B_\zeta = B_z \tan(\theta) \approx B_z \theta$ where ζ is the transverse coordinate in the plane of the wiggling beam (x, z) normal to the actual beam trajectory. The field component B_ζ can be expressed with Eq. 2.33 and Eq. 2.36 as

$$\begin{aligned} B_\zeta &= \frac{e}{p_0} B_0^2 \left[\sum_{m \geq 0} \sum_{n \geq 0} b_{2m+1} b_{2n+1} \sin((2m+1)k_u z) \sin((2n+1)k_u z) \right. \\ &\quad \left. \times \frac{\sinh((2m+1)k_u y) \cosh((2n+1)k_u y)}{(2n+1)k_u} \right] \end{aligned} \quad (2.40)$$

The magnetic field B_ζ deflects the electron in vertical direction. For a slow variation of the vertical position the deflection $\Delta y'$ of an electron while passing half an undulator pole can be estimated by

$$\Delta y' \approx -\frac{e}{p_0} \int_0^{\lambda_u/4} dz B_\zeta(z) = -\frac{e^2}{p_0^2} B_0^2 \frac{\lambda}{8} \sum_{n \geq 0} b_{2n+1}^2 \frac{\sinh(2(2n+1)k_u y)}{2(2n+1)k_u}. \quad (2.41)$$

The Lorentz force due to B_ζ deflects the electron in vertical direction toward the undulator axis independent of the polarity of the poles. This causes a net focusing of the undulator in vertical direction comparable to a cylindrical lens in light optics. The focusing strength depends non-linearly on the coordinate y via the hyperbolic function in Eq. 2.41. The non-linearity causes geometrical aberration of the undulator focusing at large vertical electron offsets. Since the vertical electron motion is restricted to the radius R_{und} of the undulator aperture, the product $k_u y$ is limited by

$$k_u y < k_u \cdot R_{und} \approx 1.09 \quad (2.42)$$

An upper estimate of the contribution for the third undulator harmonic compared to the first is given by

$$\frac{b_3^2 \sinh(6k_u R_{und})}{3b_1^2 \sinh(2k_u R_{und})} = 2.2 \cdot 10^{-3}, \quad (2.43)$$

which is a small correction of the undulator focusing. Therefore the influence of higher undulator harmonics on the focusing is neglected in the following.

Non-linear magnetic fields

It has been shown that the influence on the electron motion due to the higher harmonics of the undulator dipole field b_{2n+1} with $n \geq 1$ is small and can be neglected. But, the hyperbolic dependence of the field amplitude on the vertical position introduces high-order field-errors which can be determined by expanding the hyperbolic functions in Taylor series

$$\cosh(k_u y) = 1 + \frac{(k_u y)^2}{2!} + \frac{(k_u y)^4}{4!} + \frac{(k_u y)^6}{6!} + \dots, \quad (2.44)$$

$$\sinh(k_u y) = (k_u y) + \frac{(k_u y)^3}{3!} + \frac{(k_u y)^5}{5!} + \dots \quad (2.45)$$

Due to the fast convergence of the series expansions only a few terms from each expansions are required to obtain an accurate expression for the hyperbolic function within the undulator aperture. For the electrons of the beam core, propagating close to the undulator axis $k_u y \ll 1$, it is sufficient to consider only the constant and the linear terms, while the propagation of the electron of the beam halo is affected by the non-linearities.

2.4.4 Hard-edge model of undulator magnets

For fast numerical optics calculations it is desirable to describe the effect of the undulator magnets in the form of hard-edge models. For a proper modeling of the undulator magnet structure, two conditions have to be fulfilled: the deflection angle for each pole should be the same as that for the equivalent hard-edge model and the undulator focusing must be the same as the one by the edge focusing⁴. The undulator poles can be modeled by hard-edge rectangular dipoles with magnetic field B_h and length l_h . The deflection angle θ_h of the hard-edge dipole is

$$\theta_h = \frac{e}{p_0} B_h l_h. \quad (2.46)$$

⁴Alternative to the deflection angle the maximum orbit amplitude can be chosen.

The deflection angle for half an undulator period $\theta_{\lambda/2}$ is twice times the maximum deflection angle $\theta_{1/2}$ (see Eq. 2.37). Neglecting the contribution of the higher undulator harmonics, the deflection angle is

$$\theta_{\lambda/2} = 2 \cdot \theta_{1/2} = \frac{e}{p_0} B_0 b_1 \frac{\lambda}{\pi}. \quad (2.47)$$

The edge focusing introduced by a rectangular bending magnet is (see App. A)

$$\frac{1}{f_y} = \frac{\theta_h \tan(\theta_h/2)}{l_h} \approx \frac{\theta_h^2}{2l_h} = \frac{e^2}{p_0^2} B_h^2 \frac{l_h}{2}. \quad (2.48)$$

By expanding the hyperbolic functions of the expression in Eq. 2.41 it can be written as

$$\Delta y' = -\frac{e^2}{p_0^2} B_0^2 b_1^2 \frac{\lambda_u}{8} y \left[1 + \frac{2(k_u y)^2}{3} + \frac{2(k_u y)^4}{15} + \dots \right].$$

Only the term linear in y , which dominates at small vertical offsets, can be expressed by the vertical focusing in rectangular dipole magnets. The focal length per undulator half pole is

$$\frac{1}{f_u} = \frac{e}{p_0} B_0^2 b_1^2 \frac{\lambda_u}{8}. \quad (2.49)$$

Finally, by collecting the expressions for the bending angles and the focal lengths

$$\theta_h = \theta_{\lambda/2} \quad \longrightarrow \quad B_h l_h = B_0 b_1 \frac{\lambda_u}{\pi} \quad (2.50)$$

$$\frac{1}{f_y} = \frac{1}{f_u} \quad \longrightarrow \quad B_h^2 l_h = B_0^2 b_1^2 \frac{\lambda_u}{4} \quad (2.51)$$

the magnetic length l_h and the constant magnetic field B_h are determined by

$$l_h = \frac{4}{\pi^2} \lambda_u \quad B_h = \frac{\pi}{4} B_0 b_1. \quad (2.52)$$

Note that $l_h < \lambda_u/2$, which results in a sequence of bending magnets and drift spaces. The difference in path length between the sinusoidal reference trajectory and a straight line is much smaller than the undulator period. Thus the difference between magnetic length l_h and its straight line length can be neglected⁵ and the length of the drift space l_d is approximately given by

$$2(l_d + l_h) \approx \lambda_u \quad \Rightarrow \quad l_d \approx \left(\frac{1}{2} - \frac{4}{\pi^2} \right) \lambda_u. \quad (2.53)$$

The hard edge model for half an undulator magnet period is shown in Fig. 2.27.

⁵For a rectangular bending magnet the magnetic length is $l_h = \rho\theta$, the drift length is $l = \rho \sin(\theta)$ and the straight line length is $L_h = 2\rho \sin(\theta/2)$.

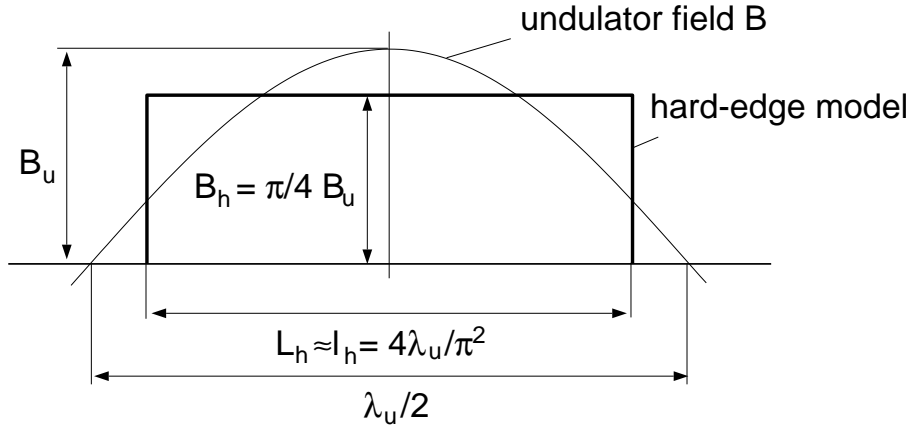


Figure 2.27: Hard-edge model for half an undulator magnet period.

2.4.5 Hard-edge model of the undulator modules

To describe the sinusoidal magnetic field pattern of the undulator, a hard-edge model consisting of sequence of drift spaces and alternating rectangular dipole magnets of constant magnetic field has been introduced. The longitudinal field component of the undulator produces a weak vertical focusing of the beam. To obtain the high charge density which is required to achieve exponential gain in the SASE-process, a FODO-channel is superimposed to the array of dipole magnets. The quadrupoles are made by placing thin permanent magnet plates between the iron poles of the hybrid structure. In Fig. 2.28 a scheme of the transverse cross-section of the undulator is sketched, showing the field lines produced by the additional permanent magnets. The additional permanent magnets point either in positive or negative vertical direction. Twelve such magnet arrangements, corre-

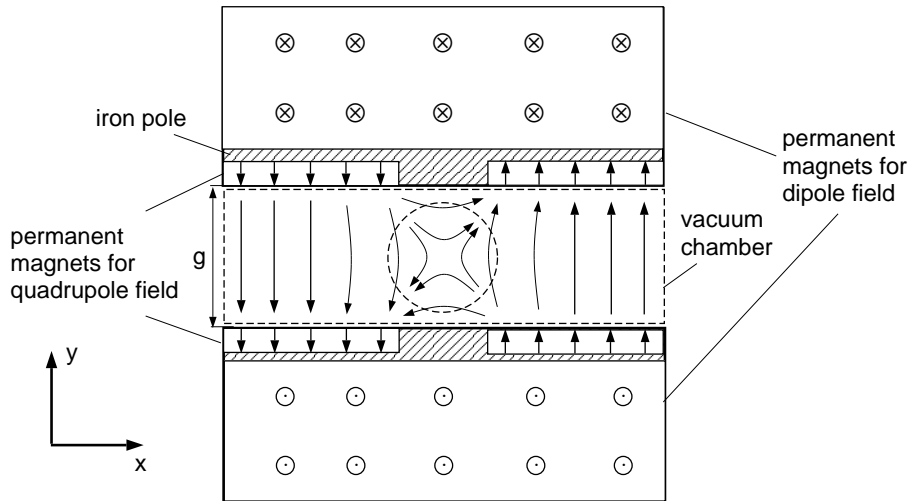


Figure 2.28: Scheme of the transverse undulator cross-section. The arrows show the field lines created by the additional four thin permanent magnet blocks that are used to produce a quadrupole field. The vacuum chamber is indicated by the dashed line.

sponding to six undulator wavelength, are used to achieve a sufficiently strong integrated quadrupole field. To create a FODO-cells two quadrupoles are required, one horizontally focusing, the second horizontally defocusing. In each undulator module five FODO-cell

are installed, resulting in a total number of thirty quadrupoles. The integrated gradient of each quadrupole has been measured [57, 63]. The result of the measurement is shown in Fig. 2.29. The average values of the integrated quadrupole gradient for the first and

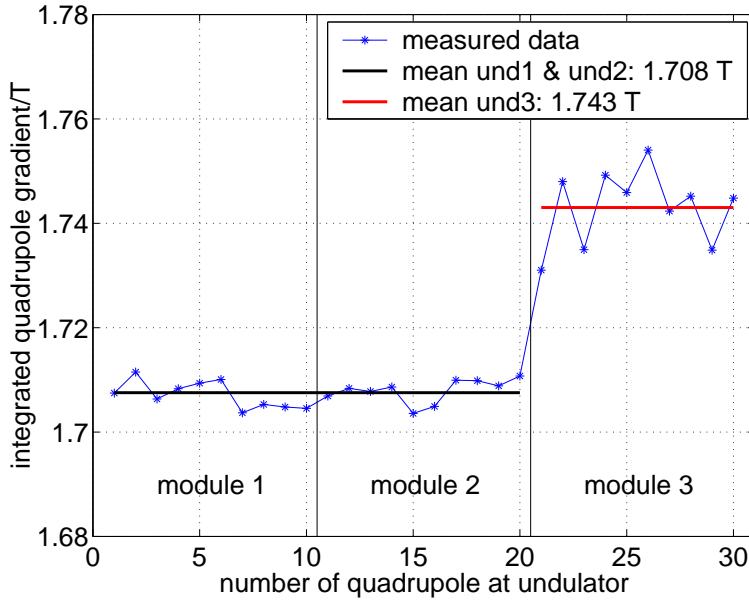


Figure 2.29: Integrated gradients of the undulator quadrupoles. In the first and second undulator modules the quadrupole strength deviate by less than $\pm 0.3\%$ from the mean value taken over the first 20 quadrupoles. In the third undulator module the mean value is 2.1% larger than for the first two modules and scatters by $\pm 0.7\%$.

the second undulator module differ by 2.1% from that of the third module, while the scattering of the individual quadrupole strength within a module is comparably small. Thus, for the simulations, the two mean values representing the first two and the third undulator module are used to calculate the optics. The length of the quadrupoles l_q has been set to $6\lambda_u = 163.8$ mm. The total length of the FODO-cell is $L_{FODO} = 955.5$ mm. In Fig. 2.30 the cross-section of undulator entrance is shown together with the magnetic fields used for the hard-edge model [64]. The parameters for the hard-edge model of the undulator are summarized in Table 2.7.

length of dipole	l_h	11.064 mm
magnetic dipole field	B_h	± 356.5 mT
drift space between dipoles	l_d	2.586 mm
quadrupole length	l_q	163.8 mm
quadrupole gradient UND1	g_1	± 10.425 T/m
quadrupole gradient UND2	g_2	± 10.425 T/m
quadrupole gradient UND3	g_3	± 10.641 T/m
length of FODO-cell	λ_{FODO}	955.5 mm

Table 2.7: Input parameters for the hard-edge model of the undulator.

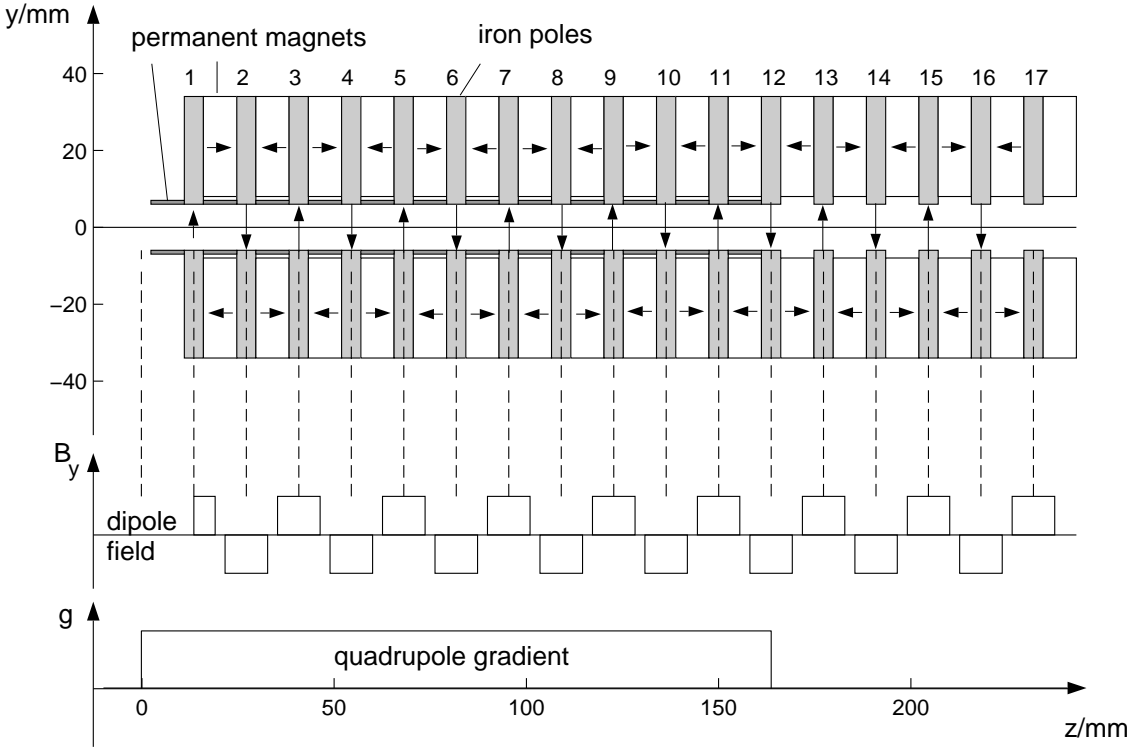


Figure 2.30: Scheme of the undulator modeled by hard-edge magnets. The upper plot shows the cross-section of the undulator entrance. The corresponding dipole field is shown in the middle and the quadrupole gradient at the bottom.

2.4.6 Periodic solution for a the FODO-cell and instability limit

A simple way to calculate the periodic solution for the β -function with period length of λ_{FODO} is, to transport the β -matrix

$$\beta = \begin{pmatrix} \beta & -\alpha \\ -\alpha & \gamma \end{pmatrix} \quad (2.54)$$

by one FODO-cell starting from the mid point of the focusing quadrupole ($F_{1/2}ODOF_{1/2}$). By symmetry, α vanishes at the center of the quadrupole. According to Eq. 1.9

$$\beta_i = \mathbf{M}_i \cdot \beta_i \cdot \mathbf{M}_i^T \quad \text{with } i = x, y \quad (2.55)$$

for the transformation of the β -matrices, the periodic solution can be determined by

$$\beta^2 = \frac{M_{12}^2}{1 - M_{11}^2}. \quad (2.56)$$

The transfer matrices are calculated numerically using the parameters listed in Table 2.7. Solution for the horizontal and vertical β -functions and their phase advances at three different energies are shown in Fig. 2.31. The β -function increases with the beam energy. The edge-focusing of the dipoles causes in the vertical direction a slightly smaller β -function and larger phase advance than in the horizontal direction. The small difference in the quadrupole gradients for the last undulator module causes slightly different periodic

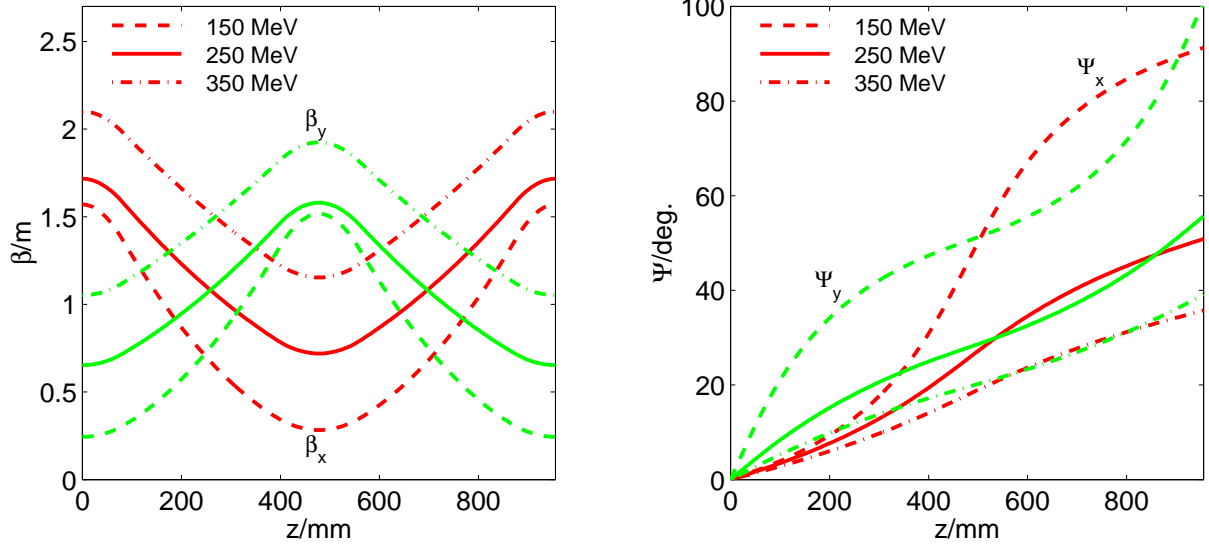


Figure 2.31: β -functions and phase advances of the undulator FODO-cell for 150 MeV, 250 MeV and 350 MeV (first or second undulator).

solutions for its FODO-cells.

If the beam energy is decreased below 114 MeV the FODO-channel gets unstable and the β -function grows along the undulator. The stability criterion is

$$Tr(M_i) < 2 \quad (2.57)$$

which must be fulfilled in both planes. Equation Eq. 2.57 is equivalent to phase advances smaller than 180° per FODO-cell. The phase advances Ψ_x and Ψ_y per cell as a function of the beam energy are plotted in Fig. 2.32.

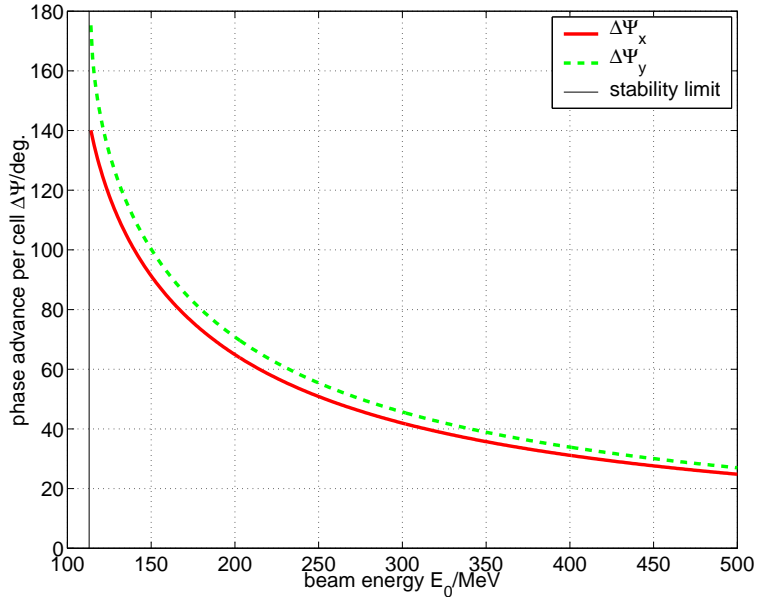


Figure 2.32: Phase advances per undulator FODO-cell versus the beam energy. The FODO-cell has no periodic solutions in vertical direction for energies below 114 MeV (stability limit).

2.4.7 Linear beam optics of the undulator

Within an undulator module the periodic solution shown in Fig. 2.31 repeats five times. It follows a drift space for the diagnostic stations installed between the undulator modules. The periodic solution for the β -function along the second and third undulator modules is perturbed since

- the distance between the quadrupole center of the last quadrupole of the upstream undulator module to the center of the first quadrupole of the downstream module is 517.4 mm and thus 8.2% longer than the length of a half FODO-cell $\lambda_{FODO}/2$.
- there is no vertical focusing along the drift space between the undulator modules
- the quadrupole strengths are different in the last undulator compared to the first and the second ones.

Because of these reasons, beats of the β -functions in horizontal and vertical direction occur which reduce the acceptance phase space of the undulator. The β -functions along the undulator modules for a beam energy of 230 MeV are plotted in Fig. 2.33 (periodic in first undulator module). For a mono-energetic electron beam the clearance of the electrons to the undulator vacuum chamber is reduced by 170 μ m, about 12% of the total clearance of 1.4 mm (see Sec. 1.2.3 p.27). Particularly large values for the horizontal β -function appear at the first and the seventh quadrupole in the second module. The position of the β -function along the second and third module with large peak values vary with energy. The beat of the β -function is one of the reasons why beam losses in the second and third undulator modules have been observed. The impact of the miss-match between the undulator modules is investigated with tracking calculations in chapter 3.

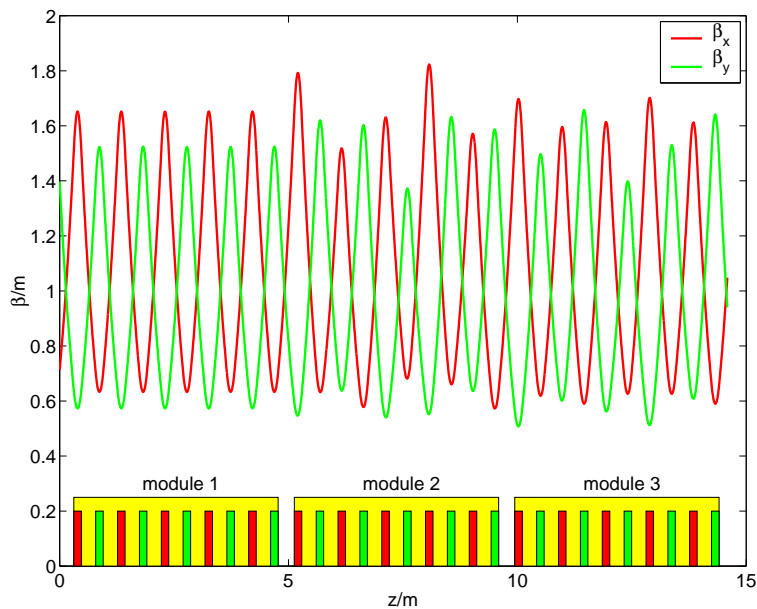


Figure 2.33: Development of the β -functions along the undulator for 230 MeV beam energy. The initial Twiss parameters are chosen such that the β -functions are periodical in the first undulator module. The periodicity is perturbed between the undulator modules and beats of the β -functions are observable.

2.4.8 Octupoles

The field quality of the quadrupoles is strongly perturbed due to the dipole geometry (see Fig. 2.28). This causes higher order magnetic fields at the positions where the quadrupoles are installed in the hybrid structure. Unfortunately, the contribution of higher-order multipole fields has not been measured for the undulator modules before the installation in the TTF linac. From a short prototype structure of the undulator the variation of the vertical magnetic field with the horizontal position x is available. The data are shown in Fig. 2.34. To extract the coefficients describing the behavior of the field the relevant multipoles have to be identified. For a given point (x, y) , by symmetry, the horizontal and vertical field components induced by the additional permanent magnets must fulfill

$$B_x(x, y) = -B_x(-x, -y) \quad \text{and} \quad B_y(x, y) = -B_y(-x, -y). \quad (2.58)$$

These conditions exclude multipoles of odd order (dipoles, sextupoles, decapoles). The remaining normal and skew multipoles up to octupoles are [8]

$$\begin{aligned} \text{normal quadrupole} \quad B_x &= gy & B_y &= gx \\ \text{skew quadrupole} \quad B_x &= -\underline{g}x & B_y &= \underline{g}y \\ \text{normal octupole} \quad B_x &= \frac{1}{6}o(3x^2y - y^3) & B_y &= \frac{1}{6}o(x^3 - 3xy^2) \\ \text{skew octupole} \quad B_x &= -\frac{1}{6}\underline{o}(x^3 - 3xy^2) & B_y &= \frac{1}{6}\underline{o}(3x^2y - y^3). \end{aligned} \quad (2.59)$$

In the horizontal symmetry plane the contributions of the four permanent magnets embedded in the hybrid structure cause a vanishing horizontal field ($B_x(x, 0) \equiv 0$). Hence, the skew multipoles can be set to zero ($\underline{g} = 0, \underline{o} = 0$). The dependence of a quadrupole and an octupole on the coordinate x for $y = 0$ is used to describe the measured magnetic field and to determine the multipole coefficients g and o . As seen in Fig. 2.34, the field B_y within the vacuum chamber is well described by a superposition of a quadrupole and an octupole, while higher order multipoles are required for larger values of x . The quadrupole and the octupole term have an opposite sign.

The quadrupole gradient of the prototype is 15.7 T/m, while the quadrupole gradients in the undulator are 10.5 T/m. It has been assumed that the ratio g/o is approximately constant and can be scaled, which may overestimate the octupole field strength. The scaled octupole contributions of the undulator modules installed at TTF are listed in Table 2.8. The octupole fields are included in the tracking calculations.

octupole length	l_o	163.8 mm
octupole strength UND1	o_1	$\mp 5.153 \cdot 10^5 \text{ T/m}^3$
octupole strength UND2	o_2	$\mp 5.153 \cdot 10^5 \text{ T/m}^3$
octupole strength UND3	o_3	$\mp 5.260 \cdot 10^5 \text{ T/m}^3$

Table 2.8: Octupole field strength derived from prototype measurements.

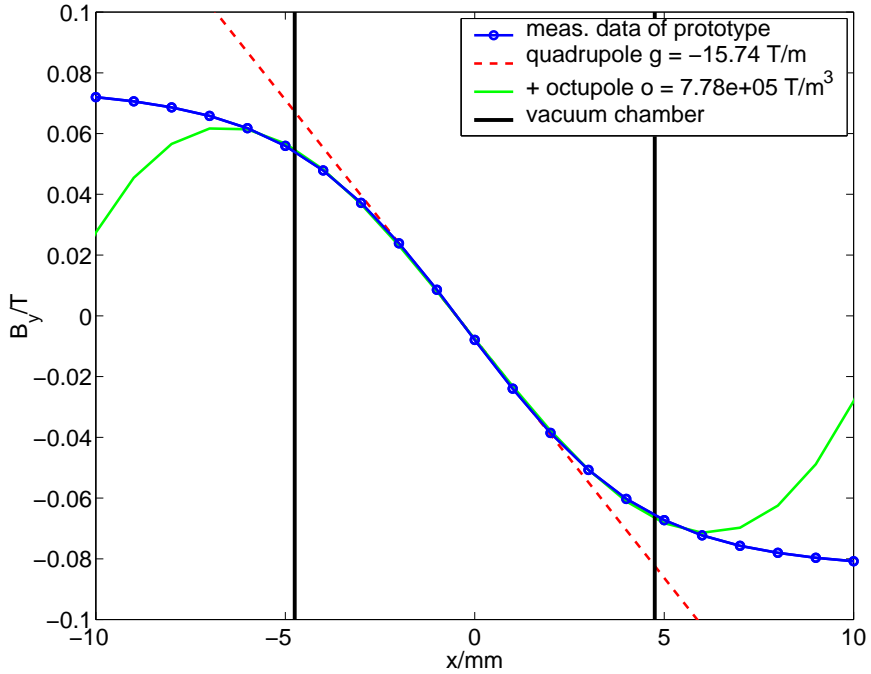


Figure 2.34: Measurement of vertical magnetic field B_y as a function of the horizontal position x in the plane $y = 0$ for a prototype structure of the undulator [62]. The dashed line is a fit representing the quadrupole field. By superimposing the field dependence of an octupole an accurate description of the vertical magnetic field within the vacuum chamber is achieved.

2.4.9 Dark current transport through undulator

In the previous sections the magnetic multipoles required for tracking calculations have been derived. The tracking of electrons through the undulator takes into account:

- the fast wave-like orbit of the electrons due to the alternating dipole field,
- linear and non-linear vertical focusing (geometric aberration up to order $1/f_y \propto y^4$),
- the focusing quadrupoles,
- the octupole components of the quadrupoles,
- chromatic effects,
- and the vacuum chamber geometry.

Additional field errors, misalignments of magnets or aperture displacements are not taken into account. The dark current emitted at the cathode area of the electron gun is transported through the different sections of the linac: the injector, acceleration module 1, bunch compressor 2 section, acceleration module 2, section ACC3, the collimator section and finally through the undulator. The magnetic fields from dipole correctors along the sections are not included in the simulation. Particles hitting the vacuum chamber are stopped and not followed anymore. The coordinates of the lost particles are stored.

The linac setting, focusing strength and the rf-parameters (phase and amplitude) strongly influence the amount of dark current transported to the entrance of the undulator and the amount of dark current which is lost in the undulator. A parameter scan of the various

components along the linac is too time consuming. Therefore three different cases are studied in detail. The first and the second case correspond to the magnet and rf settings during the run period for SASE operation in February to April 2000. The first and the second case differ in the focusing strengths of last three quadrupoles in BC2. In case 3 the same magnetic gradients are used as for case 2, but a low-energy scraper in the straight section of the magnetic chicane removes parts of the dark current. The transmission of the dark current through the different sections and its phase space distribution are discussed in Sec. 2.1.4, 2.2.6, and 2.3. The important parameters of case 1-3 are summarized in Table 2.9. The rf-phase of the first acceleration module is adjusted to compress the beam to the minimum bunch length and the rf-phase of the second acceleration module is set

case	beam energies [MeV]			quad. gradients [T/m]			scraper
	INJ	BC2	ACC3	Q5BC2	Q6BC2	Q7BC2	
1	16.5	138	242	-0.78	1.38	-0.78	no
2	16.5	138	242	-0.82	1.65	-0.90	no
3	16.5	138	242	-0.82	1.65	-0.90	low-energy

Table 2.9: Main parameters of different cases studied for the transmission of dark current

for maximum energy gain of the beam.

For each simulation, initially $5 \cdot 10^5$ electrons are emitted from the cathode area and tracked through the linac. The transmission probability to the position where the dark current can be measured is listed in Table 2.10. Most of the dark current is lost in the injector,

case	Transmission of dark current [%]			
	gun Faraday cup	BPM2INJ2	BPM1COL1	BPM2COL1
1	75	24	5.5	2.5
2	75	24	9.0	5.0
3	75	24	5.1	3.3

Table 2.10: Transmission probability of dark current to the position where dark current monitors are installed or three different linac settings. 100% corresponds to the emitted electrons from the cathode area.

the entrance of the bunch compressor and at the collimator section. Between 2-5% of the electrons reach the entrance of the undulator and less than 0.1% is lost in the undulator section (about 500 tracked electrons). The fraction of electrons lost inside the undulator modules, at the entrance of the first undulator and along the undulator section including diagnostic stations for the different cases is listed in Table 2.11.

In case 1 the dark current loss in the undulator is a factor 10 smaller than in case 2, while the total dark current transported through the undulator differs only by a factor 2 (see Table 2.11 and Fig. 2.20). This result is astonishing since the focal strength of the quadrupoles in the bunch compressor differs only by 5%, 20%, and 5% which is small compared to other magnet settings also been used for linac operation. Hence the distribution of the dark current in the transverse 4-dimensional phase space is the important criterion for the transmission probability through the undulator. Neither from the ratio between the dark current monitors BPM1COL1 and BPM2COL1, before and behind the

case	deposited e^- emitted e^- from cathode [10 ⁻⁴]				
	UND1	UND2	UND3	UND-section	UND1 (0.55 m)
1	0.76	0.06	0.06	0.94	0.46
2	7.30	1.02	0.48	8.82	5.50
3	0	0	0	0	0
deposited energy emitted charge from cathode [mJ/ μ C]					
1	11.6	1.08	0.95	14.4	7.24
2	121.5	17.2	8.16	147.1	91.8
3	0	0	0	0	0

Table 2.11: From the cathode emitted dark current deposited in the undulator.

first spoiler, nor from the total amount of dark current transported between the injector and the collimator section it can be decided if the loss probability of the dark current in the undulator is large or small.

A scraper in BC2 removing the low energy tail of the dark current turns out to be very effective. In the studied case no electrons are dumped in the undulator.

The largest losses occur within a distance of 0.5 m from the entrance of the first undulator module. The second and third undulator module are weakly exposed. The deposited energy of the simulated electrons is added to Table 2.11. The energy deposition per unit length for 1 μ C charge emitted from the cathode as a function of the axial position is plotted in Fig. 2.35(a). The largest energy deposition (for case 2 $dE_{dep}/(qdz) = 0.32$ J/ μ Cm) occurs between the first and the second quadrupole in UND1. The losses appear dominantly upstream of vertically focusing quadrupoles. The energy of the electrons hitting the undulator chamber is shown in Fig. 2.35(b). No losses occur due to electrons with energy above 195 MeV. The lost electrons incident upstream of the undulator towards smaller energies.

The transverse position of incidence is plotted in Fig. 2.36(a). About 90% of the electrons have a horizontal offset x smaller ± 1.5 mm when they hit the undulator vacuum chamber and are lost in vertical direction. The vertical angles of the electrons is shown in Fig. 2.36(b).

Estimate of the absorbed dose in the permanent magnets

With the results of the tracking calculation a first estimate for the expected absorbed dose in the permanent magnets can be given. The charge emitted from the cathode area depends on the rf-pulse duration t_{rf} , the repetition rate f_{rep} , the dark current I_{dark} and the considered run duration t_{run} . Since the dark current emitted from the cathode is not directly accessible, one can use the measured dark current i.e. at the gun Faraday cup $I_{Faraday}$ to determine the emitted charge

$$q_{dark} = \frac{I_{Faraday}}{0.75} \cdot t_{rf} \cdot f_{rep} \cdot t_{run}. \quad (2.60)$$

The factor 1/0.75 corrects the measured dark current to the emitted one (see Table 2.11). Typical parameters are $I_{Faraday} = 100 \mu A$, $t_{rf} = 800 \mu s$ and $f_{rep} = 1$ Hz. For one week

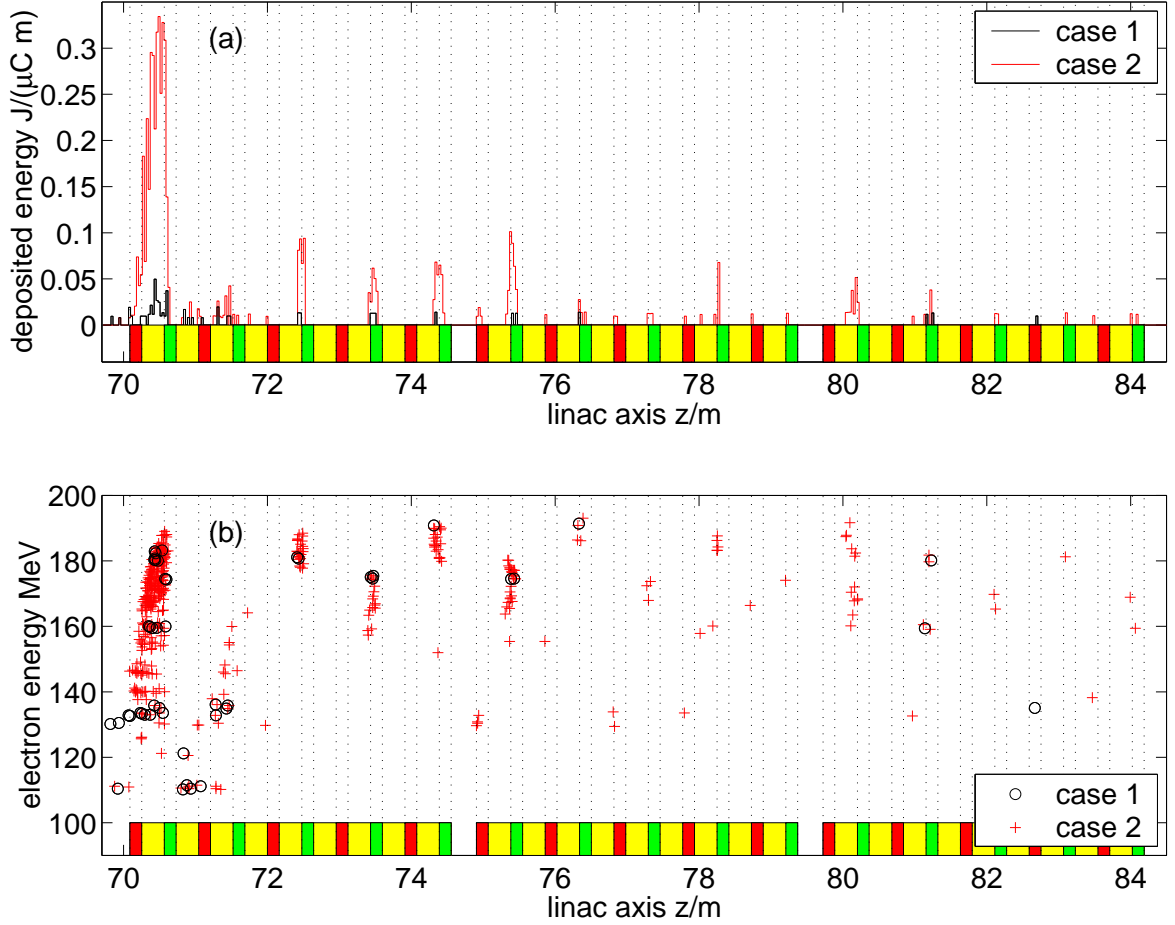


Figure 2.35: Simulation of energy deposition by dark current in undulator modules. In (a) the energy deposition per unit length for $1\mu\text{C}$ dark current emitted at the gun cathode for two linac settings is shown. In Figure (b) the energy of the electrons hitting the undulator chamber is plotted.

operation $t_{run} \approx 120$ h the emitted charged from the cathode is

$$q_{dark}(\text{one week}) \approx 50 \text{ mC.} \quad (2.61)$$

The energy deposition per unit length close to the second quadrupole of the first undulator is approximately

$$\frac{dE_{dep}}{dz}(\text{one week}) = \begin{cases} 1.5 \text{ kJ/m} & \text{for case 1} \\ 17 \text{ kJ/m} & \text{for case 2} \end{cases}. \quad (2.62)$$

Nearly all electrons hit the vacuum chamber with a vertical offset close to the surface of the magnets. The thickness of the vacuum chamber in vertical direction is 1 mm and due to multiple scattering in the material the electrons immediately leave the the chamber. Approximately 50% of the secondary particles are back-scattered into the vacuum while 50% of the shower energy is absorbed in the hybrid structure. The energy deposition in the vacuum chamber can be neglected. Inside the magnet the axial distance in which the shower develops is about $6X_0 \approx 10$ cm. The variation of the energy deposition per unit length, Eq. 2.62, is small along this axial distance and can be assumed to be constant. The shower extends radially to about the Molière radius $R_M = 1.5$ cm. The absorbed

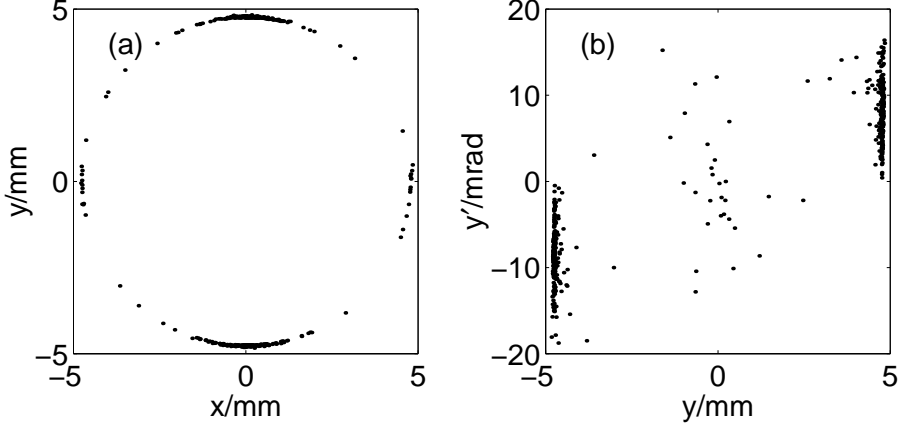


Figure 2.36: Transverse distribution of the electrons hitting the undulator chamber. (a) horizontal and vertical positions (b) vertical phase space.

dose per week in the magnets close to the second quadrupoles is approximately

$$D = \frac{E_{dep}}{m} = 0.5 \cdot \frac{\frac{dE_{dep}}{dz}(\text{one week})}{\pi R_M^2 \rho} \left\{ \begin{array}{ll} 0.14 \text{ kGy} & \text{for case 1} \\ 1.6 \text{ kGy} & \text{for case 2} \end{array} \right. . \quad (2.63)$$

where m is the mass of the exposed magnet volume and $\rho = 7.6 \text{ g/cm}^3$ the density of the material (NdFeB). Equation 2.63 shows the possible range within the dose rates may vary, even when the dark current of the gun remains constant, but the linac settings are slightly different (further details see Sec. 3.3.4). For a 10 Hz repetition rate the absorbed dose due to dark current is totally unacceptable and could damage the first undulator within 1-2 months. A careful operation of a low-energy scraper in the bunch compressor 2 section allows higher linac repetition rates at dark current levels of $100 \mu\text{A}$.

2.4.10 Demagnetization of NdFeB permanent magnets

Advances in rare earth permanent magnets technology have made possible new applications, such as the use of permanent magnet lenses in beam transport systems and the extensive use in undulator and wigglers of synchrotron radiation sources and free electron laser systems. The applications involve potential exposure of the permanent magnets to high radiation fields. To determine the damage thresholds for the permanent magnets, several studies by exposing the magnets to various types of radiation have been performed. Because of the large energy product ($B \cdot H$), the high remanence field (B_r), and the mechanical properties, NdFeB is the preferable material for undulators and has been used in the TTF undulator. The higher suppleness of NdFeB as compared to e.g. SmCo based magnets, enables to produce the 2 mm thin magnet plates required for the undulator quadrupoles. The magnetic properties of the NdFeB permanent magnets⁶ (VACODYM 396) used in TTF is listed in Tab. 2.12. The disadvantage of this type of permanent magnet is a higher sensitivity to exposure of electrons and photons as compared to e.g. SmCo [65]. To predict the likelihood of radiation-induced damage of the NdFeB magnet type used in TTF undulator, the important observations and reports are summarized. A comparison of the reported dose rates that cause a demagnetization is complicated by such factors as the particular magnet material, the techniques applied during manufacture and difference in the radiation field of exposure. For better understanding of the various results and the applicability to TTF, experiments performed at the ESRF⁷ and at POSTECH⁸ are analyzed in detail by Monte Carlo simulations.

The most important observation for the understanding of the demagnetization mechanism is, that the flux loss of the exposed magnet does not only depend on the total absorbed dose. The energy spectrum of the radiation field strongly influence the degree of magnet damage. Okuda et al. [66, 67] have measured no influence on the remanent field of NdFeB magnets⁹ for absorbed dose of up to 2.9 MGy if these were irradiated by γ -rays from a ^{60}Co -source with energies of 1.17 MeV and 1.33 MeV. But the same type of magnet exposed to 17 MeV electrons shows remanence loss of 9% at an absorbed dose of 2.6 MGy. The damaging effects of the γ -rays are due to the irradiation by the secondary electrons emitted in the sample. The main difference between the irradiation by electron beams and by γ -rays is in the electrons contributing to the effect, their direction of travel and the absorbed dose rates per unit length.

Similar results were reported at higher electron beam energies in the work by Luna et al. [68], who exposed NdFeB magnets to an 85 MeV electron beam directly and to a mixed photon-electron radiation field generated from a bremsstrahlung production target¹⁰. A 1.5% remanence loss of the magnet has been measured after only a 360 Gy direct exposure. The same type of magnet¹¹ shows 1.4% demagnetization at an absorbed dose of 13.7 MGy in the mixed radiation field, whereas a magnet¹² from a different manufacturer,

⁶Density 7.6 g/cm³, composition: Fe 68%, Nd 24%, Dy 7%, B 1%

⁷European Synchrotron Radiation Facility (ESRF)

⁸Pohang Accelerator Laboratory (POSTECH)

⁹Used magnet type: N-33H, Nd₂Fe₁₂B, coercivity 1420 kA/m, remanence 1.18 T

¹⁰Target: 2.5 mm heavimet, composed of 4% copper, 7% nickel and 89% tungsten with density of 17.1 g/cm³. The target was mounted behind a water cooled 8 mm thick copper jacket.

¹¹Magnet type: CRUMAX 355, Nd₂Fe₁₂B, Crumax Magnets

¹²Magnet type: HICOREX 94EB, Nd₂Fe₁₂B, remanence 1.18-1.28, coercivity 1275 kA/m, Hitachi Metals

but with identical stoichiometry showed a 5.5% remanence loss after an absorbed dose of 4.5 MGy.

By Luna et al. [68], also the effect of neutrons in causing the radiation induced remanence loss has been investigated. The magnet samples were equipped with neutron dosimeter. A reference magnet was shielded against bremsstrahlung radiation by lead bricks. No magnetization loss has been observed for the reference magnet, even though it was exposed by a larger neutron dose as compared to the other magnets.

It was possible to remagnetize the NdFeB magnets after irradiation with electrons of 17 MeV up to its nominal value. Therefore the damage of permanent magnets does not occur to the crystallographic structure of the magnet [66].

The Curie temperature T_C of NdFeB permanent magnet is about 350 °C. In most of the experiments either the temperature of the magnets was monitored or the magnets were temperature stabilized when required [66]. Therefore, the demagnetization due to a temperature rise of the bulk material above T_C can be excluded for most of the experiments. The mechanisms for demagnetization are not fully understood. Nevertheless Talvitie et al. [69] explain the mechanism of flux loss, caused by protons, principally by a local thermal heating. It seems that during the penetration of charged particles of sufficiently high energy the radiation heats the magnet locally in a very small volume, although the bulk temperature does not increase significantly. This heated region acts as a nucleation center for the change of domain orientation and leads to the initiation of the demagnetization process.

A dependence of the remanence loss on the geometry of the magnet is reported in [70]. The magnets with the highest demagnetizing field show the highest decay rates [70]. This means that the radiation hardness of a particular undulator also depends on the magnetic design [71].

Irradiation of NdFeB magnets at the ESRF

A significant relation between the radiation hardness, the remanence and the coercivity of the NdFeB magnets has been observed at the ESRF [65]. A stack of five different permanent magnets was exposed simultaneously to the electron beam from the ESRF linac. The experimental setup is sketched in Fig. 2.37. The magnets with a size of $11 \times 11 \times 2 \text{ mm}^3$ were placed behind the exit window (1 mm steel). The samples were arranged in a periodic way (see Fig. 2.37). The magnetic properties of the permanent magnets are listed in Table 2.12. The electron beam energy of the linac was 180 MeV, the current 50 mA and the pulse duration 2 μs . The magnets have been exposed during 1 hour with an average beam power of 18 W. The measured demagnetization of the permanent magnets versus the position within the stack is shown in Fig. 2.38(a). The samarium cobalt samples have not shown any significant demagnetization while all NdFeB samples have been partially demagnetized. It has been observed that the higher the remanence and the lower the co-



Figure 2.37: Experimental setup used at ESRF.

Permanent magnets used for the TTF undulator			
Magnet type	stoichiometric	Remanence [T]	Coercivity [kA/m]
VACODYM 396	Nd-Dy-Fe-B	1.15 T	2150
Permanent magnets used in ESRF experiment [65]			
VACOMAX 145	SmCo ₅	0.85-0.94	1700
VACOMAX 225 HR	Sm ₂ (Co,Cu,Fe,Zr) ₁₇	1.00-1.15	1200
VACODYM 351 HR	Nd ₂ Fe ₁₂ B	1.20-1.30	1200
VACODYM 370 HR	(Nd,Dy) ₁₅ Fe ₇₇ B ₈	1.15-1.25	1450
VACODYM 400 HR	Nd ₂ Fe ₁₂ B	1.05-1.15	1800
Permanent magnets used by Okuda and Ikeda [67]			
N33H	Nd ₂ Fe ₁₂ B	1.18	1420
N34UH	Nd-Fe-B	1.19	1990
NEOMAX-32EH	Nd-Fe-B	1.11	2387
NEOMAX-35H	Nd-Fe-B	1.25	1353
Permanent magnets used at POSTECH [72]			
VACODYM411	Nd ₂ Fe ₁₄ B	1.00	3260
VACODYM400	Nd ₂ Fe ₁₄ B	1.10	2470
VACODYM411	Nd-Dy-Fe-B	1.15	2150
NEOMAX-32EH	Nd ₂ Fe ₁₄ B	1.11	2387
NEOMAX-35EH	Nd ₂ Fe ₁₄ B	1.17	1989
NEOMAX-44H	Nd ₂ Fe ₁₄ B	1.36	1273

Table 2.12: Magnetic properties of permanent magnets.

ercivity, the more the magnet is demagnetized by the electron beam. In [65] the absorbed dose of the first samples in the stack has been estimated to be 0.7 MGy.

The strong dependence of the demagnetization on the axial position in the stack indicates that the results of the exposure from a ⁶⁰Co-source determine only a lower limit on the energy for harmless secondary particles.

To investigate the development of the electromagnetic shower in the magnet array the Monte Carlo code EGS4 [73] has been used. The absorbed dose in the magnets and the mean energy of the charged particles (electrons and positrons) entering a magnet are shown in Fig. 2.38(b).

Unfortunately, the precise values for the beam size and the distance from the steel plate to the magnet stack are unknown. For the simulation an rms-beam size of 1 mm and a distance 5 cm to the exit window has been assumed. The maximum absorbed dose is computed to be 0.9 MGy. 40% of the beam energy is deposited in the magnets. 32% of the energy carried by degraded electrons and secondary particles transmits through the last magnet and 28% leaves the samples transversely. If the rms-beam size is varied between 0.1 and 10 mm the distribution of the energy deposition and the mean particle energy do not differ significantly (about 20%), but the maximum absorbed dose decreases strongly for rms-beam sizes larger than 3 mm. A similar effect is calculated for variations

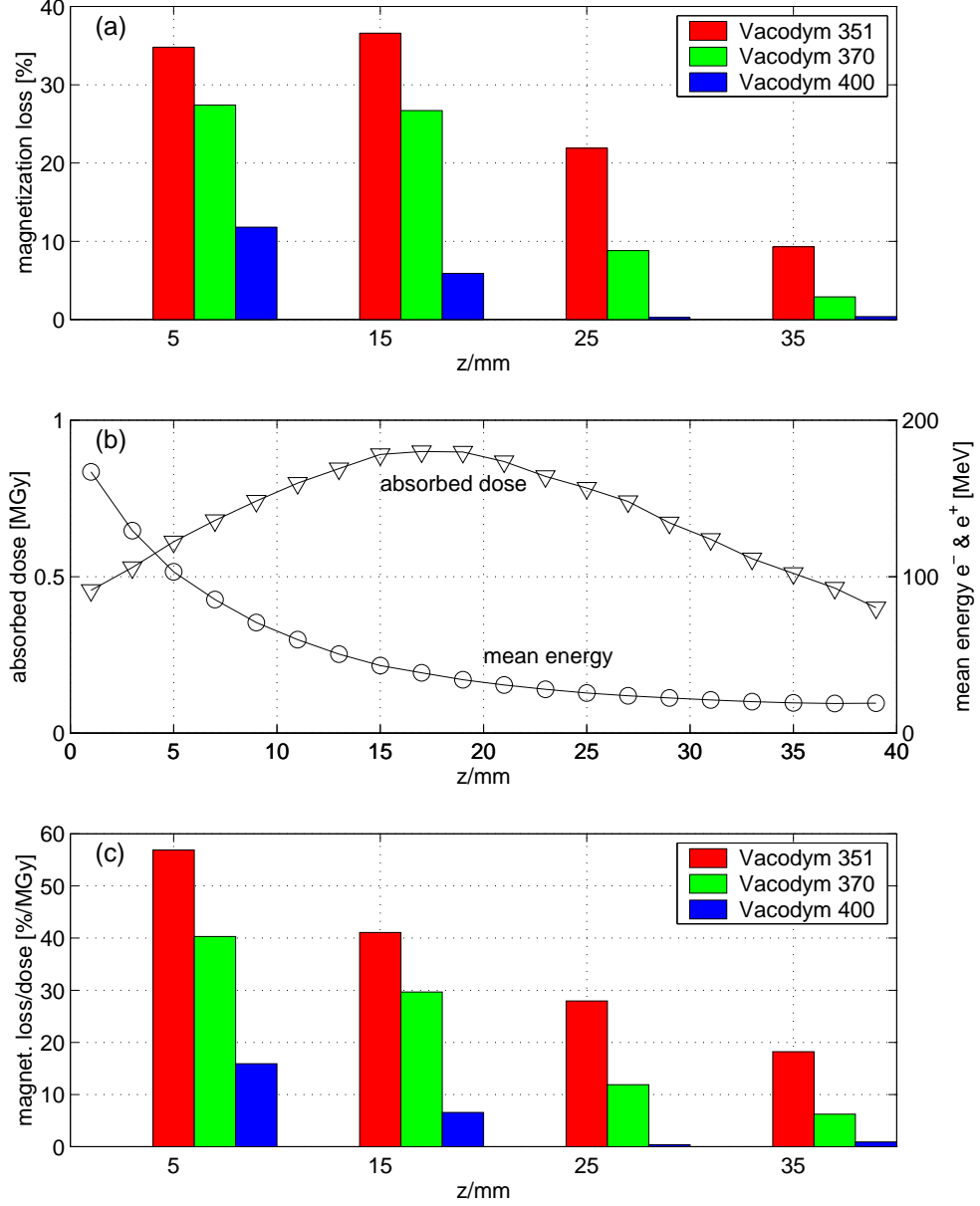


Figure 2.38: (a) Measured demagnetization of permanent magnets at ESRF [65]. (b) Result of EGS4 Monte Carlo simulation on the absorbed dose rate for the permanent magnets within the stack (triangle). The mean energy of electrons and positrons penetrating the magnets is added by circles. (c) Ratio of magnetization loss and absorbed dose rate.

of distance between the exit window and the magnets sample which results in a variation of the electron beam size at the first magnet.

In Fig. 2.38(c) the measured remanence loss is normalized to the absorbed dose. The curve approximately follows the mean energy of charged particles irradiating the magnets. Hence, the higher the energy is the stronger the effect of demagnetization on the magnet sample.

The magnets with the highest coercivity (VACODYM 400) show a demagnetization below 1% at the last two positions in the stack ($z = 29$ and 39 mm), while the 2nd magnet losses 6% magnetization. The energy spectrum of the electrons, photons and positrons penetrating these magnets is shown in Fig. 2.39. The photon and positron spectra vary

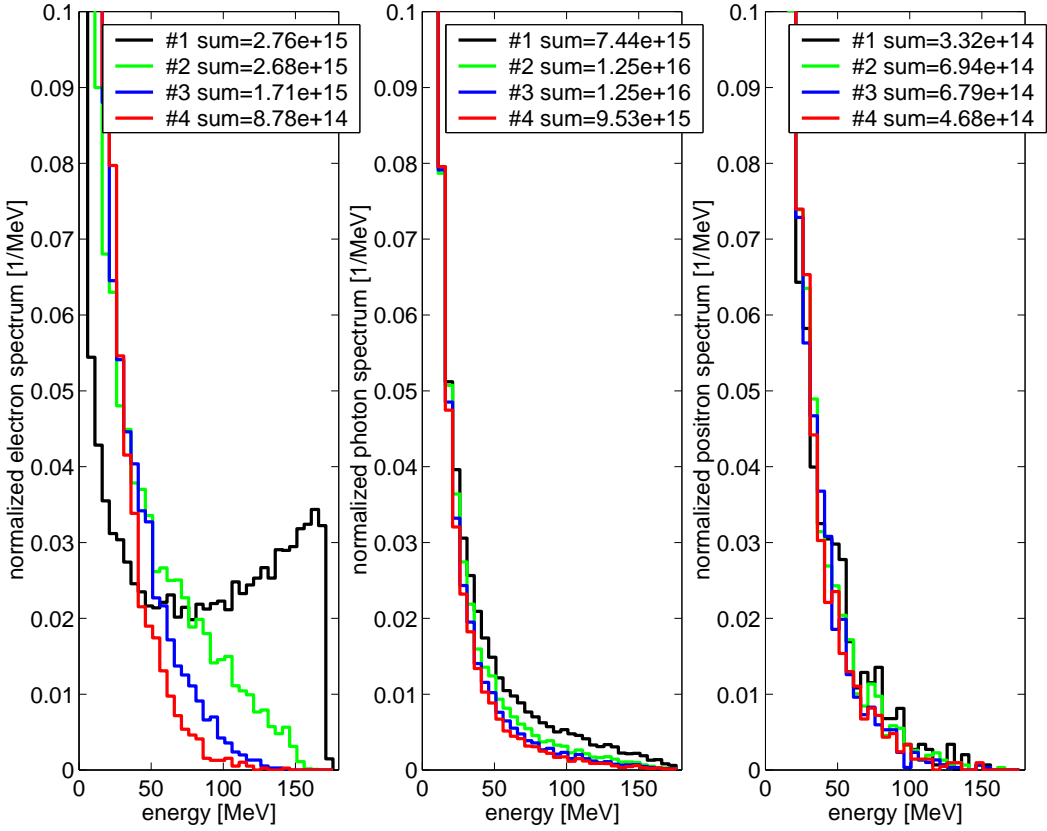


Figure 2.39: Energy spectrum and total number of particles exposing the magnet type VACODYM400 at the positions #1 to #4 in the stack.

only weakly with the magnet position in the stack. It is unlikely that they are causing the demagnetization. The electrons spectra at the positions #2 to #4 differ significantly above 50 MeV, while that for #1 differs over the entire energy range. For this type of permanent magnet, the effect of exposure at energies below 50 MeV and dose rates up to 0.7 MGy seems to be negligible. However, this is not the case for the other type of NdFeB magnets with a smaller coercivity.

The report by Ikeda and Okuda [67] supports the results from the shower calculation. The exposure of 17 MeV electrons shows a very small effect on the magnets with high coercivity. The properties of the magnets used in this experiment are included in Table 2.12. The geometry of the samples and the magnetization direction with respect to the radiation field are comparable to the experiment performed at the ESRF¹³. The magnetic flux loss and the irradiation dose for the different magnets are listed in Table 2.13. For comparison with the ESRF results, the losses at the 4th position and the magnets with similar coercivity have to be considered. The remanence loss per absorbed dose of VACODYM370 agrees within a factor 2 with that for N33H. For VACODYM400 the loss is below 1% and the one for N34UH amounts to 0.4%. Nearly no magnetization loss has been observed for 32EH with the highest coercivity. However, beside the coercivity of the magnet additional factors are important as seen by the magnet with the trace name 35H from a different manufacturer. The magnet shows a higher radiation hardness than the

¹³The magnet samples are cylindrical disks of 2 mm length with a diameter of 10 mm. The magnetization direction and electron beam axis are parallel to the cylinder axis.

Magnet type	electron dose C/cm ²	absorbed dose MGy	loss of magnetization
N33H	$1.4\text{-}1.5\cdot10^{-3}$	1.7-1.9	5.6%
N34UH	$1.4\cdot10^{-3}$	1.7	0.4%
32EH	$1.3\text{-}1.4\cdot10^{-3}$	1.7	0.2%
35H	$1.4\cdot10^{-3}$	1.5-1.7	0.8%

Table 2.13: Observed demagnetization of magnets exposed to 17 MeV electrons [67]. N33H and N34UH are manufactured by Shin-Etsu Chemical Co. 32EH and 35H are manufactured by Sumitomo Special Metals Co.

magnet N33H, though it has an even lower coercivity.

Exposure of permanent magnets at TTF

In 1998, permanent magnet samples of the type used in the TTF undulator have been mounted onto the stainless steel vacuum beam pipe in the dispersive area, section EXP3, where regularly an increased activation caused by beam losses has been observed. The magnet size was $8.65\text{\times}9.8\text{\times}9.8\text{ mm}^3$. The magnetic moment has been measured before and after irradiation. Silver-activated radio-photoluminescence (RPL) glass dosimeters (1 mm diameter \times 6 mm length) were used to measure the absorbed dose. The RPLs have been installed on the upstream and downstream surface of each magnet. The magnets were placed in the linac during a run period of 10 weeks. During this time the beam energy was in the range between 20 MeV and 120 MeV. About 90% of the total dose measured by the RPLs was collected at an operation energy of 23 MeV. The typical length the electrons travel through matter until they could reach the magnet has been estimated to be between 1 and 2 radiation length. Thus, dominantly electrons below 10 MeV were contributing to the dose rate. The largest dose measured at the beam pipe was 2.8 MGy. The largest dose at the magnet was 0.8 MGy. The change of the magnetic moments is listed in Table 2.14. Sample No.1 was mechanically damaged while cleaning. A small increase of the magnetic moment has been observed for most of the magnets. It could not be clarified, if this was related to a systematic measurement error or caused by the irradiation. Nevertheless, the exposure of the mixed electron-photon radiation field up to about 10 MeV energy and a dose of 0.8 MGy did not significantly influence the magnetic flux of this type of NdFeB permanent magnets which agrees to results discussed before.

Magnet exposure with 2 GeV electrons

Results recently reported by Bizen et al. [72] lead to another picture of the demagnetization process than discussed above. At Pohang Accelerator Laboratory, POSTECH, a 2 GeV electron beam was used to investigate the dependence of the magnetic field change on various parameters like the position of the magnet in a magnet array, the magnet shape, the magnetization direction, the influence of target materials upstream of magnets, and the radiation hardness of magnets produced by different manufacturers. Also, to study the dependence on the magnet design a short piece of a pure type permanent undulator and a hybrid type undulator, as installed in SPring-8, has been exposed to the electron beam.

sample No.	change of magnetic moment [%]	RPL dose (MGy)	
		upstream	downstream
1	-	0.050	0.065
2	+0.21	0.180	0.065
3	+0.51	0.360	0.120
4	+0.31	0.280	0.280
5	+0.21	0.120	0.080
6	+0.10	0.160	0.085
7	+0.21	0.420	0.420
8	0.0	0.850	0.320

Table 2.14: Relative change of magnetic moment after exposure to mixed electron-photon radiation field. The radiation is produced dominantly by about 20 MeV electrons hitting the beam pipe walls.

In most of the experiments NEOMAX35EH magnets were irradiated. In one experiment, this type of magnet has been compared to the type used in TTF (VACODYM396). In [72], the measured magnet field changes versus the accumulated beam charge used for the exposures is reported. The charge has been determined by current monitors installed close to the exit window. To analyze the most important experiments the absorbed dose rates in the magnets are calculated by Monte Carlo simulations. The setup of these experiments is sketched in Fig. 2.40.

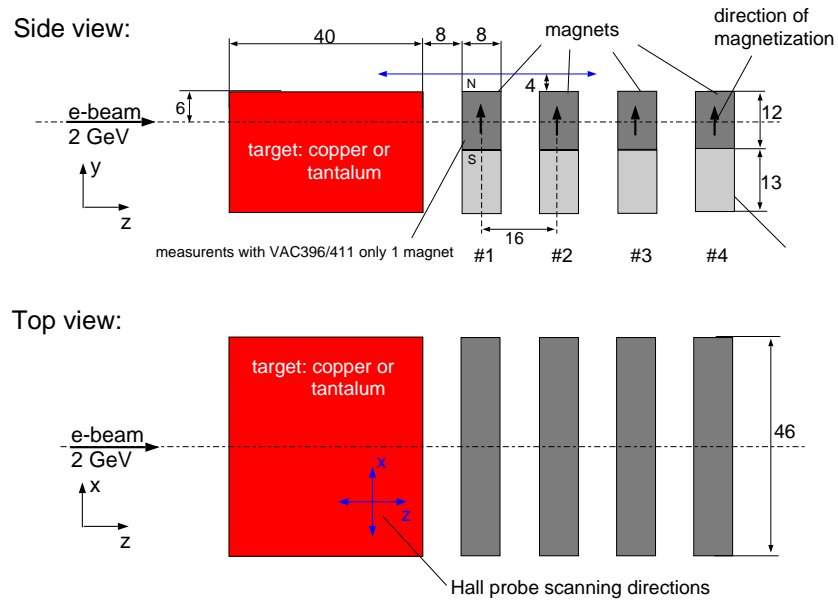


Figure 2.40: Experimental setup used for magnet exposure in POSTECH.

In this part of the experiment, the electron beam hits the magnet array either directly (only NEOMAX35EH) or through a 40 mm thick targets mounted upstream of the magnet array. Copper and tantalum targets were used. The radiation hardness of different types of magnets was investigated using a single magnet at position #1 exposed to a radiation field generated by a copper target.

The vertical magnetic field was measured after exposure along the x and z direction with a movable hall-probe. The average beam current was 600 mA with a pulse duration of

1 ns. The repetition rate of the linac was 10 Hz. The average beam power in the experiments was 12 W. The beam size at the target was ± 10 mm in horizontal direction and ± 5 mm in vertical direction. For the Monte Carlo simulations a gaussian distribution with $\sigma_x = 5$ mm and $\sigma_y = 2.5$ mm and the geometry shown in Fig. 2.40 is used.

First, the observations for an array of magnets exposed directly and with targets will be discussed. The measured maximum magnetic field losses versus the accumulated electron dose is shown in Fig. 2.41(a) (see [72]). The accumulated electron dose varies from $3.1 \cdot 10^{13}$ electrons incident on tantalum to $95 \cdot 10^{13}$ electrons incident on a copper target. The magnetic field loss differs in the range between 0.3% and 3%. The largest demagnetization for the smallest accumulated electron dose has been observed for tantalum. The

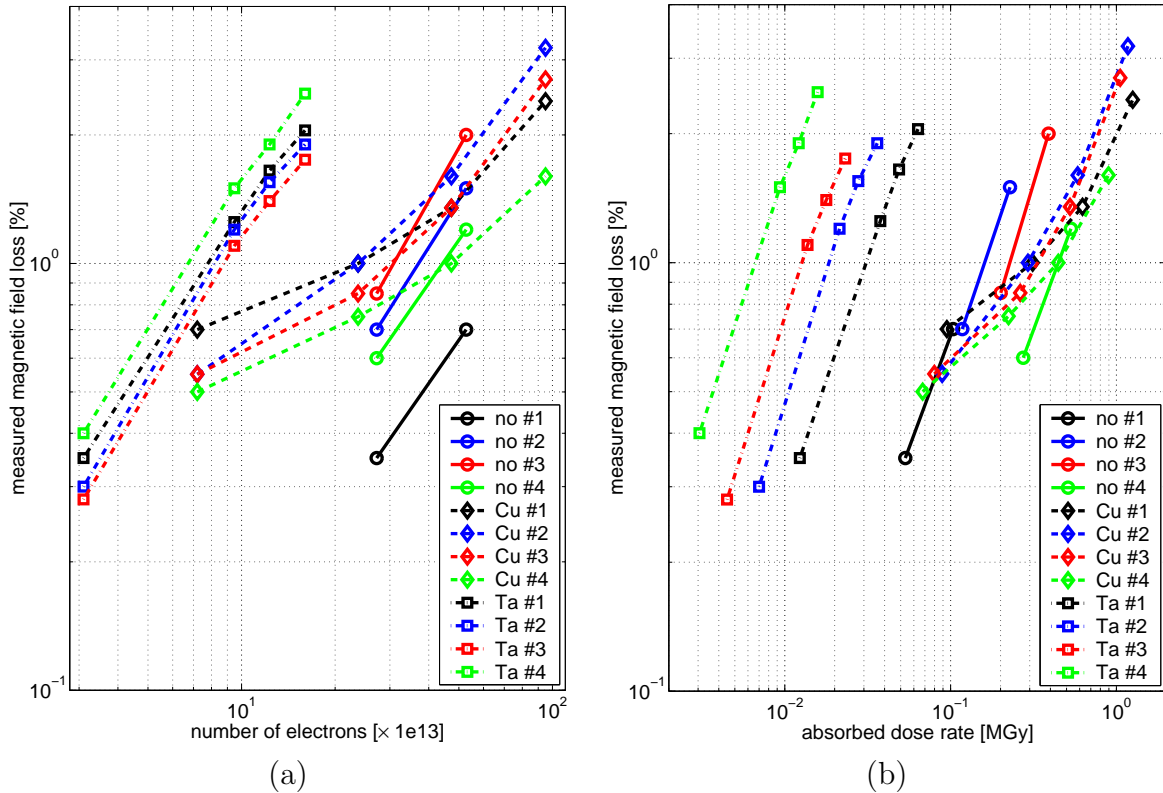


Figure 2.41: Irradiation of NdFeB permanent magnets at 2 GeV. The vertical magnetic field loss is plotted against the accumulated electrons used for exposure (a) and against the calculated absorbed dose rates in (b). Four magnets (NEOMAX35EH) at the position #1 to #4 have been irradiated either directly (labelled with “no”) or by using the target materials copper and tantalum.

magnets are not uniformly irradiated. The radiation field drops with larger transverse coordinates x and y . The energy deposition is calculated in a volume of $12 \times 12 \times 8$ mm 3 at magnet center. The magnetic field losses plotted against the absorbed doses are shown in Fig. 2.41(b). For an electron incidence of $1 \cdot 10^{13}$ the dose is summarized in Table 2.15.

The dose for a magnetic field loss of 1% scatters from 6.5 kGy (tantalum target) to 430 kGy (direct exposure). The demagnetization of the permanent magnets scales approximately linear with the absorbed dose. The largest deviation from a linear dependence is observed for the copper target and small dose rates. A clear discrepancy is seen between the case of a tantalum target (6.5-30 kGy per % field loss) and the cases of direct beam exposure or secondary particles exposure from a copper target (150-450 kGy per % field loss). The result is particularly astonishing, since from the previous discussion it has been

		absorbed dose for $1 \cdot 10^{13}$ electrons [kGy]			
target		stack position			
		#1	#2	#3	#4
direct		1.96	4.32	7.38	10.07
copper		13.30	12.35	11.09	9.43
tantalum		3.97	2.26	1.45	0.99

Table 2.15: Absorbed dose in magnets for the different targets exposed to $1 \cdot 10^{13}$ electrons with 2 GeV energy (3.2 kJ total energy).

concluded that the exposure to electrons with not too high energies ($< 20\text{-}50\text{ MeV}$) is less damaging up to very large absorbed dose.

With a radiation length of $X_0 = 4.1\text{ mm}$ for tantalum the target block has a thickness of $9.8 X_0$. Thus, the shower maximum is located in the target block and the mean energy of the charged particles exposing the first magnet in the stack amounts to $\langle E \rangle = 18.9\text{ MeV}$ only, in contrast to the observation mentioned above. About 93% of the electrons have an energy below 50 MeV and 98% below 100 MeV. In average, per incident electron on the tantalum target 0.54 electrons and 0.38 positrons per square centimeter hit the first magnet. The yield of secondary particles and their spectral properties are summarized in Table 2.16. The number of electrons and positrons exposing the first magnet are four

tantalum target, thickness 40 mm						
	yield/cm ² per incident e ⁻	percentage of spectrum reached at E[MeV]				
		50%	80%	90%	95%	99%
electrons	0.54	9	25	41	65	157
positrons	0.38	11	31	51	75	185
photons	13.5	3	9	15	25	69
copper target, thickness 40 mm						
electrons	2.07	31	115	217	361	749
positrons	1.38	37	113	205	315	675
photons	15.4	5	31	71	141	493

Table 2.16: Yield of secondary particles from the tantalum and the copper target per incident electron (second row) exposing the first magnet in the magnet array. The last rows inform about energies in which the integrated spectrum contains a given percentage of secondary particles.

times larger for the copper target than for the tantalum target, while the number of photons is approximately equal. Neither the amount of secondary particles nor its energy spectrum give a clear explanation why the demagnetization of the magnets is an order of magnitude larger for the tantalum as compared to the copper target.

Next, the spread of the curves in Fig. 2.41(b) for the mixed radiation field from a copper target or the direct exposure is analyzed in detail. In [72] a non-linear transient dependence of magnetic field change at very small accumulated electron dose is reported. After a rapid decrease the magnetic field approaches a more linear behavior for higher dose¹⁴. Thus it can be expected that the data points for the copper target at an electron dose of

¹⁴Observed for a single magnet at position #1 with copper target see Fig. 8 in [72]

$7.2 \cdot 10^{13}$ deviate from the other curves if normalized to 1% magnetic field change. Figure 2.42(a) shows the absorbed dose normalized to 1% magnetic field loss for versus the position in the magnet array. To estimate if electrons with lower energy are less damaging, in Fig. 2.42(b) the dose caused by charged particles above 20 MeV is shown. It is seen that, the spread of the curves without target and copper target is much smaller and deviates only by 50% from the mean value of 0.12 MGy absorbed dose per 1% field loss. The mean values in Fig. 2.42 have been calculated without the data for Cu “ $7.2 \cdot 10^{13}$ ”.

The data points for tantalum deviated from the others by about two orders of magnitude. This discrepancy becomes even more obvious, if one considers the charge irradiation dose (C/cm^2). For tantalum, the largest irradiation dose amounts to $24 \mu\text{C}/\text{cm}^2$ with 1.8% magnetic field loss. In the experiment by Okuda, listed in Table 2.13, same magnet type shows 0.2% demagnetization at a 60 times larger irradiation dose of $1.4 \text{ mC}/\text{cm}^2$. This difference is difficult to explain by the sample size, the magnetization direction or the presence of demagnetizing fields. It seems that the mechanism of the remanence loss in this experiment is not anymore related to the ionization process by electrons or positrons generated in the electromagnetic shower of the target material.

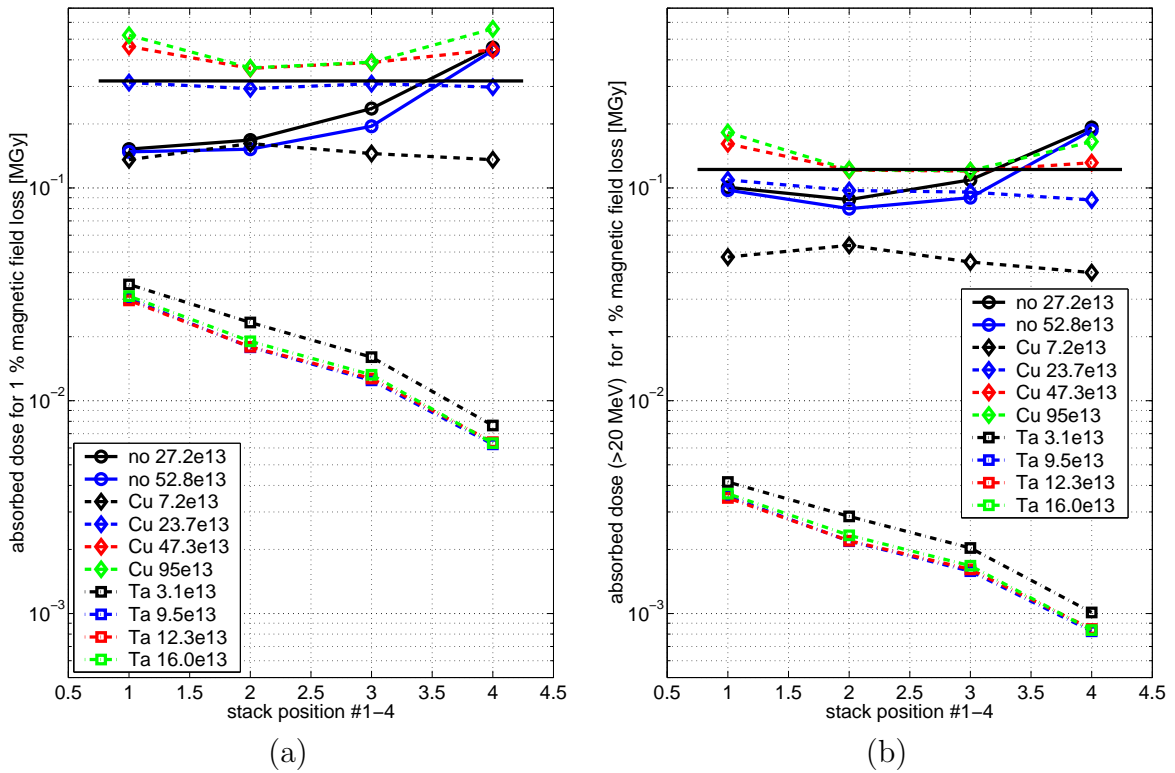


Figure 2.42: Maximum vertical magnetic field loss per absorbed dose rates of NEOMAX35EH permanent magnets at different the stack positions #1-#4. (a) calculated absorbed dose disregarding the energy of charged particles. (b) calculated absorbed dose due to charged particles with energy above 20 MeV only.

A possible explanation is that for thick targets at very high electron energies, neutron production plays a major role in the demagnetization process. Fast-neutrons induced damages of NdFeB magnets reported in [74] partially support this assumption. By using a ^{252}Cf source an 0.5% remanence loss has been measured at a fast-neutron fluence of $2.33 \cdot 10^{13} \text{n}/\text{cm}^2$. For comparison, a 10 kJ beam incident on a thick tantalum target produces approximately $2.6 \cdot 10^{13}$ neutrons below 25 MeV and $0.83 \cdot 10^{12}$ neutrons peaked in the

forward directions with an energy above 25 MeV¹⁵. The produced neutron fluence differ by about a factor of 10, but a ²⁵²Cf transmits neutrons with a peak energy of 1-2 MeV only [74] whereas the release of neutrons from a target stroked by high energy electron beam contains also neutrons with much higher energies.

Thus, to distinguish between hadron and electromagnetic induced demagnetization processes, the hadron dose and hadron spectra of the experiments have to be calculated by Monte Carlo codes taking into account the hadron production and the transport through matter (i.e. the code FLUKA [11, 12]).

Several types of magnets have been exposed to a mixed radiation field using the copper target, where only at the position #1 a magnet has been placed. Since the contribution from back-scattered particles from downstream magnets can be neglected, the properties of the radiation field listed in Table 2.16 are still valid. In Fig. 2.43 the magnetic field change is shown for different magnets as a function of the absorbed dose due to charged particles above >20 MeV. In the following this dose is called the “restricted” absorbed dose. The ratio between the total and the restricted absorbed dose for the magnet at position #1 in case of a copper target is 2.86.

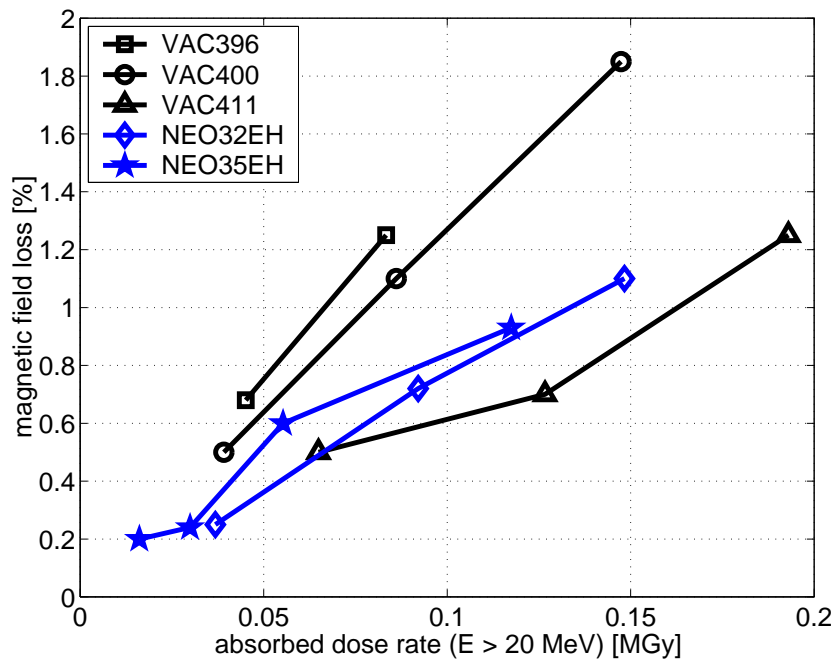


Figure 2.43: Magnetic field change with the accumulated electron dose incident on a copper target for various types of NdFeB magnets.

The radiation hardness of the five types of permanent magnets differ by about a factor of 2.4. The absorbed dose for 1% field change is 67 kGy for VACODYM396, 122 kGy for NEOMAX-35EH, and 162 kGy for VACODYM411.

¹⁵The neutron yield from a tantalum target has been estimated by the neutrons produced from a thick lead target (see [9]).

Chapter 3

Collimator Section

In section 1.2 the principle and the basic layout of the collimator has been described. The acceptance phase spaces of the collimator and the undulator are analyzed using linear optics calculations. In linear optics, the diameter of the spoilers are sufficiently small to allow the linac operation up to beam energies of 500 MeV where for the typical beam energy of 230 MeV the clearance of the electrons to the undulator vacuum chamber is 1.4 mm or about 30% of the chamber radius. Due to chromatic aberration in the quadrupoles matching the beam from the collimator to the undulator the energy bandwidth of the collimator is rather small (at 230 MeV: -7.1% to +8.2%). The magnetic fields and field errors of the undulator are discussed in section 2.4 where the important parameters for modeling the undulator by hard-edge magnets have been derived. The transmission probability of electrons through the undulator is influenced by non-linearities. The dominant non-linearities are geometric aberration of the undulator focusing and octupole field components in the quadrupoles. To study the performance of the collimator these non-linearities cannot be ignored and have already been taken into account for the calculation of the dark current transmission through the undulator (see Sec. 2.4.9).

In this chapter, the influence of imperfections such as gradient errors, quadrupole displacements, displacements of beamline components, etc. on the removal efficiency of the collimator is investigated. The tolerances on the alignments are studied by tracking calculations. The initial distribution simulate the beam halo or beams which are mismatched or displaced. For small imperfections, the transmission probability through the undulator remains 100% for beams with small energy spread. If the energy spread grows electrons are lost in the undulator. Thus, it is suggestive to describe the performance of the collimator by its reduction of the energy bandwidth due to the imperfections. Imperfections causing a reduction of the energy bandwidth below the energy width of the regular electron beam (with the bunch compressor in operation) are unacceptable and must be corrected.

In the first step, section 3.2, the primary electrons are tracked through the collimator until they hit the vacuum chamber of the undulator. The spatial distribution of the lost primary electrons in the undulator is used, in a second step in section 3.3, by Monte Carlo calculations with EGS4 to determine the absorbed dose and the irradiation spectrum (particle and energy) in the magnets hybrid structure. Since electrons hitting the collimator contribute to the irradiation of the undulator the electromagnetic shower initiated at the collimator spoilers is investigated in section 3.4. From the results the removal efficiency of the collimator section for secondary particles is derived.

In section 3.7, the influence of quadrupole displacements on the beam injection into the

undulator is discussed. A beam based alignment method using the FEL photon beam is presented and an orbit correction with steerers in the collimator is derived.

Finally, in section 3.8 the contributions of the wakefields generated in the collimator sections are estimated. The effect on the energy spread and the emittance of the beam is calculated.

3.1 Geometry of the collimator section

In Fig. 3.1 the side-view of the collimator section is shown. The collimator section is 5.577 m long and ends with the first diagnostic station in the undulator section. The beam pipes at the entrance and the center of the collimator section are 60 mm in diameter. The order of the collimators are: spoiler 1, absorber 1, spoiler 2, absorber 2 and absorber 3. The inner diameters of the collimators are listed in Table 3.1.

collimator diameters				
spoiler 1	spoiler 2	absorber 1	absorber 2	absorber 3
6 mm	6 mm	9.5 mm	8 mm	8 mm

Table 3.1: Collimator diameters.

The diameter of the beam pipe between spoiler 1 and absorber 1 and between spoiler 2 and absorber 2 is 16 mm. The longitudinal gaps due to the second and fifth pump port are 24 mm. The inner diameter of the BPM_B is 25 mm. This BPM is used to measure the influence of higher-order modes excited in the acceleration modules on the beam orbit. The valve before absorber 3 is rf-shielded by a cylinder with the same diameter as the attached beam pipes (16 mm) when the valve is opened. The longitudinal gaps between the cylinder and the beam pipes are 0.5 mm.

All five collimators are tapered to reduce the excitation of geometrical wakefields. The

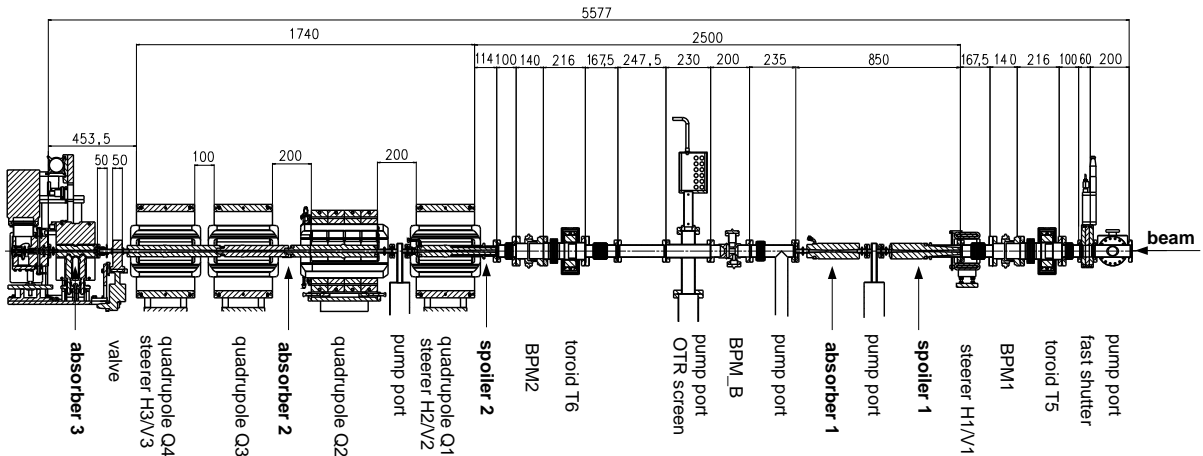


Figure 3.1: Side-view of the collimator section.

shapes of the collimators are shown in Fig. 3.2. The material of the spoilers is AIMg3. The absorbers are made from copper (OF HC). Except of absorber 3, all collimators are water cooled. To avoid erosion by ions the aluminum spoilers have a separated water

circuit which is connected by heat exchanger to the linac cooling system. To estimate the upper limit for the heat load on the spoilers the temperature rise for a heat source located at the upstream surface of spoiler 1 has been calculated numerically [75]. For a 250 W heat source the equilibrium temperature in the spoiler is 80°C. Mechanical properties of aluminum such as the tensile strength depend sensitively on the temperature, larger heat loads than 250 W should be avoided.

The distance between the center of the spoilers is 2.582 m. The section of the spoiler at the smallest radius of 3 mm is 100 mm long, which corresponds to $1.12X_0$ radiation length. Due to the smooth entrance and exit tapers the radiation length of the spoiler rapidly grows with the larger radius and approaches $4X_0$ for $r = 6$ mm in the first spoiler and $4.5X_0$ for $r = 8$ mm in the second spoiler. The entrance taper and 30 mm of the cylindrical part of the spoilers which are most likely hit by the beam is surrounded by a stainless pipe. In case the material cracks in transverse direction the ultra-high vacuum remains unperturbed. The part of the construction is indicated in Fig. 3.2 by “insulation vacuum”. Spoiler 2 and absorber 2 are installed in quadrupoles. They lie with polished contact surface on the iron poles of the quadrupoles. The tolerance between the center of the inner diameter and the contact surface is less than 100 μm .

The opening of the collimators have been made by wire erosion. Absorber 2 has a transition from a cylindrical cross-section ($\mathcal{O}16$ mm) to an elliptical (large half axis 5 mm and small half axis 4 mm) to a cylindrical cross-section ($\mathcal{O}8$ mm). The shape has been chosen because of the large β -function in the vertical direction at the second quadrupole Q2. Small bellows are used to correct angular errors of the beamline devices.

3.2 Removal efficiency of the collimator for primary electrons

The permanent magnets can be exposed to radiation initiated by electrons from the beam hitting the undulator vacuum chamber or by secondary particles created in the spoilers of the collimator section which escape through the absorber system. The contribution of the two sources to the undulator dose budget depends on the linac parameters. Thus it is important to distinguish between the removal efficiency of the collimator section for primary electrons η_{pri} and the removal efficiency for secondary particles η_{sec} . Let denote L_{sec} the loss probability for the secondary particles produced in the collimator section by the ratio between the deposited energy in the undulator and the energy of the primary electrons incident on the spoilers

$$L_{sec} \equiv \frac{\text{energy deposited in undulator due to secondary particles}}{\text{energy of primary electrons incident on the spoilers}}. \quad (3.1)$$

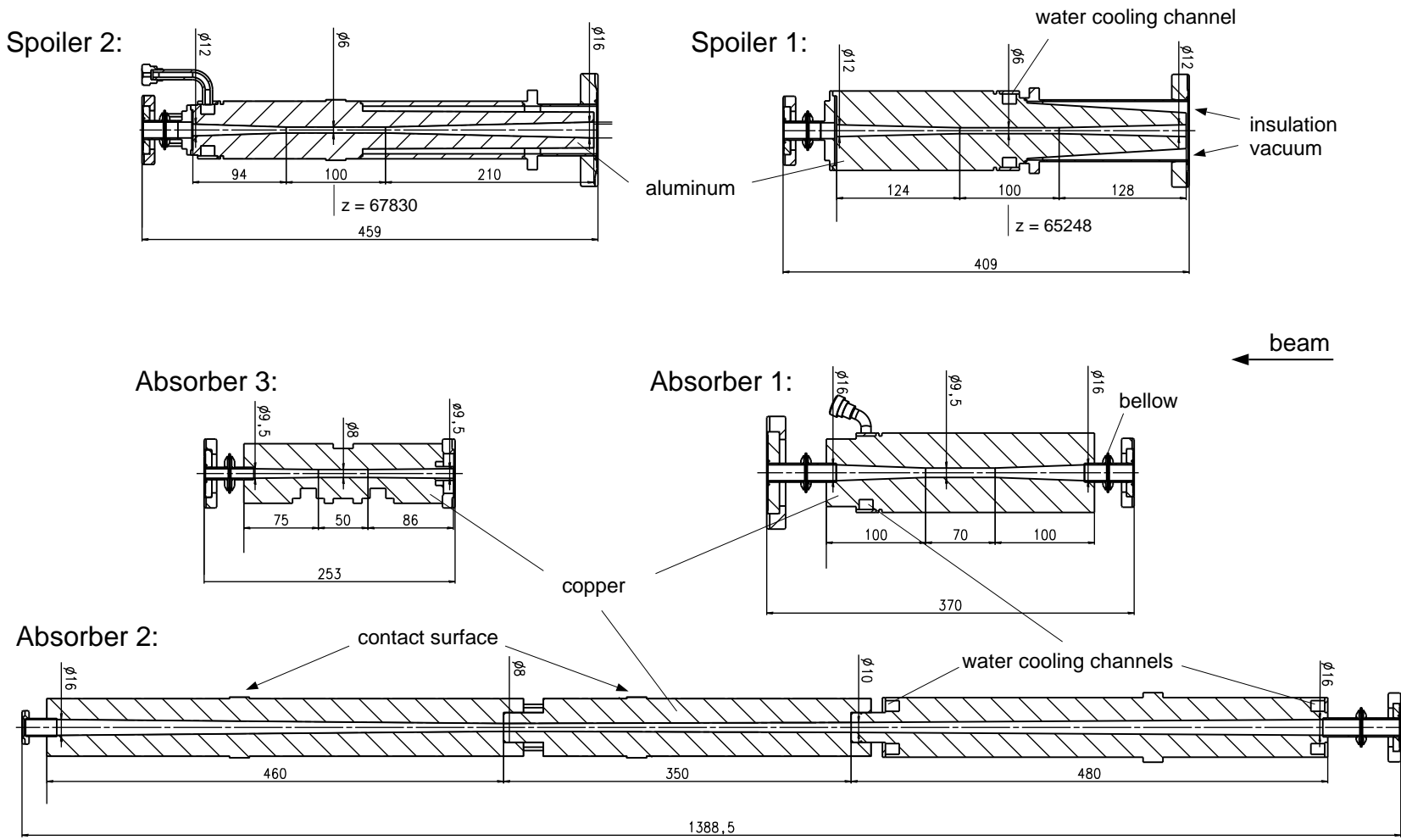
The removal efficiency for secondary particles can be defined as

$$\eta_{sec} \equiv 1 - L_{sec}. \quad (3.2)$$

Since the contribution of secondary particle losses in the undulator is different for the two spoilers it is useful to separate L_{sec} into $L_{sec,1}$ for the first and $L_{sec,2}$ for the second spoiler. The removal efficiency for secondary particles is calculated in Sec. 3.4.

Let denote L_{pri} the loss probability for primary electrons as the ratio between the number

Figure 3.2: Cross-sections of the spoilers and the absorbers in the collimator section.



of electrons lost in the undulator and the initial number of electrons before the collimator section

$$L_{pri} \equiv \frac{\text{number of primary electrons lost in undulator}}{\text{number of primary electrons before the collimator section}} \quad (3.3)$$

and define the removal efficiency for primary electrons as

$$\eta_{pri} \equiv 1 - L_{pri}. \quad (3.4)$$

The transmission probability of the electrons through the collimator is denoted by T_{col}

$$T_{col} \equiv \frac{\text{number of primary electrons passing through collimator section}}{\text{number of primary electrons before the collimator section}}$$

with $R_{col} = 1 - T_{col}$ the removal probability and

$$T_{und} \equiv \frac{\text{number of primary electrons passing through undulator}}{\text{number of primary electrons before the undulator}}$$

the transmission probability through the undulator and $L_{und} = 1 - T_{und}$ the corresponding loss probability. With

$$L_{pri} = T_{col} \cdot L_{und} = T_{col} \cdot (1 - T_{und}) \quad (3.5)$$

the removal efficiency for primary electrons can be written as

$$\eta_{pri} = 1 - T_{col} + T_{col} \cdot T_{und}. \quad (3.6)$$

If the transmission probability T_{und} of the collimated beam through the undulator is 100%, which means that no electron passing the collimator hits the undulator chamber, then the removal efficiency is 100%. The other extreme is a very poor transmission probability $T_{und} \rightarrow 0$ then η_{pri} approaches R_{col} , the removal probability of the collimator while the passing electrons are lost inside the undulator.

The values of the transmission and loss probabilities depend on the initial charge distribution. An electron beam with design parameters would have transmission of 100% through the collimator and the undulator. In section 2.1.3 it has been shown that the presence of space charge forces creates a beam halo. The electrons of the halo propagate with much larger offsets than the electrons of the beam core. Four examples of beam distributions transported from the gun to the center of the collimator¹ are shown in horizontal phase space in Fig. 3.3. The tentacles of the distributions are caused by electrons crossing the beam center in the space charge dominated regime. The beams (a) and (b) in Fig. 3.3 (see case 1 and case 2 in Sec. 2.4.9) are mismatched. The latter has an angular offset due to mis-steering. The beam in (c) in Fig. 3.3 is obtained by correcting the matching such that the Twiss parameters calculated from the second order moment (100% of the beam) corresponds to the design values of the collimator section ($\beta_{x,y} = 1.25$ m and $\alpha_{x,y} = 0$). The beam has a 1 mm offset in the horizontal direction. Caused by chromaticity the normalized rms-emittance ϵ_x of the beams amounts to 14 μm which is 40% larger than at the

¹The effect of coherent synchrotron radiation on the beam transport through the bunch compressor is not taken into account.

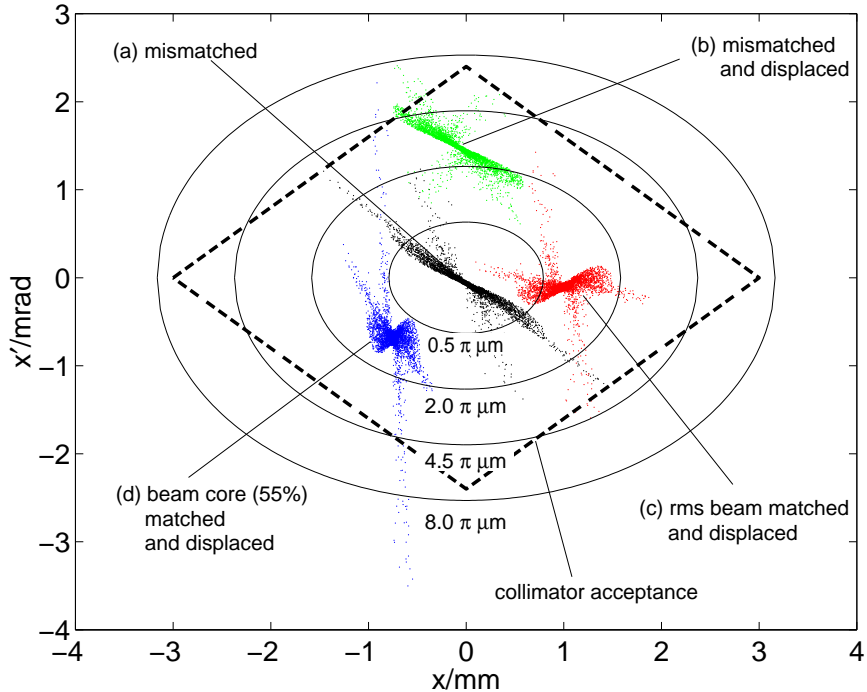


Figure 3.3: Horizontal phase space distributions of electron beams at the center of the collimator section. The distributions are calculated by particle tracking from the injector (CSR not taken into account). (a) mismatched beam centered at collimator section. Magnet currents as case 1 in section 2.4.9. (b) mismatched and displaced beam. Magnet currents as case 2 in section 2.4.9. (c) the rms-beam is matched but the beam is displaced. (d) the core of the beam (55%) is matched but beam is displaced.

exit of the first acceleration module. The beam (d) in Fig. 3.3 has a matched beam core, containing 55% of the beam. The normalized emittance of the beam core is below $3 \mu\text{m}$. If the orbit is corrected, this beam would produce the highest FEL output power, but it also produces a beam loss in the collimators because it exceeds the collimator phase space acceptance in horizontal direction shown by the dashed lines.

Transverse beam distributions similar to the ones shown in Fig. 3.3 occur during linac operation. The largest fraction of these charge distributions pass through the collimator section and the undulator. Most of the time the beam core will stay within the phase ellipse with an area of $1.0\pi\mu\text{m}$. The area contains 97.5% to 99.8% of the beams (a) to (d) if centered in phase space. The electrons within this ellipse cannot cause any damage to the undulator. The beam halo, an improper orbit or a strong mismatch yield a distribution with a larger area but also a much smaller charge density. For calculating the performance of the collimator and for the safety of the undulator only the halo electrons are important. The superposition of the transverse phase space distribution averaged over a longer operation period (weeks, month) will loose the specific properties shown by the four beams in Fig. 3.3. A reasonable way to model the time averaged transverse distribution is to assume two gaussian charge distributions as sketched for one phase space coordinate in Fig. 3.4. The largest amount of charge is contained in a narrow gaussian while a wide gaussian is used to represent the beam halo. The fraction of charge carried by the wide gaussian is not well known, but from the observed beam losses at the collimator it is typical in the range of 0.1% to 1%. Different sizes of the beam halo can be investigated by

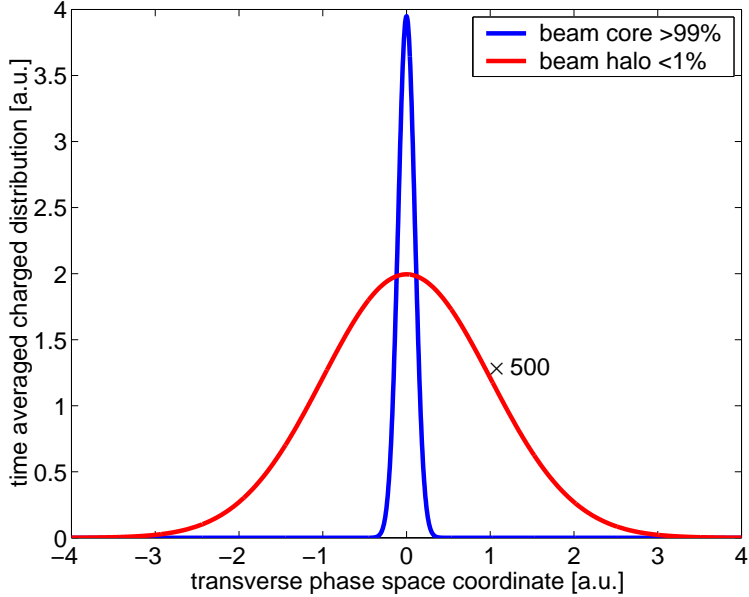


Figure 3.4: Scheme of the time averaged charge distribution by two gaussian curve representing the beam core and the beam halo. In the plot is assumed that the beam halo contains less than 1% of the total charge while 99% of the beam is contained in a narrow gaussian.

tracking calculations to estimate the influence on the collimation efficiency and to derive the loss probability at the spoilers which allows a rough approximation of the typical time averaged beam halo size.

Transmission and loss probability in the collimator section

The time averaged beam halo is modeled by a matched four-dimensional gaussian distribution with equal emittances in x and y ($\epsilon_x = \epsilon_y$). Because the spoilers are separated by a drift space the transmission and the removal probability, T_{col} and R_{col} , are independent of the energy². The variation of T_{col} and R_{col} with the rms-emittance is plotted in Fig. 3.5. At $\epsilon_{x,y} = 0.22 \mu\text{m}$ about 0.2% of the electrons are lost at the spoilers. The value corresponds to $100 \mu\text{m}$ normalized emittances at 230 MeV. A transmission of 50% is obtained for $\epsilon_{x,y} = 1.41 \mu\text{m}$. For large emittances ($>4 \mu\text{m}$) the collimator phase space acceptance is approximately uniformly distributed with electrons and the transmission probability decreases quadratically $\propto 1/(\epsilon_x \epsilon_y)$ with increasing $\epsilon_{x,y}$. The curves marked with triangles in Fig. 3.5 show the fraction of the initial charge dumped at the first or at the second spoiler. For $\epsilon_{x,y} < 1 \mu\text{m}$ the losses are equal. For large emittances more charge is dumped at the first spoiler than at the second one. The losses at the second spoiler decrease for emittances larger than $2.4 \mu\text{m}$.

Transmission probability T_{und} and loss probability L_{pri}

The quadrupoles between the collimator and the undulator are adjusted for a proper beam

²For very large energy deviations electrons might be lost in the absorber system, which in addition reduces the transmission probability through the collimator section. For most of the calculations the effect can be neglected.

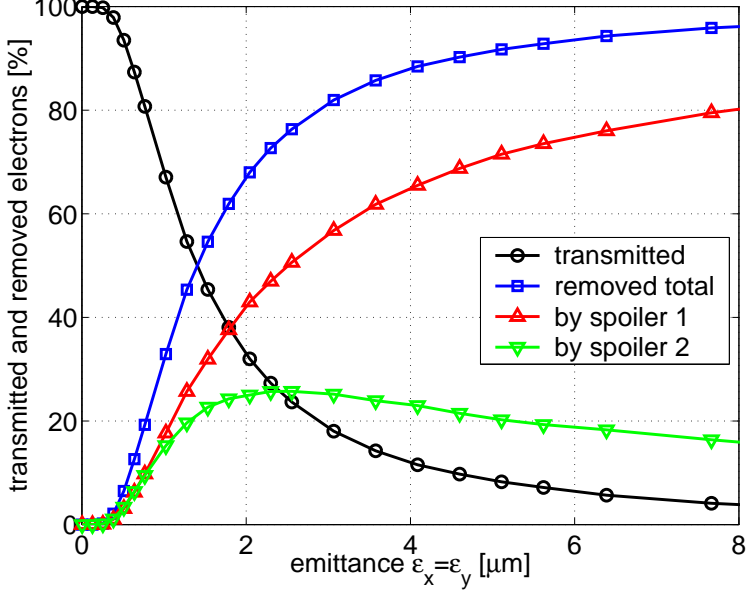


Figure 3.5: Transmission T_{col} and loss probability R_{col} through the collimator spoilers as a function of the transverse emittance. The fraction of the incoming charge removed by the spoiler 1 and the spoiler 2 are also plotted.

matching at an energy E_0 . The transmission probability T_{und} is 100% for a mono-energetic beam with $E = E_0$ independent of the initial emittances. To study the dependence of T_{und} on the emittance the beam must have an energy deviation $\delta = \Delta E/E_0$ with respect to E_0 . At $E_0 = 200$ MeV, the transmission probabilities T_{und} as a function of the energy deviation δ for different emittances are shown in Fig. 3.6(a). The transmission probability T_{col} through the collimator varies between 5.7% and 93.4%. The smallest transmission probability through the undulator is obtained for a poor transmission through the collimator, while the reverse is true for the loss probability L_{pri}

$$L_{pri} = T_{col} \cdot (1 - T_{und}), \quad (3.7)$$

shown in Fig. 3.6(b). The largest losses are observed for the curve with $T_{col} = 80.3\%$. The energy range for which no electrons are lost inside the undulator is $\pm 6.9\%$ (energy bandwidth). Within this energy range the removal efficiency η_{pri} of the collimator for primary particles is 100%. For smaller beam energies, below $\delta < -6.9\%$, the transmission through the undulator rapidly drops, much faster than for higher beam energies above $\delta > 6.9\%$.

The curves $T_{und}(T_{col} = 50\%)$ and $L_{pri}(T_{col} = 50\%)$ for a transmission probability of 50% through the collimator approximate the smallest values obtained from the curves for T_{und} as well as the largest values of the curves for L_{pri} . For numerical computation of the losses in the undulator the emittances with $T_{col} = 50\%$ is well suited and is used in the following simulations.

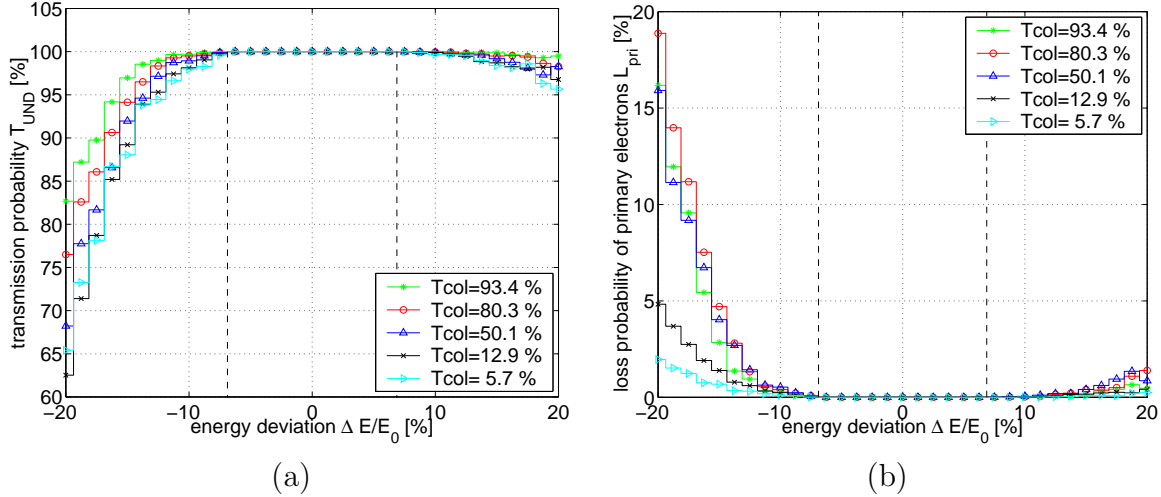


Figure 3.6: (a) Transmission probability T_{und} of the collimated beam through the undulator versus the energy deviation δ for different transmission probability T_{col} . The quadrupole gradients are set for a proper beam matching at 200 MeV ($\delta = 0$). (b) Loss probability in the undulator for primary electrons.

3.2.1 Energy bandwidth of the collimator for different beam energies

The energy bandwidth of the collimator changes with the beam energy E_0 . In Fig. 3.7 the transmission probability T_{und} of the collimated beam through the undulator is plotted for E_0 from 150 MeV to 350 MeV. In the simulations the emittance is $1.41 \mu\text{m}$ in horizontal and vertical direction which results in a transmission probability of 50% through the collimator. At 150 MeV about 2% of the initial charge is additionally lost at the absorber system. Initially $5 \cdot 10^5$ simulation particles are used with gaussian energy distribution and an energy spread σ_E/E of 10%. The smaller number of particles at larger energy deviation is corrected, and Fig. 3.7 shows the numerical result for an uniform energy distribution.

For $E_0 = 150$ MeV the energy bandwidth is only -4% to $+2\%$ and the transmission probability T_{und} decreases to about 90% at an energy deviation of $\delta = -8.5\%$. At this beam energy operation of the linac is difficult and small changes in the rf-phase can cause an insufficient collimation efficiency for primary particles. For instance, if the halo amounts to 1% of the beam current and the energy of the beam is 137 MeV instead of 150 MeV ($\delta = -8.5\%$) then at design current a damage of the undulator can occur within 1 hour of operation. In such cases, only the active protection system can prevent the undulator against radiation damage.

In Table 3.2 the energy bandwidth of the collimator for the different energies is listed. Above 150 MeV the energy bandwidth increases and reaches its maximum range of 18% at 230 MeV and 250 MeV, and decreases again for higher energies. The transmission probability T_{und} of the collimator for energy deviations larger than the bandwidth is graphically shown in Fig. 3.8. The dark area, the energy bandwidth of the collimator, shows the energy range where no electrons are lost in the undulator. In this range the collimator efficiency depends only on the removal efficiency for secondary particles while the losses of electron can be neglected. The area with $T_{und} > 99.9\%$ shows the energy range where 0.1% of the collimated beam is lost in the undulator. A beam operation at a reduced beam current or for a short time period (< 100 hours) is acceptable. The areas

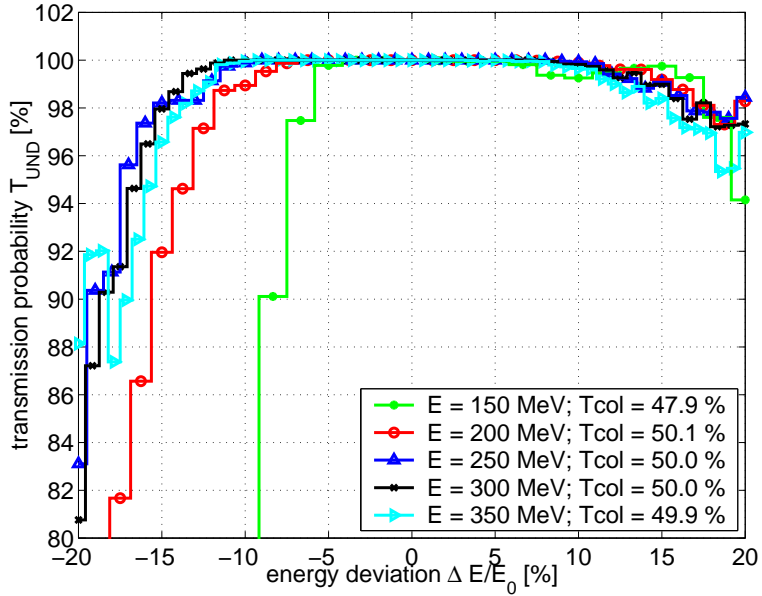


Figure 3.7: Transmission probability of the collimated beam through the undulator at different energies E_0 .

	quadrupole gradient adjusted to energy E_0					
	150 MeV	200 MeV	230 MeV	250 MeV	300 MeV	350 MeV
$\delta_{col,-}$ [%]	-3.5	-6.5	-10.5	-9.5	-10.5	-9.5
$\delta_{col,+}$ [%]	1.5	6.5	7.5	8.5	6.5	3.5
$\delta_{col,+} - \delta_{col,-}$ [%]	5	13	18	18	17	13

Table 3.2: Energy bandwidth of the collimator at different energies E_0 .

with $T_{und} > 99\%$, $T_{und} > 90\%$ and $T_{und} < 90\%$ are insufficient for safe beam operation.

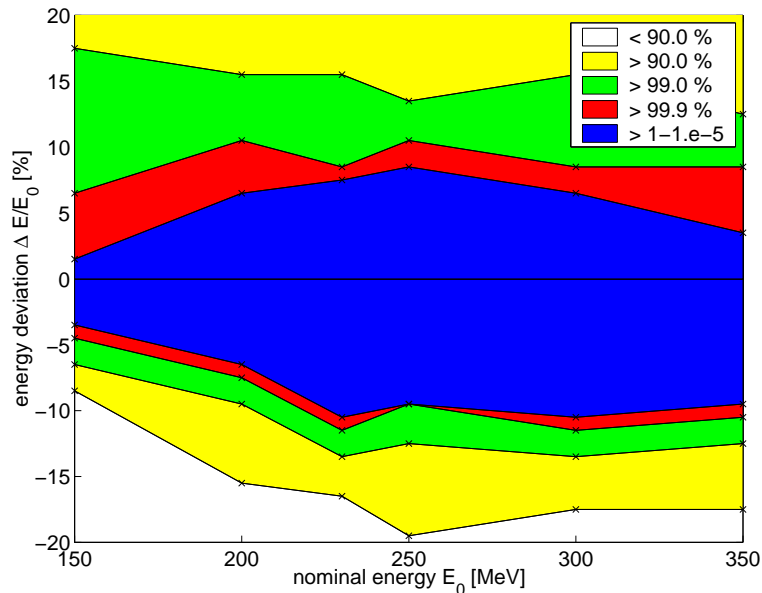


Figure 3.8: Energy bandwidth and transmission probability for different beam energies E_0 .

3.2.2 Clearance of the collimated beam to the undulator vacuum chamber

For a charge distribution of 0.1% energy spread (quasi mono-energetic) and an energy of 230 MeV the clearance along the undulator is plotted in Fig. 3.9. In the first undulator the minimum clearance is 1.4 mm, but reduces to 1.1 mm in the second undulator module and 1.2 mm in the third. The smaller clearance in the second and third undulator modules is caused by the β -function mis-match between the undulator modules (see Sec. 2.4.7). Due to the undulator focusing the smallest clearance occurs in horizontal direction at the horizontally focusing quadrupoles.

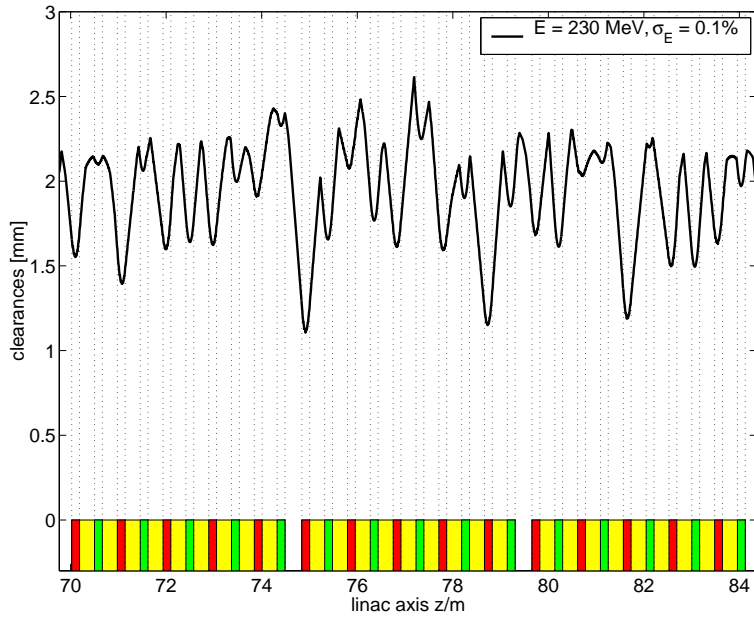


Figure 3.9: Clearance of a quasi mono-energetic beam with 230 MeV energy to the vacuum chamber of the undulator.

The variation of the clearance in the undulator modules with an energy deviation $\delta = \Delta E/E_0$ is shown in Fig. 3.10. Caused by chromaticity the clearance first grows towards smaller energies with its maximum of 1.3 mm at $\delta = -3\%$, where the β -function mismatch in the second and third module reaches its minimum. In the range of $|\delta| \leq 3\%$ the clearances in all modules are dominated by electrons with large offsets in horizontal direction. For energy deviations above $\delta > 3\%$ the chromatic effect of the second matching quadrupole Q2 causes larger vertical electron offsets than horizontal ones and the clearance rapidly drops with increasingly $|\delta|$. At $\delta = +8\%$ the loss probabilities L_{und} of the collimated beam in the second and third undulator module are $1.6 \cdot 10^{-4}$ and $2.8 \cdot 10^{-4}$. For $\delta = -8\%$ the mis-match of the undulator modules causes much smaller clearances in the second (0.5 mm) and third module (0.25 mm) than in the first (0.8 mm). The energy range of the electrons in a proper FEL beam is between -3% and $+2\%$ (see Sec. 2.2.6). Thus, the beam tails pass through the undulator with a minimum clearance of 0.75 mm.

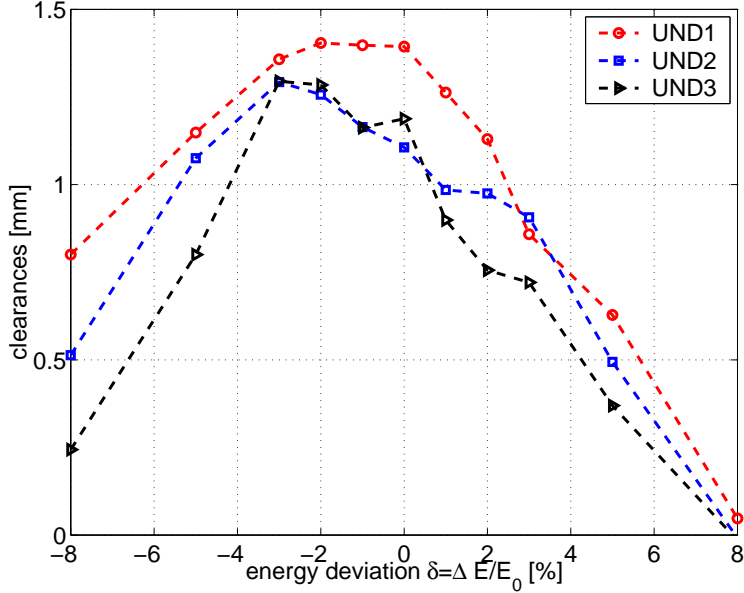


Figure 3.10: Variation of the clearance in the undulator modules for a quasi mono-energetic beam with energy deviation $\delta = \Delta E/E_0$ at $E_0 = 230$ MeV.

3.2.3 Loss distribution along the undulator caused by energy deviation

For initial distributions with an energy spread larger than the energy bandwidth of the collimator electrons are lost inside the undulator. The loss probability per unit length dL_{und}/dz in the undulator section of an initial distribution with $\sigma_E/E = 10\%$ is shown in Fig. 3.11(a). The loss probabilities in the first and second module are shown in Fig. 3.12(a) and (b). The thick solid curves shows dL_{und}/dz for all electrons, while the dashed and thin solid curves show the loss probability of electrons with energy deviation $|\delta|$ smaller than 15% and 20%. The mean energy of the distribution is 230 MeV. The transmission probability through the collimator is 50% ($\epsilon = 1.41 \mu\text{m}$). The number of tracked electrons is $5 \cdot 10^5$. About 1% hit the vacuum chamber. The energies of these electrons is plotted in Fig. 3.11(b). The results of the tracking simulation are summarized in Table 3.3.

energy range of electrons	Loss probability L_{und} [%]				
	UND1	UND2	UND3	UND-section	UND1 (0.60 m)
$ \delta < 15\%$	0.05	0.04	0.01	0.10	0.03
$ \delta < 20\%$	0.53	0.14	0.06	0.73	0.26
any δ	1.28	0.29	0.13	1.71	0.82

Table 3.3: Loss probability in the undulator modules caused by energy deviations.

The most electrons are lost in the first undulator module with an energy deviation δ larger than 15%. Between 30% ($|\delta| < 15\%$) and 46% (all δ) of the lost electrons are dumped at the entrance of the first module (within 0.6 m). The loss probability dL_{und}/dz grows in the drift spaces before vertical focusing quadrupoles and reaches its peak values at the quadrupole entrance. Inside the quadrupole dL_{und}/dz drops to zero. The largest peaks of dL_{und}/dz appear in front of the 2nd, 6th and 10th quadrupole in first module.

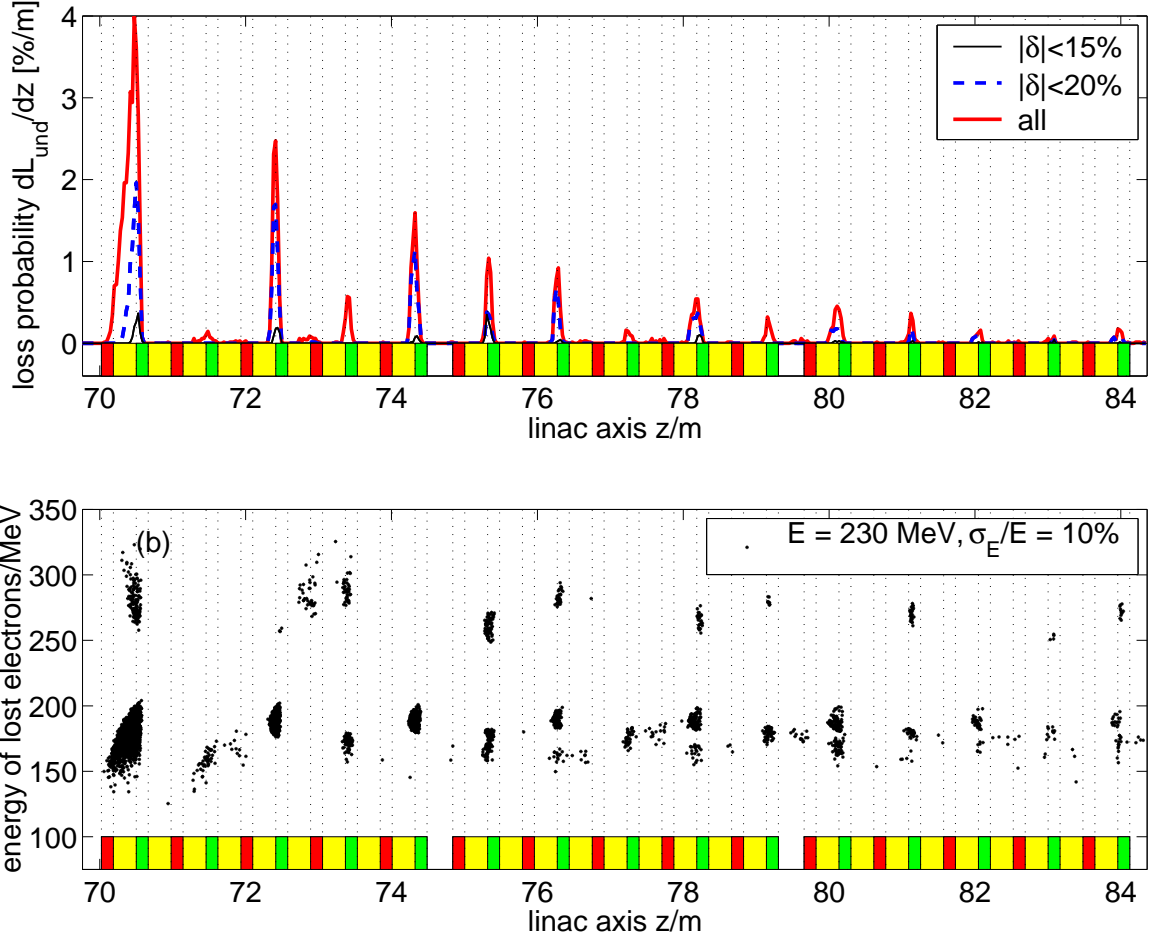


Figure 3.11: (a) Loss probability of electrons in the undulator per unit length dL_{und}/dz with energy deviation δ below 15%, 20% and for all tracked electrons. The initial charge distribution has an energy of 230 MeV with a spread of $\sigma_E/E = 10\%$. (b) Energies of the lost electrons in the undulator

The losses are confined to a rather small undulator length. In Fig. 3.11 is plotted the percentage of lost electron versus the undulator length in which the losses appear for the three different cases: $|\delta| < 15\%$, $|\delta| < 20\%$, and all δ . Within 0.5 m of the undulator more than 60% of the electrons are dumped and within 1 m more than 80%. Thus even through a 15 m long undulator section the energy deposited by primary electrons of a beam halo which has a large energy deviation is limited to about 1 m. This volume of the undulator is particularly endangered.

3.2.4 Collimator quadrupole gradient errors

Gradient errors of the collimator matching quadrupoles cause an improper adaption of the collimator phase space acceptance to the undulator phase space acceptance. First the influence of a gradient error for one of the four matching quadrupoles is studied. To obtain an estimate on the gradient tolerances an initial distribution with $\sigma_E/E = 1\%$ is used. The variation of the transmission probability T_{und} with the gradient deviation $\Delta g/g$ at a beam energy of 230 MeV is plotted in Fig. 3.14(a). Only the second matching quadrupole Q2COL1 shows a significant influence on the transmission probability which decreases to about 99% at $\Delta g/g = -5.5\%$ and at $\Delta g/g = +8\%$.

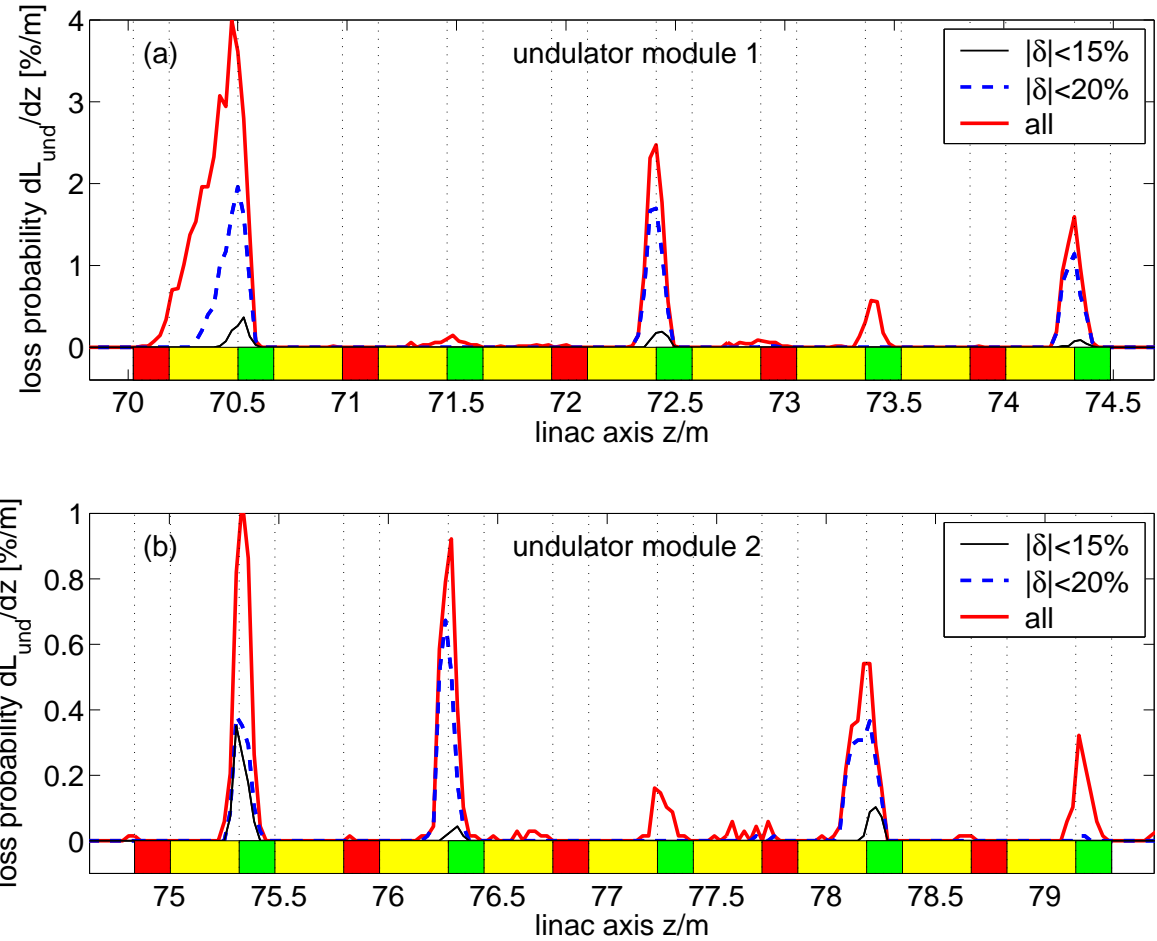


Figure 3.12: (a) Loss probability of electrons in the first undulator module and (b) in the second undulator module.

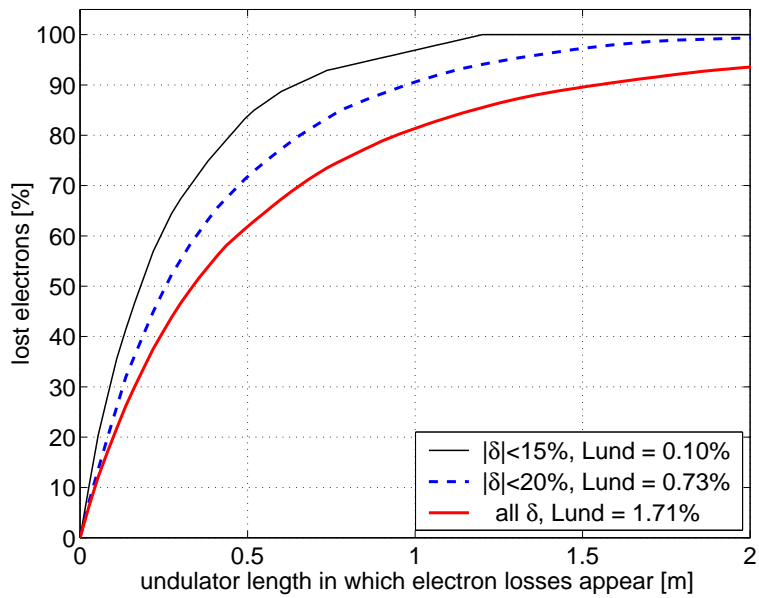


Figure 3.13: Undulator length in which electron losses caused by energy deviation appear.

The gradient errors can be assumed to be uncorrelated. Using a gaussian distributed gradient errors with an equal width for all four quadrupoles, the transmission probability T_{und} varies with rms-width of the distribution as shown in Fig. 3.14(b). The transmission remains 100% for 1% rms gradient errors. For a rms gradient errors of 2% the loss probability L_{und} in the undulator is 0.05% and increases to 0.16% for 3% rms errors.

The energy bandwidth of the collimation without and with 1% rms gradient errors at

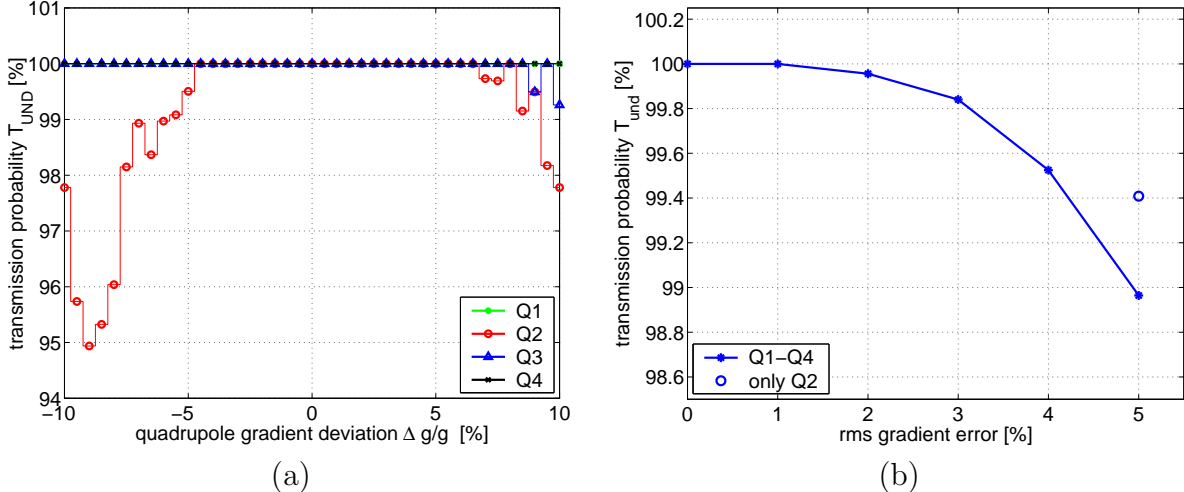


Figure 3.14: (a) Influence of quadrupole gradient errors on the transmission probability T_{und} of the collimated beam. The energy of the charge distribution is 230 MeV with an energy spread of $\sigma_E/E = 1\%$. (b) Influence of combined quadrupole gradient errors. The errors are assumed to be statistically independent for each quadrupole. The abscissa gives the rms-width of the gaussian distributed gradient error used for each quadrupole. Charge distribution as in (a).

the collimator quadrupoles is shown in Fig. 3.15. The energy bandwidth reduces from -10.5% to -7.5% and from $+7.5\%$ to $+4.5\%$. In the simulation about 10^4 electrons are tracked through the undulator in an 1% energy bin. The loss probability L_{und} per bin in the energy range $\delta = [-7.5\%, +4.5\%]$ is smaller than $1 \cdot 10^{-4}$ and in the large range from -10.5% to -7.5% it is limited to $5 \cdot 10^{-4}$. For adjustments of the matching quadrupole gradients within 1% rms error the influence on the energy bandwidth of the collimation is acceptable. By monitoring the beam losses along the undulator the four gradients of the matching quadrupoles can be readjusted within an 1% range.

3.2.5 Collimator quadrupole displacements

A transverse displaced quadrupole generates a magnetic dipole field on axis. The dipole field causes a kick to the collimated beam in transverse direction and electrons can be lost inside the undulator. The kick to the electrons is proportional to the quadrupole displacement. The variation of the transmission probability T_{und} with horizontal and vertical displacements of a quadrupole in the collimator section is shown in Fig. 3.16(a) and Fig. 3.16(b). The initial distribution has an energy spread of $\sigma_E/E = 1\%$. The energy is 230 MeV.

For quadrupole displacements in horizontal direction the influence of Q3 dominates. For displacements of Q3 large than $350\ \mu\text{m}$ the transmission probability reduces significantly. The influence of vertical displacements on the transmission probability is much stronger

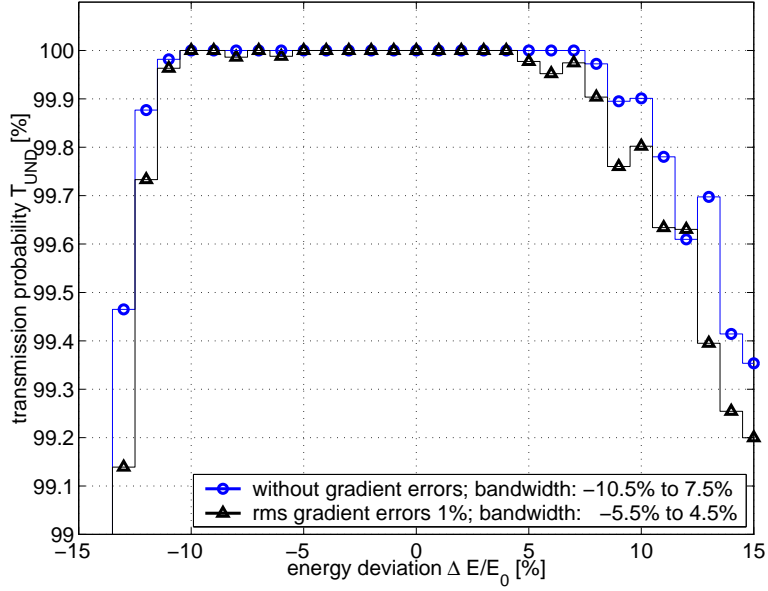


Figure 3.15: Energy bandwidth of the collimation without gradient errors and for 1% rms gradient errors.

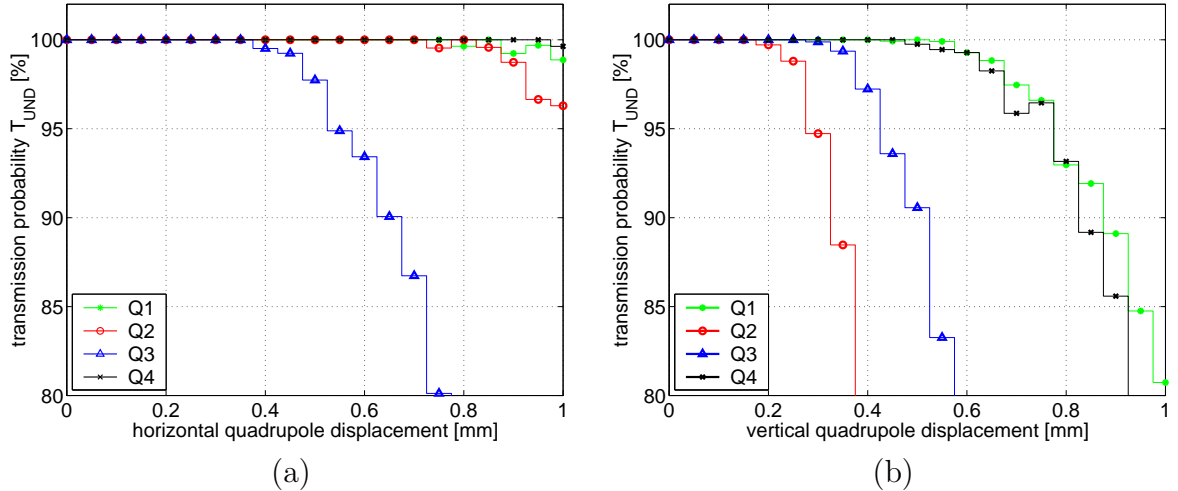


Figure 3.16: (a) Influence of a quadrupole displacement in horizontal direction on the transmission probability T_{und} of the collimated beam through the undulator. The energy of the initial distribution is 230 MeV with $\sigma_E/E = 1\%$. (b) vertical displacement of a quadrupole.

than for horizontal displacements. The quadrupoles Q2 and Q3 cause unacceptable beam losses for vertical displacements above 150 μm and 250 μm .

For gaussian distributed displacements with equal width for all quadrupoles in both direction x and y the variation of the transmission probability T_{und} with the rms-value is shown in Fig. 3.17. The transmission through the undulator remains 100% for rms displacements of 50 μm . At 100 μm the transmission T_{und} reduces to 99.5%. The survey group has positioned the collimator quadrupoles within 100-300 μm rms. Thus the orbit of the collimated beam has to be corrected with the dipole steerers superimposed in quadrupoles to compensate the kicks by quadrupole displacements.

The energy bandwidth of the collimation for rms displacements of 50 μm is shown in Fig. 3.18. The influence of quadrupole displacements on the transmission probability

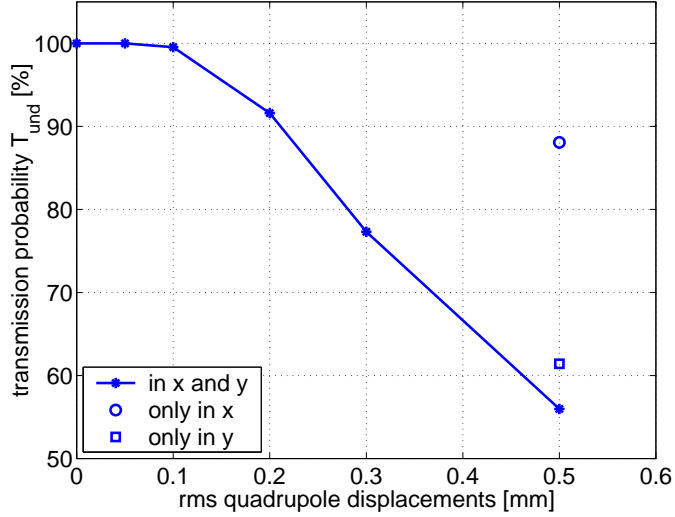


Figure 3.17: Influence of random quadrupole displacements on the transmission probability. The curve shows the result for horizontal and vertical displacements of the quadrupole Q1 to Q4. The results for 0.5 mm rms-displacement only in x (circle) and only in y (square) direction is also shown.

for positive $\delta = \Delta E/E$ is stronger than for negative δ . The energy range for which no electrons are lost inside the undulator is -4.5% to $+2.5\%$. The use of the dipole correctors to compensate the quadrupole displacements is mandatory for a proper work of the collimator system.

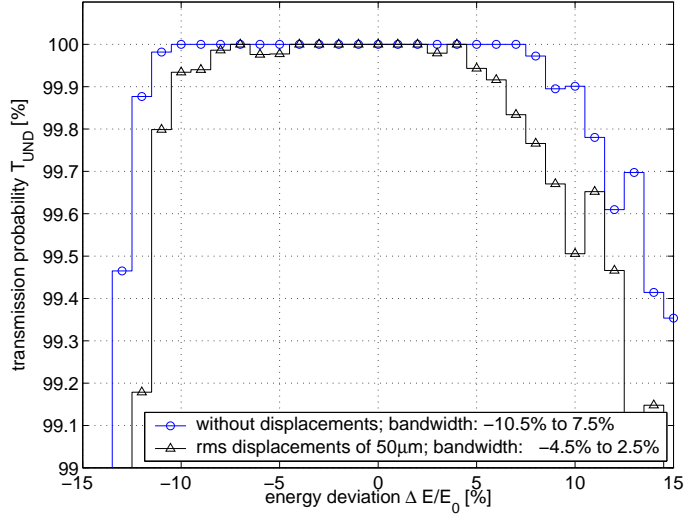


Figure 3.18: Energy bandwidth of the collimation for perfectly aligned quadrupoles and for quadrupoles with rms displacements of $50\mu\text{m}$.

3.2.6 Loss distribution along the undulator caused by quadrupole displacements

For a proper compensation of the quadrupole displacements by dipole correctors the centers of the phase space acceptance of the collimator and of the undulator have to be

known. Alignment methods based on beam position measurements can be applied to relate first the center of the beam to the center of the phase space acceptances and second the center of the acceptances to each other. The electrical center of the beam position monitors can be displaced by more than $100\text{ }\mu\text{m}$ from the mechanical center of the relevant apertures i.e. the collimators or the undulator vacuum chamber. The applicable beam based alignment methods for the collimator can be rather complicated.

In the first running period of TTF phase I only a limited number of beam position monitors were available and beam based alignment using BPMs was not possible. The first compensation of collimator quadrupole displacements has used the FEL photon beam and is systematically investigated in Sec. 3.7.2. The required corrections of the beam trajectory from the collimator to the undulator is larger than expected (1.3 mm, 1.5 mrad horizontally and 0.4 mm, 0.5 mrad vertically). In the horizontal plane the required corrections are three times larger than in the vertical plane. Some remaining uncompensated quadrupole displacements cannot be excluded. Therefore in the following, the loss distribution along the undulator of the collimated beam in cases of quadrupole displacements is studied.

As the level of losses in the undulator, the shape of the loss distribution depends strongly on the displacements of each individual quadrupole in the collimator section. Since these displacements are unknown, only most likely loss distributions can be calculated. Three different cases for uncompensated displacements are investigated:

1. random rms-displacements of $200\text{ }\mu\text{m}$ in x and y direction,
2. random rms-displacements of $300\text{ }\mu\text{m}$ in x and y direction,
3. and random rms-displacements of $500\text{ }\mu\text{m}$ only in x direction

for all quadrupoles. In the first and second case the displacements of $Q2$ and $Q3$ in vertical direction will dominate the loss distribution. Towards larger random displacements the fraction of lost electron in the first undulator module will increase while the fractions of losses in the other modules decrease. The third case is suited to yield an estimate for loss induced by very large displacements in the horizontal plane. To cause losses only by quadrupole displacements for the simulations an energy spread of $\sigma_E/E = 1\%$ for the initial distribution is chosen. The loss probability in the undulator modules are listed in Table 3.4.

The loss probability per unit length along the undulator normalized to the total losses

case	loss probability L_{und} [%]				
	UND1	UND2	UND3	UND-section	UND1 (0.60 m)
$\sigma = 200\text{ }\mu\text{m, x and y}$	5.94	0.90	1.42	8.39	4.81
$\sigma = 200\text{ }\mu\text{m, x and y}$	17.67	1.40	2.20	22.69	14.63
$\sigma = 500\text{ }\mu\text{m, only x}$	5.63	0.70	0.25	11.92	1.41

Table 3.4: Loss probability in the undulator modules caused by quadrupole displacements.

for the three cases is shown in Fig. 3.19. The losses occur for displacements in vertical direction dominantly at the drift space before the second and the sixth quadrupole in each of the undulator modules. The peak values are located nearby the quadrupole entrances. For rms-displacements of $300\text{ }\mu\text{m}$ the losses are more spread with smaller peak values that

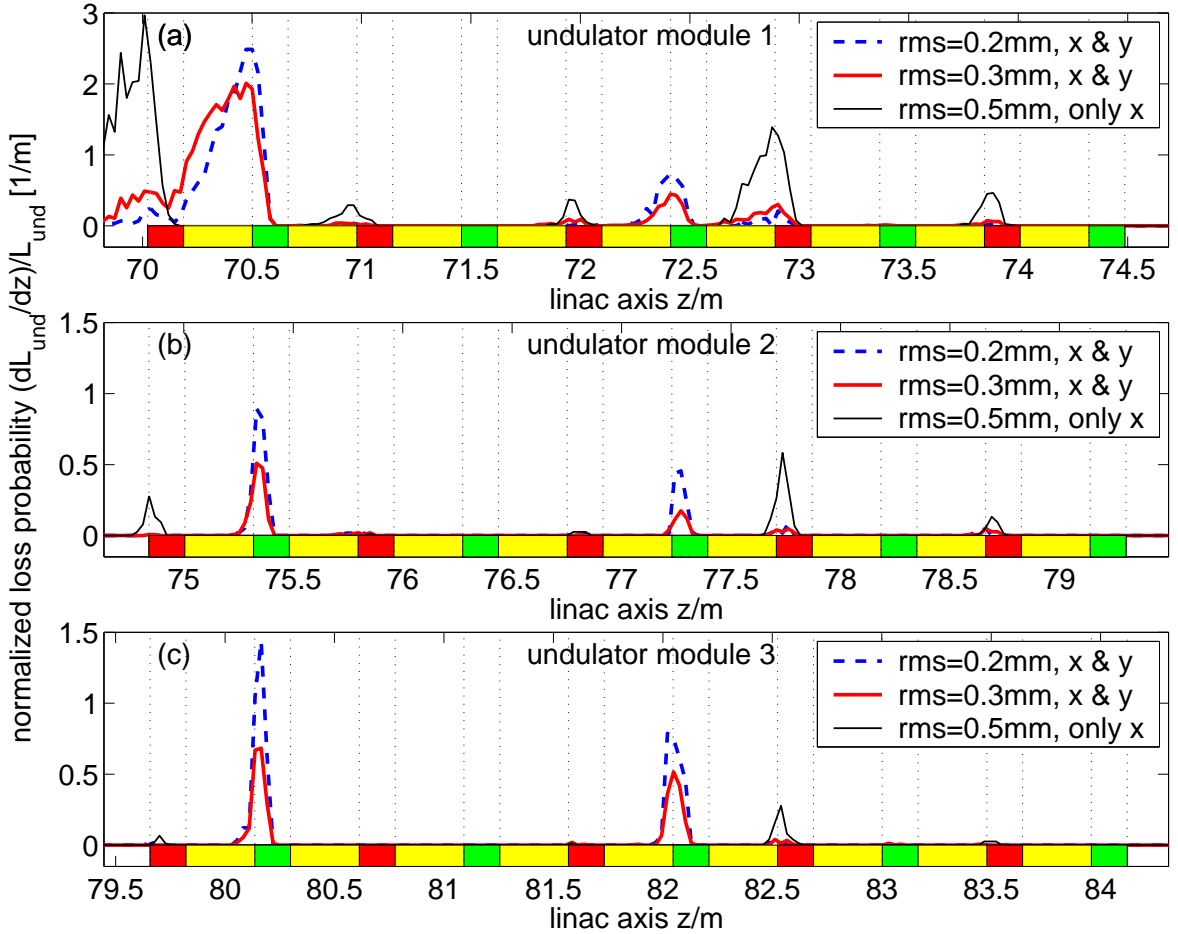


Figure 3.19: Loss probability per unit length normalized to the total losses in the undulator modules. The losses are caused by three different cases of random quadrupole displacements. The energy of the initial distribution is 230 MeV, the energy spread is 1%. The transmission probability for the three different cases through the collimator section are 49.8%, 48.2% and 46.3%.

for $\sigma = 200 \mu\text{m}$. Larger losses appear at the first horizontal focusing quadrupole and some small losses at seventh quadrupole in module 1 and 2.

For rms-quadrupole displacements of $500 \mu\text{m}$ in horizontal direction only, the losses dominantly occur at the 1st, 7th and 9th quadrupole in the modules. In the first undulator module larger losses are also observed in the 5th and 7th quadrupole.

The undulator length in which the losses due to quadrupole displacements occur is shown in Fig. 3.20. Within 0.5 m more than 60% of the electrons are lost in the undulator and more than 85% within a length of 1 m. The slope of the curves at the origin reflects the highest loss rate per unit length. They amount to about 2%/cm for three cases.

3.2.7 Comparison of different spoiler apertures

The radius of the spoilers defines the phase space acceptance of the collimator. Towards a smaller radius the energy bandwidth of the collimator increases, but the transmission probability through the spoilers decreases. For 230 MeV and an emittance $\epsilon_{x,y} = 1.41 \mu\text{m}$ the transmission probability T_{und} of the collimated beam through the undulator is plotted in Fig. 3.21. The dark grey area shows the energy range in which no electrons hit the

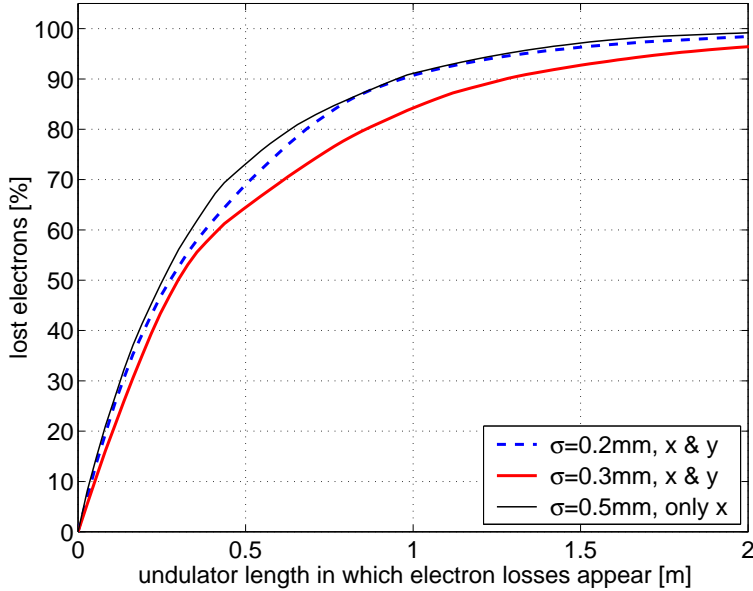


Figure 3.20: Undulator length in which losses caused by quadrupole displacements appear.

undulator vacuum chamber. The energy bandwidth for positive energy deviations ($\delta > 0$) rapidly grows with decreasing spoiler radius R_{sp} while for negative energy deviation the grows above $R_{sp} = 3$ mm is weaker. Towards a spoiler radius of 4.0 mm the energy bandwidth becomes too small for a safe operation. The values for the energy bandwidth and the transmission probability T_{col} through the collimator are summarized in Table 3.5. The transmission T_{col} for $\epsilon = 1.41 \mu\text{m}$ reduces to 66% at $R_{sp} = 2.5$ mm and to 35% at $R_{sp} = 2.0$ mm compared to the one for $R_{sp} = 3$ mm.

R_{sp}	2 mm	2.5 mm	3 mm	3.5 mm	4.0 mm
T_{col}	17.7%	33.0%	50.0%	65.7%	77.0%
$\delta_{col,-}$	-16.5%	-13.5%	-10.5%	-5.5%	-3.5%
$\delta_{col,+}$	>20%	13.5%	7.5%	3.5%	1.5%

Table 3.5: Transmission probability T_{col} through collimator and energy bandwidth $[\delta_{col,-}, \delta_{col,+}]$ at 230 MeV for different radius R_{sp} of the spoilers.

3.2.8 Summary of collimator efficiency for primary electrons

An initial distribution, representing a time averaged beam halo, with a transmission probability T_{col} of 50% or $\epsilon = 1.41 \mu\text{m}$, is found to be reasonable choice for numerical tracking calculations, because it well approximates the losses in the undulator normalized to the beam power before the collimator as well as the losses in the undulator normalized to the beam power behind the collimator. This allows to derive from the tracking results for $T_{col} = 50\%$ the losses for different initial emittances by considering the T_{col} as a function of ϵ only (see Fig. 3.5).

The energy bandwidth δ_{col} of the collimator at $E_0 = 230$ MeV energy is 18%. It is asymmetrical distributed from $\delta_{col,-} = -10.5\%$ to $\delta_{col,+} = 7.5\%$. The bandwidth reduces toward

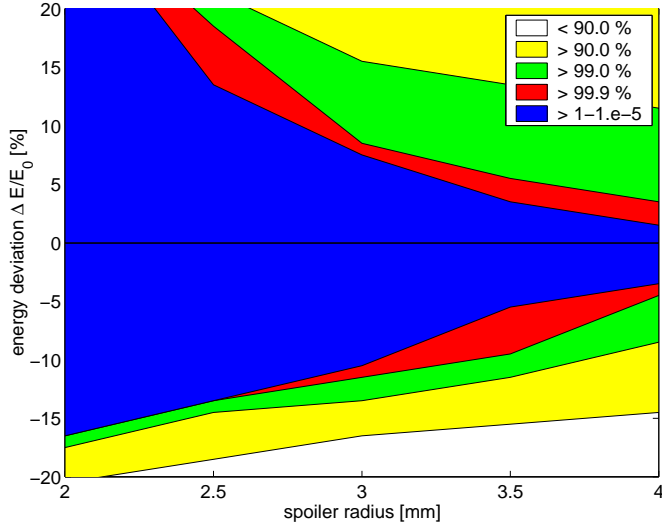


Figure 3.21: Energy bandwidth for different spoiler radius. The areas show the transmission probability T_{und} of the collimated beam through the undulator. The matching quadrupoles are adjusted for a beam energy of 230 MeV.

smaller energies or larger energies E_0 . The transmission probability T_{und} decreases rapidly with energy deviation below $\delta_{col,-}$. A safe operation in the range is not possible.

The clearance of the regular beam to the undulator vacuum chamber is 1.1 mm at 230 MeV. If the bunch compressor 2 is operated the electrons in the bunch tails have a clearance of 0.7 mm.

Quadrupole displacements have to be corrected to a level of $50 \mu\text{m}$ rms to guarantee that no electrons of the collimated beam intercept the vacuum chamber. At $100 \mu\text{m}$ rms displacements about 0.5% of the electron transmitting the collimator are dumped in the undulator. Dominantly vertical displacements are responsible for beam losses. Quadrupole displacements have to be corrected by beam based alignment methods. Losses due to quadrupole gradient error of 1% rms are tolerable.

The losses in the undulator are local. 50% of the losses appear within 0.5 m undulator length. Energy deviation of the beam, collimator quadrupole gradient errors or displacements cause losses in vertical direction at the vertical focusing quadrupole, mainly in the first undulator module. Beam losses at the horizontal focusing quadrupoles occur only for horizontal collimator quadrupole displacements above $400 \mu\text{m}$.

3.3 Energy deposition due to primary electrons in the undulator

Electrons of the beam or the dark current which are lost in the undulator first hit the aluminum vacuum chamber where an electromagnetic shower is initiated. A fraction of the secondary particles dissipate there energy in the permanent magnets of the undulator. In this section, the distribution of energy deposition in the permanent magnets is studied. Because the loss distribution of the electrons depends on the considered case, i.e. losses due to dark current, losses of beam halo caused by an energy deviation or losses due to quadrupole displacements, several Monte Carlo simulations are presented.

3.3.1 Parameters for the Monte Carlo simulation

The electromagnetic shower has been simulated using the Monte Carlo code EGS4 [73]. In the code, the undulator is modeled by small volume elements. For each volume element, the energy deposition and the absorbed dose is calculated. Since the demagnetization process also depends on the irradiation spectrum, the secondary particles entering the volume elements are partially stored. In Fig. 3.22 the cross-section of the undulator shows the material and the geometrical size of the volume elements in x and y direction.

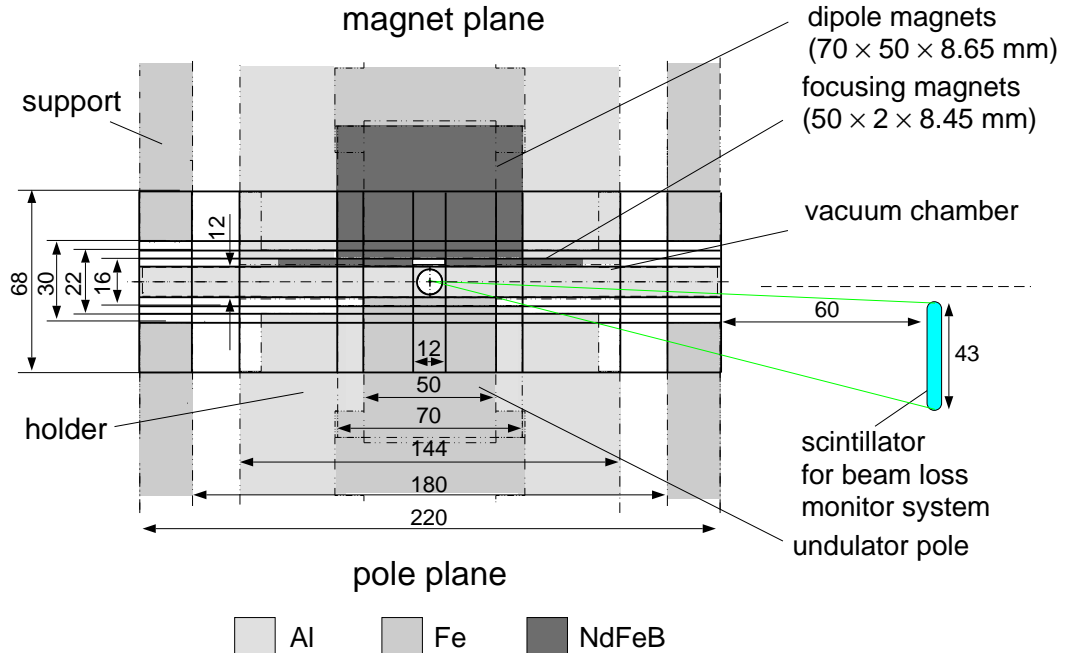


Figure 3.22: Cross-section of the undulator. By the area of size 220 mm horizontally and 68 mm vertically the subdivided of the undulator into small volume elements (solid lines) as used for the Monte Carlo simulation is shown. The magnet slice of the hybrid structure is shown in the upper half of the plot, and the pole slice is sketched in the lower half.

In z direction, there is an alternating arrangement of magnet and pole slices. The upper half of the drawing shows the magnet slice of the hybrid structure. The large permanent magnets produce the undulator dipole field and the thin magnet plates the quadrupole field. The holder of the magnets are made of aluminum and the support for the magnet holder are made of steel. The lower half of the drawing in Fig. 3.22 shows a pole slice of

the hybrid structure.

The vertical size of the dipole magnets in which the electromagnetic shower is calculated is larger than the Molière radius $R_M = 1.5$ cm. Only a small fraction (a few percent) of the energy is carried by secondary particles (mainly photons) in vertical direction to the boundary of the simulated undulator volume. In the horizontal direction, the shower is calculated up to the support of the magnet holder at $x = \pm 110$ mm. Particles leaving the undulator in horizontal direction are stored. This allows to determine the dependence of the energy deposition in the scintillators on the transverse and longitudinal position of the losses. The variation of the energy deposition with x and y is larger in volume elements close to the vacuum tube than in the ones more distant. These volumes are chosen smaller in size to achieve a good approximation for the maximum absorbed dose within the volume.

In Fig. 3.23, a side-view of the undulator at the exit of a quadrupole shows the longitudinal subdivisions. The pole slice (5 mm long) and magnet slice (8.65 mm long) belong to discernible regions with 100 volume elements transversely. Altogether, more than 200000 volume elements have been defined to model the three undulator modules.

Presently, two types of dosimeters, silver-activated radio-photoluminescence (RPL) glass dosimeters³ and thermo-luminescence (TLD) lithium fluoride dosimeters⁴, are installed at the exit of the horizontally defocusing quadrupoles in the undulator. For the Monte Carlo simulations, the TLD and RPL material fill the horizontally centered volume elements between two poles (for x from -6 mm to 6 mm and for y from ± 6 mm to ± 8 mm) behind each quadrupole in the undulator. The real size of the dosimeters is much smaller ($\varnothing 1$ mm \times 6 mm). With the increased dosimeter volume, less particles need to be tracked to yield an accurate result for the deposited energy. Due to the small density of the dosimeter material the influence on the electromagnetic shower in the permanent magnets can be neglected.

A secondary particle is tracked through the material until it reaches a cutoff energy. Below the cutoff energy, which has been chosen to be 1 MeV (total energy) for charged particles and 0.1 MeV for photons, the history is terminated. The kinetic energy of electrons, photons, and additionally twice the mass of positrons are deposited in the region where the history of the particle is stopped. The small photon cutoff energy is required to calculate accurately the absorbed dose measured by dosimeters.

The magnetic fields in the undulator have an influence on the trajectories of the charged particles. The regions with magnetic fields are shown in Fig. 3.24. The regions 1 to 9 (solid lines) for the magnet slice and the regions 10 and 11 (dashed lines) for the pole plane show the volume elements in which different fields are implemented. The following list summarizes the magnetic fields which have been taken into account:

- Regions 3,4 and 5: the non-linear periodic undulator field B_y and B_z as described in Sec. 2.4.3, Eq.2.32 and Eq.2.33 with a peak field value of $B_0 b_1 = 454.0$ mT (only the first harmonic).
- Region 4: quadrupole and octupole fields

³RPL technical data: size $\varnothing 1$ mm \times 6 mm; composed of 53.6% O, 33.2% P, 4.7% Al, 4.1% Ag, 3.5% Li and 0.9% B; density is 2.6 g/cm³; applicable for dose measurements between 1 Gy and 1 MGy.

⁴TLD technical data: size $\varnothing 1$ mm \times 6 mm; Li 26.8%, F 73.2%, density is 2.6 g/cm³, applicable for dose measurements between 0.05 mGy and 1 kGy.

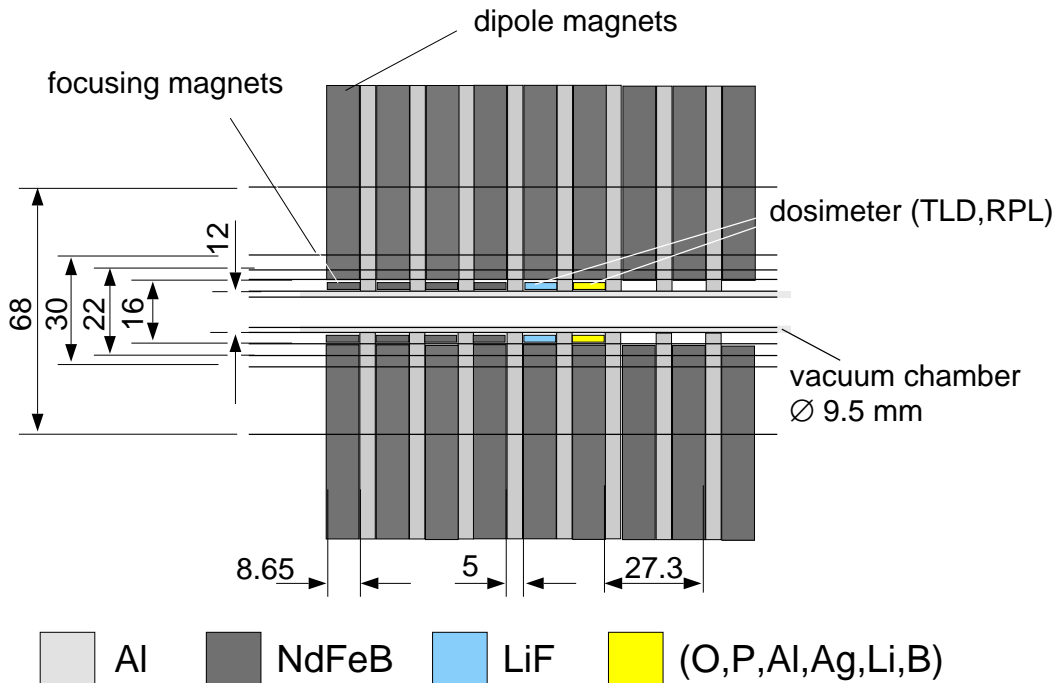


Figure 3.23: Side-view of undulator at the exit of a quadrupole showing the volume elements used for the Monte Carlo calculations.

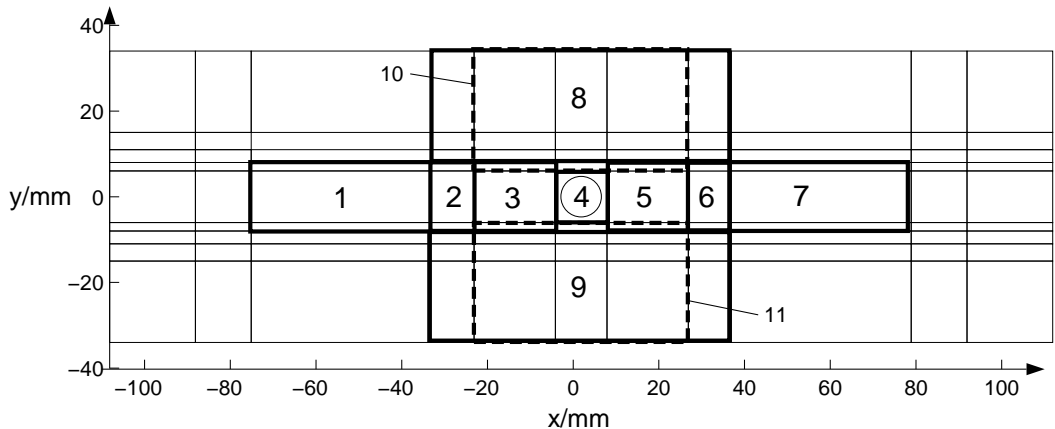


Figure 3.24: Regions with different magnetic fields pattern as used for the Monte Carlo simulations.

- Regions 2,3,5 and 6: (additional) constant vertical field caused by the thin magnet plates. From the vertical field measurement for large horizontal offsets the constant field is approximately $B_y \approx 53$ mT (scaled to gradient of 10.5 T/m see Sec. 2.4.8).
- Regions 1 and 7: as regions 2,3,5 and 6 with $B_y \approx 25$ mT. The smaller magnetic field has been chosen because the size of thin permanent magnets are shorter in x -direction than the size of the regions (about a factor 2).
- Regions 8 and 9: remnant field of the permanent magnets $B_z = 1.15$ T
- Regions 10 and 11: vertical magnetic field in the undulator poles $B_y = 1.075$ T. The field is approximated by the pole tip field calculated for $y = 6$ mm using Eq. 2.32 (first to fifth harmonic).

In the tracking simulation the magnetic field is calculated for the actual position of charged particle. From the magnetic field the curvature radius is determined depending on the polarity and the particle momentum. The bending angle caused by the Lorentz force is added to the angular kicks in the particle motion due to multiple scattering in the material.

3.3.2 Energy deposition in the undulator for point-like losses

In this section, the energy depositions and the absorbed doses caused by point-like losses in vertical and horizontal direction are investigated.

Point-like losses in vertical direction

The highest loss probability of electrons with large energy deviations occur at the entrance of the 2nd quadrupole (see Sec. 3.2.3). For quadrupole gradients adjusted for a proper beam matching at 230 MeV, on average the vertical angle of the lost electrons at the 2nd quadrupole is 7 mrad.

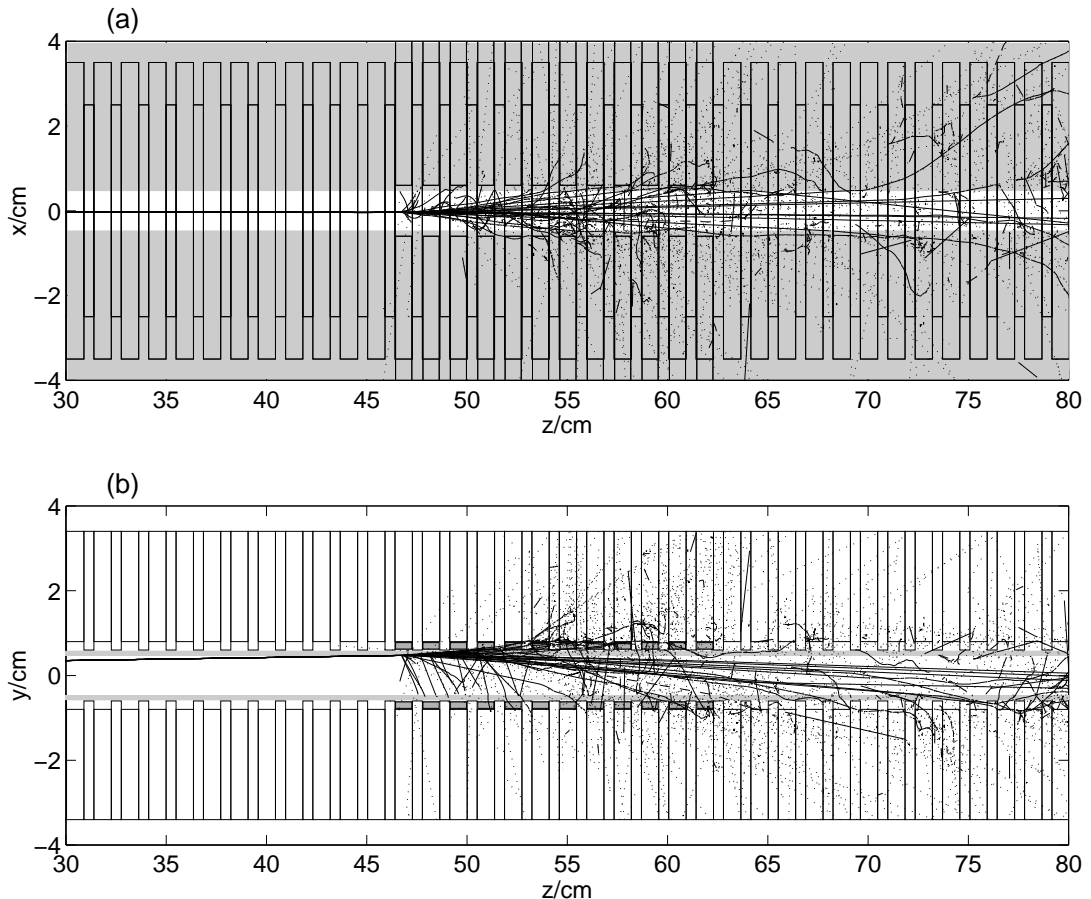


Figure 3.25: Electromagnetic shower in the undulator produced by 20 electrons with a vertical angle of 7 mrad and an energy of 190 MeV. (a) shows the trajectories in the horizontal plane (x, z) and (b) in the vertical plane (y, z). Solid lines are electrons, dots are photons and dashed lines are positrons. The geometry of the poles, dipole magnets, quadrupole magnets (thin magnet plates) and the vacuum chamber (grew area) are shown.

In Fig. 3.25(a) (horizontal plane) and Fig. 3.25(b) (vertical plane) the trajectories of 20 primary electrons hitting the vacuum chamber and the trajectories of the produced secondary particles are shown. The geometry of the iron poles, the dipole magnets, the thin permanent magnets and the vacuum chamber are sketched. The solid lines corresponds to the electrons, the dotted to the photons and the dashed lines to the positrons. The primary electrons propagate from the left to the right and hit the vacuum chamber wall at the center of the first focusing permanent magnet (at $z = 42$ cm). The most secondary particle trajectories appear within the first 15-20 cm in the upper half of the undulator. The electromagnetic shower develops about 5-8 cm (at $z = 55$ cm) in longitudinal direction until it reaches the dipole magnets vertically and the quadrupole magnets horizontally. About half of the electrons are back-scattered to the vacuum chamber and initiate an electromagnetic shower downstream the quadrupole in opposite direction to the incident primary electrons ($y < 0$).

The transverse shower development for 1000 initial electrons behind 1, 2, 3, and 4 un-

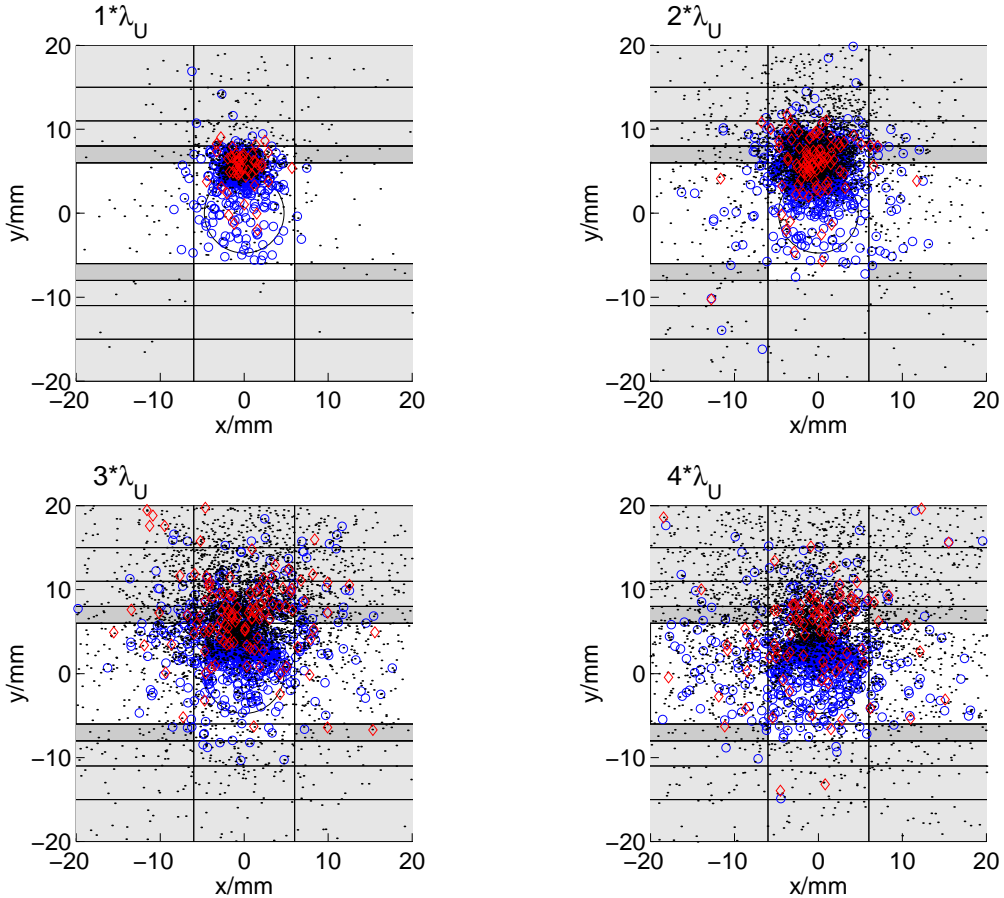


Figure 3.26: Electromagnetic shower after 1, 2, 3, and 4 undulator periods. Circles show the electrons, dots the photons and diamonds the positrons. The dipole magnets are light grey, the quadrupole magnets are grey.

dulator periods are shown in Fig. 3.26. Electrons are plotted by circles, photons by dots and positrons by diamonds. After one period the number of electrons is slightly increased to 1139. 491 electrons have a vertical offset above 4.75 mm, 196 above 6 mm but only 10 above 8 mm inside the dipole. The number of positrons is 51, the one for photons 2529.

The shower is concentrated in the vacuum chamber and the pole region. After the second period, the transverse size of the shower has grown. The number of electrons is approximately equal (1139), the number of positrons grows to 96 and 4160 photons cross the x-y plane. Now 291 electrons have an vertical offset above 6 mm and 130 electrons incident on the dipole magnet. The shower is concentrate in the pole region and the edge of the dipole and the amount of secondary particles in the vacuum chamber has increased. After the third undulator period the number of electrons has dropped to 992, the number for photons and positrons increased to 5103 and 121, respectively. The shower has a diameter of about 3 cm. The shower reaches the inner area of the dipole magnet, the number of incident electrons decreased to 108, the positrons slightly increased from 25 to 48. After the fourth period, 11 cm behind the incident, the number of electrons decrease to 857, the number for positrons is 99 and 4771 photons are counted. The shower has passed its maximum. The most electrons, 543, travel inside the vacuum tube and carry 60% of the remaining shower energy.

The energy deposition in the undulator has been calculated using 50000 primary electrons. The absorbed doses per 1 kJ beam energy for selected volume elements with transverse centers at (x, y) as a function of the longitudinal position in the undulator are shown Fig. 3.27. The volume elements within the dipole magnets are plotted with triangles (pointing up for $y > 0$ and pointing down for $y < 0$), the ones within the quadrupole magnets by diamonds ($y > 0$) and squares ($y < 0$). The doses deposited in the test volumes filled with dosimeter material are shown by circles and pentagrams. The entrance and exit of the quadrupoles are indicated by vertical dashed lines.

The peak values of the absorbed doses in the upper half of the undulator are reached close to the center of the quadrupoles. A peak dose of 2.9 kGy is calculated in the dipole magnets at 9.5 mm vertical offset. At $y = 13$ mm the peak dose decreases to 0.84 kGy and at $y = 25$ mm it reaches only 91 Gy. The peak values of the absorbed dose for the dipole magnet volumes with horizontal center at $x = \pm 7$ mm are one of magnitude smaller than the ones calculated at $x = 0$ and at $x = \pm 30$ mm the calculated doses are two orders of magnitude smaller. The full width half height of the absorbed dose curves for the volumes in the upper undulator is about 13 cm. Behind the vertical focusing quadrupole the dose rapidly drops below the one calculated for the volume elements in the lower part of the undulator ($y < 0$). The magnets volumes with $y < 0$ are uniformly irradiated in z direction along a distance of 60 cm. The largest value of 0.3 kGy in the dipole at $y = -9.5$ mm is an order of magnitude smaller than the peak absorbed dose for the upper undulator. At a distance of 80 cm from the beam incidence the curves with $y > 0$ approach the ones for $y < 0$.

The energy deposited in the simulated dosimeters are in the range of 0.5 kGy to 0.8 kGy behind the second quadrupole ($z = 65$ cm) and between 100 Gy to 245 Gy behind the third quadrupole ($z = 112$ cm). The absorbed dose is larger than the one deposited in the permanent magnets since the material is not shielded by the iron poles of the hybrid structure and is in direct contact to the aluminum vacuum chamber. The maximum absorbed dose in the dipole magnets is underestimated by a factor 10-30 by the dosimeters behind the 3rd quadrupole (horizontal focusing) and still by a factor 4-6 in case of dosimeters positioned behind the 2nd quadrupole (vertical focusing).

The energy deposition in the undulator is summarized in Table 3.6. The largest fraction of energy is absorbed in the aluminum vacuum chamber. Approximately the same energy is deposited in the iron poles as in the dipole magnets, even through the iron pole fill a

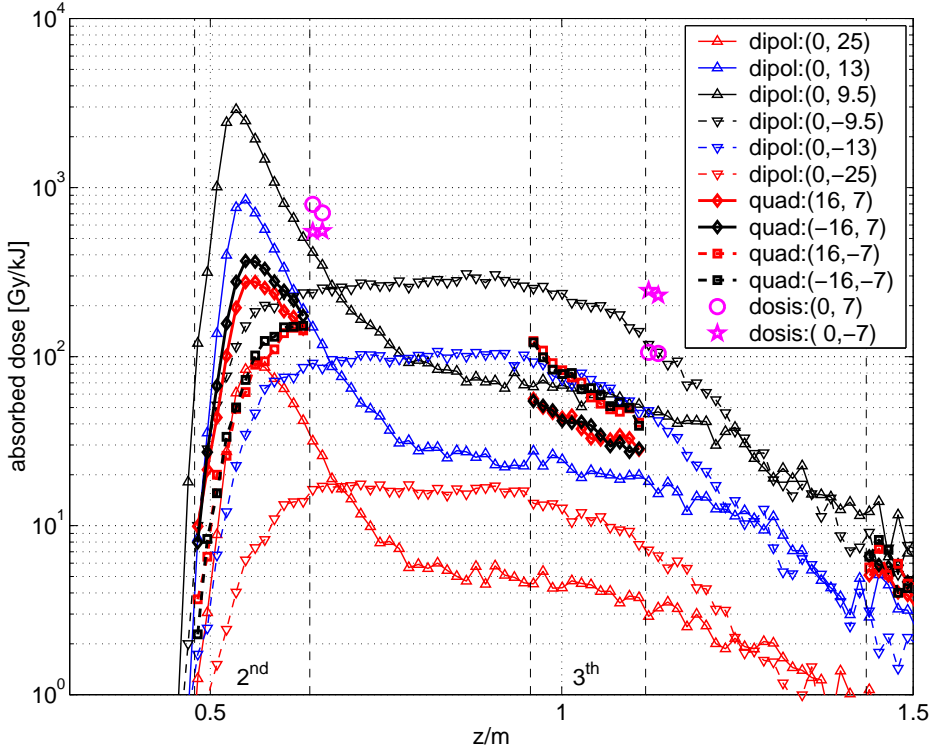


Figure 3.27: Absorbed dose in permanent magnets for an incidence in vertical direction. The dose for volumes with the center (x, y) in dipole magnets are plotted with triangles, for quadrupole magnets with diamonds and squares and for the volume elements filled with dosimeter material circle and pentagrams are used. The dashed lines indicate the entrance and exit of the integrated quadrupoles in the first undulator module.

energy deposition [%]								
dipoles			quads.	chamber	poles	sum	outside boundary	
sum	$y > 0$	in 0.1 m	sum	sum	sum	sum	$ y > 34 \text{ mm}$	$x > 110 \text{ mm}$
27.0	15.1	8.1	2.6	35.6	24.8	7.1	5.9	0.56

Table 3.6: Energy deposition for vertical electron incidence in undulator.

much smaller undulator volume. This is caused by the vertical displacement of 2 mm of the dipole magnets from the vacuum chamber. Hence the iron poles prevent the magnets from much higher radiation dose.

5.9% of the energy is carried by secondary particles escape through to the upper and lower boundary. These particle contribute to an irradiation in the permanent magnet outside the simulated volume. Since the distribution is spread in longitudinal and horizontal direction the caused dose in the magnets are small ($< 1 \text{ Gy}$). A small fraction of 0.6% leaves the undulator in horizontal direction and can be monitored by scintillation counters.

The extension of the electromagnetic shower in the magnets is plotted in Fig. 3.28, which shows the charged particle current in a distance Δz from the location of incident. In Fig. 3.28(a) and (b), only particles with a vertical offset larger than 6 mm are plotted. In horizontal direction, Fig. 3.28(a), the shower is concentrated in $|x| < 3 \text{ mm}$ and only a small fraction of the shower strikes the quadrupole magnets. The particle current in the vertical plane, shown in Fig. 3.28(b), is about 4 times larger in the pole region than

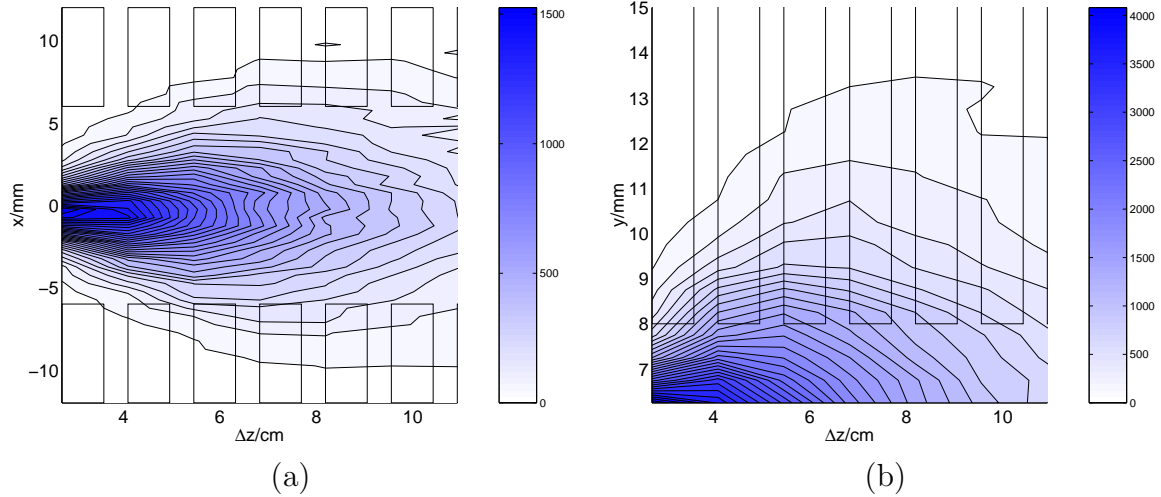


Figure 3.28: Development of the electromagnetic shower as a function of the distance Δz from the point of intercept. In the simulation 50000 electrons hit the vacuum chamber. (a) charged particles with $y > 6$ mm in the horizontal plane (dipoles are shown) and (b) charged particles with $y > 6$ mm in the vertical plane (quadrupoles are shown).

at the edge of the dipoles. The shower penetrates vertically about 3 to 5 mm into the dipole magnets. At $y = 18$ mm, the number of charged particles is reduced to less than 1% compared to the pole region and the shower depth in the dipole reaches a maximum about 3 undulator periods behind the incidence. The two pictures show that only a small part of the undulator magnets are exposed to radiation by charged particles, while i.e. 80% of a dipole magnet is radiated dominantly by low energy photons.

The energy spectrum of the electrons and positrons incident on the dipole magnets at different longitudinal positions is plotted in Fig. 3.29(a). High energy particles dominantly occur at $\Delta z = 2\lambda_U$. The yield is small for $\Delta z < 2\lambda_U$ because the shower is still concentrated in the pole area. For $\Delta z > 2\lambda_U$ the charged particles have lost their energy due to the emission of bremsstrahlung photons. Figure 3.29(b) shows the number of charged particles versus their mean energy with $y > 8$ mm, $y > 11$ mm, and $y > 14$ mm. The data points on each curve represent one dipole magnet at the position $\Delta z = \lambda_U, 1.5\lambda_U, \dots, 5.5\lambda_U$. The mean energy of charged particles incident on the dipole magnet with $y > 11$ mm is below 25 MeV and the rate is reduced by a factor 3 compared to $y > 8$ mm.

In section 2.4.10 has been shown that the demagnetization process of the NdFeB permanent magnets is mainly related to the exposure of charged particles above ≈ 20 MeV. To estimate the content of higher energy particles irradiate the permanent magnets, the absorbed dose caused by electrons and positrons with $E > 20$ MeV has been calculated. The reduced dose in case of an vertical incidence is shown in Fig. 3.30. The ratio of the reduced dose to the total absorbed dose vary between 5% for volume elements far away from the undulator axis ($y = \pm 25$ mm) and 33% for the maximum dose calculated in the dipoles at $y = 9.5$ mm. The doses in the magnet blocks for the quadrupoles at $x = \pm 16$ mm and $y = \pm 7$ mm are for times smaller than of the doses shown in Fig. 3.27. The result of this calculations is summarized in Table 3.7.

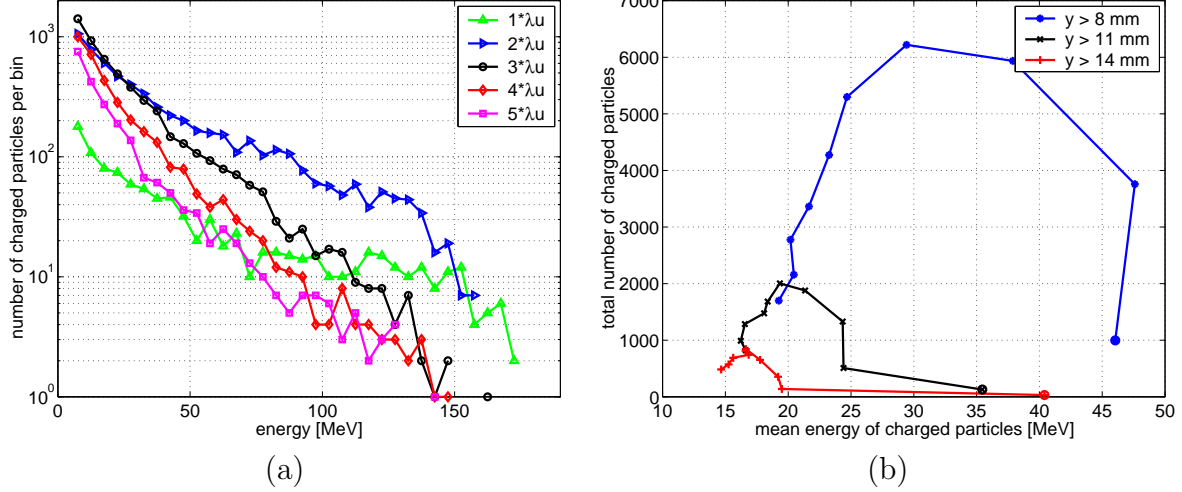


Figure 3.29: (a) energy spectrum of charged particles at different longitudinal positions (b) total number of charged particles versus mean energy for λ_U (circle), $1.5\cdot\lambda_U,\dots,5.5\cdot\lambda_U$. The three curves show the electrons and positrons exposing the dipole magnets with vertical coordinate $y > 8\text{ mm}$, $y > 11\text{ mm}$, and $y > 14\text{ mm}$.

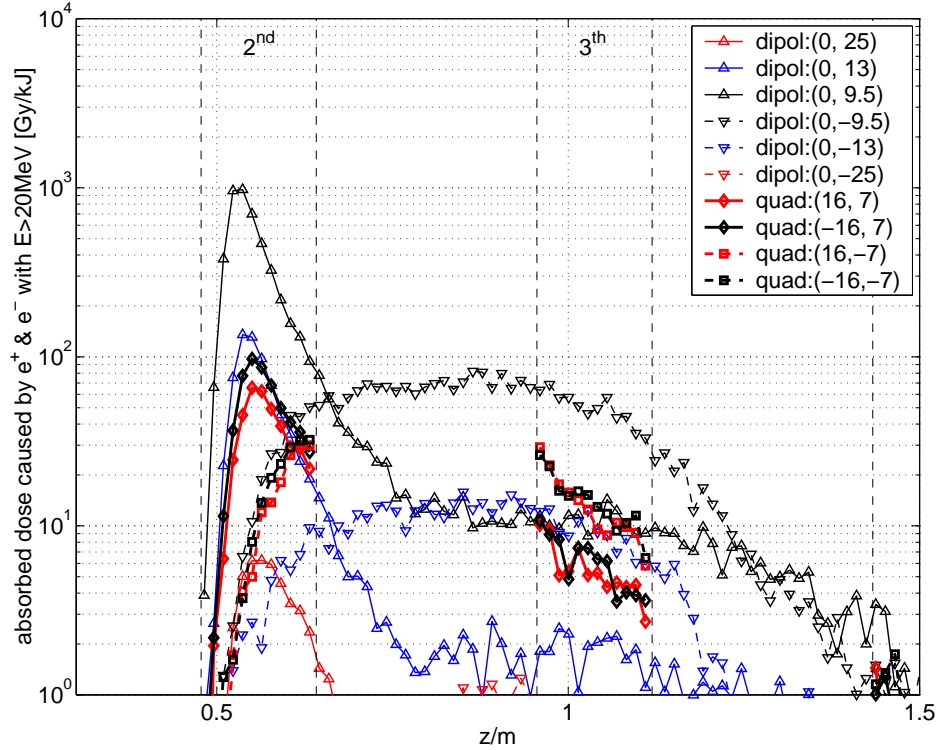


Figure 3.30: Absorbed dose in permanent magnets caused by charged particles with energy above 20 MeV for a vertical incidence.

Point-like losses in horizontal direction

To compare the losses of electrons incident in vertical direction to the ones incident in horizontal direction, the primary energy is chosen 190 MeV and the angle $x' = 7\text{ mrad}$. The electrons intercept the vacuum chamber at the entrance of a horizontally focusing quadrupole (3^{rd}) with $x = 4.75\text{ mm}$ offset. The electromagnetic shower of 20 initial elec-

	dipoles at y ($x = 0$)			quadrupoles at x ($y = 7$ mm)	
	-9.5 mm	9.5 mm	13 mm	-16 mm	16 mm
peak value	82 Gy	975 Gy	135 Gy	97 Gy	66 Gy
FWHH	48 cm	4 cm	5.5 cm	5.5 cm	5.5 cm

Table 3.7: Peak absorbed dose caused by charged particles with $E > 20$ MeV for vertical incidence. The full width half height (FWHH) in z -direction for the dose distribution is given in the third row.

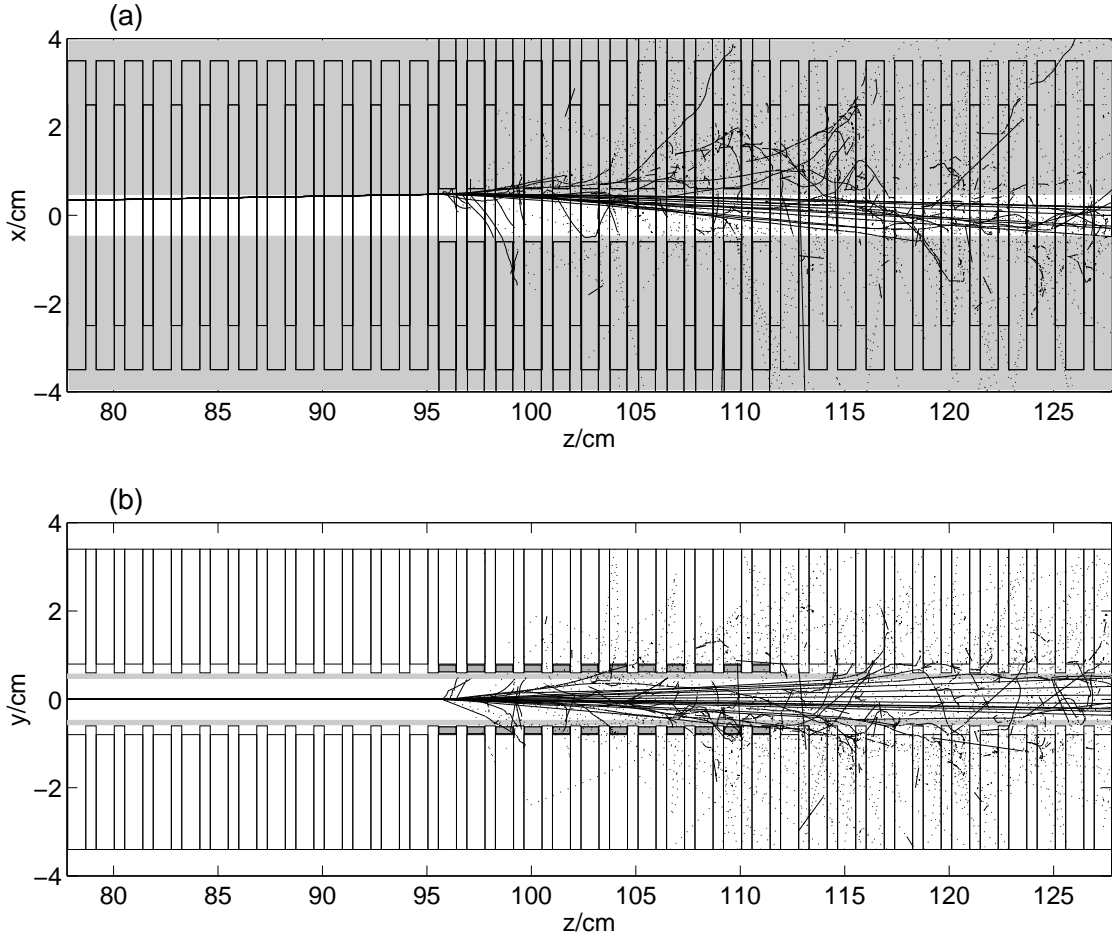


Figure 3.31: Electromagnetic shower produced by 20 electrons with an horizontal angle of 7 mrad and an energy of 190 MeV. (a) shows the trajectories in the horizontal plane (x, z) and (b) in the vertical plane (y, z).

trons is shown in Fig. 3.31(a) (horizontal plane) and Fig. 3.31(b) (vertical plane). Most of the secondary particles are back-scattered into the vacuum tube or stay within the vacuum chamber of the undulator. The electromagnetic shower reaches the permanent magnets about 12 to 15 cm downstream of the position where the electrons hit the wall ($z = 96$ cm). The shower penetrates deeply into the aluminum chamber.

The absorbed dose in the permanent magnets for 1 kJ primary electron energy is shown in Fig. 3.32. The largest dose of 523 Gy occur in the quadrupole magnets ($x = 16$ mm) near the exit of the 3rd quadrupole. The maximum dose in the quadrupole magnets reduces at $x = 30$ mm to 64 Gy and amounts to 120 Gy in opposite direction at $x = -16$ mm.

The energy deposition in the upper ($y > 0$) and the lower ($y < 0$) part of the undulator is equal. The absorbed energy in the dipole decreases exponentially behind the 3^{rd} quadrupole. The peak dose at $y = \pm 9.5$ mm and $x = 0$ are 406 Gy and 372 Gy. The dose in the volumes filled with dosimeter materials are 660 Gy at $z = 130$ cm and 160 Gy at $z = 161$ cm. The simulation show that dosimeters placed behind 3^{rd} quadrupole should reflect accurately dose deposited in the quadrupole permanent magnets. The dosimeter

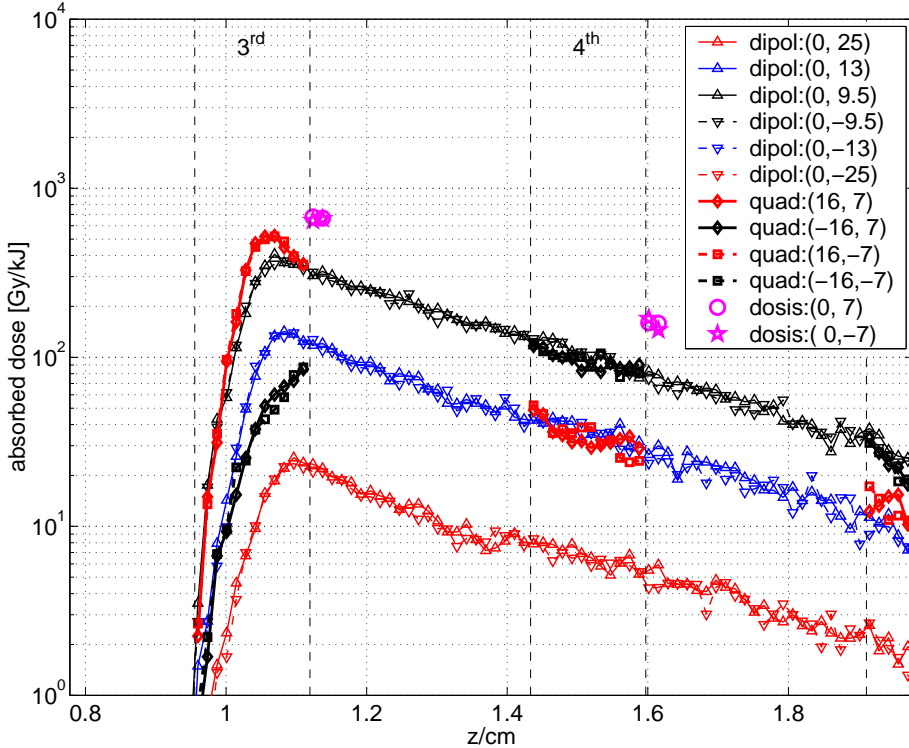


Figure 3.32: Absorbed dose in permanent magnets for an incidence in horizontal direction.

behind the 4^{th} quadrupole overestimates the dose absorbed in the dipole at $z = 16$ cm by a factor of 2.

The energy deposition in the undulator is summarized in Table 3.8. The energy of the particles exiting the undulator at $x > 110$ mm is 12% larger than at $x < -110$ mm. The difference between an incident in x or y direction is 15%. Thus, the usage of a scintillator at one side of the undulator is sufficient for an accurate detection of beam losses. The influence of the signal level on the transverse direction for point-like losses is found in the simulation to be less than 15%.

energy deposition [%]							
dipoles			quads.	chamber	poles	outside boundary	
sum	$x > 0$	in 0.1 m	sum	sum	sum	$ y > 34$ mm	$x > 110$ mm
23.2	12.0	5.1	3.3	43.3	20.0	6.9	5.7
							0.65

Table 3.8: Energy deposition for horizontal electron incidence in the undulator.

The extension of the electromagnetic shower in transverse direction is shown in Fig. 3.33 by the charged particle current crossing the $x - y$ planes at different position Δz . In

the simulation $5 \cdot 10^5$ electrons hit the undulator vacuum chamber. The shower penetrates horizontally about 12 mm into the chamber and the shower maximum is reached at a depth of 9 cm behind the location of incidence (see Fig 3.33(a)). The fraction of charged particle current at a given position Δz in the range $|x| < 4.75$ mm increases from 62% at $\Delta z = 2.73$ cm to 79% at $\Delta z = 20.5$ cm. In vertical direction, the shower develops mainly in the region between the poles of the undulator (see Fig 3.33(b)). For $\Delta z > 11$ cm the fraction of the charge radiating the dipoles approaches to 6% and the charge which is located in the range $|y| < 4.75$ mm decreases from 99% at $\Delta z = 2.73$ cm to 82% at $\Delta z = 20.5$ cm. Hence, in case of a horizontal incidence, the shower first develops into the vacuum chamber in x -direction, but leaves soon the chamber and deposits slowly its energy in the region between the dipoles and close to vacuum tube.

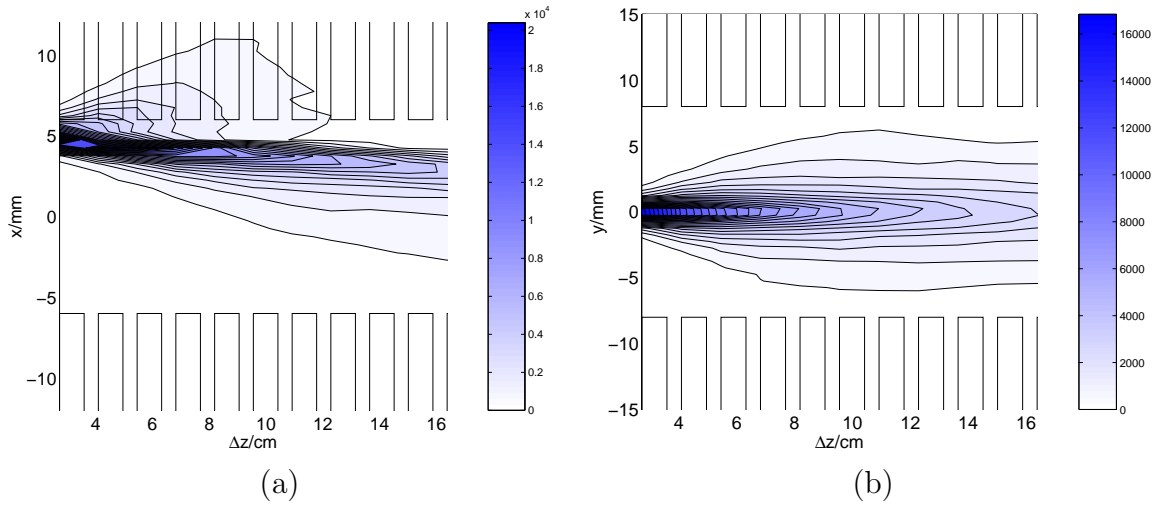


Figure 3.33: Development of the electromagnetic shower as a function of the distance Δz from the location of intercept. In the simulation 50000 electrons hit the vacuum chamber. (a) projected charged particle current in the horizontal plane (dipoles are shown) and (b) projected charged particle current in the vertical plane (quadrupoles are shown).

The energy spectrum of the electrons and positrons exposing the dipoles for $\Delta z = 3\lambda_U, \dots, 7\lambda_U$ is plotted in Fig. 3.34. The spectrum decreases exponentially. Charged particles which irradiate the dipoles with an energy above 100 MeV are nearly absent. The variation of the energy spectrum with the longitudinal position δz is small.

The mean energy versus the number of charges for different vertical ranges in the dipole magnets is shown in Fig. 3.34(b). After four undulator periods the number of charged particles reach a maximum which is 10 times smaller than in the case of vertical electron incidence. The mean energies of the secondary electrons and positron striking the dipole is below 30 MeV.

The dose deposited by secondary particles with energy above 20 MeV, shown in Fig. 3.35, reflects that the development of shower dominantly takes place in the aluminum chamber and the pole region. The fraction of the absorbed dose is less than one third for the quadrupole magnets and less than one fourth for the dipole magnets. The volume elements of the quadrupole magnets with center $x = 16$ mm are exposed to the highest radiation level with a peak dose of 160 Gy. The reduced doses are summarized in Tab. 3.9.

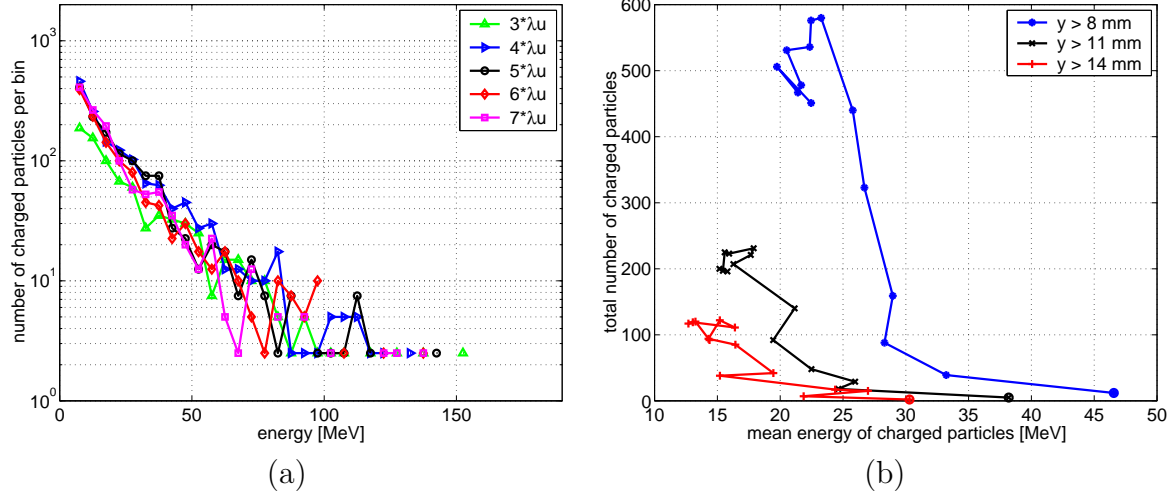


Figure 3.34: (a) energy spectrum of charged particles at different longitudinal positions (b) total number of charged particles versus mean energy for λ_U (circle), $1.5\cdot\lambda_U,\dots,7.5\cdot\lambda_U$. The three curves show the electrons and positrons exposing the dipole magnets with vertical coordinate $y > 8$ mm, $y > 11$ mm, and $y > 14$ mm.

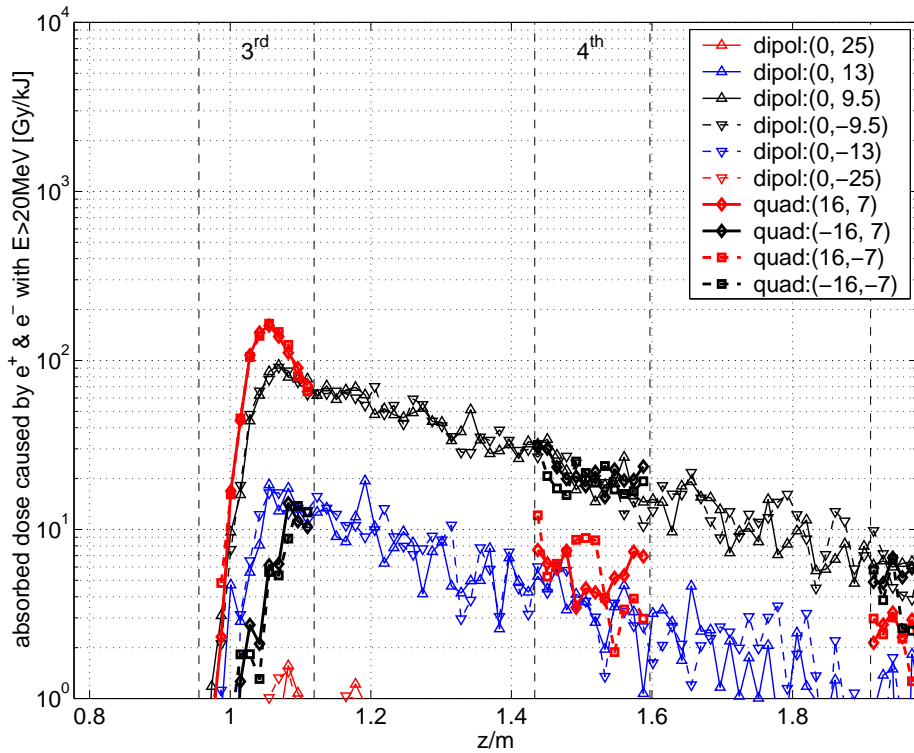


Figure 3.35: Fraction of the absorbed dose in permanent magnets caused by charged particles with energy above 20 MeV for a horizontal incidence. The dose rates are calculated for 1 kJ incident electron energy.

Summary of point-like losses in vertical and horizontal direction

The energy deposited in the undulator magnets (dipoles and quadrupoles) is 29.6% of the incoming primary electron energy for a vertical incidence and 26.5% for a horizontal incidence. The distribution of the energy deposition is more localized for a vertical beam

	dipoles at y ($x = 0$)			quadrupoles at x ($y = 7$ mm)	
	-9.5 mm	9.5 mm	13 mm	-16 mm	16 mm
peak value	91 Gy	93 Gy	13 Gy	30 Gy	160 Gy
FWHH	26 cm	30 cm	19 cm	-	5.5 cm

Table 3.9: Peak absorbed dose caused by charged particles with $E > 20$ MeV for horizontal incidence.

incidence. This causes 6 times higher peak dose rates in the magnets (2.9 kGy compared to 0.52 kGy). For a horizontal incidence the high-energy part of the electromagnetic shower develops dominantly in the vacuum pipe or the pole region but only weakly exposes the permanent magnets of the undulator. The maximum dose caused by charged particles with $E > 20$ MeV amounts to 160 Gy for horizontal incidence and to 975 Gy for vertical incidence. The electromagnetic shower penetrates horizontally and vertically about 5 mm deep into the magnets and the high-energy part of the shower less than 3 mm.

The variation of the secondary particles detectable by the beam loss system with the direction of incidence is less than 15%.

The peak absorbed dose in the magnets is underestimated by a factor 5 for a vertical beam incidence and overestimated by 20% for a horizontal incidence. An accurate measurement requires the installation of at least one dosimeter behind each undulator quadrupole.

3.3.3 Doses in permanent magnets for loss distributions

For a loss distribution the peak absorbed doses in the magnets will be smaller while the irradiated magnet volumes are larger. The cases of beam losses occurring dominantly in vertical and occurring dominantly in horizontal direction are investigated. The loss distribution calculated by tracking simulations for large energy deviations (vertical losses) and for 0.5 mm rms-horizontal quadrupole displacements (horizontal losses) are used.

Absorbed doses for losses caused by large energy deviations

The loss probability for electrons with large energy deviations is discussed in Sec. 3.2.3. The gradients of the collimator quadrupole match the beam properly for 230 MeV. The energy spread of the initial distribution is 10%. The energy bandwidth of the collimator is -10.5% and $+7.5\%$. The transmission probability T_{col} of the initial distribution through the collimator is 50%. The loss probability L_{und} of the collimated beam in the undulator is 1.3%. From the lost electrons 93% have an energy below 215 MeV.

For the Monte Carlo simulation $5 \cdot 10^4$ primary particles are used. The absorbed dose in the dipoles, the quadrupoles and the volume elements filled with dosimeter material in the first module for 1 kJ energy of the primary electrons is plotted in Fig. 3.36. The energy per unit length incidence on the vacuum chamber, plotted by the solid curve, shows the origin of the electromagnetic shower causing the doses in the magnets. At the 2nd, 6th, 8th, and 10th quadrupole losses occur. The peaks in the absorbed doses are shifted by about 10 cm with respect to the peaks of the loss distribution. The electromagnetic showers initiated at the different loss locations overlap only weakly. The absorbed dose in the magnets after one undulator FODO-cell is reduced to a few percent of the upstream peak values.

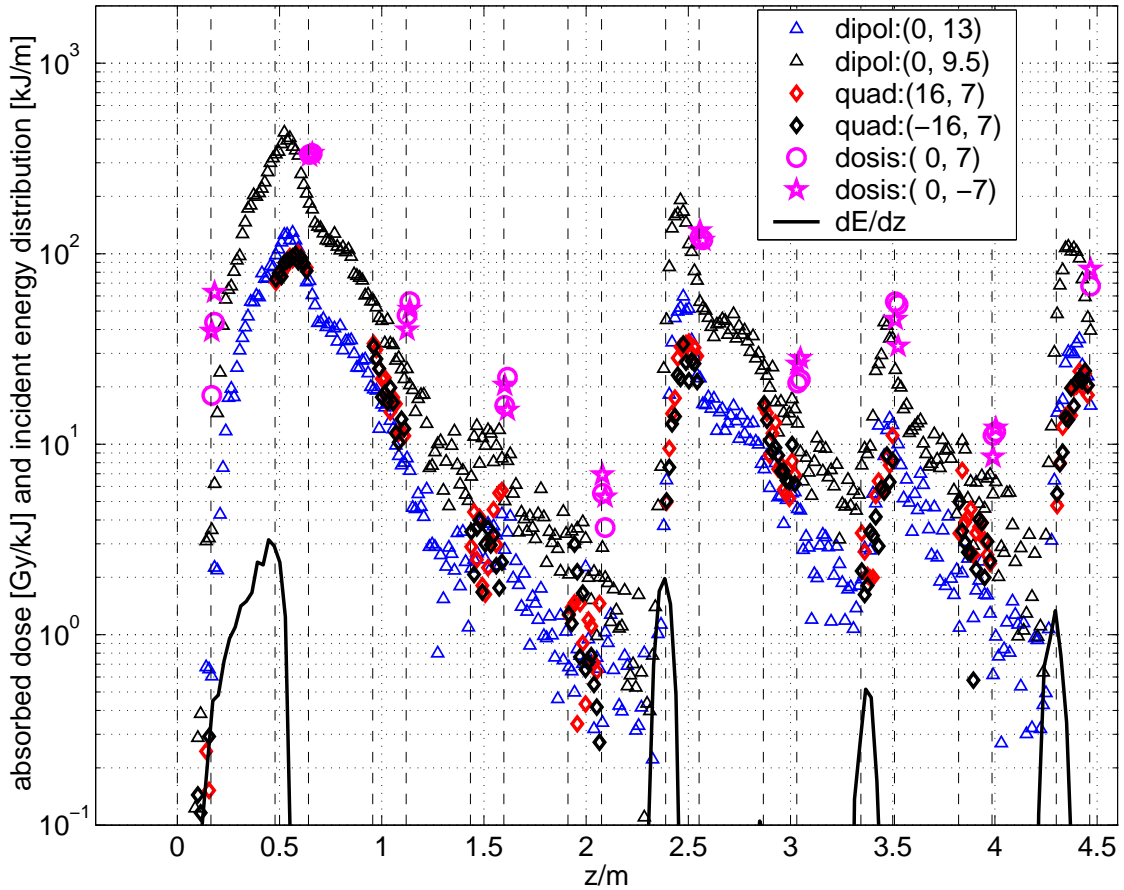


Figure 3.36: Absorbed dose in the permanent magnets in the first undulator module for a loss distribution caused by energy deviation. Volume elements with center (x, y) in a dipole magnet are plotted by triangles, in quadrupole magnets by diamonds and for volume element that are filled with dosimeter material circles and pentagrams are used. The energy per unit length carried by the primary electrons incidence on the vacuum chamber is also shown (solid curve). The entrance and the exit of quadrupoles are indicated by dashed vertical lines.

The energy of the electrons incident at the 6th quadrupole amount to 174 J. The losses appear within a distance of 15 cm. The peak dose in the dipoles is 190 Gy. If the result of the peak doses for point-like losses in vertical direction (2.9 kGy upper dipole and 0.8 kGy lower dipole at 1 kJ) is scaled to 174 J one yields 320 Gy which overestimates the doses by 70%.

The largest energy deposition appears at the center of the 2nd quadrupole with doses in the dipoles of 400 Gy at $y = 10$ mm, and 130 Gy at $y = 13$ mm and in the quadrupoles the dose reaches 100 Gy. The calculated doses at the position where dosimeters are installed behind the 1st and 3rd quadrupole amounts to 40 to 50 Gy and would underestimate the peak dose by one order of magnitude.

The energy deposition for the distribution is summarized in Table 3.10. 10% of the incident energy is deposited in the permanent dipole magnets within a undulator length of 0.4 m.

energy deposition [%]				
dipoles	quads.	chamber	poles	$x > 110 \text{ mm}$
25.1	2.4	33.9	23.3	0.54

Table 3.10: Energy deposition for loss distribution causes by energy deviations.

Absorbed doses for losses caused by horizontal quadrupole displacements

The dose absorbed in the permanent magnets for beam losses caused by rms-quadrupole displacements of 0.5 mm in horizontal directions is plotted in Fig. 3.37. The loss probability L_{und} in the first undulator module is 5.63% and in the first diagnostic station about 5.61% of the beam passing the collimator section is dumped. The beam energy is 230 MeV and the energy spread amounts to 1%.

The largest dose of 210 Gy for the dipole magnets is calculated at the exit of 1st quadrupole. The peak doses are 15 cm downstream of the peaks for the energy deposition by the primary electrons hitting the chamber. The dose in the volumes of the dipoles at $x = 10 \text{ mm}$ is larger than ones for the quadrupoles which is different from the calculation for point-like losses with horizontal incidence. The dosimeters along the undulator module overestimate the losses by a factor 2. The shower for large horizontal quadrupole displacements is initiated already in the first diagnostic station. The photomultiplier connected to the scintillator at this station can easily detect such losses. The energy deposition in the different elements of the undulator are listed in Table 3.11. 10% of the total energy is deposited in the dipole magnets within an undulator length of 45 cm.

energy deposition [%]				
dipoles	quads.	chamber	poles	$x > 110 \text{ mm}$
20.7	2.9	34.2	17.3	0.70

Table 3.11: Energy deposition for loss distribution causes by rms-energy quadrupole displacements of 0.5 mm in horizontal direction.

3.3.4 Absorbed dose in magnets caused by dark current

The loss distribution of the dark current has been calculated in Sec. 2.4.9 for two optics. For the second considered optics (case 2), the electron distribution of the dark current causes ten times larger losses in the undulator than for the first optics. The obtained loss distribution for case 2 is used to estimate the absorbed dose in the permanent magnets.

The energy dumped in the first undulator module is 121 J per mC charge emitted from the gun cathode. The electrons can hit the vacuum chamber because of chromatic aberration in the collimator quadrupoles. The absorbed dose in the different volumes of the dipole and quadrupole magnets normalized to 1 kJ total dumped energy is shown in Fig. 3.38. The largest dose of 505 Gy occur in the dipole magnets at the entrance of the 2nd quadrupole. The dose in dipole volumes decreases to 153 Gy and 21 Gy (not drawn) at $y = \pm 13 \text{ mm}$ and $y = \pm 25 \text{ mm}$ for $x = 0$. In horizontal direction for $y = -10 \text{ mm}$ and $x = \pm 16$ the maximum dose is 74 Gy and amount to 16 Gy at $x = \pm 30 \text{ mm}$.

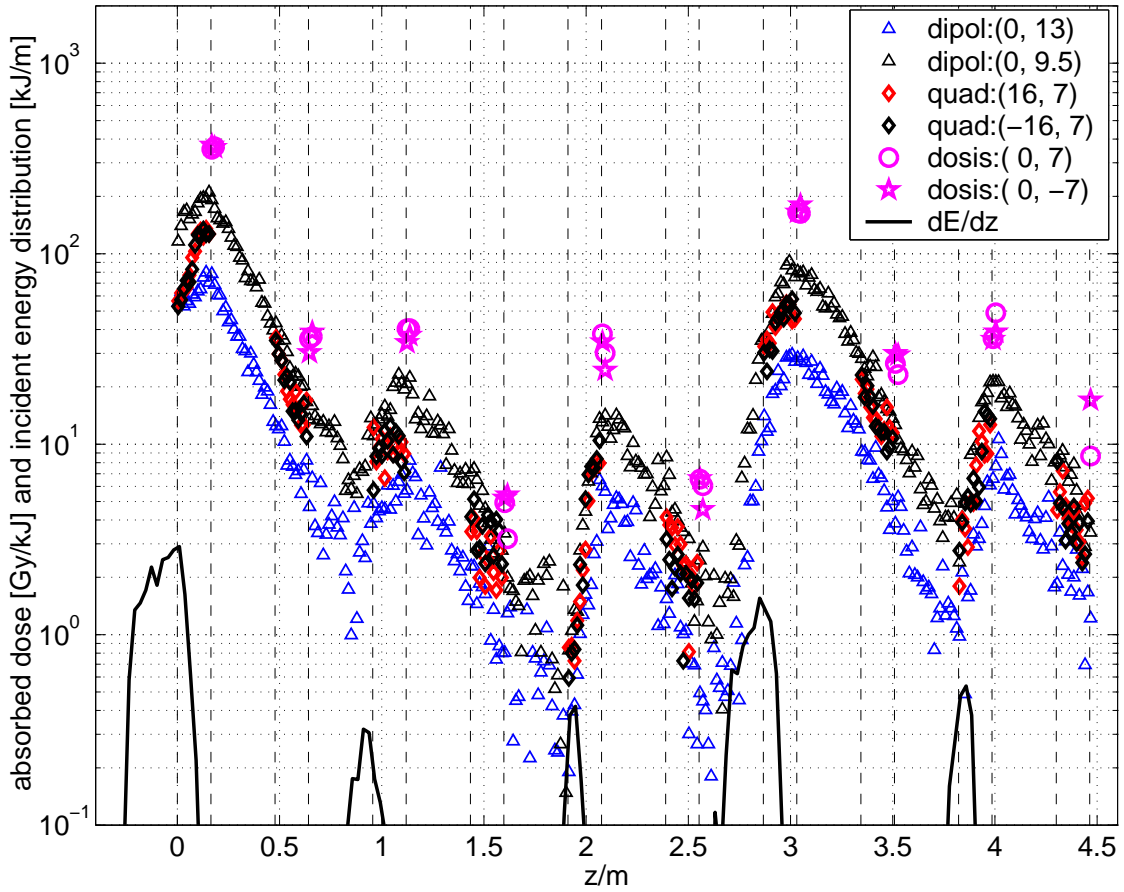


Figure 3.37: Absorbed dose in permanent magnets in the first undulator module for a loss distribution caused by horizontal quadrupole displacements.

The peak doses in the dipole magnets at the 6th, 8th, and 10th quadrupole (vertical focusing) are 5 times smaller than at the 2nd quadrupole. The dose absorbed in the thin magnet plates for the quadrupole are comparable to the ones determined for the dipole magnets at $y = \pm 13$ mm and $x = 0$. The absorbed doses in the volumes behind the vertical quadrupoles filled with dosimeter materials underestimate the peak doses by a factor 2 and behind the horizontal focusing quadrupoles the peak doses are underestimated by about a factor 15. Behind the first quadrupole the absorbed dose in the dosimeter material are 200 Gy and 310 Gy for $y = +7$ mm, but only 115 Gy for $y = -7$ mm. The difference is caused by the small number of the incident electrons (about 24 electrons which are tracked 100 times) with a positive vertical offset when they hit the chamber wall in the first quadrupole. These electrons are dumped close to the exit of the quadrupole and cause large energy depositions in the dosimeter material. An asymmetric distribution, here due to statistics, is present if dipole correctors in the linac are used which is always the case. The mean value (185 Gy) of the four volumes (TLD and RPL, up and down) is 2.7 times smaller than the peak value in the dipole magnets.

In one week, typically 50 mC dark current is emitted from the gun ($I_{Faraday} = 100 \mu\text{A}$, 120 hours operation). In case 2, 6.05 kJ energy is dumped by dark current in the first undulator module. The largest dose in the magnets yields 3 kGy while about 1.1 kGy is simulated for the dosimeters behind the 1st quadrupole. Dose rates larger than 1 kGy in

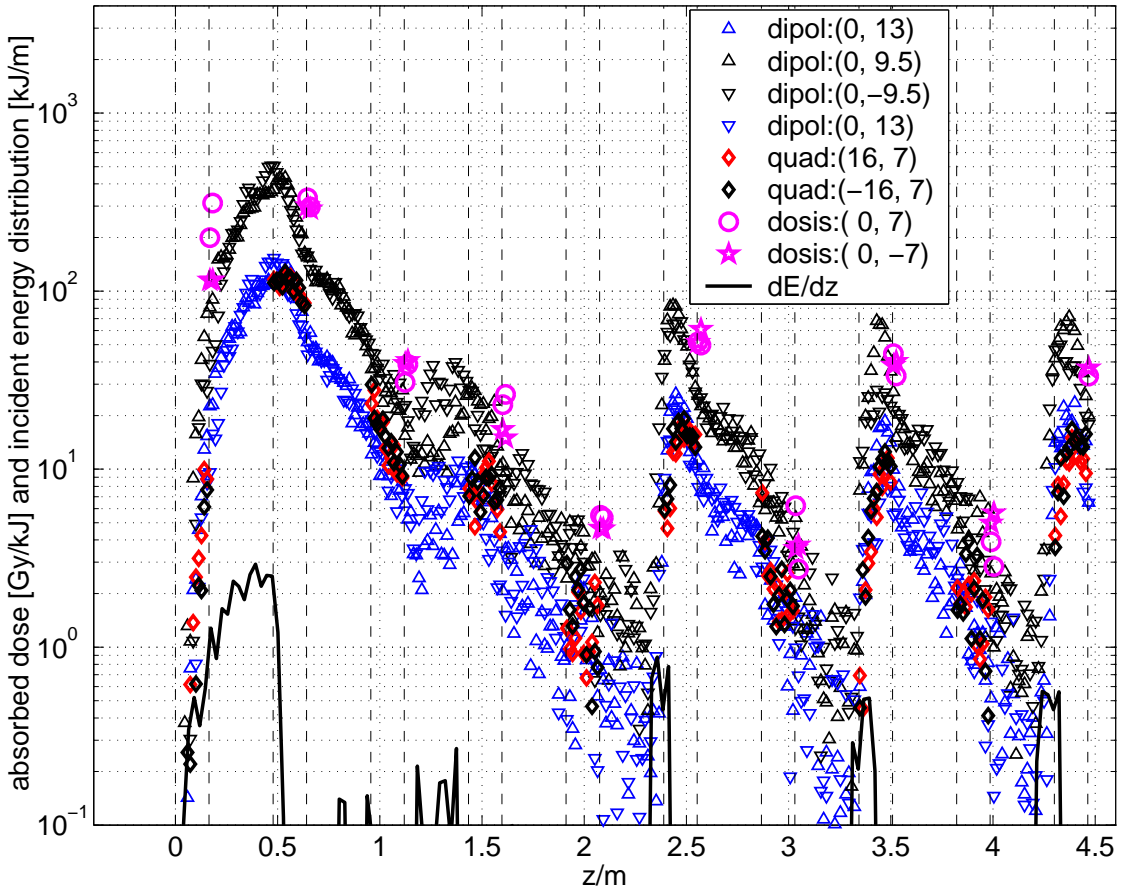


Figure 3.38: Absorbed dose in the permanent magnets in the first undulator module for dark current losses. Volume elements with center (x, y) in a dipole magnet are plotted by triangles, in quadrupole magnets by diamonds and for volume elements filled with dosimeter material circles and pentagrams are used. The energy per unit length carried by the electrons incidence on the vacuum chamber is shown by the solid curve. The entrance and the exit of quadrupoles are indicated by dashed vertical lines.

the magnets occur from $z = 0.25$ m to $z = 0.65$ m. The dose per week in the quadrupole magnets reaches 770 Gy and reaches 900 Gy in the dipoles at $y = +13$ mm.

For the optics considered in case 1, the doses per week are approximately ten times smaller.

The numerical results from the Monte Carlo simulation confirm the first dose estimation (1.6 kGy) in the magnets performed by simple geometrical considerations in Sec. 2.4.9. The energy deposition in the different elements of the undulator are listed in Table 3.12. 10% of the total energy is deposited in the dipole magnets within an undulator length of 23 cm.

energy deposition [%]				
dipoles	quads.	chamber	poles	$x > 110$ mm
26.0	2.3	35.0	24.0	0.55

Table 3.12: Energy deposition in the first undulator module by dark current.

3.4 Propagation of secondary particles from the spoilers

In this section, the propagation of the secondary particles produced at the spoilers is investigated. The energy deposited in the components of the collimator section and transmitted to the undulator is derived. It is shown that the largest fraction of the transmitted secondary particles is dumped in the undulator. The absorbed doses in the magnets are estimated in Sec. 3.4.3.

3.4.1 Clearances of the collimated beam to the absorbers

To achieve a high removal efficiency for secondary particles the absorbers are placed as close as tolerable to the collimated beam. Absorber 1 has been installed to reduce the background perturbing the diagnostic components in the collimator. The distance to the beam amounts to 1.5 mm and is chosen larger than the distance to the beam of the other absorbers.

The geometry of absorber 2 and absorber 3 determines the removal efficiency for secondary particles of the collimator. For an energy of 230 MeV, the collimated beam and the apertures behind spoiler 2 are shown in Fig. 3.39. In the horizontal plane, the size of

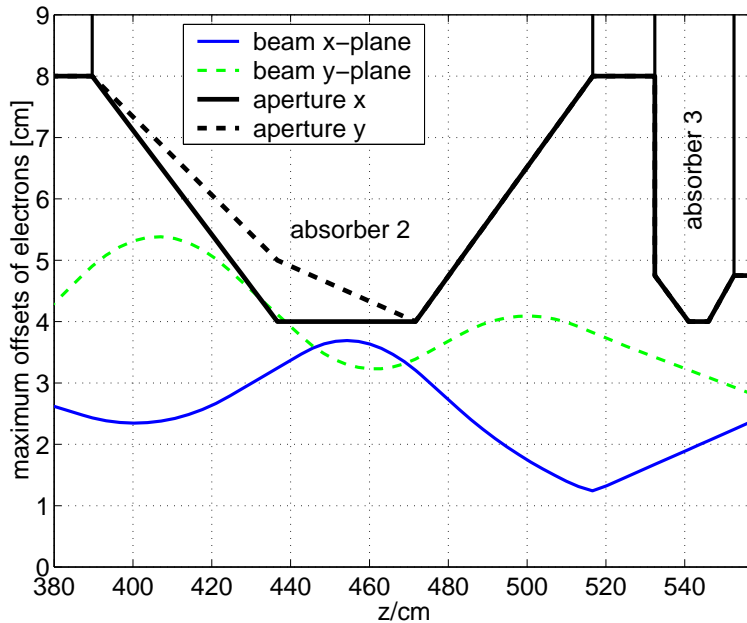


Figure 3.39: Clearance of collimated beam to absorber 2 and absorber 3 at an energy of 230 MeV. The x-plane is shown by solid lines, the y-plane with dashed lines.

the collimated beam varies between 1.2 mm and 3.7 mm. Only absorber 2, with a clearance of 300 μ m contributes in the x direction to the removal of secondary particles, while the distance of about 2 mm to absorber 3 is too large to stop degraded electrons, i.e. from the edge of the spoilers.

In the vertical plane, the beam size varies between 2.8 mm and 5.5 mm. Absorber 2 follows the envelope of the beam with a minimum distance of 0.6 mm. The clearance in

y-direction to absorber 3 is 0.8 mm. Because of the different beam sizes in x and y direction, absorber 2 has an elliptic shape.

The envelope of the collimated beam varies with the energy. The apertures of the absorbers 2 and 3 have been chosen such that at least a clearance of $200\text{ }\mu\text{m}$ to the beam is obtained for beam energies between 200 MeV and 500 MeV.

3.4.2 Energy deposition in the collimator section

The geometry of the collimator section used for Monte Carlo calculation with EGS4 [73] is shown in Fig. 3.40. The electromagnetic shower is calculated in transverse direction up to a radius of 10 cm. The tapers of the collimators are taken into account. The elliptical taper geometry of absorber 2 is approximated by a cylindrical one with transition from $r = 8\text{ mm}$ to 4.75 mm , to 4 mm and to 8 mm . This slightly overestimates the efficiency of the absorber 2 for particles scattered in vertical direction, but underestimates the removal efficiency for particles scattered in horizontal direction. The vacuum beam pipes are made of iron with a thickness of 1.5 mm. To estimate the photon leakage from the collimators, the lead shields at spoiler 1, absorber 1 and absorber 3 are taken into account.

The cutoff energy for photons is 0.1 MeV, and 1.5 MeV for electrons and positrons.

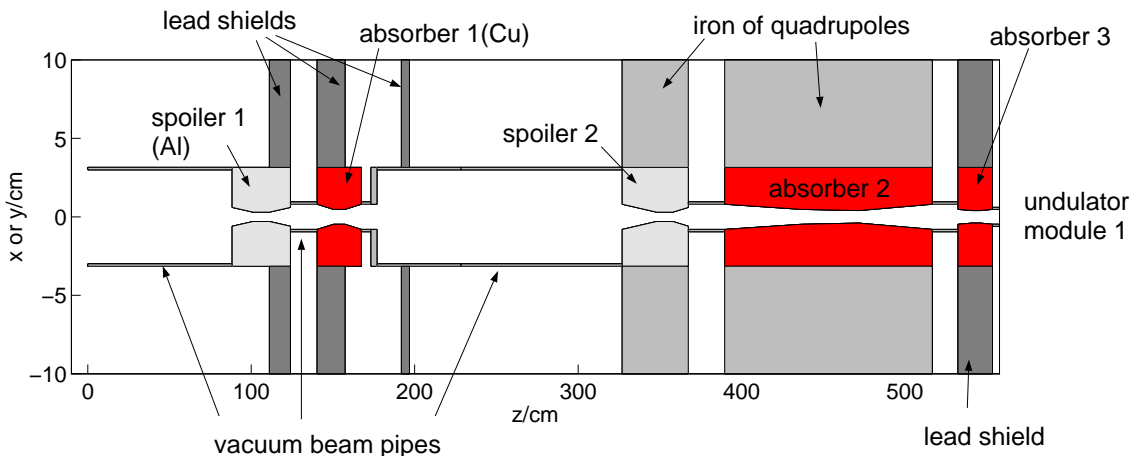


Figure 3.40: Geometry of the collimator used in EGS4.

The removal efficiency for secondary particles is studied for electrons incident on the spoilers with an energy of 230 MeV. Secondary particles can be produced either at the first or at the second spoiler. The amount of secondary particles reaching the undulator is different for the two cases.

An electromagnetic shower initiated by 100 electrons incident on the spoiler 1 is sketched in Fig. 3.41. Because of absorber 1, the dominant yield of secondary particles is dumped within a distance of 50 cm behind the first spoiler. Only a few particles hit the downstream beam pipe equipped with diagnostic components (screen, BPM, BPM electrons, etc.). The photon leakage from spoiler 1 and absorber 1 is stopped by the first of two concrete blocks, see Fig. 1.20.

Some secondary particles escape absorber 1. Most of these particles are removed by the second spoiler. But, as shown in this example, 2 photons and 1 electron reach the undulator. The most secondary particles which are lost in the undulator are low energy photons scattered with small angles in the forward direction. They cannot be removed

by the absorber system. In this example, the photons have an energy of 13 MeV and 17 MeV. Also degraded electrons scattered in the forward direction from the edge of the spoiler reach the undulator. If the energy of these electrons is below the bandwidth of the collimator they can hit the undulator. In this example, the electron energy is 214 MeV ($\delta E/E = -7\%$) within the collimator bandwidth (see Sec. 3.2.1) and therefore passes

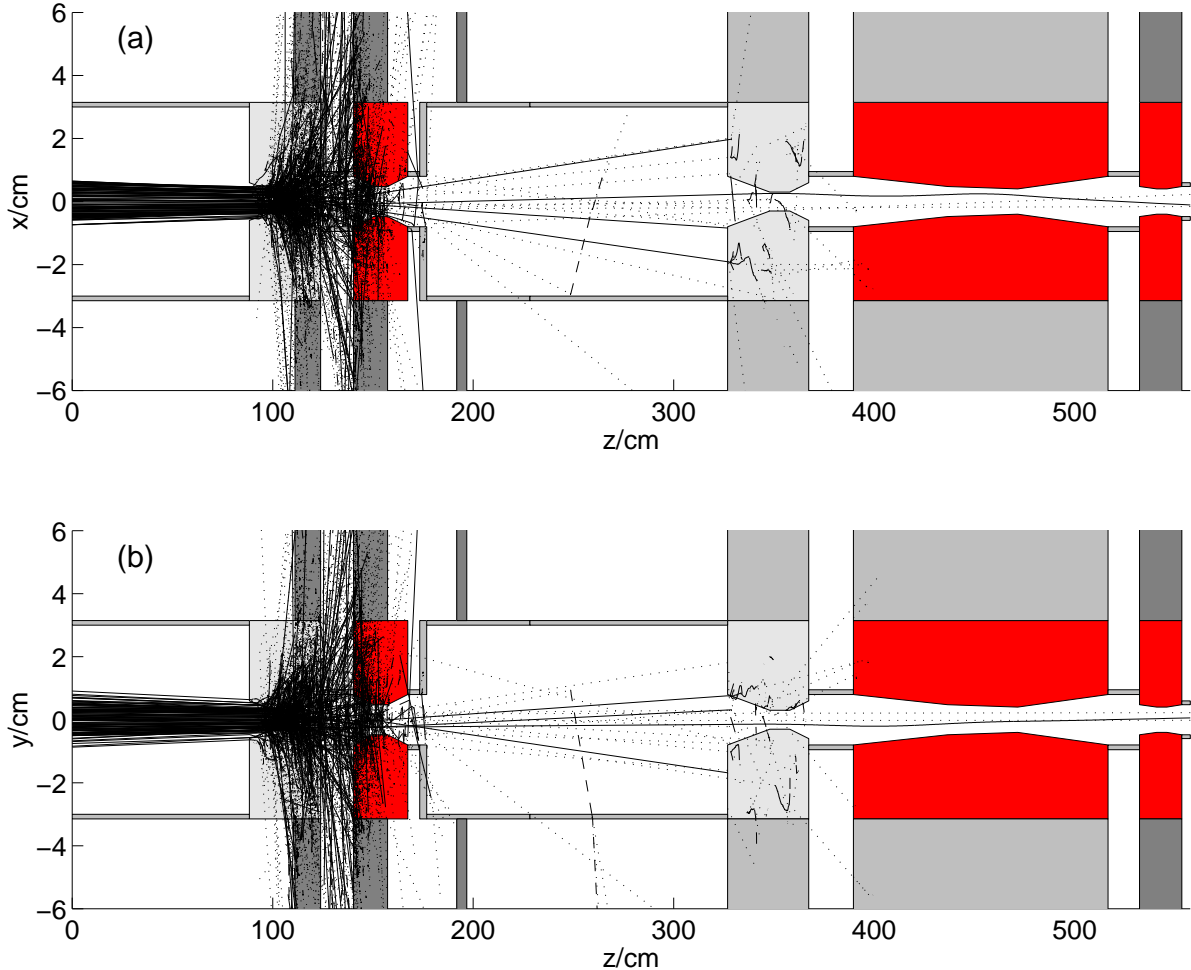


Figure 3.41: Electromagnetic shower initiated at spoiler 1 ($E_0 = 230$ MeV). (a) shows the trajectory of the particles in the horizontal plane and (b) in the vertical plane. Photons are plotted by dots (photons above 1 MeV only), electrons by solid lines and positrons by dashed lines.

through the undulator.

The electromagnetic shower initiated by 100 electrons incident on the second spoiler is shown in Fig. 3.42. The central part of the shower is confined to a longitudinal distance of about 50 cm to 70 cm behind spoiler 2. Unlike to edge-scattered electrons from the first spoiler, degraded electrons from the edge of the second spoiler, which escape the absorbers 2 and 3, can be lost in the undulator, even through their energy is within the energy bandwidth of the collimator. In the example shown in Fig. 3.42, the passing electron has lost 0.5% of its energy, but is dumped in the first quadrupole of the undulator (not drawn).

The difference between edge-scattered electrons from the first or the second spoiler is caused by the functionality of the spoilers which is to define the collimator phase space

acceptance. An electron which is scattered at the edge of spoiler 1 has a transverse offset within the radius of spoiler 1. If the angle is large, the electron hit the second spoiler and is removed from the beamline. In other words, edge-scattered electrons from spoiler 1 which transmit spoiler 2 are in the collimator phase space acceptance and transmit the undulator if their energies are within the collimator energy bandwidth. For edge-scattered electrons from the second spoiler, the absorber system limits the scattering angles of the transmitted electrons. The phase space acceptance of the aperture system consistent of spoiler 2, absorber 2 and absorber 3, however, is larger than the undulator acceptance. Thus, electrons from the second spoiler can be lost in the undulator.

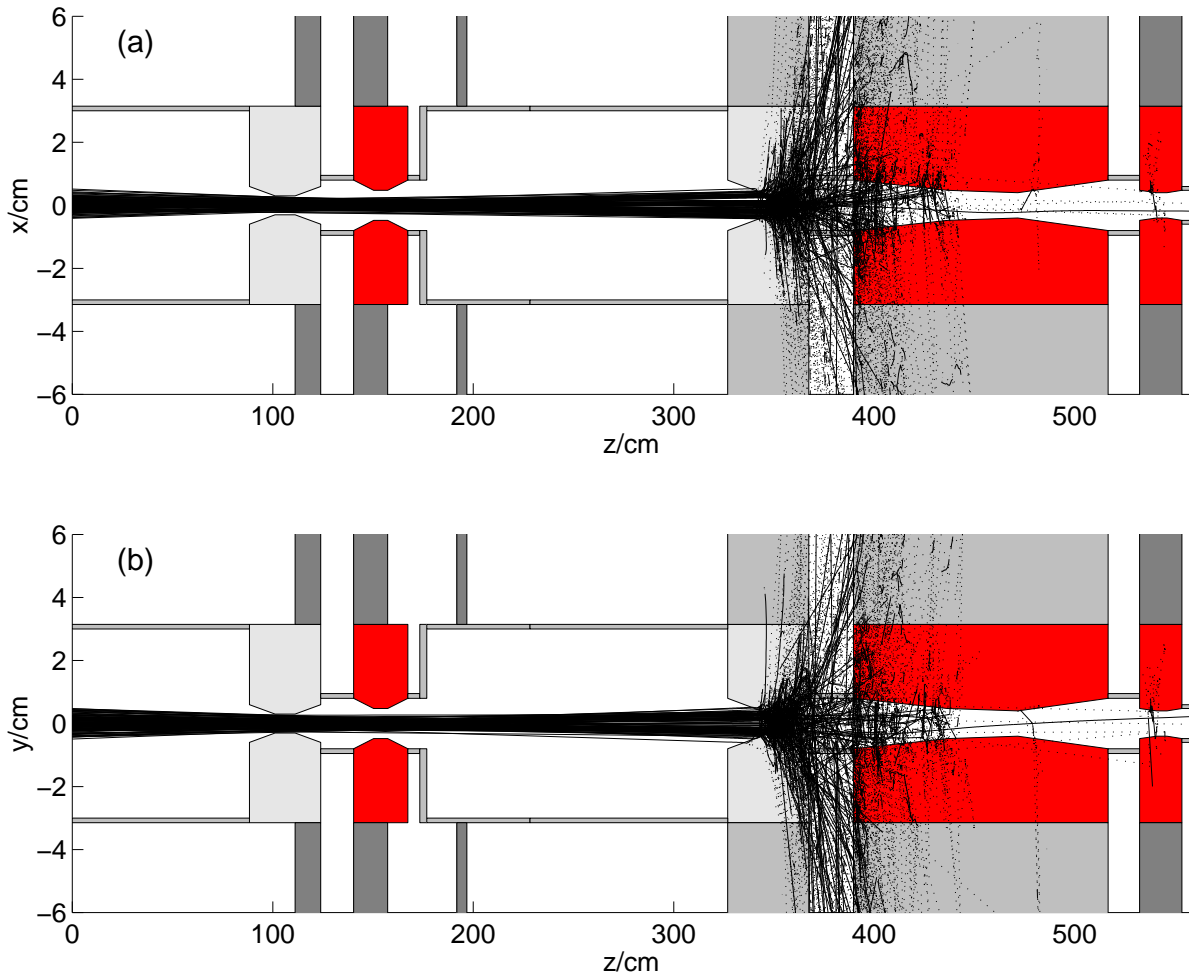


Figure 3.42: Electromagnetic shower initiated at spoiler 2 ($E_0 = 230$ MeV). (a) horizontal plane and (b) in the vertical plane.

The removal probability L_{col} through the collimator section depends on the emittance ϵ of the initial charge distribution (see Sec. 3.2). Also, the ratio between electrons hitting the first and the second spoiler is a function of ϵ . For $L_{col} = 50\%$ ($\epsilon = 1.41 \mu\text{m}$), 28.8% of the electrons are removed at the first spoiler and 21.2% at the second spoiler. To compute the energy deposition in the components of the collimator section, 10^5 incidental electrons on the spoiler are tracked. The result of the Monte Carlo simulation is summarized in Table 3.13.

The first and second column list the cases where electrons either hit the first or the

second spoiler. In both cases, the largest fraction of energy is dissipated in the spoilers (52% and 43.9%). The remaining energy is deposited mainly in the absorbers and the radiation shields (lead shields or quadrupoles). The energies carried by secondary particles reaching the undulator amount to 0.04% or 0.43% of the incidental energy and differ by an order of magnitude depending whether the secondaries are produced at spoiler 1 or 2. The last column in Table 3.13 lists the result for a particle distribution with $T_{col} = 50\%$. The energy of 1 kJ splits to 576 J incident on the first spoiler and 424 J on the second spoiler. About 2.0 J, 1.32 J carried by electrons and 0.66 J carried by photons, leaves the collimator section in direction to the undulator. The energy of the positrons is less than 0.02 J.

The energy spectra of the electrons and photons are shown in Fig. 3.43. 80% of the

energy deposition and transmission of secondary particles [%]			
	e^- incidence on spoiler 1 $E_{dep,1}$ [%]	e^- incidence on spoiler 2 $E_{dep,2}$ [%]	1 kJ energy incident on the spoilers $57.6\% \cdot E_{dep,1} + 42.2\% \cdot E_{dep,2}$ [J]
spoiler 1	52.5	0.0	302.1
spoiler 2	1.8	43.9	196.3
absorber 1	17.3	0.0	100.0
absorber 2	0.2	22.8	97.6
absorber 3	0.0	0.5	2.2
beam pipes	3.0	4.2	35.0
lead shield	20.5	0.0	118.6
quadrupoles	0.6	16.0	74.4
outside boundary	4.0	12.1	71.8
transmit to undulator	0.04	0.43	2.0
sum	100	100	1000

Table 3.13: Energy deposition in the collimator section. The incident beam energy is 230 MeV. The transmission probability through the collimator is $T_{col} = 50\%$. The loss probability at the first spoiler is $L_{spo1} = 28.8\%$ and $L_{spo1} = 21.2\%$ at the second spoiler.

electrons have an energy above 215 MeV (edge-scattered) while 80% of the photons have an energy below 50 MeV. The photon spectrum decreases above 50 MeV inversely with the photon energy. Hence, the power spectrum of the photons is approximately constant.

3.4.3 Energy deposition of secondary particles in the undulator

The transverse distributions of the secondary particles at entrance of the undulator, between the undulator modules and at the exit of the undulator are shown in Fig. 3.44. Most of the particles are lost in the first undulator module. The number of photons decreases with increasing undulator length, faster than the number of electrons. After the undulator, the electrons carry 94% of the energy and have mean energy is 226 MeV. 79% of the energy passing the collimator is deposited in the first undulator module. Only 5% and 1% is dumped in module 2 and module 3, respectively. 15% is transmitted through

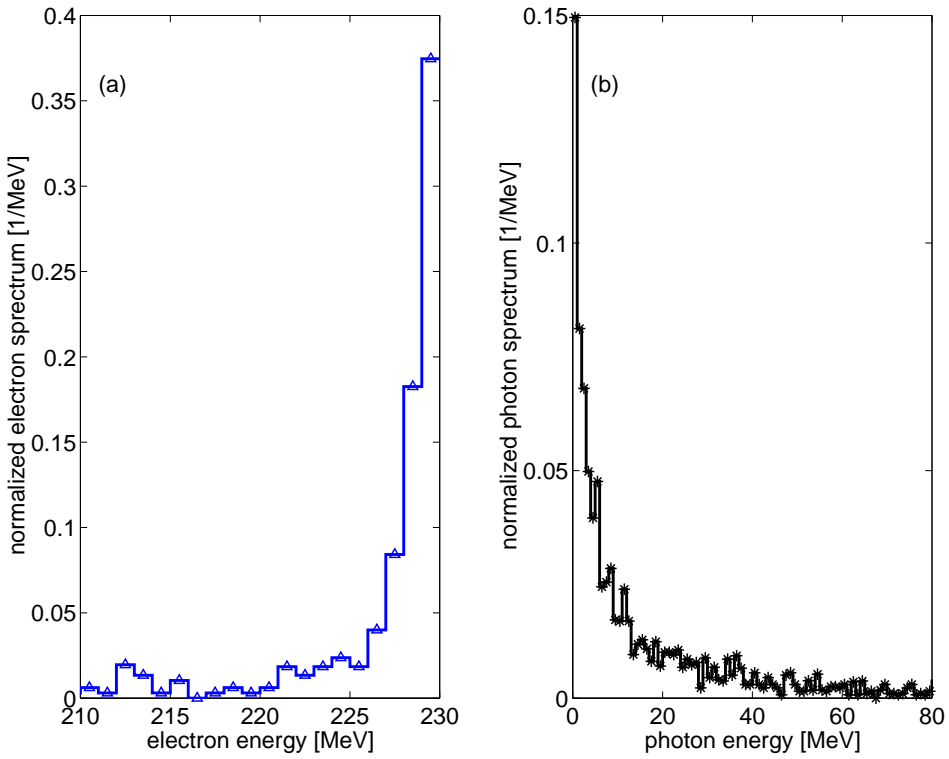


Figure 3.43: Spectrum of secondary particles escaping the absorber system to the undulator. (a) shows the normalized electron spectrum and (b) normalized photon spectrum. The initial electron energy is 230 MeV.

the undulator. The loss probability for secondary particles L_{sec} given by the ratio between the deposited energy in the undulator and the energy of the primary electrons incident on the spoiler amounts to 0.17%. The removal efficiency η_{sec} yields

$$\eta_{sec} = 1 - L_{sec} = 99.83\%. \quad (3.8)$$

94% of the secondary particles lost in the undulator are generated at the second spoiler. The results of the shower calculations are summarized in Table 3.14.

	Energy of the secondary particles [J]				
	deposited at				survive
	UND1	UND2	UND3	sum UND	
generated at spoiler 1	0.09	0.01	0.01	0.11	0.07
generated at spoiler 2	1.49	0.09	0.03	1.61	0.23
sum of both spoilers	1.58	0.10	0.02	1.72	0.30

Table 3.14: Energy deposition of secondary particles in the undulator generated at the collimator. The incidental energy is 1 kJ, 576 J on spoiler 1 and 424 J on spoiler 2. The primary electrons hitting the spoilers have an energy of 230 MeV.

Absorbed dose caused by secondary particles of the collimator

The absorbed dose in the permanent magnets caused by the secondary particles of the

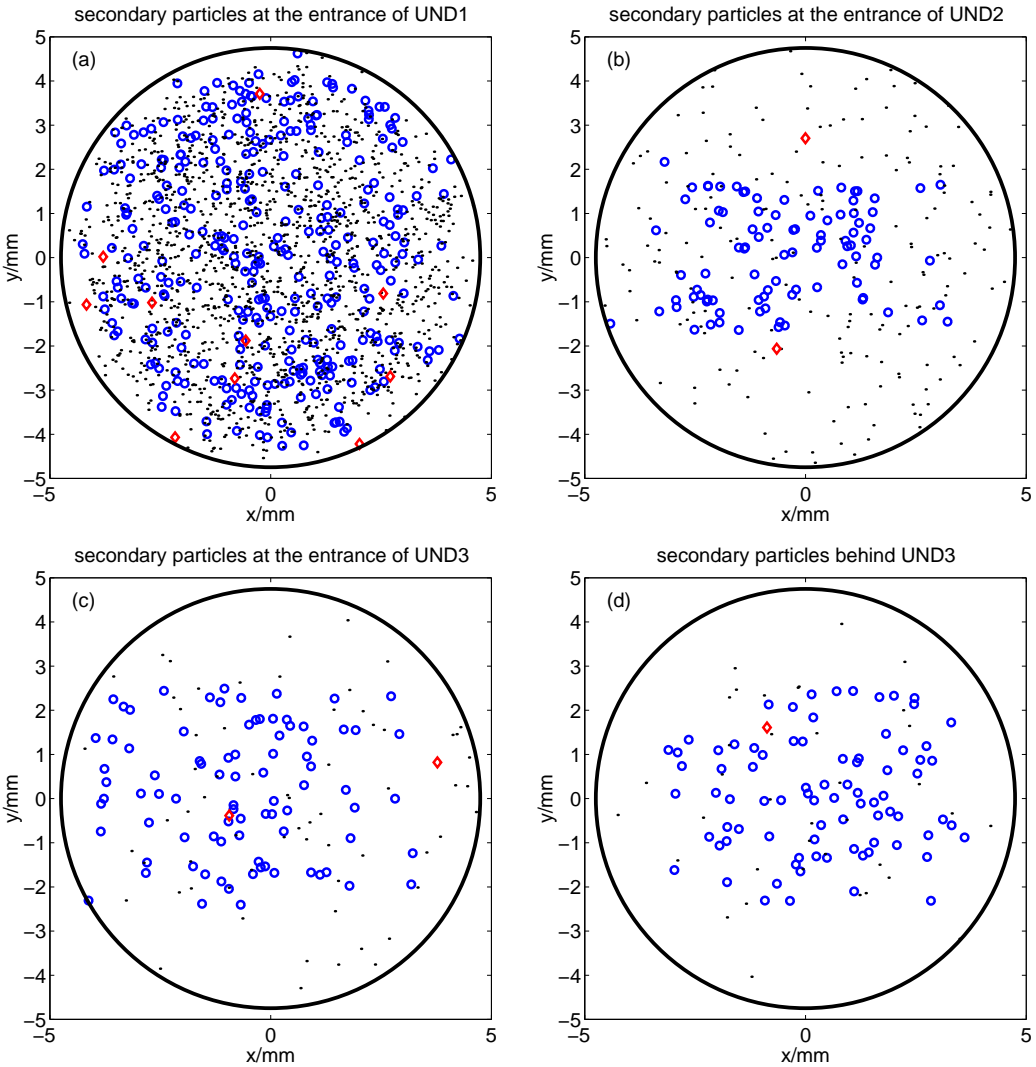


Figure 3.44: Transmission of secondary particles generated at the spoilers of the collimator through the undulator. Photons are shown by dots, electrons by cycles and positrons by diamonds. (a) 2000 particles with summed energy of 132 GeV entering the first undulator module. (b) entrance of UND2, $\sum E = 28$ GeV or 21%. (c) entrance of UND3, $\sum E = 22$ GeV or 16%. (d) exit of UND3, $\sum E = 20$ GeV or 15%.

collimator is shown in Fig. 3.45. The maximum dose of 0.45 Gy occurs in the dipoles behind the first quadrupole. After the 1st quadrupole, the absorbed dose decreases exponentially with z until $z \approx 2$ m. At 7th quadrupole at $z = 3$ m the dose slightly increases to a maximum value of 45 mGy and decreases again behind the quadrupole. The dose deposited in volumes filled with dosimeter material is by a factor of 2 to 2.5 larger than the local dose deposit in the dipoles.

The absorbed dose caused by charged particles with an energy above 20 MeV, the “reduced” dose, is shown in Fig. 3.46. The peak value is 0.120 Gy per 1 kJ beam energy lost in the collimator. The dose is on average 4 time smaller than the one calculated by taking all secondary particles into account.

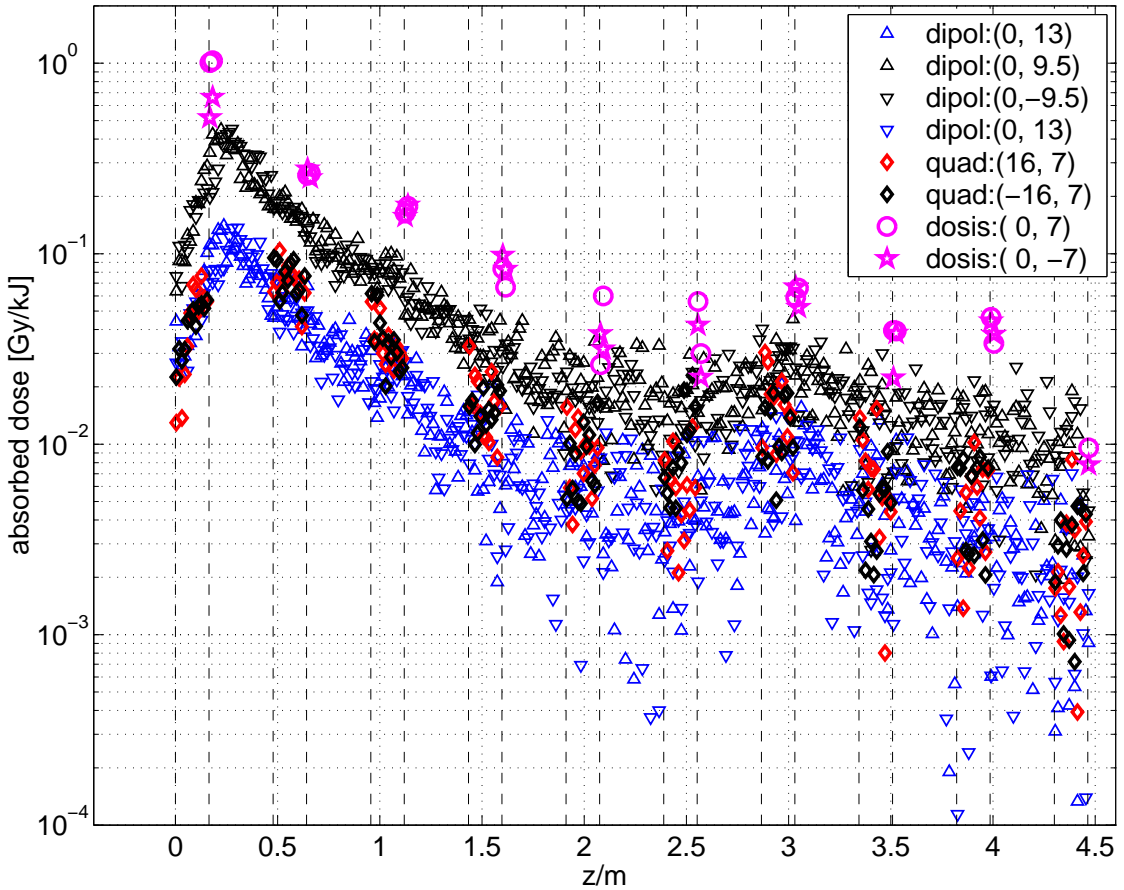


Figure 3.45: Absorbed dose in the magnets of the first undulator module caused by secondary particles from the collimator. The dose is calculated for 1 kJ primary electron energy incidence on the spoilers. The entrance and exit of quadrupoles are indicated by dashed vertical lines.

3.5 Limits for beam losses preventing damages of the undulator

Any losses of primary electrons in the undulator can be avoided by a proper adjustments of the quadrupole gradients and the quadrupole correction coils. Improper adjustments, i.e. due to technical failures or operational errors can produce losses. In this section, the acceptable losses of primary electrons in the undulator is estimated.

The energy deposition in the undulator caused by secondary particles from the collimator limits the allowable current losses at the spoilers. In general, the amount of secondary particles transmitted to the undulator can be influenced by adjusting the phase advance along the linac such that primary electrons hit mainly the first spoiler. However, because of several constrains in the different linac sections, this may is not possible.

In Sec. 3.3 and Sec. 3.4 the absorbed dose in the permanent magnets of the undulator have been studied for the following cases:

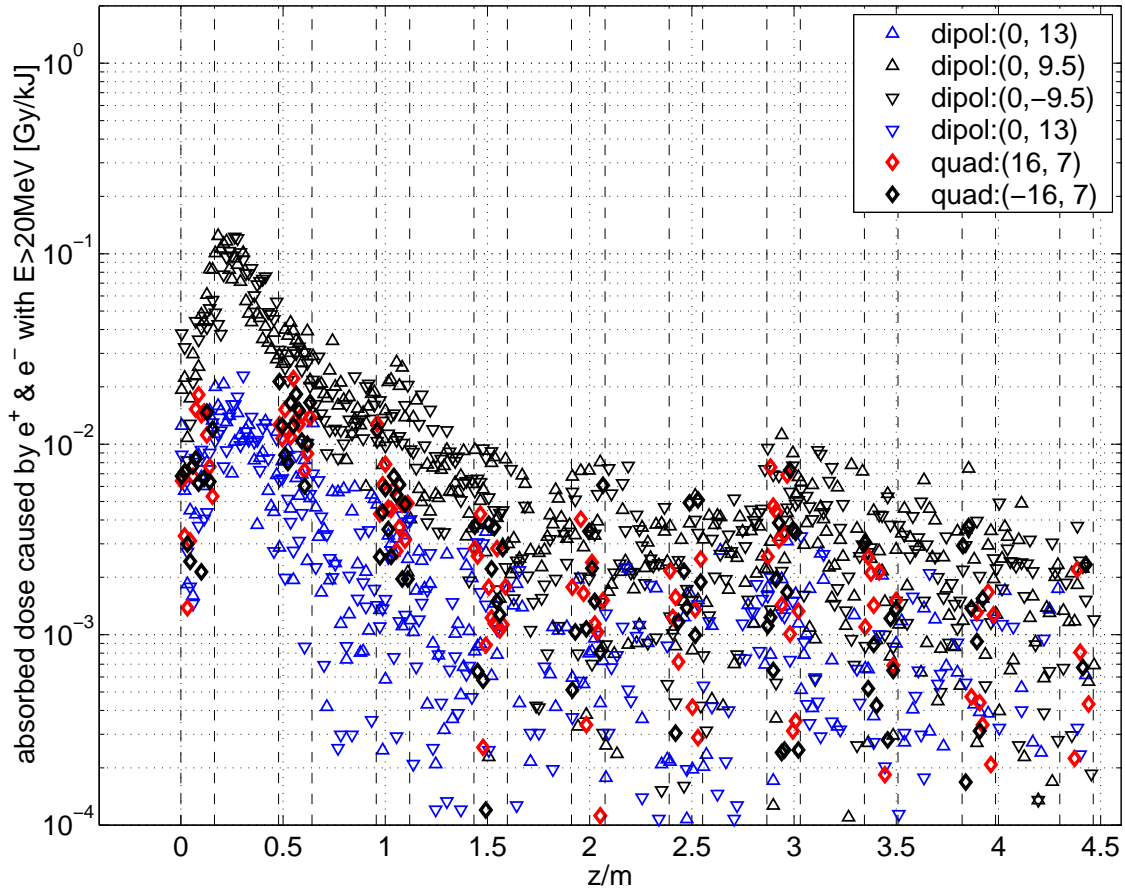


Figure 3.46: Absorbed dose in the magnets of the first undulator module caused by charged particles with an energy above 20 MeV.

1. primary electron losses in the undulator
 - (a) point-like with incidence in vertical direction (see p. 130 ff),
 - (b) point-like with incidence in horizontal direction (see p. 135 ff),
 - (c) distributed and caused by energy deviations of primary electrons (see p. 140 ff),
 - (d) distributed and caused by horizontal quadrupole displacements (see p. 142 ff),
2. losses of secondary particles in the undulator (see p. 150 ff).

The maximum absorbed and “reduce” absorbed dose for 1 kJ beam incidence is summarized in Table 3.15.

In Sec. 2.4.10 the radiation hardness of NdFeB-magnets is discussed. It has been found that 1% demagnetization of the magnets is expected at an absorbed dose value of 70 kGy deposited by charged particles with an energy above 20 MeV (“reduced” dose). The current losses are calculated for 1% maximum demagnetization of the permanent magnets. Consider an operation period of 1000 hours with nominal beam current of 8 mA and long macropulses (800 μ s) at 10 Hz repetition rate. At a beam energy of 230 MeV the average power amounts to 14.7 kW. The total energy transported by the beam after 1000 hours

	1 kJ primary electron losses in first undulator module				1 kJ incidence on collimator spoilers
case	1(a)	1(b)	1(c)	1(d)	2
maximum absorbed dose	2900 Gy	523 Gy	400 Gy	210 Gy	0.45 Gy
maximum “reduce” absorbed dose	975 Gy	160 Gy	134 Gy	64 Gy	0.12 Gy
limits on beam losses after 1000 hours operation in the undulator				in the collimator	
I_{loss}/I_{beam}	$1.4 \cdot 10^{-6}$	$8.3 \cdot 10^{-6}$	$9.9 \cdot 10^{-6}$	$20.6 \cdot 10^{-6}$	1.1%

Table 3.15: Summary of the maximum absorbed dose and maximum “reduced” absorbed dose in the undulator. The dose values are calculated for 1 kJ incidence in the first undulator module in case of primary electron losses (1(a)-1(d)) or for 1 kJ electron energy incident on the spoilers of the collimator section. The last row lists the ratio of the beam current losses I_{loss} versus the regular beam current I_{beam} for 1000 hours beam operation for linac design parameter for which 70 kGy would be accumulated in the undulator.

operation adds to 53.0 GJ. The beam losses for which 70 kGy are accumulated during this time period for the different cases 1(a)-1(d) and 2 are given in the last row of Table 3.15. The limit for beam losses at the spoilers amounts to 1.1%. This value agrees to other limits in the collimator section like the water cooling capability of the spoilers (about 2% at 230 MeV), or the radiation shielding from neutrons (0.6% at 230 MeV). Critical in this context is that the tracking simulation of the FEL beam from the injector to the collimator for an optimized FEL operation (matched beam core), shown in Fig. 3.3 beam (d), already predicts beam losses of the order of 1% at the spoilers. Because there is no safety margin, the design of the absorber system and the collimator section as a whole is not suited for 10 Hz repetition rate and 1000 hours operation time at full beam current. But the losses of primary electrons in the collimator section are allowed to be 3 to 4 orders of magnitude higher than the one in the undulator which amounts to 10^{-6} (case 1(a)) to $2 \cdot 10^{-5}$ (case 1(d)).

3.6 Spoiler protection

The required phase advance of 90° between the two spoilers and the space limitations in TTF phase 1 forces to chose small β -function at the location of the spoilers ($\beta_{x,y} = 2.5$ m). The rms-beam size is only $90 \mu\text{m}$ for the design emittance $\epsilon_{x,y} = 2 \mu\text{m}$ and a beam energy of $E_0 = 300$ MeV. In a bunch train, with $I_{train} = 8$ mA beam current, the beam exhibits an enormous power density $E_0 I / 2\pi\sigma_x\sigma_y \approx 50$ MW/mm 2 . Of course there is no material which could withstand such power density for a longer time. On the other hand the spoilers are close to the beam and one has to take into account the possibility that a mis-steered beam hits the spoiler head on. In that case the enhanced loss rates trigger the Pockels cell of the laser to interrupt the beam operation. In order to allow a few μs reaction time for the safety system, the spoilers have to accept the loss of several bunches. The electron beam penetrating the spoiler wall deposit energy by ionization in the material. The instantaneous temperature rise ΔT_{inst} due to ionization can be estimated by a

simple analytic model [76]:

$$\Delta T_{inst} = \frac{N_e}{2\pi\sigma_x\sigma_y} \left(\frac{dE}{\rho dx} \right)_{min} \frac{1}{c} \quad (3.9)$$

which ignores the effect of the shower buildup and the variation of the specific heat c of the material with temperature. For beam energies of a few 100 MeV, the model overestimates the temperature rise in greater depth of the spoiler. Multiple scattering of the electrons in the material leads to an increase of the angular beam divergence and the beam cross-section rapidly growth during the passage through the spoiler. The energy deposition of the beam is largest at the first few millimeters in spite of the increasing number of secondary particles. The temperature rise in the spoiler caused by an 1 nC bunch with $\sigma_{x,y} = 90 \mu\text{m}$ in a head-on collision is show in Fig. 3.47. The maximum temperature rise

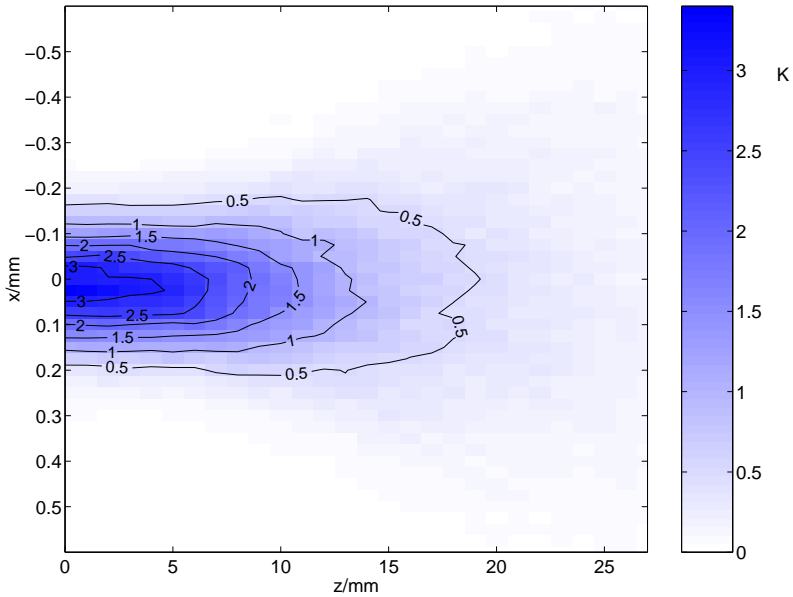


Figure 3.47: Temperature rise for a head on collision to an aluminum spoiler. The beam penetrates the spoiler at $z = 0$. The rms-beam size is $90 \mu\text{m}$, the beam energy 300 MeV.

is 3.4 K, in agreement with Eq. 3.9. After 1 cm path length the temperature rise amounts to 1.5 K and in a depth of 2 cm it drop below 0.5 K.

The local heating induces thermal stresses in the material. If the temperature rise exceeds the stress limit microfractures can develop in the material and damage the spoiler. The temperature limit T_{stress} for thermal induced stress can be estimated from [77]

$$\Delta T_{stress} \approx \frac{2\sigma_{UTS}}{\alpha E} \quad (3.10)$$

with σ_{UTS} the ultimate tensile strength, α the coefficient of linear expansion and E the modulus of elasticity. The material data for two different aluminum alloys and for titanium are listed in Table 3.16. Presently, the spoiler are made of AlMg3. For a bunch repetition rate of 9 MHz (FEL operation mode) the protection system has to interrupt the bunch train within $7 \mu\text{s}$. A pair of spare spoilers has been made of the aluminum alloy AlMg4.5Mn G35 with a larger ultimate tensile strength. This enlarges the required

material	E [kN/mm ²]	σ_{UTS} [N/mm ²]	α [10 ⁻⁶ K ⁻¹]	c [Jg ⁻¹ K ⁻¹]	T_{stress} [K]	# bunches $\sigma = 90\mu\text{m}$
AlMg3	70	180	23.8	0.897	216	64
AlMg4.5Mn G35	70	405	23.8	0.897	486	142
titanium	110	500	8.6	0.523	1057	310

Table 3.16: Spoiler material properties at room temperature. The last row is an estimate for the number of bunches a spoiler can withstand until the stress limit is reached.

inhibition time of the interlock system to 15 μs . A titanium spoiler can withstand even more bunches and is the preferable choice for TTF phase 2.

Since the thermal stress and a surface failure of the material can only occur at the front part of the spoiler, a potential vacuum failure is further reduce due to the specific spoiler design, shown in Fig. 3.2, which has foreseen an “isolation vacuum”.

3.7 Orbit Correction

In section 3.2.5 the influence of displaced quadrupoles on the transmission probability of the collimated beam through the undulator has been investigated. Displacements of 400 μm horizontally of the third quadrupole and 200 μm vertically of the second quadrupole reduce the performance of the collimator in an unacceptable way. Moreover, if random rms displacements of 50 μm are applied to all quadrupoles and in both directions, the collimator energy bandwidth is a factor 2 smaller compared to an ideal alignment. Therefore, in this section the influence of quadrupole displacements is studied and the results of a beam based alignment using the SASE photon radiation is presented.

3.7.1 Shift of the beam orbit due to quadrupole displacements

A quadrupole displacement Δu with respect to the linac axis, where u points either in horizontal or in vertical direction, shifts the beam centroid after the passage through a quadrupole by

$$\delta u_{off} = (1 - M_{11}) \Delta u, \quad (3.11)$$

$$\delta u'_{off} = -M_{12} \Delta u, \quad (3.12)$$

where M_{11} and M_{12} are the transport matrix element of the quadrupole. The offset δu_{off} and angle $\delta u'_{off}$ add linear to the beam centroid for an unperturbed motion

$$\mathbf{u}_1 = \mathbf{M} \cdot \mathbf{u}_0 + \delta \mathbf{u}_{off}, \quad (3.13)$$

with $\mathbf{u}_0 = (u, u')$ the incoming beam centroid at the entrance of the quadrupole and \mathbf{u}_1 the centroid at the quadrupole exit. The dipole correctors superimposed in the first and fourth collimator quadrupole moves the magnetic center of the quadrupole and can be described in the same way. With κ_C the curvature of a beam due to the dipole corrector field and k quadrupole field strength, the displacement of the magnetic center is $\Delta u_C = \kappa_C/k$. The optic system in the collimator section consists of four quadrupoles and two dipole correctors in each plane. The beam transport through the system to the entrance of the undulator (at position z) can be written as

$$\mathbf{u} = M(z_{b,1}, z) \mathbf{u}_0 + \sum_{i=1}^4 M(z_{e,i}, z) \cdot \delta \mathbf{u}_{off,i} + \sum_{i=1,4} M(z_{e,i}, z) \cdot \delta \mathbf{u}_{C,i}, \quad (3.14)$$

where the subscripted (b, i) and (e, i) indicate the entrance and exit of the i^{th} quadrupole. The first term on the right hand side of Eq. 3.14 describes the beam centroid for the unperturbed motion which can have an offset or angle due to mis-steering into the collimator. The second term describes the perturbation of the motion caused by quadrupole displacements Δu_i via Eq. 3.11 and the last term the steering of the beam due to the dipole correctors($\Delta u_{C,i}$). The shift of the beam centroid in the horizontal and vertical phase space at the entrance of the undulator (vertical wire scanner) for a quadrupole displacement of 200 μm and beam energies between 150 MeV and 350 MeV is plotted in Fig. 3.48. The required change in the quadrupole gradient to match the beam properly into the undulator is taken into account. The solid ellipse shows the 1σ phase ellipse of a beam with normalized emittance of 5 μm at an energy of 230 MeV. The dashed ellipse

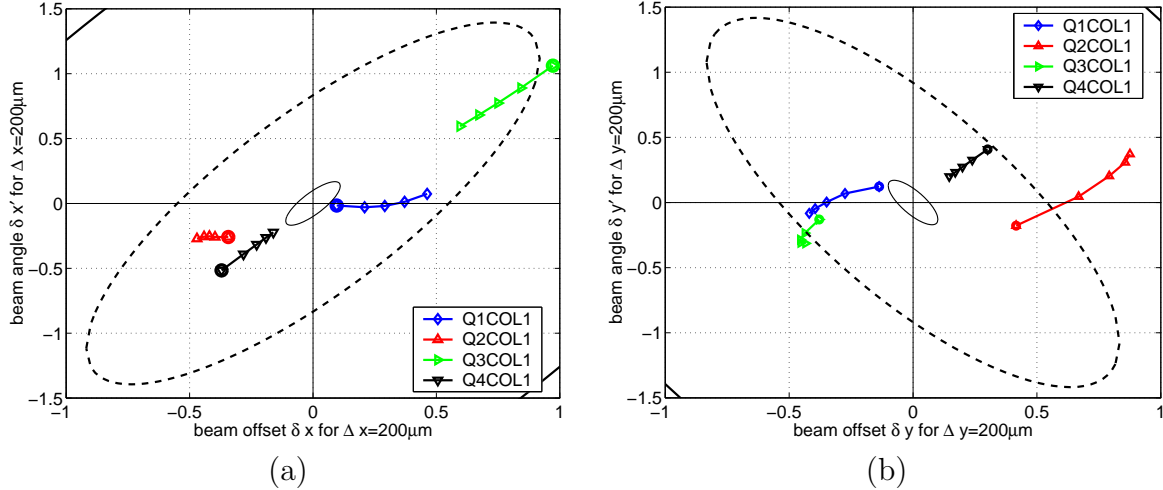


Figure 3.48: Beam centroid at the entrance of the undulator (vertical wire scanner) caused by $200\mu\text{m}$ quadrupole displacements. In (a) the horizontal phase space is shown and in (b) vertical phase space. The markers show the shift for beam energy of 150 MeV (circle), 200 MeV, ..., 350 MeV. The dashed phase ellipse shows 20% of the collimator acceptance phase space. The solid ellipse a 1σ beam with normalized emittance of $5\mu\text{m}$ at 230 MeV.

shows 20% of the outer acceptance phase ellipse of the collimator at the same energy. The clearance of the beam to the undulator vacuum chamber is reduced by about $350\mu\text{m}$ if the beam centroid is shifted to the dashed ellipse.

The shift of the beam in phase space depends for most of the quadrupoles sensitively on the beam energy. For quadrupole Q1 and Q2 the shift grows with the energy, but decreases for Q4. For Q3 it decreases in the horizontal plane and increases slightly with energy in the vertical plane. The variation of the shift with energy is caused by a change of the transfer function through the collimator matching system with energy (phase advance and β -function amplitude) and the change of the induced kick to the beam by the difference in the quadrupole strengths.

For a beam energy of 250 MeV, the middle point of each curve, the strongest effect in the horizontal plane (see Fig. 3.48(a)) is caused by the third quadrupole ($\delta\mathbf{x} = (750\mu\text{m}, 770\mu\text{rad})$). In the vertical plane, the second quadrupole leads to the largest orbit perturbation ($\delta\mathbf{y} = (790\mu\text{m}, 200\mu\text{rad})$) and is far outside the dashed ellipse. As investigated by tracking calculations (see Sec. 3.2.5) 200 μm displacement of Q2 in vertical direction causes already beam losses in the undulator and the orbit perturbation has to be corrected.

3.7.2 Beam based alignment by using the SASE photon beam

If a regular beam (small emittance, short bunch length) is injected to the center axis of the undulator, the photon beam is exponentially amplified during the electron beam passage through the undulator. For small electron beam offset or angles, the induced collective betatron motion in the undulator reduces the overlap between the electron and the photon beam. In this case, the FEL output power is very poor or only spontaneous emission of the undulator can be observed. To find the proper injection condition an automatic orbit scan procedure (SASE scans) has been implemented in the control system [78]. During an SASE scan, the beam is deflected by four steerers (H1ACC1, V1ACC1, H1COL1,

V1COL1) yielding different orbits in the collimator section, while the photon signal is monitored by a photo-diode in the experimental area II. The orbit in the collimator section is measured by BPM1COL1 and BPM2COL1 located in front of the spoilers. The successful SASE scans can be used to analyze the displacements of the collimator quadrupoles and based on the results optimized corrector strength are derived.

The method assumes small offsets ($< 200 \mu\text{m}$) between the mechanical centers of the spoilers and the electrical centers of the BPMs, which allows to relate the beam centroid to the center of the collimator phase space acceptance.

The photo-diode signal versus the measured beam positions in the collimator section of a typical SASE scan is shown in Fig. 3.49. In a small range between $100 \mu\text{m}$ and $300 \mu\text{m}$

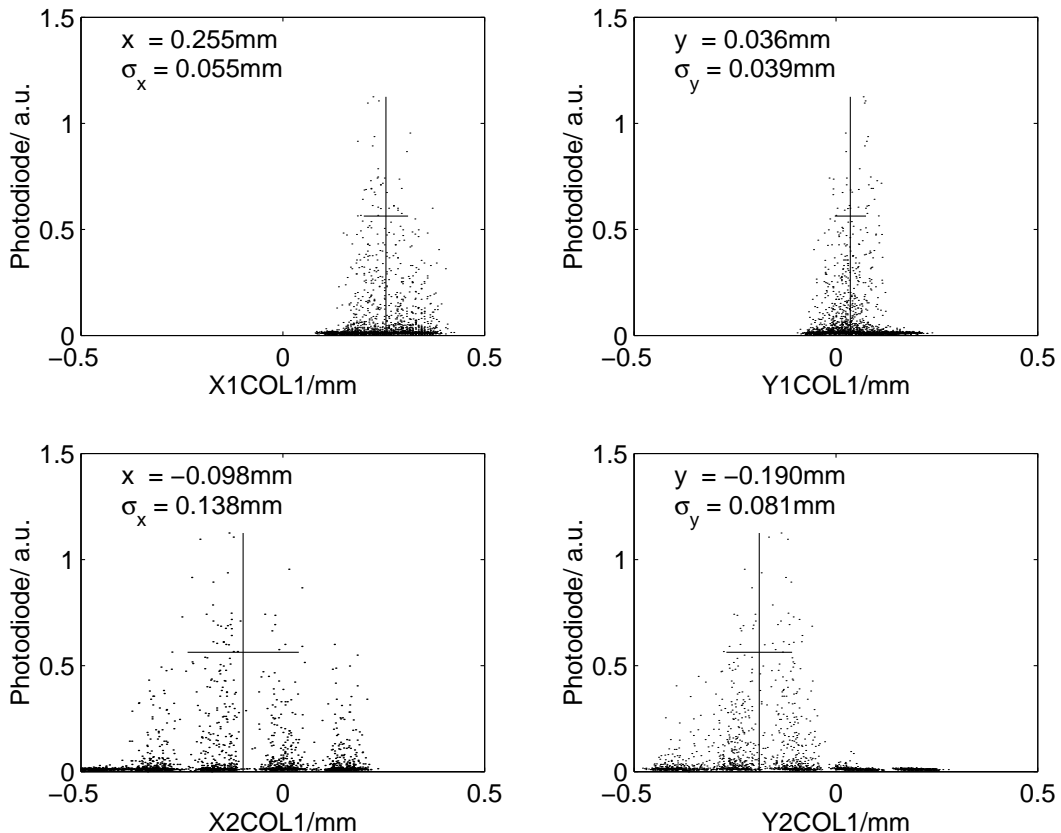


Figure 3.49: Photo-diode signal versus beam positions measured at the collimator BPMs in a SASE scan. The periodic structure for X2COL1 and Y2COL1 is an artifact of the SASE scan caused by the discrete steps of the steerer currents.

a SASE signal in all BPMs is observed. Outside this range the overlap between electron and photon beam was insufficient to observe a reasonable FEL-gain.

For the analysis only scans with bunch charges between 0.6 nC and 1.6 nC are used. The dependence of the BPM reading on the bunch charge is removed using the current measurements at toroid T7 (EXP 1). The center of SASE distribution

$$x_1 = \frac{\sum U_{\text{diode},j} x_{1,j}}{\sum U_{\text{diode},j}} \quad (3.15)$$

x_2, y_1 and y_2 , respectively, reflects the beam injection to the center axis of the undulator. The offsets (x_1, x_2) and (y_1, y_2) are transformed to positions and angles at the entrance of

the first collimator quadrupole yielding \mathbf{u}_0 in Eq. 3.14. From the currents of the dipole correctors (H2COL1, H3COL1, V2COL1 and V3COL1) the kick on the beam is computed (Δu_1 and Δu_4). Finally, by using Eq. 3.14 for zero quadrupole offsets (Δu_i), the injection at the entrance of the undulator is calculated. The result for 185 SASE scans is shown in Fig. 3.50.

The positions and angles of the beam scatters over a large area in the phase space. To remove dispersion effects in displaced quadrupoles and differences in the transfer matrices caused by different quadrupole currents the energy range has been limited to 230 ± 10 MeV (114 scans marked with pluses). This reduces the spread of the SASE scans in the horizontal phase space. Because the center of the SASE distribution in the x -plane is shifted by more than 1 mm and 1 mrad a strong variation with energy can be expected. However, the energy cut does not reduce the spread of SASE scans observable in the vertical phase space. Hence, it is not induced by an energy dependence of the orbit through the collimator section.

To exclude orbit deviations from the center axis of the undulator due to steerers in the undulator, only scans with bending angles $\alpha_{x,y} < 150 \mu\text{m}$ are excepted (91 scans marked with circles). A minor influence on the horizontal distribution in Fig. 3.50 is observed while in the vertical plane the scans with negative offset and large positive angles are removed. The parameters of the remaining scans are summarized in Table 3.17.

$\langle x \rangle$	1.36 mm	β_x	1.59 m	β_x^e	1.10 m
$\langle x' \rangle$	1.51 mrad	α_x	-1.81	α_x^e	-1.34
$\langle y \rangle$	0.44 mm	β_y	0.98 m	β_y^e	0.91 m
$\langle y' \rangle$	0.55 mrad	α_y	1.38	α_y^e	1.17

Table 3.17: Required correction of the beam centroid at the entrance of the undulator determined from the center of the SASE distribution and the collimator dipole correctors. The second row shows the Twiss parameters computed from the second order moment of the distribution. The design Twiss parameters of the beam are listed in the third row.

In the first row of Table 3.17 the mean values of the required correction of the beam centroids at the entrance of the undulator are listed. Thus, a beam centered in the collimator BPMs has to be corrected by 1.36 mm and 1.51 mrad in the horizontal plane and by 0.44 mm and 0.55 mrad in the vertical plane to be injected onto the undulator axis. In this case, the dipole correctors cancel the angular kick due to quadrupole displacements. The four parameters derived for the required orbit corrections are insufficient to determine the eight free displacements of the quadrupole quadruplet. The most likely configuration thus the one with the smallest quadrupole displacements that could create such an orbit correction is shown in Fig. 3.51. Mainly orbit kick due to the third and fourth quadrupole seem to contribute while the displacements of the first and second quadrupole are comparably small. The displacements are within the tolerances of the survey group.

The presented method of beam based alignment was required because of the lack of beam position monitors in the undulator during the first run period. Using this BPMs, the orbit in the undulator can be recorded for an optimized SASE operation. With the recorded orbit the injection condition into the undulator can always be recovered. By centering the beam in the collimator the steerers in the collimator quadrupoles can be used to inject the beam properly into the undulator. The observed rms displacements of the BPMs inside the undulator are $300 \mu\text{m}$ in horizontal and $230 \mu\text{m}$ in vertical direction

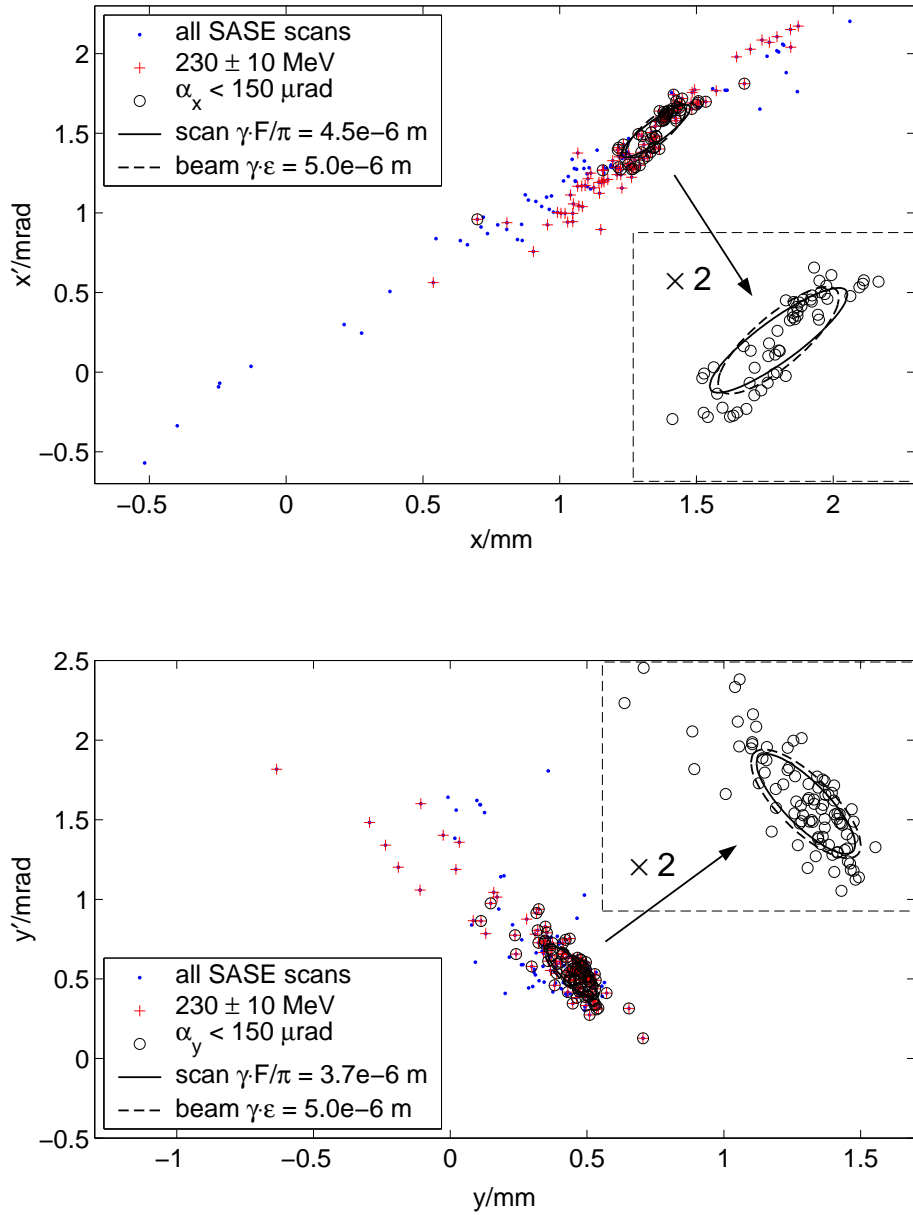


Figure 3.50: Injection into the undulator calculated from the center of the SASE distribution and the used orbit correction due to steerers in the collimator quadrupoles. The shift from zero is caused by quadrupole displacements. The points show all 185 SASE scans used for the analysis. An plus sign indicates the scans with beam energy between 220 MeV and 240 MeV and a circle is drawn when in addition no the steerer inside the undulator deflect the beam more than $150 \mu\text{rad}$. This scans are zoomed by a factor 2 and the corresponding rms phase ellipse is plotted (solid curve). For comparison is drawn the phase ellipse for a beam with $\epsilon_x^N = 5 \mu\text{m}$ (dashed curve).

[79].

With the BPMs in the undulator more powerful beam based alignment methods can be applied which also allows the precise measurement of the quadrupole displacements, e.g.

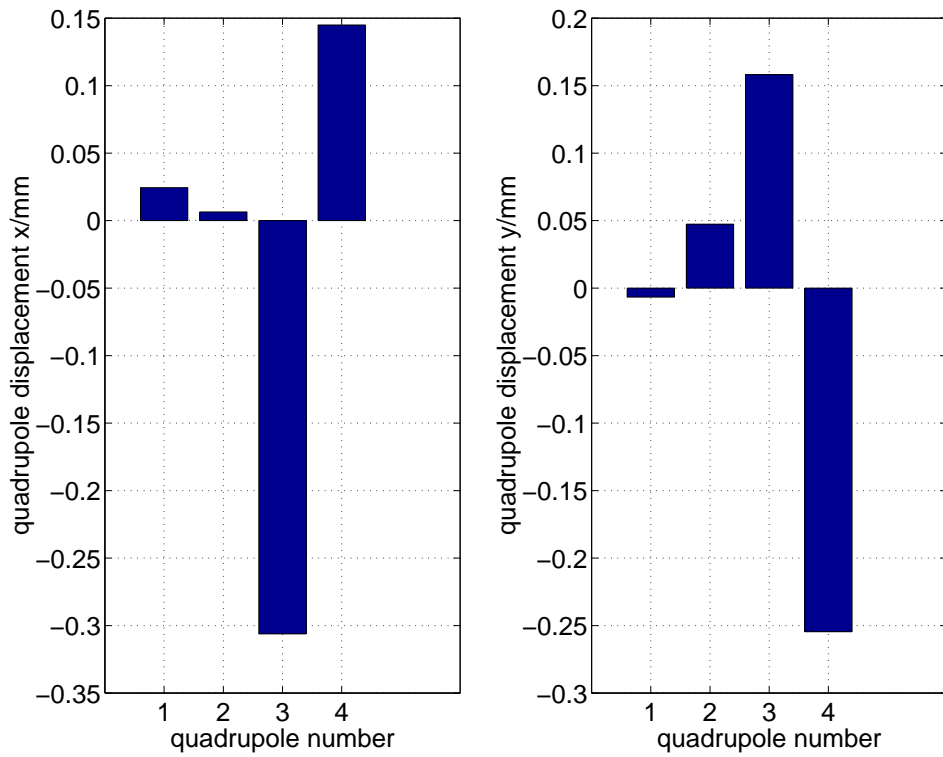


Figure 3.51: Most likely quadrupole displacements in the collimator section.

by changing the quadrupole gradients while monitoring the difference orbits in the undulator. With the knowledge of the quadrupole displacements the required orbit correction for any beam energy is predictable.

3.8 Wake fields induced at the Collimator

A bunched beam of charged particles acts with its immediate surroundings by means of the co-moving electromagnetic fields. Towards shorter bunch length (< 1 mm) with peak currents of kA the perturbation created by the interaction can seriously affect the beam quality. Therefore, the design of the collimator has to take into account that neither the longitudinal energy spread of the beam nor the transverse beam emittance is strongly degraded. The cross-section changes in the collimators and the adjacent beam pipes of small diameter couple strongly to the beam and must be carefully optimized.

The electromagnetic fields excited by the beam are known as wake fields. The short-range wake fields perturb the generating bunch itself while the long-range wake fields affect the following bunches in a train. The field energy carried by the wake fields is taken from the kinetic energy of the electrons in a bunch. The energy losses of the electrons depend on their longitudinal position ζ within the bunch. The dependence on ζ is non-linear and causes an increase of the correlated energy distribution which can only partly be removed by an off-crest acceleration. Similar to the longitudinal momenta, the transverse momenta of a bunch is perturbed as function of ζ if the beam has an offset with respect to center of the entire beam line component. While in general the centroid bunch positions in a bunch train can be corrected using fast orbit feedback systems, the impressed intra-bunch perturbations are difficult to remove. An increase of the projected emittance is the

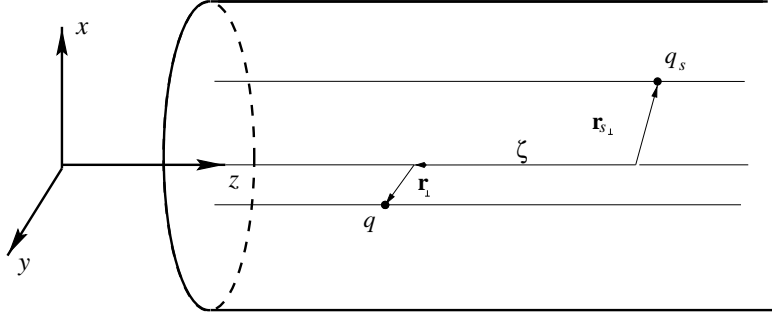


Figure 3.52: Coordinates of the source and the test particles. The test particle follows the source for $\zeta > 0$ and vice versa for $\zeta < 0$.

consequence.

The net effect on the beam due to wake fields in a beam pipe is described by the wake potentials. The action of the wake potential of a point-like source q_s on a small test charge q is called the wake function. In literature the wake function is also called delta wake potential. Using the coordinate system shown in Fig. 3.52 the wake function is defined by [80]

$$\mathbf{W}^\delta(\mathbf{r}_\perp, \mathbf{r}_{s\perp}, \zeta) = \frac{1}{q_s} \int dz \{ \mathbf{E}(\mathbf{r}_\perp, \mathbf{r}_{s\perp}, z, t) + v \mathbf{e}_z \times \mathbf{B}(\mathbf{r}_\perp, \mathbf{r}_{s\perp}, z, t) \}_{t=(z+\zeta)/v} . \quad (3.16)$$

where in Ref. [80] an opposite sign for the wake function has been chosen. The electromagnetic fields \mathbf{E} and \mathbf{B} are solutions of the Maxwell equations with boundary conditions. The integral is performed at a longitudinal distance ζ from the generating source to the co-traveling test charge. The variation of the particle coordinates is assumed to be small

along the integration path z . For ultra-relativistic particles ($\gamma \rightarrow \infty$) the wake function vanishes for $\zeta < 0$ ($\mathbf{W}^\delta(\zeta < 0) \equiv 0$). The wake function has the meaning of a Greens function. The wake potential for an arbitrary charge distribution $\lambda(\zeta')$ is obtained by the convolution with the wake function

$$\mathbf{W}(\zeta) = \int_{-\infty}^{\infty} d\zeta' \lambda(\zeta') \mathbf{W}^\delta(\zeta - \zeta') , \quad (3.17)$$

where the charge distribution is normalized to unity

$$\int_{-\infty}^{\infty} dz \lambda(z) = 1 . \quad (3.18)$$

The longitudinal wake potential W_{\parallel} and the transverse wake potential \mathbf{W}_{\perp} are related by the Panofsky-Wenzel theorem [81]:

$$\partial_{\zeta} \mathbf{W}_{\perp}(\mathbf{r}_{\perp}, \zeta) = -\nabla_{\perp} W_{\parallel}(\mathbf{r}_{\perp}, \zeta) , \quad (3.19)$$

where the spatial derivative acts on the coordinate of the test charge. The wake potential is related to the impedance by an inverse Fourier transformation

$$W_{\parallel}(\mathbf{r}_{\perp} = \mathbf{r}_{s\perp}, \zeta) = -\frac{1}{2\pi} \int_{-\infty}^{\infty} d\omega \tilde{\lambda}(\omega) Z_{\parallel}(\mathbf{r}_{\perp} = \mathbf{r}_{s\perp}, \omega) e^{-i(\omega/\beta c)\zeta} , \quad (3.20)$$

with $\tilde{\lambda}(\omega) = \int_{-\infty}^{\infty} d\zeta' \lambda(\zeta') \exp[-(\omega/\beta c)\zeta']$ the Fourier transform of λ . Defining the loss factor by

$$\mathbf{k} = \int_{-\infty}^{\infty} d\zeta' \lambda(\zeta') \mathbf{W}^{\lambda}(\zeta') , \quad (3.21)$$

the mean energy loss and transverse kick received by the electrons in the bunch are

$$\langle \Delta E \rangle = Nek_{\parallel} \quad \text{and} \quad \langle \mathbf{r}'_{\perp} \rangle = \frac{Nek_{\perp}}{cp_0} , \quad (3.22)$$

with N the number of electrons in the bunch. For further details on wake fields see [82], [83].

3.8.1 Short range wake fields

Slowly tapered structure

Under the condition of perfectly conducting walls, the impedance for cylinder symmetric structures with slowly varying radius $b(z)$ has been derived in [84]. The impedance is valid in the wave number range $1 \ll kb \ll 1/b'$ with $b' = db/dz$ the taper angle of the beam

pipe. The longitudinal monopole and the transverse dipole wake function calculated for the purely imaginary impedance is given by

$$W_{\parallel,0}^\delta(\zeta) = \frac{Z_0 c}{4\pi} \cdot \delta'(\zeta) \cdot \int_{-\infty}^{\infty} dz b'^2, \quad (3.23)$$

$$\mathbf{W}_{\perp,1}^\delta(\zeta) = \frac{Z_0 c}{2\pi} \cdot \delta(\zeta) \cdot \mathbf{r} \int_{-\infty}^{\infty} dz \left[\frac{b'}{b} \right]^2. \quad (3.24)$$

Equation 3.23 assumes equal beam pipe radius before and behind the taper ($b(\infty) = b(-\infty)$), otherwise an additional logarithmic term ($Z_0 c / 2\pi \ln[b(-\infty)/b(\infty)]$) has to be added to the right-hand side.

For a symmetric scraper with constant taper angles $\theta = (b_> - b_<)/L$, where $b_<$ and $b_>$ are the smaller and large pipe radii, and L the taper length the wake potentials are

$$W_{\parallel,0}(\zeta) = \frac{Z_0 c}{2\pi} \cdot \lambda'(\zeta) \cdot \theta \cdot (b_> - b_<) \quad (3.25)$$

$$\mathbf{W}_{\perp,1}(\zeta) = \frac{Z_0 c}{\pi} \cdot \lambda(\zeta) \cdot \mathbf{r} \cdot \theta \cdot \left[\frac{1}{b_<} - \frac{1}{b_>} \right]. \quad (3.26)$$

The effect of the wake fields increases proportional to taper angle θ .

The typical upper wave number k of electromagnetic fields excited by an electron beam with bunch length σ_z is $k \approx 1/\sigma_z$. Thus, the impedance derived in [84] holds for taper angles $\theta \ll \sigma_z/b$. For σ_z in the sub-millimeter range and a beam pipe radius of millimeters the taper angles must be in the order of a few tens of mrad. A taper from the standard beam pipe with radius of 30 mm to the spoiler radius of 3 mm would have a length of several meters. If the taper angle θ is chosen larger than σ_z/b the above formulas fails and the wake fields are significantly larger. For taper angles much above σ_z/b the short range wake functions of a step-in or a step-out provides an accurate descriptions.

Numerical simulation for intermediate taper angles $\theta \approx \sigma_z/b$ are difficult. Due to the huge number of mesh points required for the discretization of the geometry for ultra-short bunches the numerical errors become critical. Because of this, the taper angles are chosen such that the wake potentials in Eq. 3.25 and Eq. 3.26 can be used as an approximation. The geometrical data of the tapers for the spoilers and absorbers at the collimator section are listed in Table 3.18. The absorber 2 has a smooth transitions from cylindrical to weakly elliptical aperture ($a = 4$ mm and $b = 5$ mm). The contribution to the wake potential is small and is taken into account using the larger taper angle.

The longitudinal and transverse wake potential induced by the tapers of the collimators is shown in Fig. 3.53. In spoiler 2 the entrance radius is larger than exit radius. Hence the beam is slightly accelerated by the geometrical wake fields of the tapers (with logarithmic term) and the longitudinal loss factor k_{\parallel} is positive. The accelerating contribution is followed by a decelerating contribution due to a step-out.

Steps in beam pipes

In Ref. [85] the transition of the high-frequency longitudinal impedance from the cavity regime to the step regime is explored. For a pill box cavity of gap length g the transition

Device	θ [mrad]	b_{up} [mm]	b_{down} [mm]	L [mm]
Spoiler 1	-23.4	6	3	128
	23.4	3	6	128
Absorber 1	-32.5	8	4.75	100
	32.5	4.75	8	100
Spoiler 2	-23.8	8	3	210
	31.2	3	6	96
Absorber 2	-8.5/-6.4	8	4/5	470
	0/-2.9	4/5	4	350
	8.9	4	8	450
Absorber 3	-8.7	4.75	4	86
	10.0	4	4.75	75

Table 3.18: The taper angles θ , the upstream and downstream radius b_{up} , b_{down} and the length of the taper for all elements at the collimator section are listed. Absorber 2 has transitions from cylindrical to weakly elliptic aperture (x/y).

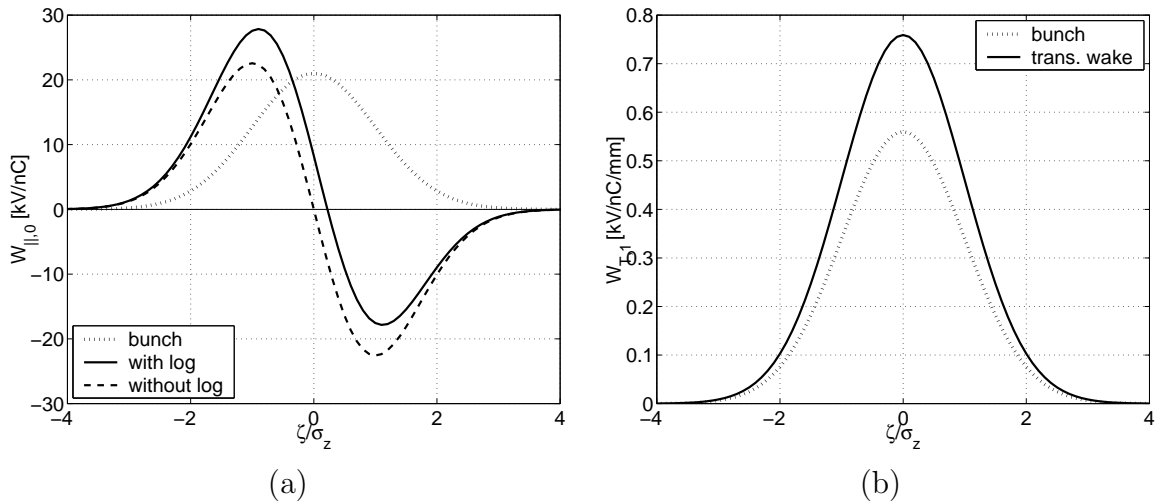


Figure 3.53: Geometric wake potentials caused by collimator tapers. (a) longitudinal monopole wake potential (b) transverse dipole wake potential of a bunch with 250 μm bunch length.

occurs at

$$g_t \approx k(b_> - b_<)^2 \quad (3.27)$$

with $b_<$ the radius of the beam pipe $b_>$ the radius of the cavity. In the cavity regime for $g < g_t(k)$ the impedance $Z_{\parallel}(k)$ depends on the cavity gap while if $g > g_t(k)$ the structure can be separated in a step-out followed by a step-in independent on the distance g . More precisely, for gap length $g \ll g_t$ the radius r of the diffraction wave increases with z as $r \propto \sqrt{2z/k}$ and the impedance is characterized by Fresnel diffraction. If the gap length is increased Fraunhofer diffraction takes place for which the radius increases $r \propto z/kb_<$. If g is in the order of g_t the cavity radius $b_>$ becomes important. Then the diffraction pattern is dominated by the cylindrical wave guide modes depending on the cavity radius $b_>$.

At the collimator section the beam pipe between absorber 1 and spoiler 2 has a radius

of 30 mm and a length 1.6 m. The transition gap g_t for $k \approx 1/\sigma_z$ and $\sigma_z = 250 \mu\text{m}$ is 1.9 m. Thus, for this bunch length the higher frequencies of the excited wake fields are still influenced by Fraunhofer diffraction. To yield an upper estimate the step-out is the best approximation for the wake fields generate at this section.

The monopole and dipole impedance for a semi-infinite pipe within an infinite pipe is derived in [86, 87]. In the limit $\gamma \rightarrow \infty$, the high frequency impedance approaches a constant value. In this limit the wake potentials for a step-out are

$$W_{\parallel,0}(\zeta) = \frac{Z_0 c}{\pi} \cdot \lambda(\zeta) \cdot \ln \left[\frac{b_<}{b_>} \right], \quad (3.28)$$

$$\mathbf{W}_{\perp,1}(\zeta) = \frac{Z_0 c}{\pi} \cdot \left(\int_{\zeta}^{\infty} d\zeta' \lambda(\zeta') \right) \cdot \mathbf{r} \cdot \left[\frac{1}{b_<^2} - \frac{1}{b_>^2} \right], \quad (3.29)$$

In case of a step-in only the resonances at the discontinuous cross-section and the difference in the two beam pipe cut-off frequencies cause contributions to the wake potential. These contributions are small and not taken into account.

For an iris the analytical formulas for the wake potentials Eq. 3.28 and Eq. 3.29 have been compared to numerical calculations using ABCI [88] at a bunch length of 250 μm . The results are plotted in Fig. 3.54. The agreement for the monopole wake potential is excellent and one finds for the transverse dipole wake potential an difference of about 20% in the range $\pm 1\sigma_z$ of the beam core. The parameters of the step-out of the iris are chosen equal to the step-out at absorber 1 (8 mm to 30 mm). The energy loss due to the

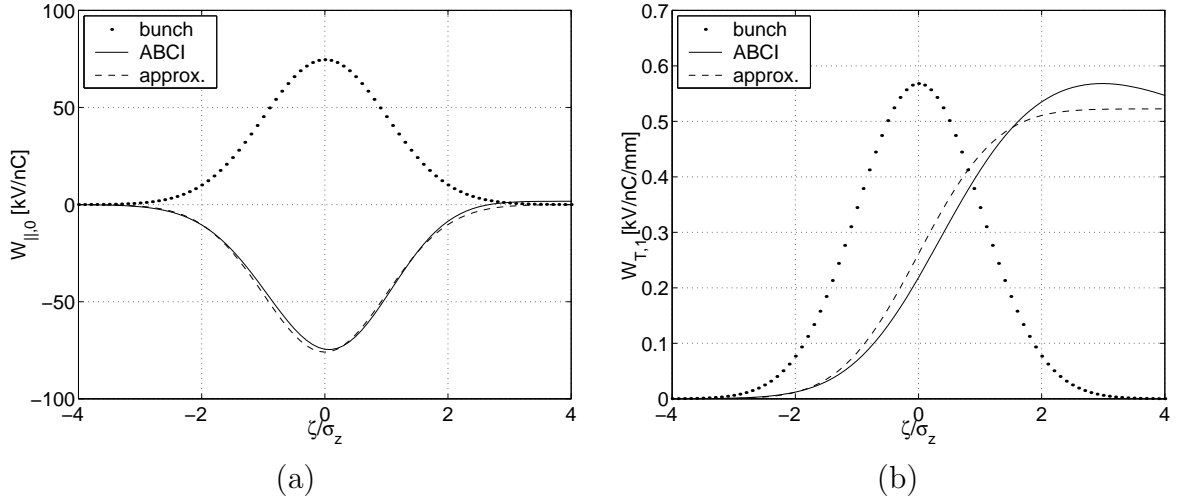


Figure 3.54: (a) longitudinal monopole wake potential (b) transverse dipole wake potential of a bunch with 250 μm bunch length induced at an iris (30 mm beam pipe radius, 8 mm iris radius, 200 mm iris length). The dashed curve represents the longitudinal charge distribution, the solid line the numerical result of the wake potential using the code ABCI [88]. The dashed lines are calculated using Eqs. 3.28 and 3.29.

geometrical wake of this step dominates the longitudinal wake potential of the collimator section. Additional step-outs are listed in Table 3.19. The sum of the wake potentials caused by steps in the beam pipe are plotted in Fig. 3.55. The small transitions behind the spoilers contribute 30% to the longitudinal and 60% to the transverse wake potential.

location	$b_<$ [mm]	$b_>$ [mm]
behind spoiler 1	6	8
behind absorber 1	8	30
behind spoiler 2	6	8

Table 3.19: Step-outs in the collimator section.

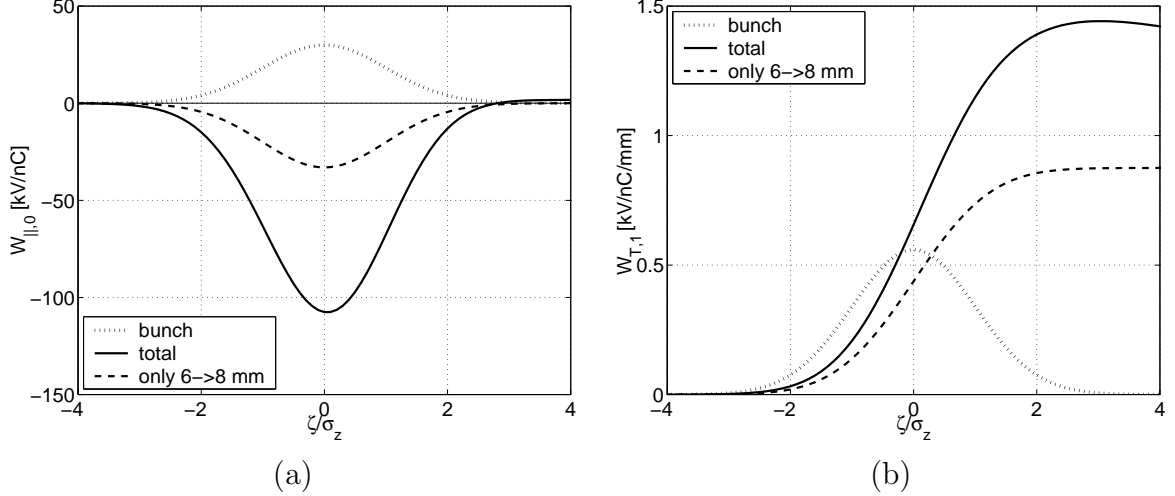


Figure 3.55: Geometric wake potentials caused by steps in the beam pipe at the collimator section. (a) longitudinal monopole wake potential (b) transverse dipole wake potential of a bunch with $250 \mu\text{m}$ rms-length.

Short gaps

The longitudinal impedance of the m^{th} -mode for short gaps of length g in a beam pipe with radius b which fulfill the conditions $g \ll kb$ and $g \ll g_t$ is (see i.e. [82]):

$$Z_{||,m} = \frac{Z_0}{2\pi^{3/2}b} [1 + i\text{sign}(\omega)] \sqrt{\frac{cg}{|\omega|}} (2 - \delta_{m,0}) \left(\frac{rr_s}{b^2} \right)^m. \quad (3.30)$$

Note that the frequency behavior of the impedance does not depend on the mode number m . The wake potential for gaussian charge distribution including all modes is

$$W_{||}(\zeta) = -\frac{Z_0 c}{2\pi b} \sqrt{\frac{g}{2\pi\sigma_z}} \mathcal{S}_{||}(rr_s/b^2, \phi) \cdot \left| \frac{\zeta}{2\sigma_z} \right|^{1/2} \{ I_{-1/4}(\tilde{u}) + \text{sign}(\zeta) I_{1/4}(\tilde{u}) \} e^{-\tilde{u}}. \quad (3.31)$$

with $\tilde{u} = (\zeta/\sigma_z)^2/4$ the argument of the modified Bessel functions of fractional order. The function

$$\mathcal{S}_{||}(x, \phi) = \sum_{m=0}^{\infty} (2 - \delta_{m,0}) x^m \cos(m\phi) = \frac{1 - x^2}{1 - 2x \cos(\phi) + x^2}. \quad (3.32)$$

describes the radial and azimuthal dependence on the transverse coordinates r, r_s and ϕ . Applying the Panofski-Wenzel theorem the transverse wake potential is given by

$$\begin{aligned}
\mathbf{W}_\perp(\zeta) &= \frac{Z_0 c}{\pi b} \sqrt{\frac{g \sigma_z}{2\pi}} \cdot \frac{r_s}{b^2} \cdot \mathcal{S}_\perp(rr_s/b^2, \phi) \\
&\quad \times 2 \left| \frac{\zeta}{2\sigma_z} \right|^{3/2} \left\{ I_{1/4}(\tilde{u}) + I_{-3/4}(\tilde{u}) + \text{sign}(\zeta) [I_{-1/4}(\tilde{u}) + I_{3/4}(\tilde{u})] \right\} e^{-\tilde{u}}, \tag{3.33}
\end{aligned}$$

with

$$\mathcal{S}_\perp(x, \phi) = \frac{[(1+x^2)\cos(\phi) - 2x]\mathbf{e}_r - [(1-x^2)\sin(\phi)]\mathbf{e}_\phi}{(1-2x\cos(\phi)+x^2)^2}. \tag{3.34}$$

If the functions $\mathcal{S}_{||}$ in Eq. 3.31 and \mathcal{S}_\perp in Eq. 3.33 are substituted by 1 and \mathbf{e}_r , respectively, the contribution of the $m = 0$ term to the longitudinal wake and the contribution of the $m = 1$ term to the transverse wake are obtained. For beam offsets much smaller than the beam pipe radius b ($x \ll 1$), the non-linear dependence described by $\mathcal{S}_{||}$ and \mathcal{S}_\perp can be neglected.

Gaps in the beam pipes at the collimator section occur at the pump ports between the spoilers and the absorbers and at rf-shielded bellow units. The geometrical data are summarized in Table 3.20.

device	units	b [mm]	g [mm]
pump port		2	8
rf-shielded bellow type A		5	8
rf-shielded bellow type B		1	4.75

Table 3.20: Geometry of short gaps in the beam pipe at the collimator section.

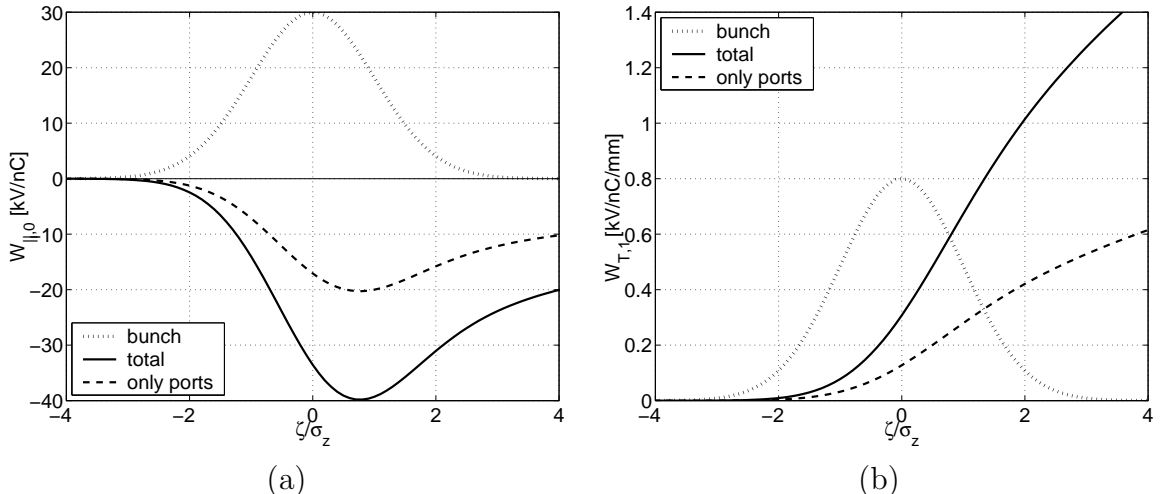


Figure 3.56: Geometric wake potentials caused by gaps in the beam pipe at the collimator section. (a) longitudinal monopole wake potential (b) transverse dipole wake potential of a bunch with 250 μm bunch length.

Resistive wall

The finite conductivity of the beam pipe walls causes an electromagnetic interaction with the beam, the so-called resistive wall wake fields (see [89, 90, 91, 92, 83]). The shape of the wake potential depends on a characteristic length

$$\zeta_0 = \left(\frac{2b^2}{Z_0\sigma_0} \right)^{1/3} \quad (3.35)$$

with σ_0 the wall conductivity and b the beam pipe radius. In the regime $z \approx \zeta_0$ (short-range) the wake function is given by a high-frequency broad-band resonance with resonance wave number $k_{res} = \sqrt{3}/\zeta_0$ and damping factor $\Gamma_{res} = 1/\zeta_0$. The broad band behavior of the resistive wall wake fields is caused by a coupling of the co-traveling electromagnetic fields of a charge to the wave guide modes of a beam pipe with finite conductivity. For bunch length $\sigma_z \approx \zeta_0$ the wake potential has to be derived by Eq. 3.17 from the wake function and its shape vary strongly with σ_z .

In case $\sigma_z \gg \zeta_0$ (long-range) the penetration of the wake fields into the beam pipe walls $\propto \sqrt{k}$ characterizes the shape of the wake potential which is independent of the pipe radius and of the specific bunch length.

For the stainless steel beam tube of 8 mm radius installed between the spoilers and absorbers, the characteristic length is $\zeta_0 = 62 \mu\text{m}$. Thus, a gaussian bunch of $\sigma_z = 250 \mu\text{m}$ cannot couple to the wave guide modes of such a pipe and the wake potential can be described by the long-range approximation for the resistive wall wake fields.

The longitudinal and transverse wake potential per unit length of a gaussian distribution in the long-range approximation are given by [89, 83]

$$\begin{aligned} W_{\parallel}(\zeta) &= \frac{Z_0 c}{4\pi b} \frac{1}{\sqrt{Z_0\sigma_0\sigma_z^3}} \cdot \mathcal{S}_{\parallel}(rr_s/b^2, \phi) \times \\ &\quad \left| \frac{\zeta}{2\sigma_z} \right|^{3/2} \{ I_{1/4}(\tilde{u}) - I_{-3/4}(\tilde{u}) + \text{sign}(\zeta) (I_{-1/4}(\tilde{u}) - I_{3/4}(\tilde{u})) \} e^{-\tilde{u}}, \quad (3.36) \\ \mathbf{W}_{\perp}(\zeta) &= \frac{Z_0 c}{2\pi b} \frac{1}{\sqrt{Z_0\sigma_0\sigma_z}} \cdot \frac{r_s}{b^2} \mathcal{S}_{\perp}(rr_s/b^2, \phi) \cdot \left| \frac{\zeta}{2\sigma_z} \right|^{1/2} \{ I_{-1/4}(\tilde{u}) + \text{sign}(\sigma_z) I_{1/4}(\tilde{u}) \} e^{-u^2/4}, \end{aligned}$$

and include all higher multi-poles. The argument of the modified Bessel functions is $\tilde{u} = (\zeta/\sigma_z)^2/4$. The wake potentials have been derived for a constant radius b . For small deviations from a constant radius as given by the smooth tapers of the collimators it can be assumed in the long-range regime that neither the excitation nor the propagation of the resistive wall wake field are too much perturbed. Thus, the effect of resistive walls can be approximated by integrating along the relevant sections in the collimator sections. Beside the collimators, listed in Table 3.18, only the attached stainless steel pipes (200 mm total length) on the collimators contribute. Because of geometric shielding effects, the sections before spoiler 1 and between absorber 1 and spoiler 2 have not to be considered.

The longitudinal monopole and transverse dipole wake potentials⁵ generated at the collimator section are plotted in Fig. 3.57. The contribution of the spoilers is 26% to the longitudinal and 42% to the transverse wake potential.

⁵The conductivity σ_0 of copper, aluminum, and stainless steel is $5.88 \cdot 10^7 \Omega^{-1}m^{-1}$, $3.65 \cdot 10^7 \Omega^{-1}m^{-1}$, and $0.19 \cdot 10^7 \Omega^{-1}m^{-1}$, respectively.

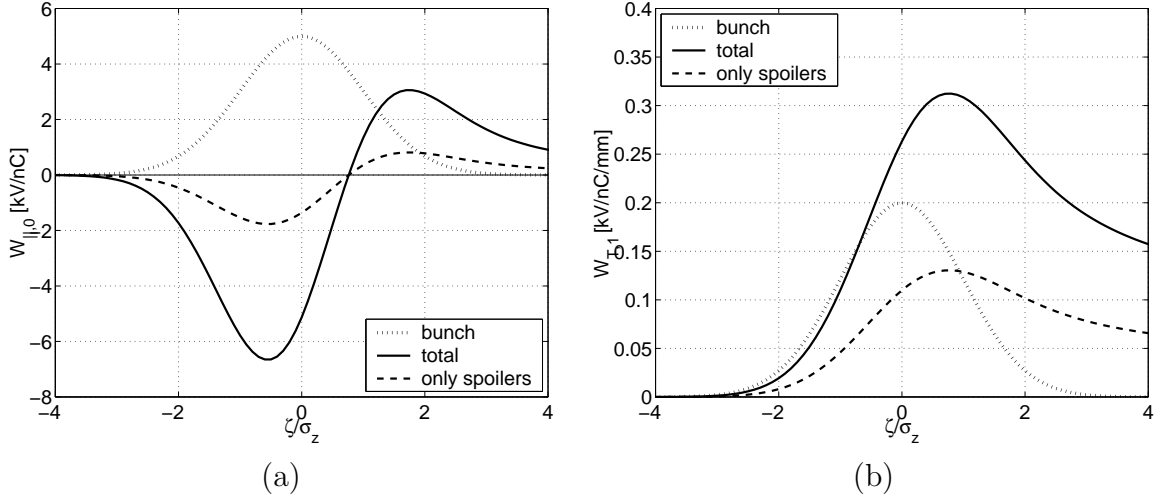


Figure 3.57: Resistive wall wake potentials (long-range approximation) excited in the collimator, (a) the longitudinal monopole and (b) the transverse dipole. The bunch length is $250 \mu\text{m}$.

Surface roughness

Due to small corrugations at the beam pipe wall the wave guide modes in the tube are slightly modified. The phase velocities v_{ph} of the modes are decreased and the dispersion curves cross the velocity of light at some high frequencies. For a single mode, the frequency with phase velocity equal c can be resonantly excited by the beam. While the beam propagates through the pipe the kinetic energy of the electrons is continuously transferred to the electromagnetic wave. Because the group velocity v_g of the mode is also below c ($v_{ph}v_g < c^2$), the time duration of the electromagnetic wave train grows proportional to the length of the rough beam pipe (typically tens of picoseconds per m). According to [93], the wake fields excited by surface roughness can be modelled by the wake fields excited in a tube with a dielectric layer of thickness δ and permittivity ϵ_r . The wake function per unit length of the m^{th} -mode in a tube with a thin dielectric layer is given by [94]

$$W_{\parallel,m}^{\delta}(\zeta) = -\frac{Z_0 c}{\pi b^2} \cdot (m+1) \left(\frac{rr_s}{b^2} \right)^m \cdot \cos(k_m \zeta) \cdot \cos(m\phi) \quad (3.37)$$

with

$$k_m = \sqrt{\frac{(m+1+\delta_{m,0})\epsilon_r}{(\epsilon_r-1)b\delta}}. \quad (3.38)$$

the resonance wave number of the mode. To calculate the resonance wave number k_m , the parameters δ and ϵ_r have to be determined from the surface roughness of a beam pipe. In case of protrusions with similar depth and longitudinal length, δ is approximately given by the rms-roughness depth of the surface δ_{rms} and $\epsilon_r \approx 2$. Several numerical studies concerning the parametrisation of the surface roughness in terms of δ and ϵ_r can be found in [94]. Up to now, a satisfying method to determine the roughness parameters has not been found, but first experimental results at TTF confirm the above approximation [95, 96, 97]. Particular important to note is, that the surface roughness of the sandblasted beam pipes used in this experiments have similar parameters e.g. rms-depth and longitudinal

spectrum, as the one of the surface roughness measured for the spoilers of the collimator section shown Fig. 3.58) [98].

In case $k_0\sigma_z \gg 1$ is the resonance mode of the wave guide not excited and (long-range approximation) the convolution of the wake function with the bunch charge distribution can be approximated by

$$W_{\parallel,m}(\zeta) = -\frac{Z_0c}{2\pi b} \frac{(\epsilon_r - 1)\delta}{\epsilon_r} \cdot \lambda'_{\parallel} \cdot (2 - \delta_{m,0}) \left(\frac{rr_s}{b^2}\right)^m \cdot \cos(m\phi) \quad (\text{long-range approx.})$$

In this case, the dependence of the wake potentials on the coordinates r, r_s and b including all multipoles is described by

$$W_{\parallel}(\zeta) = -\frac{Z_0c}{2\pi b} \frac{(\epsilon_r - 1)\delta}{\epsilon_r} \cdot \lambda'_{\parallel} \cdot \mathcal{S}_{\parallel}(rr_s/b^2, \phi) \quad (3.39)$$

and

$$\mathbf{W}_{\perp}(\zeta) = \frac{Z_0c}{\pi b} \frac{(\epsilon_r - 1)\delta}{\epsilon_r} \cdot \lambda_{\perp} \cdot \frac{r_s}{b^2} \mathcal{S}_{\perp}(rr_s/b^2, \phi). \quad (3.40)$$

The beam channel in the collimators were produced by wire erosion (spoilers and absorbers). The surface roughness of an aluminum block (spoiler material) has been treated with the same erosion parameters in order to determine the surface roughness. The measured surface profile is shown in Fig. 3.58(a). The surprisingly poor rms-surface roughness depth of $\delta_{rms} = 5 \mu\text{m}$ exceeds the specified tolerable roughness of $\delta_{rms} < 1 \mu\text{m}$ by a factor of 5.

Because of the poor surface, the resonance frequencies of the monopole and dipole mode for $\delta = \delta_{rms}$ and $\epsilon_r = 2$ are low enough to be excited by a beam with bunch length of

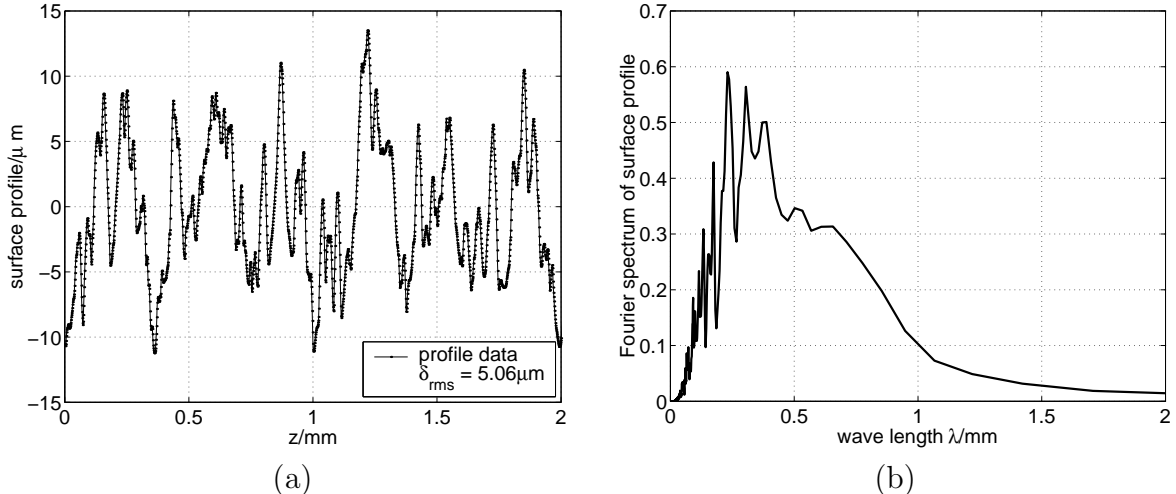


Figure 3.58: (a) surface profile of a wire eroded aluminum test block (spoiler material). (b) Fourier spectrum of the surface profile shown in (a).

250 μm .

To estimate of the contribution of surface roughness wakes, the transient behaviour of the wake fields at the entrance of the spoiler are neglected (see i.e. [95]). The variation of the beam pipe radius $b(z)$ is taken into account by integrating the wake function for a given

ζ along the spoilers and by convolving this wake function with the given charge distribution. The result is shown in Fig. 3.59. For comparison the long-range approximation, Eq. 3.39 and Eq. 3.40, are also shown in the plot (dashed curve) which demonstrates that for $\sigma_z = 250 \mu\text{m}$ the resonant waveguide mode is only weakly excited.

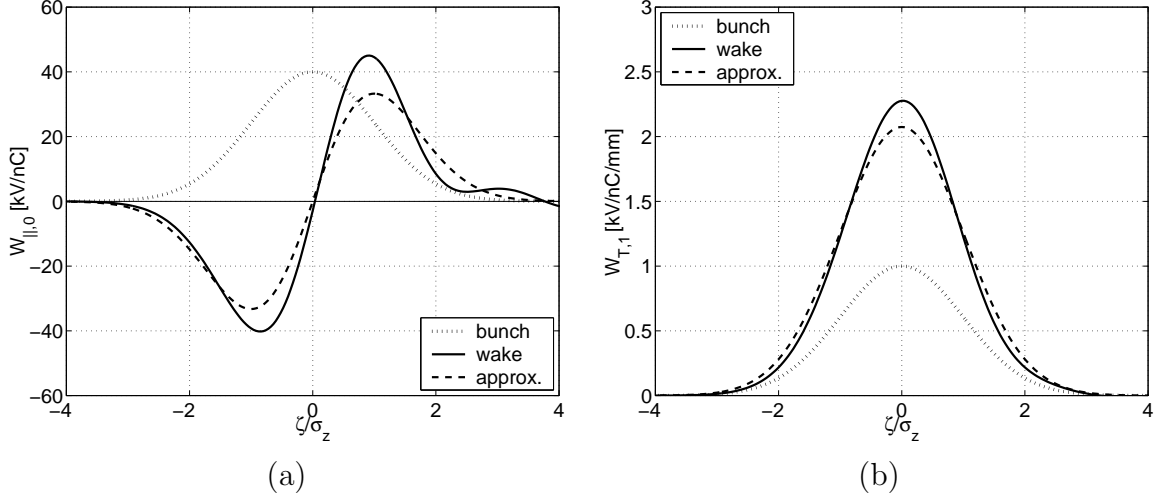


Figure 3.59: Surface roughness wake potentials excited at the spoilers in the collimator section. The long-range approximation of the potentials, Eq. 3.39 and Eq. 3.40, are plotted by dashed curves. (a) shows the longitudinal monopole mode and (b) the transverse dipole mode. The bunch length is $250 \mu\text{m}$.

For shorter bunch length the situation changes. Caused by rf-acceleration the bunch has a non-gaussian shape after passing the bunch compressor BC2 (see Sec. 2.2.3). The charge distribution rapidly rises at the bunch head and decreases slowly towards the bunch tail. The rapid rise at the bunch head can be described by an gaussian of about $40 \mu\text{m}$ variance which contains 26% of the bunch charge. For this sub-bunch, the wake potential is shown in Fig. 3.60. The amplitude of $W_{||,0}$ is 25 times larger in case of $\sigma = 40 \mu\text{m}$ compared to the case $\sigma = 250 \mu\text{m}$. Behind the sub-bunch ($\zeta > 100 \mu\text{m}$), the wake potential oscillates with an resonance wave length of $390 \mu\text{m}$ (or 770 GHz). The oscillation induces an energy modulation of the trailing electrons of up to $\pm 300 \text{ keV}$. Thus, the wake fields induced by surface roughness at the spoilers of the collimator can partially be responsible for the observed energy break-up of the bunch into almost isolated bunchlets [41]. The calculation of the wake function has been performed, ignoring the perturbation of the generation and the propagation of the wake field in the spoilers. Therefore, the above result gives only a rough estimate of the wake fields excited at this section. Unfortunately, the surface roughness of the copper absorbers are unknown and their contribution to the wake fields could not been estimated so far.

Summary of wake potentials

The various contributions of the monopole and the dipole wake fields for a bunch length of $250 \mu\text{m}$ are listed in Table 3.21. The highest energy loss of the beam is induced by steps in the beam pipe, mainly the step behind absorber 1. The energy spread of the beam is primarily increased by the steps (resistive) and surface roughness (inductive). The transverse wake fields are dominated by surface roughness wakes. The kick of a beam with 1 mm offset and 230 MeV energy, induced at the two spoilers, amounts to $6 \mu\text{rad}$. The

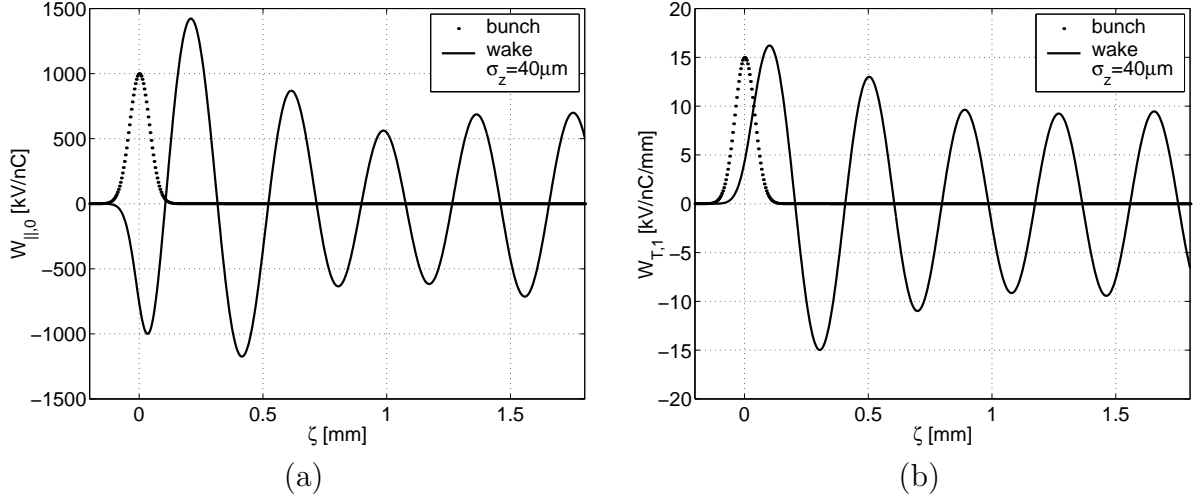


Figure 3.60: Surface roughness wake potentials excited at the spoilers for an ultra-short bunch with $\sigma_z = 40 \mu\text{m}$. The resonance frequency of the wake fields is 770 GHz or $\lambda_{res} = 390 \mu\text{m}$.

emittance growth is smaller than 1% at $\epsilon_{x,y}^N = 5 \mu\text{m}$.

wakes	$k_{ ,0}$	$(\langle (W_{ ,0} - k_{ ,0})^2 \rangle)^{1/2}$	$k_{\perp,1}$	$(\langle (W_{\perp,1} - k_{\perp,1})^2 \rangle)^{1/2}$
	[kV/nC]	[kV/nC]	[kV/nC/mm]	[kV/nC/mm]
tapers	5.84	16.5	0.54	0.21
steps	-76.1	30.0	0.67	0.40
gaps	-28.2	11.4	0.37	0.28
resistive	-3.0	3.2	0.22	0.08
roughness	-0.43	30.0	1.52	0.67

Table 3.21: Loss factors and variances of the wake fields excited in the collimator section.

Non-linear kicks

A beam with large offsets at the spoilers excites higher multipole wake fields. The superposition of the higher multipole wake fields cause a non-linear dependence of the transverse kick on the beam offset. If the beam passes close to the spoiler edge, the kick can be large enough to cause a beam loss at the downstream beam pipe. The non-linear kick induced by surface roughness wakes at the spoilers is the most dangerous one. The dependence of the kick on the beam offset r is described in the long-range approximation by the function \mathcal{S}_\perp (see Eq. 3.34).

3.8.2 Long range wake fields

A bunch which traverses a cavity-like vacuum device can excite electromagnetic modes. Trailing bunches can be affected by the electromagnetic fields of the modes. This effect is described by the so-called long range wake fields. The long range wake fields can seriously decrease the beam quality if the bunches couple strongly to a resonance mode of the device and if the damping time $1/\Gamma$ of the electromagnetic oscillations is much larger than the bunch spacing (see i.e. [39]). Since the effect on the n^{th} bunch in a bunch train is a

superposition of the long range wake fields by the leading $n-1$ bunches, the quality factor $Q = \omega/2\Gamma$ is the most critical parameter. Due to the large bunch separation in TTF ($t = 111$ ns at 9 MHz repetition rate) the required quality factors to avoid perturbations

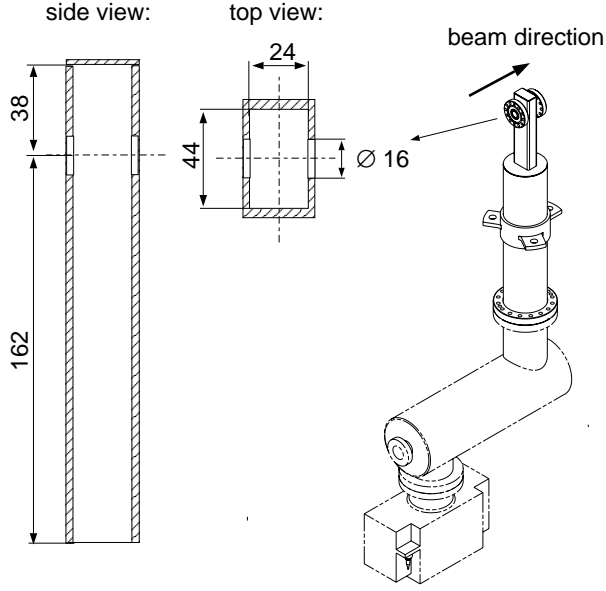


Figure 3.61: Geometry of pump-port between spoiler 1 and absorber 1.

of the beam are high (typically $Q < 10^3$ - 10^5 depends on the coupling factor R/Q). In the collimator section a cavity-like structure is the pump-port between spoiler 1 and absorber 1 shown in Fig. 3.61. This has been made of stainless steel to yield sufficiently small Q -values. With the choice of the material, an rf-shielding of the port or the implementation of higher order mode couplers to reduce the Q -factors are unnecessary. The resonances of the rectangular wave guide structure with attached beam tubes and the connections to the titan sublimation pump has been measured with an network analyser. The resonances with the largest Q -values are listed in Table 3.22. Because of the exponential decay ($\propto \exp(-\Gamma t)$) of the long range wake potential the amplitude is decreased to 2% of the maximum after already 4 bunch ($t = 444$ ns). Thus, any significant multi-bunch effect on the beam from the pump-port can be excluded. However, with copper plating ($Q \propto$ conductivity), the structure would create in the FEL operation mode a coupling of up to 120 bunches and the excited higher order modes have to be investigated in detail whether they could spoil the transverse beam quality.

mode	f_r [GHz]	Q-value	Γ [μs^{-1}]
1	6.770	1706	12.5
2	7.976	1997	12.5
3	8.839	2523	11.0
4	9.841	2373	13.0

Table 3.22: Resonance modes measured at pump-port 1.

Chapter 4

Summary

Radiation damage of the permanent magnets in the TTF-FEL undulator magnets is a serious problem. To protect the undulator from radiation damage a collimator system has been installed in the straight section before the undulator. In two stages, the electrons of the beam halo are removed by spoilers which define the phase space acceptance of the collimator section. It has been demonstrated by tracking calculation that the electrons passing the aligned collimator also pass the undulator without losses, provided their energy is within a bandwidth of $\Delta E/E = \pm 7\%$. This energy bandwidth is sufficient to guarantee a complete protection of the undulator during FEL operation.

Experimentally, however, dose rates of several hundred Gray per week have been observed in the first section of the undulator during time periods with rf-duty cycles of 0.1% and a dark current of about $10\text{-}30\,\mu\text{A}$ as measured in the collimator section. The observed dose rates are in disagreement with tracking calculations if the beam halo is assumed to have a small energy spread around the design energy. To clarify the situation, the emission of dark current from the rf gun cathode and its transport through the TTF linac has been investigated in detail. It has been found, that the energy spread of the dark current exceeds by far the energy bandwidth of the collimator. Only a fraction of about 42% of the dark current is removed by the collimator, while 0.8% is lost in the undulator. The calculated energy deposition in the undulator caused by dark current is in good agreement with the measured dose rates.

The basic reason for the low collimator efficiency in removing the dark current is the fact that no energy cut can be applied in this section. Hence an additional energy collimation in a dispersive section, for instance, between the second and third bending dipole in the bunch compressor 2, should allow the removal of the electrons outside the energy bandwidth which otherwise escape the collimator system. In the last shut down, a low energy scraper has been installed in the magnetic chicane, but has not yet been commissioned. Besides energy bandwidth limitations, alignment errors can cause an insufficient shielding of the undulator from losses of primary electrons. By Monte Carlo simulations, displacements of the collimator quadrupoles have been identified as the most critical ones. In order to compensate the kicks induced by displaced quadrupoles with the integrated correction coils, a beam based alignment method using the dependency of the FEL gain on the electron orbit has been applied.

Electrons hitting the spoilers of the collimator section initiate electromagnetic showers. Most secondary particles are removed by the absorbers downstream of the spoilers. But about 0.17% of the energy incident on the spoilers is mainly carried by the edge scattered

electrons, which escape the absorbers and are dumped in the undulator.

Experiments have been carried out in other laboratories to determine the threshold for radiation damage of the NdFeB permanent magnets at particle energies between 0.1 MeV and 2 GeV. Some of these experiments are analyzed by electromagnetic shower calculations to derive the irradiation spectra and the absorbed dose in the magnets. For the type of NdFeB permanent magnets used in the TTF undulator, 1% reduction of the remanent field has been determined at an absorbed dose of 70 kGy deposited by charged particles with energy above 20 MeV. In the case of particle energies well below 20 MeV, the absorbed dose can be more than an order of magnitude larger before 1% demagnetization of the magnets occurs. At very high energies (e.g. 2 GeV electrons incident on a thick target) the reported damage is in contradiction with the energy deposition by electromagnetic showers in the magnets. A possible explanation is that demagnetization mechanisms where neutrons are involved become important. Therefore, the analysis of the experiments at higher energies must also investigate the hadron dose and spectra. In particular, the allowable current losses for TTF phase 2 will be much smaller than for TTF phase 1. Measurements on the magnetic field profile of the disassembled undulator will provide additional important results on the radiation hardness of the magnets.

The damage threshold of 70 kGy and the removal efficiency of the collimator for secondary particles limit the accumulated energy incident on the spoilers to 580 MJ. For example, assuming an operation period of 1000 hours with the nominal duty cycle of the TTF linac (0.8%) at a beam energy of 230 MeV, the acceptable current losses in the collimator would be 1.1% of the beam current.

The electron beam has been tracked from the rf gun to the collimator to investigate the production and propagation of tails of the transverse charge distribution in phase space. Space charge forces at low energies and chromatic effects for an off-crest accelerated beam as needed for longitudinal compression have been identified to be the source of beam halo, which in the case of an optimized FEL operation exceeds the acceptance of the collimator in phase space. In the simulation, the induced beam losses at the spoilers are in the order of 1%. Thus, the demagnetization of magnets in the undulator due to the production of secondary particles escaping the absorber system may limit the total operation time of the undulator in the TTF1 arrangement.

Another limitation for beam losses in the collimator section is the production of neutrons, even though additional heavy concrete shields are added to the tunnel shielding. At 230 MeV and design current the acceptable radiation level outside the tunnel is reached at 0.6% beam losses.

The wake fields excited in the collimator section influence mainly the energy distribution of the beam. In the case of a gaussian bunch distribution with design rms-bunch length of 250 μ m and 1 nC charge, the mean energy loss and the rms-energy spread of the beam due to the wake fields sum to 100 keV and to 90 keV, respectively.

Because of the bunch length in the injector the non-linearity of the rf wave causes a non-gaussian charge distribution after the bunch compressor 2. The sharp rising peak of the bunch head, which contains about 26% of the total charge, can excite strong wake fields due to the surface roughness of the spoilers. The induced energy modulation of the bunch tail by these wake fields is more than ± 300 keV. Hence, the effect contributes to the energy break-up as observed behind the spectrometer dipole. This contribution may explain the difference between observation and numerical simulation of coherent synchrotron radiation for the energy beam break-up and has to be further investigated.

Appendix A

Beam Dynamics

A.1 Linear Beam Transfer Matrices

Drift space: A region free of electromagnetic fields is a drift space. The length of the drift space is denoted by L . The transfer matrix is

$$M_D = \begin{pmatrix} 1 & L & 0 \\ 0 & 1 & 0 \\ 0 & 0 & 1 \end{pmatrix}. \quad (\text{A.1})$$

Quadrupole: A quadrupole magnet focuses the beam in one plane, and defocuses it in the other. For a given magnetic field gradient g the strength of the quadrupole depends on the longitudinal momentum p_0 of the beam. Usually, the k -value given by $k = -e/p_0 \cdot g$ for electrons is used to describe the strength of a quadrupole. With $\Omega = \sqrt{|k|}L$ the transfer matrix in the focusing plane ($k < 0$) yields

$$M_{Qf} = \begin{pmatrix} \cos(\Omega) & \frac{1}{\sqrt{|k|}} \sin(\Omega) & 0 \\ -\sqrt{|k|} \sin(\Omega) & \cos(\Omega) & 0 \\ 0 & 0 & 1 \end{pmatrix}. \quad (\text{A.2})$$

and

$$M_{Qd} = \begin{pmatrix} \cosh(\Omega) & \frac{1}{\sqrt{k}} \sinh(\Omega) & 0 \\ \sqrt{k} \sinh(\Omega) & \cosh(\Omega) & 0 \\ 0 & 0 & 1 \end{pmatrix}. \quad (\text{A.3})$$

in case of the defocusing plane ($k > 0$).

Thin lens: Often it is sufficient to approximate the focusing of a beam by a thin lens of infinitesimal length. The transformation matrix of a thin lens is

$$M_F = \begin{pmatrix} 1 & 0 & 0 \\ -\frac{1}{f} & 1 & 0 \\ 0 & 0 & 1 \end{pmatrix}. \quad (\text{A.4})$$

with f the focusing length of the lens determined by

$$\frac{1}{f} = - \int ds k(s). \quad (\text{A.5})$$

For $f > 0$ the lens focuses the beam while it defocuses for $f < 0$.

Dipole sector magnet: At a dipole sector magnet the central trajectory crosses perpendicular the pole face of the magnet. The curved orbit of radius ρ causes a geometrical focusing term $1/\rho^2$ in the deflection plane. With the length l and a bending angle $\theta = l/\rho$ the transfer matrices in the deflection plane x is

$$M_{S,x} = \begin{pmatrix} \cos(\theta) & \rho \sin(\theta) & \rho(1 - \cos(\theta)) \\ -\sin(\theta)/\rho & \cos(\theta) & \sin(\theta) \\ 0 & 0 & 1 \end{pmatrix}. \quad (\text{A.6})$$

The vertical plane is described by a drift space $M_{S,y} = M_d$.

Finite pole gap: The previous result for a hard edge magnet takes only the effective magnetic length of the dipole into account. The fringe fields which are typically extend to about equal the gap height $2G$ of the magnet poles causes a fringe field focusing of the beam mainly in the vertical plane. The focusing is approximately given by

$$\frac{1}{f_y} \approx -\frac{G}{3\rho^2}. \quad (\text{A.7})$$

The vertical transfer matrix for a sector magnet taking the a thin length fringe field focusing into account yields

$$M_{Sf,y} = \begin{pmatrix} 1 + \frac{\theta G}{3\rho} & l & 0 \\ \frac{2G}{3\rho^2} + \frac{\theta G^2}{9\rho^3} & 1 + \frac{\theta G}{3\rho} & 0 \\ 0 & 0 & 1 \end{pmatrix}. \quad (\text{A.8})$$

Wedge magnet: Magnets with arbitrary pole face rotation angles are called wedge magnets. The sign convention for the entrance (δ_o) and the exit angle (δ_e) is shown in A.1. For small rotation angles the transfer matrix can be calculated by

$$M_W = M_{Fo} M_S M_{Fe}. \quad (\text{A.9})$$

The focusing effect due to the pole rotation and the fringe fields are approximated by thin lenses. The focal length of the lenses are

$$\frac{1}{f_{xi}} \approx \frac{\tan(\delta_i)}{\rho} \quad \text{and} \quad \frac{1}{f_{yi}} \approx -\frac{\tan(\delta_i)}{\rho} - \frac{G}{3\rho^2} \quad (\text{A.10})$$

with $i = o, e$ yielding the transfer matrices

$$M_{W,x} = \begin{pmatrix} \cos(\theta) - \frac{\rho \sin(\theta)}{f_{xo}} & \rho \sin(\theta) & \rho(1 - \cos(\theta)) \\ -\frac{\sin(\theta)}{\rho} - \frac{\cos(\theta)}{f_{xo}} - \frac{\cos(\theta)}{f_{xe}} + \frac{\rho \sin(\theta)}{f_{xo} f_{xe}} & \cos(\theta) - \frac{\rho \sin(\theta)}{f_{xe}} & \sin(\theta) - \frac{\rho(1 - \cos(\theta))}{f_{xe}} \\ 0 & 0 & 1 \end{pmatrix} \quad (\text{A.11})$$

for the horizontal plane and

$$M_{W,y} = \begin{pmatrix} 1 - \frac{l}{f_{yo}} & l & 0 \\ -\frac{l}{f_{yo}} - \frac{l}{f_{ye}} + \frac{l}{f_{yo} f_{ye}} & 1 - \frac{l}{f_{ye}} & 0 \\ 0 & 0 & 1 \end{pmatrix} \quad (\text{A.12})$$

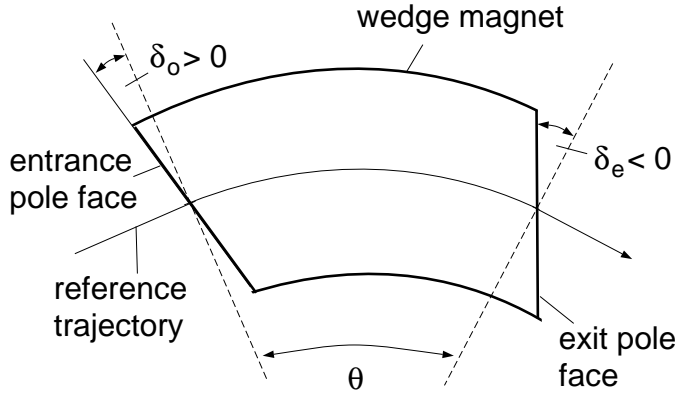


Figure A.1: Scheme of wedge magnet showing the sign convention for the pole rotation angles δ_o and δ_e .

for the vertical plane.

Rectangular dipole magnet with ($\delta_o = \delta_e$): A particular case of a symmetric wedge magnet is the rectangular magnet which has parallel end faces. If the magnet is installed symmetrically to the reference trajectory of the beam, the entrance and exit angles equal to half the bending angle ($\delta_o = \delta_e = -|\theta|/2$). The transformation matrix in the deflection plane x is from Eq. A.9

$$M_{R,x} = \begin{pmatrix} 1 & \rho \sin(\theta) & \rho(1 - \cos(\theta)) \\ 0 & 1 & 2 \tan(\theta/2) \\ 0 & 0 & 1 \end{pmatrix}. \quad (\text{A.13})$$

The rectangular dipole magnet transforms in the deflection plane like a drift space of length $\rho \sin(\theta)$ and does not focus the beam. The magnetic length l defined by the deflection angle $\theta = l/\rho$ is related to the straight magnet length L by

$$L = 2\rho \sin\left(\frac{l}{2\rho}\right). \quad (\text{A.14})$$

The transport matrix in the non-deflecting plane is

$$M_{R,y} = \begin{pmatrix} 1 - \frac{l}{f_y} & l & 0 \\ -\frac{2}{f_y} + \frac{l}{f_y^2} & 1 - \frac{l}{f_y} & 0 \\ 0 & 0 & 1 \end{pmatrix}, \quad (\text{A.15})$$

with ($G = 0$)

$$\frac{1}{f_y} = \frac{\tan(\theta/2)}{\rho}. \quad (\text{A.16})$$

For a rectangular dipole the beam is focused in vertical direction.

Combined function magnet: For separated function magnets either θ or k is set to zero while for combined function magnets both parameter are nonzero. The weak focusing from a dipole sector magnet and the focusing from the quadrupole can be combined as

$$K_x = k - \frac{1}{\rho^2} \quad \text{and} \quad K_y = -k, \quad (\text{A.17})$$

with K_x and K_y the effective horizontal and vertical focusing strengths. With $\Omega_x = \sqrt{|K_x|}l$ the beam transfer matrix for the horizontal plane in case of an effective focusing $K_x < 0$

$$M_{C,x} = \begin{pmatrix} \cos(\Omega_x) & \frac{1}{\sqrt{|K_x|}} \sin(\Omega_x) & \frac{1}{\rho|K_x|}(1 - \cos(\Omega_x)) \\ -\sqrt{|K_x|} \sin(\Omega_x) & \cos(\Omega_x) & \frac{1}{\rho\sqrt{|K_x|}} \sin(\Omega_x) \\ 0 & 0 & 1 \end{pmatrix} \quad (\text{A.18})$$

and

$$M_{C,x} = \begin{pmatrix} \cosh(\Omega_x) & \frac{1}{\sqrt{K_x}} \sinh(\Omega_x) & \frac{1}{\rho K_x}(\cosh(\Omega_x) - 1) \\ \sqrt{K_x} \sinh(\Omega_x) & \cosh(\Omega_x) & \frac{1}{\rho\sqrt{K_x}}(\sinh(\Omega_x)) \\ 0 & 0 & 1 \end{pmatrix} \quad (\text{A.19})$$

in case of an effective defocusing $K_x > 0$. The transfer matrix for the vertical plane is equal to that for a quadrupole (see Eqs. A.2 and A.3). The transformation matrix in cases of rotated entrance or exit pole faces can be obtained from Eq. A.9 by replacing the matrix M_S by M_C . The thin lenses used in Eq. A.9 remains unchanged and depend only on the dipole radius ρ , bending angle θ or the gab G . The fringe fields induced by the quadrupole gradient causes higher order non-linear field contributions which can not be taken into account by transfer matrices.

Standing wave cavity: In standing wave field pattern, the alternating transverse electromagnetic forces acting on the particles traveling off-axis and cause a net focusing effect which can be strong at low energy and high accelerating fields. Let E_{acc} denote the average acceleration gradient per cavity length L received by an ultra-relativistic particle injected at the rf-phase of maximum energy gain. For a particle injected at the phase $\Delta\phi = \phi_{rf} - \phi_{beam}$ the energy gain is then reduces to

$$\Delta E = eE_{acc}L \cos(\Delta\phi). \quad (\text{A.20})$$

An expression for the transfer matrix including off-crest acceleration has been derived in [99]

$$M_{acc} = \begin{pmatrix} \cos(\alpha) - \sqrt{2} \cos(\Delta\phi) \sin(\alpha) & \sqrt{8} \frac{LE_i}{\Delta E} \cos(\Delta\phi) \sin(\alpha) & 0 \\ -\frac{\Delta E}{LE_f} \left[\frac{2 \cos^2(\Delta\phi) + 1}{\sqrt{8} \cos(\Delta\phi)} \right] \sin(\alpha) & \frac{E_i}{E_f} \left[\cos(\Delta\phi) + \sqrt{2} \cos(\Delta\phi) \sin(\alpha) \right] & 0 \\ 0 & 0 & \frac{E_i}{E_f} \end{pmatrix}, \quad (\text{A.21})$$

with E_i and E_f the initial and final particle energy, respectively. The parameter α takes into account the net focusing effect of the cavity by using a thick lens approximation which has an effective lengths that is modified due to the reduced transverse momentum spread of the beam after passing an acceleration structure:

$$\alpha = \frac{1}{\sqrt{8} \cos(\Delta\phi)} \cdot \ln \left(\frac{E_f}{E_i} \right). \quad (\text{A.22})$$

Appendix B

Energy Measurement

In this appendix an orbit correction of the energy measurement at the dispersive section is discussed.

B.1 Layout of the spectrometer

The beam energy can be measured in a magnetic spectrometer. In Fig. B.1 the spectrometer dipole and the optical elements are shown. The electron beam is bend with the spectrometer dipole by 20° into the beam dump. The beam position in the dispersive section is measured with BPM3, 3.721 m downstream of the dipole. The beam energy is derived from the beam position in the dispersive section and the position and angle of the beam at the entrance of the spectrometer dipole. To adjust the beam orbit upstream the dipole two correction steerers, H1 and H2, build in quadrupoles have been foreseen. The beam trajectories are determined by BPM1 and BPM2. The position monitors in this areas are stripline BPMs [100].

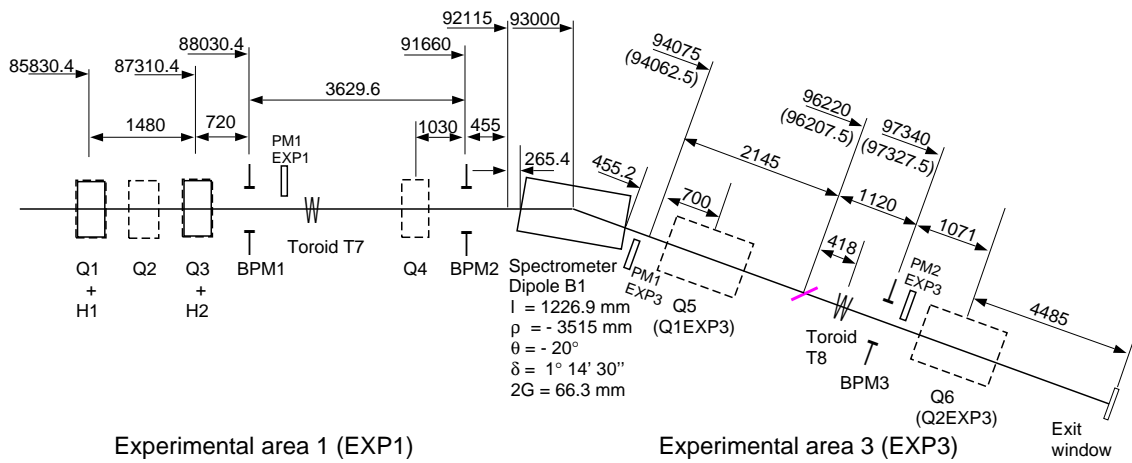


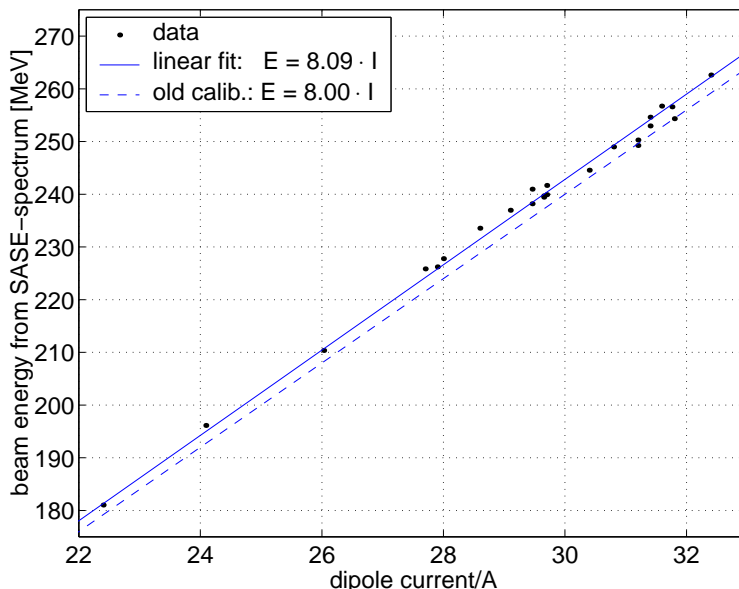
Figure B.1: Beam line close to the spectrometer dipole.

If the quadrupoles Q4 and Q5 are switched off, only drift spaces and the dipole with wedge poles have to be considered. By centering the beam in the monitors BPM1 and BPM2 and adjusting the spectrometer dipole current such that the beam passes through the horizontal center of the beam position monitor at EXP3 an accurate ($\sigma_E/E < 2 \cdot 10^{-4}$)

and reproducible energy measurement is obtained. The energy measurement is independent of the BPM calibration (readout voltage per unit beam offset) which otherwise can introduce systematic errors. The absolute energy depends on the integrated vertical magnetic field along the design trajectory of the beam through the spectrometer dipole. Unfortunately, the magnetic field of the spectrometer dipole has not been measured before installation. By measuring the central wavelength of the FEL-spectrum, shown in Fig. B.2 [101], the electron beam energy has been determined with an accuracy of about 1% to the spectrometer dipole current

$$p_0[\text{MeV}/c] = (8.09 \pm 0.1) \cdot I_{B1}[\text{A}] . \quad (\text{B.1})$$

Due to transverse beam jitter or orbit misalignments before and behind the spectrometer dipole the energy measurement includes systematic errors. The systematic errors cause the scattering of the data in Fig. B.2. With some effort using this method although an accuracy 0.1% for the absolute energy measurement can be achieved.



where $D_x(s_3)$ is the value of the dispersion function at the monitor BPM3 and Δx_3 the beam offset due to dispersion for an off-energy beam ($p \neq p_0$). In absence of a collective betatron motion the measured beam offset x_3 equals Δx_3 . The collective betatron motion δx_β occurs as a small perturbation of the measured beam position:

$$x_3 = \Delta x_3 + \delta x_\beta. \quad (\text{B.3})$$

Calling x_1 and x_2 the beam offsets at BPM1 and BPM2. The horizontal beam position and angle at the entrance of the dipole are given by

$$x = x_2 + l_{2d} \cdot x', \quad (\text{B.4})$$

$$x' = \frac{x_2 - x_1}{l_{12}}, \quad (\text{B.5})$$

with $l_{12} = 3.63$ m and $l_{2d} = 0.72$ m the drift spaces between the monitors and the dipole. With the transfer matrix elements from the entrance of the dipole at s_d to the BPM3 at s_3 , the correction term results to

$$\delta x_\beta = M_{11}(s_d, s_3)x + M_{12}(s_d, s_3)x' \quad (\text{B.6})$$

Combining Eqs. B.2-B.6 and the values for $M_{11} = 0.628$, $M_{12} = 4.726 \text{ m}^{-1}$ and the dispersion $D_x(s_3) = -1.489$ m the relative momentum deviation is

$$\frac{\Delta p}{p_0} = a_1 x_1 + a_2 x_2 + a_3 x_3 \quad \text{with} \quad (\text{B.7})$$

$$\begin{aligned} a_1 &= \frac{1}{D_x l_{12}} \cdot (M_{11} l_{2d} + M_{12}) = -0.958 \text{ m}^{-1} \\ a_2 &= -\frac{1}{D_x l_{12}} \cdot (M_{11}(l_{12} + l_{2d}) + M_{12}) = 1.380 \text{ m}^{-1} \\ a_3 &= \frac{1}{D_x} = -0.672 \text{ m}^{-1}. \end{aligned} \quad (\text{B.8})$$

The coefficients a_1 and a_2 reflect the sensitivity of the energy measurement to an orbit jitter. A beam offset of 1 mm at the BPM2 causes a systematic error in the energy measurement of 0.14 percent.

B.2.1 Calibration of the beam position monitors

The calibration of a BPM by evaluation of the individual response of different parts of the electronics is complicated and often carries excessive errors. In addition, the electronics of the stripline monitors does not include a sample and hold circuit which implies a high sensitivity to timing errors when the output signal of the electronics is digitized by ADCs. To obtain a correct position reading of the beam, a calibrated steerer and the knowledge of the transfer matrix can be used to measure the electronic response. To reduce other sources of systematic errors, the quadrupoles in the sections EXP1 and EXP3 have been cycled and the remnant magnetic fields compensated by an offset current. Table B.1 lists the measured magnetic fields at the pole tips of the quadrupoles and the required compensation currents.

The correction coil H1 bends the beam in the horizontal plane. The matrix elements

Name	cycling procedure [A]	remnant field at $I=0$ A [mT]	compensation current I_c [A]	remnant field at $I = I_c$ [mT]
Q1	0→-210→0	-1.0	0.45	≈ 0.1
Q2	0→-210→0	-1.5	0.7	≈ 0.1
Q3	0→210→0	1.0	-0.35	≈ 0.1
Q4	0→-120→0	-3.1	1.2	≈ 0.05
Q5	0→120→0	1.3	-0.5	≈ 0.1
Q6	0→120→0	1.1	-0.35	≈ 0.2

Table B.1: Required compensation currents for different quadrupoles to remove the remnant magnetic fields. The third row describes the used cycling procedure.

M_{12} transforming the kick of the correction coil to an offset at the location of BPM1, BPM2 and BPM3 are 2.2 m, 5.83 m and 8.84 m, respectively. The results of the calibration measurements are shown in Fig. B.3. During the measurement the bunch charge was 2 ± 0.2 nC.

The linear response differs for the BPMs by a factor of 2 and becomes non-linear for larger displacements. The response functions are described by third order polynomials (coefficients denoted by P_i). The asymmetric behavior of the BPMs with respect to the zero voltage reading causes a non-vanishing quadratic term P_2 . The spread of the measured values is induced by a position and energy jitter of the beam during the measurement. It is desirable that the response function of a beam position monitor is independent on the bunch charge. This has not yet been investigated experimentally.

BPM resolution:

To determine the BPM resolution for a single bunch the beam pickup signal induced in one of the horizontal striplines has been split [102, 100] by a -3 dB power divider. The two signals have been connected to both input channels of the electronics (see Fig. B.4). This guarantees that the original amplitude and shape of the signals created by ultra-short bunches in a stripline BPM are used for the measurement. The signals from the power divider are practically equal and the voltage output from the ideal difference over sum electronics would be zero. However, a real electronics generates an electronic noise which is recorded by the ADC. The voltage jitter transforms to a position jitter by using the response functions, shown in Fig. B.3. A bunch charge of 4 nC has been used to generate the equivalent signal of a 2 nC bunch after the power divider. For a single bunch per second the position jitter produced by the electronic noise is plotted in Fig. B.5. The rms-jitter of the BPMs varies between $80 \mu\text{m}$ and $280 \mu\text{m}$. The ratio between the rms-jitter and the linear coefficient P_1 (linear amplification) is best for the BPM2. All BPMs show a small electronic offset in the order of 20 mV which shifts the beam reading by $-210 \mu\text{m}$, $-370 \mu\text{m}$ and $380 \mu\text{m}$. The BPM3 shows a fairly poor resolution with a non-gaussian distribution. Because of this, the BPM resolution of a single bunch is characterized by two values

$$\text{the rms resolution: } \frac{\delta p_{res}}{p_0} = \sqrt{\sum_i (a_i \delta x_{i,res})^2} = 0.25 \cdot 10^{-3} \quad \text{and} \quad (\text{B.9})$$

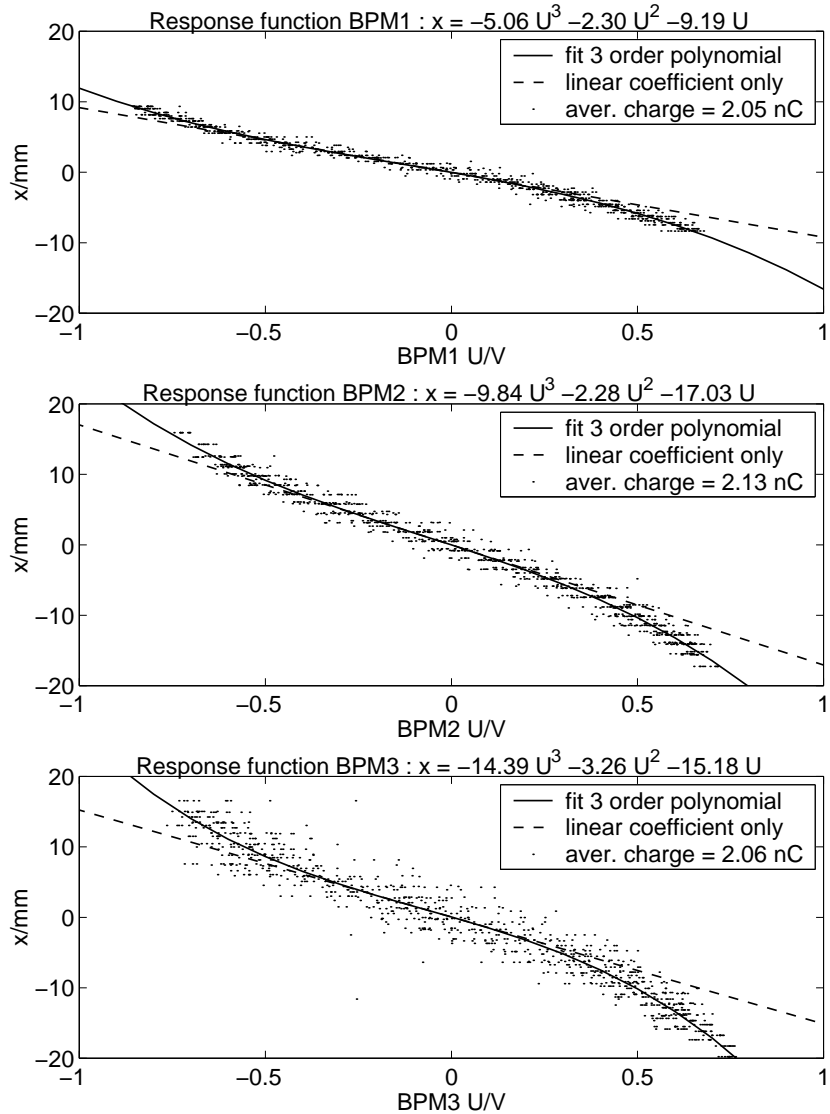


Figure B.3: Response functions of the BPM1, BPM2 and BPM3 in EXP1 and EXP3. The electron beam has been displaced with steerer H1. Each point represents the average of 10 bunches in a macro pulse.

$$\text{the peak to peak resolution: } \frac{\Delta p_{res}}{p_0} = \sum_i |a_i \Delta x_{i,res}| = 1.82 \cdot 10^{-3}. \quad (\text{B.10})$$

Since the coefficient for the orbit correction of the energy measurement a_3 is small compared to a_2 both BPMs, BPM2 and BPM3, reduce the final precision of the energy measurement.

B.2.2 First test of the orbit corrected energy measurement

For the calibration of the beam position monitors, all quadrupoles were switched off. In general the quadrupoles Q1-Q3 are required for a proper beam transport to the beam dump. The goal of an energy measurement to be independent on the initial conditions for the beam centroid has been cross-checked using the steerers H1 and H2 in the design optics. For this purpose, a sinusoidal current has been imposed to the corrector while the

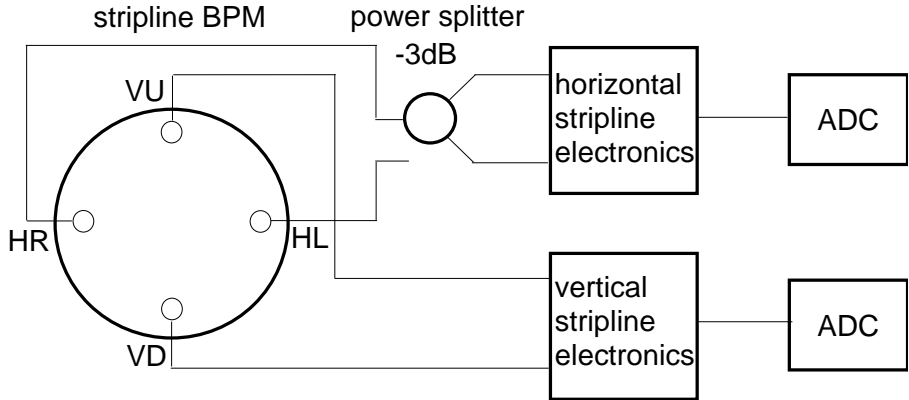


Figure B.4: Setup used to determine the resolution of the stripline electronics. The signal of only one stripline was used and fed to both inputs of the horizontal beam position detection electronics (difference over sum).

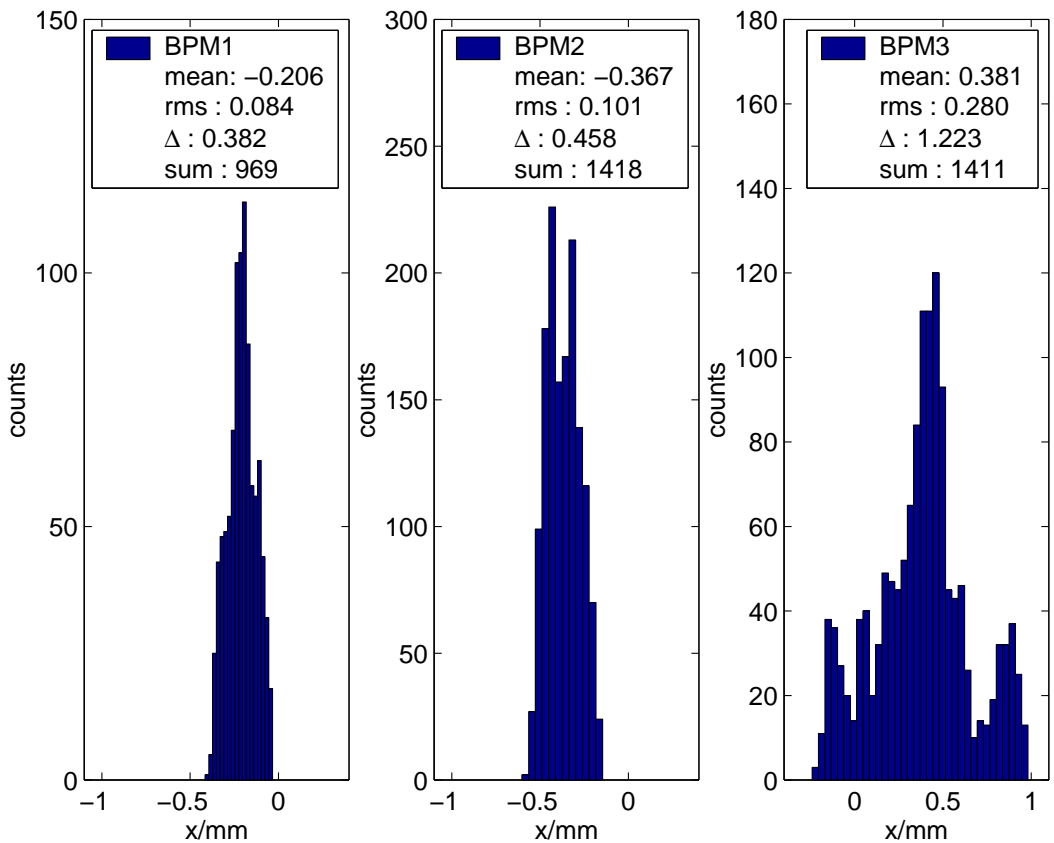


Figure B.5: Distribution of the position jitter caused by electronic noise of the stripline BPM. The bunch charge during the measurement was 4 nC.

beam position is recorded. If the perturbation of the orbit due to the corrector is large compared to the orbit and energy jitter of the beam, the computation of the transfer matrix and the calibration of the BPMs can be verified.

Figure B.6(a)-(c) shows the measured beam positions in the experimental area during the excitation of the steerers. In the time segment from 1400 s to 2200 s, only the steerer H1 was excited while the current of H2 was kept constant. The beam positions vary by about

1 cm in all BPMs. In the time segment from 2600 s to 3600 s, the steerer H2 was excited while the current of H1 was unchanged. Due to the small distance between the steerer H2 and the BPM1, an orbit variation has been observed mainly in BPM2 and BPM3. The energy deviation derived from BPM3 only is indicated at the vertical axis of Fig. B.6(c). Figure B.6(d) shows the bunch energy including the orbit correction. As can be seen from Fig. B.6(d), the beam energy is almost independent on the orbit variations. Only a very small synchronous variation still exists, particularly during the time period when H1 was excited. To analyze this error, the coefficients a_1 and a_2 have been varied to minimize the remaining periodic component. The result is shown in Fig. B.6(e) where Eq. B.7 has been extended to

$$\frac{\delta p}{p} = (1 + \delta_1)a_1x_1 + (1 + \delta_2)a_2x_2 + a_3x_3. \quad (\text{B.11})$$

The required corrections are $\delta_1 = -3.4\%$ and $\delta_2 = 5.64\%$. The systematic errors might be related to small imperfection of modeling the beamline or due to the quite noisy calibration of the BPMs. By repeating this measurement for different quadrupole setting and at more stable beam conditions the accuracy of the corrected coefficients can be evaluated and the systematic error might be identified.

B.3 First long macropulses with $800\mu\text{s}$ pulse duration.

After adjusting the optics for long pulse operation (see App. C) and an operational check of the fast protection system the macropulse duration had been increased to $800\mu\text{s}$. With a bunch spacing of 444 ns (2.25 MHz operation mode) a macropulse contains 1800 bunches. Since the ADC data acquisition rate is 1 MHz the number of measurable bunches are reduced to 201. Fig. B.7 shows the energy and beam positions of the individual bunches in a macropulse after a long pulse operation of about 1 hour. The average beam current was 7 mA . The current was 9 mA at the head of the macropulse, but drops to 6 mA at its end. The droop of the beam current was later compensated by a laser flash lamp power which increases over the macropulse duration.

The pulse to pulse charge jitter, the charge droop and a considerable number of missing beam pulses during operation caused either by the machine interlock or by gun events introduced difficulties for the adaptive feed forward system to adjust the beam loading compensation within the macropulse automatically [103]. To stabilize the bunch energy distribution the beam loading had been compensated in 8 time steps manually [104]. In Fig. B.7(a) the bunch energies in a macropulse is shown. The peaks indicated the beginning of the next beam loading compensation step where the forward power of the klystron has been changed. Already by using this rough method an rms-macropulse energy spread of 0.11% has been reached close to the TESLA design of 0.1% .

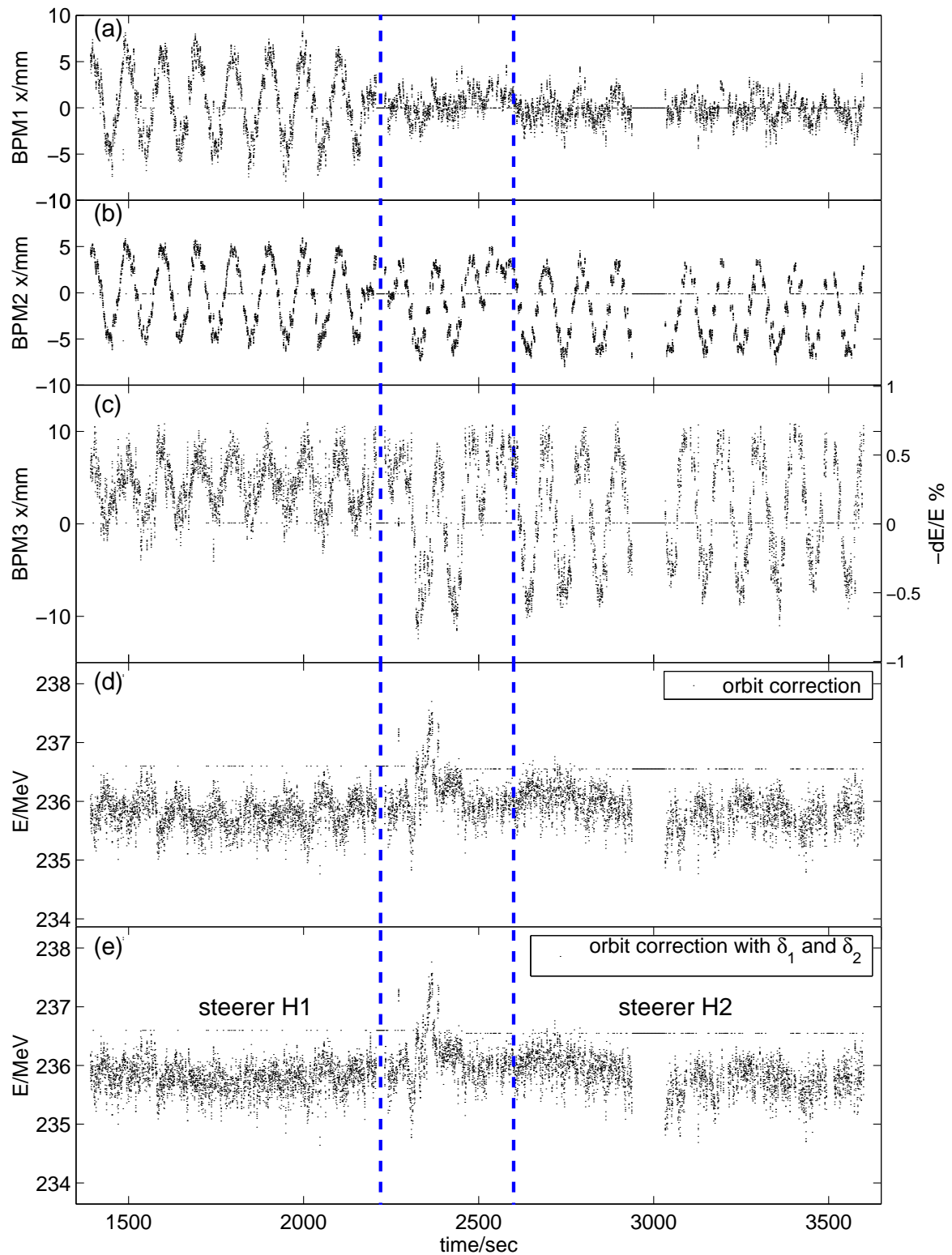
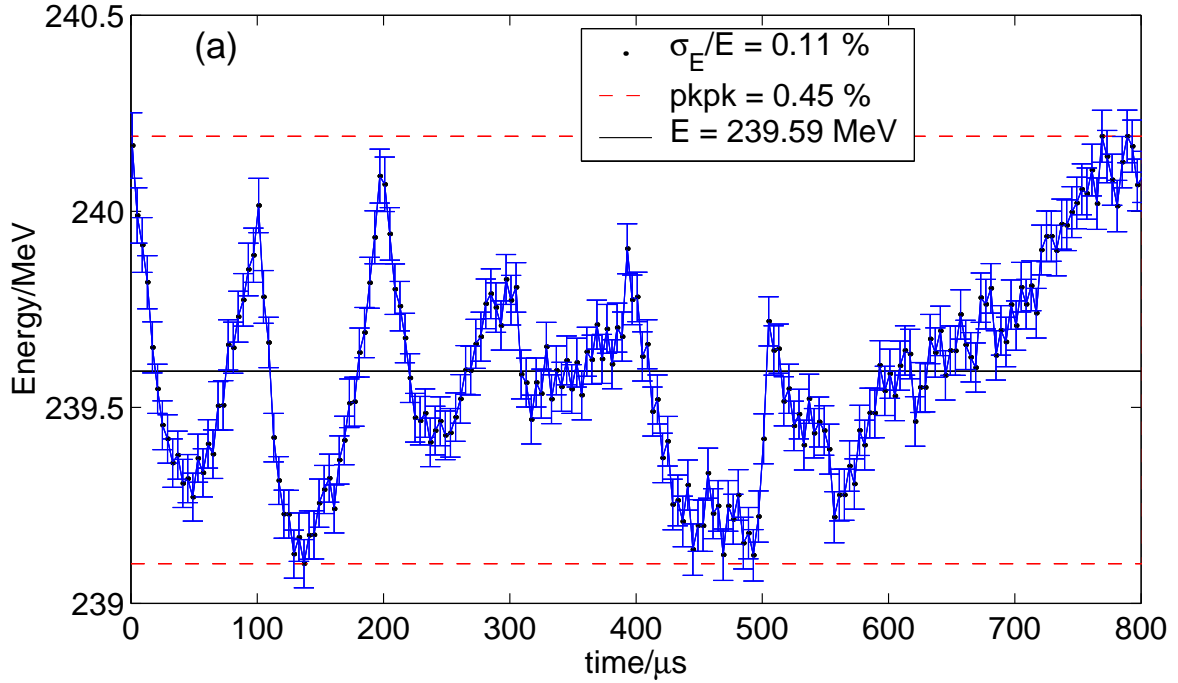


Figure B.6: First test of an orbit-independent energy determination. With the steerers H1 and H2 a sinusoidal orbit variation has been induced. Plot (a), (b) and (c) show the beam positions at BPM1, BPM2 and BPM3. The determined beam energy using the BPM3 only is shown in (c), with applied orbit correction the energy is plotted in (d), and including δ_1 and δ_2 for the orbit correction (see Eq. B.11) is shown in (e).

Macropulse at TTF 2001–01–18 23:02:47



Macropulse at TTF 2001–01–18 23:02:47

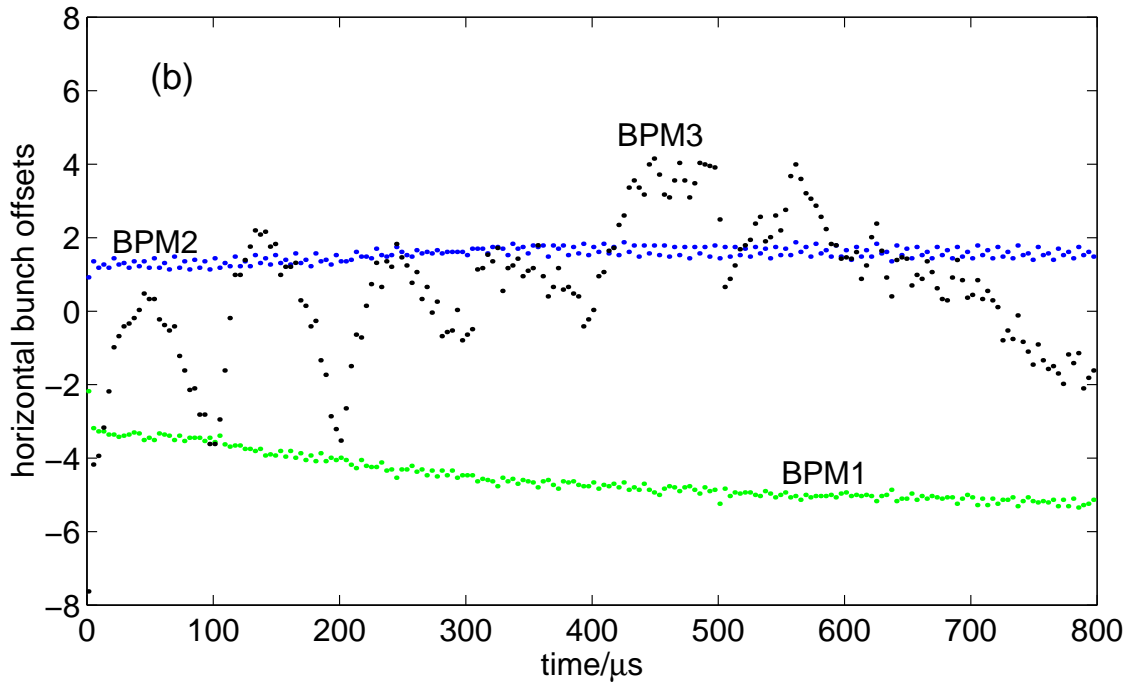


Figure B.7: (a) the bunch energy distribution in one of the first macropulse with 7 mA average beam current and pulse duration of 800 μ s. The beam loading compensation has been adjusted manually in 8 time steps within the macropulse. The peaks indicate the beginning of the next compensation step. The TESLA design energy spread of 0.1% has nearly been achieved after 1 hour long pulse operation. The errors are calculated from the rms-resolutions of the BPMs. (b) shows the measured horizontal beam positions in the experimental area in the macropulse.

B.4 Influence of quadrupoles Q4 and Q5 on the energy measurement

An orbit correction of the energy measurement is also possible if the quadrupoles Q4 and Q5 are used. In this case the measurement is more complex and the probability for systematic errors is increased. The formula in Eq. B.7 remains unchanged, but the coefficients (a_1, a_2, a_3) are now functions of the quadrupole strength k_{Q4} and k_{Q5} . If the transfer matrix between BPM1 and BPM2 is denoted by R one can write

$$a_1(k_{Q4}, k_{Q5}) = \frac{1}{D_x R_{12}} \cdot (M_{11} l_{2d} + M_{12}) \quad (\text{B.12})$$

$$a_2(k_{Q4}, k_{Q5}) = -\frac{1}{D_x R_{12}} \cdot (M_{11}(R_{12} + l_{2d}R_{22}) + M_{12}R_{22}) \quad (\text{B.13})$$

$$a_3(k_{Q5}) = \frac{1}{D_x} \cdot \quad (\text{B.14})$$

The measurement fails if the dispersion at the BPM3 vanishes ($D_x = 0$) or if the BPM1 is map to BPM2 via the quadrupole Q4. For quadrupole strength close to this cases, unacceptable large systematic errors are expected. For moderate focal length of the quadrupoles the dependence of the coefficients on one of the quadrupoles (zero gradient for the second one) is shown in Fig. B.8.

The magnitude of the coefficients together with resolution of the corresponding BPM

Coefficient	Q4		Q5	
	foc. 3.1 mT	foc. 0.05 mT	foc. 1.2 mT	foc. 0.2 mT
$\frac{\Delta a_1}{a_1} \%$	3.0	0.5	-1.5	-0.2
$\frac{\Delta a_2}{a_2} \%$	-0.8	-0.1	-4.1	-0.6
$\frac{\Delta a_3}{a_3} \%$	0	0	-4.1	0.6

Table B.2: Deviation of the coefficients a_i caused by remnant magnetic fields of the quadrupoles Q4 and Q5. First and third row shows the error made if no compensation current was used, while the second and forth row shows the remaining error after compensation (see also Tab.B.1).

define the achievable resolution for the energy measurement. Thus quadrupole gradients are preferred which lead to small values for the coefficients particular for those BPM with a poor resolution.

The derivative of a_i with respect to k determines the sensitivity of the coefficient to quadrupole gradient errors. The field strength k caused by not compensated remnant fields of the quadrupoles are indicated in Fig. B.8 by vertical lines. The estimated error of the coefficient in case of compensated and not compensated remnant quadrupole fields are listed in Table B.2.

For large slopes of the coefficients a_i chromatic correction of the quadrupole k-values have been taken into account. This might occur if it is desired to increase the range of the energy measurement by focusing the beam after the dipole ($k_{Q5} < 0$).

For non-vanishing gradients of Q4 and Q5 additional systematic errors for the energy measurement can be caused by quadrupole displacements. The kick induced by the quadrupoles have to be included to the calculations which requires the knowledge of the quadrupole displacements with respect to the linac axis.

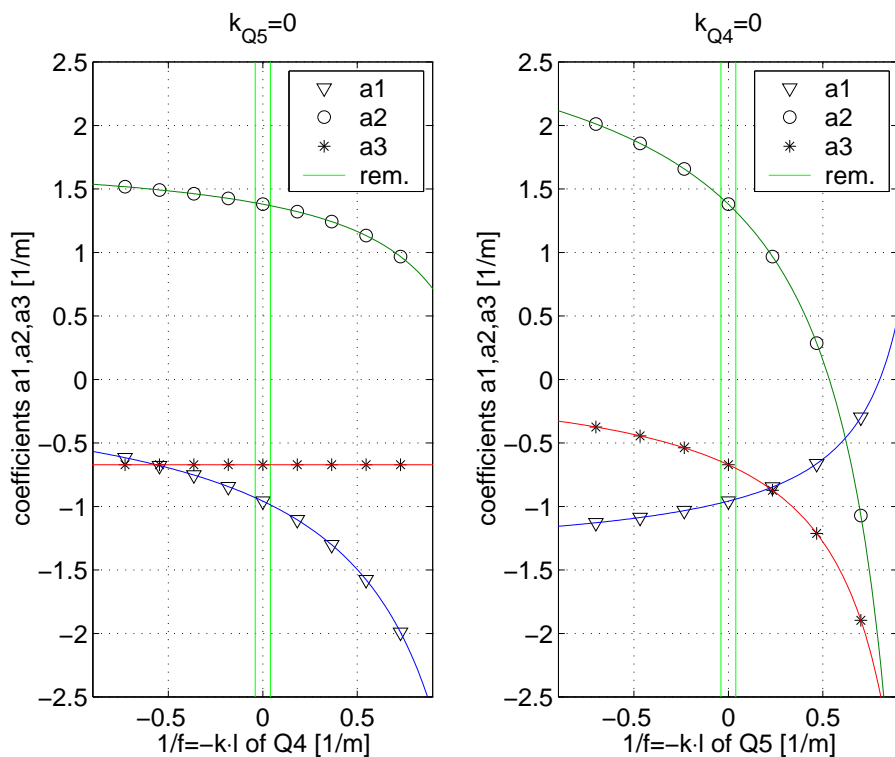


Figure B.8: Dependence of coefficients (a_1, a_2, a_3) on the k -values of Q_4 (left plot) and Q_5 (right plot). The values for not compensated remnant field of the quadrupoles at 230 MeV beam energy is indicated by vertical lines.

Appendix C

Safety of the Exit Window

The electron beam passing the dispersive dipole penetrates 9.3 m downstream a 1.0 mm thin CuCo0.5Be¹ vacuum window in front of the beam dump (exit window). The water cooled exit window has a diameter of 125 mm and has to survive

- the stress induced by the instantaneous temperature rise T_{inst} caused by the $4 \cdot 10^{13}$ electrons of a macropulse
- and the cycled thermal stress due to the heating up and cooling down of the material from macropulse to macropulse.

The latter is studied in the so-called Goodman diagram.

Instantaneous temperature rise:

During the short passage time $\tau = 800 \mu\text{s}$ of a bunch train the deposited heat is spread transversally by a typical diffusion length of $\langle d \rangle = \sqrt{\lambda\tau/\rho c} \approx 260 \mu\text{m}^2$. Since the beam size at the dump window is of the order of a few millimeters, it can be assumed that the instantaneous heating is proportional to the particle density. Including a linear approximation for the temperature dependence of the heat capacity $c(T) = c_0 + c_1 \cdot T$ ($c_0 = 0.3562 [\text{J/kgK}]$ and $c_1 = 1.0228 \cdot 10^{-4} [\text{J/kgK}^2]$)³ the instantaneous temperature rise at the center of the beam incidence can be expressed as

$$\Delta T_{inst} = \frac{c(T_{ini})}{c_1} \left[\sqrt{1 + \frac{2c_1}{c(T_{ini})} \Delta T(T_{ini})} - 1 \right] \quad (\text{C.1})$$

with

$$\Delta T(T_{ini}) = \left(\frac{dE}{\rho dx} \right) \frac{N_{train}}{2\pi\sigma_x\sigma_y c(T_{ini})}, \quad (\text{C.2})$$

the temperature rise obtained for a constant heat capacity at the initial temperature T_{ini} . With an energy deposition per unit length of $(dE/\rho dx) \approx 1.5 \frac{\text{MeV}}{\text{g/cm}^2}$ and a beam size of $\sigma_x\sigma_y = 1 \text{ mm}^2$ the instantaneous temperature rise starting from room temperature is

¹Chemical composition [%]: Co 0.48, Be 0.31, Fe 0.03, Si 0.03, Al 0.03, Cu rest. [105]

²Thermal conductivity $\lambda = 221\text{-}262 \text{ W/m K}$, density $\rho = 8.3 \text{ g/cm}^3$, heat capacity of $c = 0.380 \text{ J/g}$.

³Fit to data between 300 K and 600 K taken from [106].

376 K. The minimum beam size must be chosen large enough to guarantee that at least a single macropulse cannot destroy the metal plate.

Cyclic thermal stress:

Following the calculation in [107, 108] the equilibrium temperature at the center of the cylindrical symmetric exit window with water cooled flange of constant temperature T_{edge} can be estimated by ($\sigma_x = \sigma_y = \sigma_{\perp}$)

$$T_{eq}(r = 0) = T_{edge} + \left(\frac{dE}{dx} \right) \cdot \frac{\nu N_{train}}{4\pi\lambda} \ln \left(1 + \frac{b^2}{2\sigma_{\perp}^2} \right). \quad (\text{C.3})$$

The equilibrium temperature is proportional to the repetition rate of the bunch trains ν (1-10 Hz), but depends only logarithmically on the beam cross-section σ_{\perp} and the radius of the exit window $b = 62.5$ mm. Figure C.1 shows the equilibrium temperature as a function of the rms-beam size. The upper and lower temperature is approximated by $T_{max,min} \approx T_{eq} \pm T_{inst}(T_{min})/2$ and calculated using Eq. C.1 and Eq. C.3⁴.

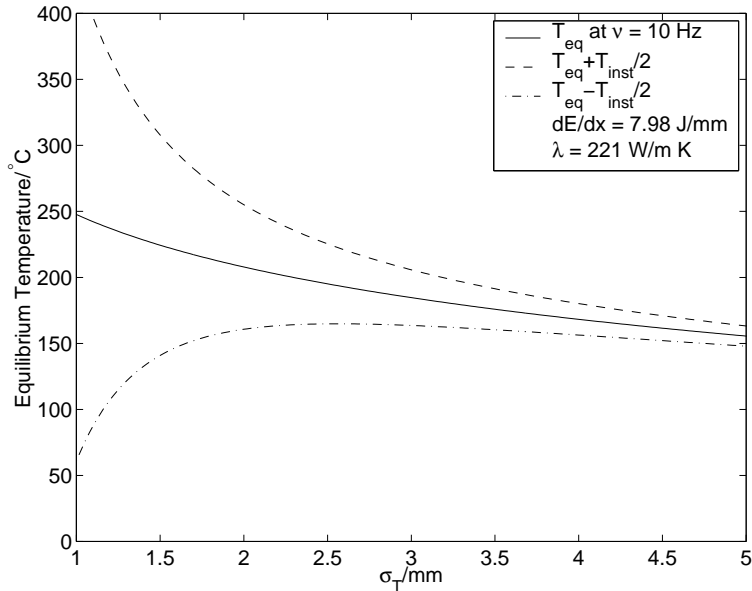


Figure C.1: Equilibrium temperature at the center of the exit window for different rms-beam size σ_{\perp} . The dashed and dotted lines are the temperatures before and after a beam train passage (10 Hz macropulse repetition rate).

The decision whether a material withstands the combination of the static stress σ_{static} caused by the atmospheric air pressure and the dynamic stress σ_{cyc} due to the periodic heat load by the energy deposition of the electron beam can be made using a so called Goodman diagram⁵. On the ordinate the endurance limit σ_E at the working (equilibrium) temperature is plotted. The endurance limit is the stress maximum of a material to a large number of cycles (typically 10^8). The ultimate tensile strength σ_{UTS} at the working point has to be plotted on the abscissa. The ultimate tensile strength is the maximum stress that

⁴Obviously, the calculation breaks down if $T_{min} \approx T_{edge}$. Then heat equation has to be solved to calculate the evolution of the temperature of the dump window.

⁵In the German literature the so called *Dauerfestigkeitsschaubild* is known as similar diagram.

a specimen withstand in a single test. At room temperature the endurance limit and the ultimate tensile strength for CuCo0.5Be are $\sigma_E = 275\text{-}310 \text{ N/mm}^2$ and $\sigma_{UTS} = 858 \text{ N/mm}^2$ [105].

A working point is determined in this plot by the coordinates (σ_m, σ_{cyc}) where $\sigma_m = \sigma_{static} + \sigma_{cyc}/2$ [107].

The static stress of a circular plate which is fixed at the edge is given by [109]

$$\sigma_{static} = \left\{ \begin{array}{l} 0.49 \\ 0.75 \end{array} \right\} \frac{b^2}{d^2} p = \left\{ \begin{array}{l} 191 \\ 293 \end{array} \right\} \text{ N/mm}^2 \quad \text{at} \quad \left\{ \begin{array}{l} \text{midpoint of plate} \\ \text{edge of plate} \end{array} \right\} \quad (\text{C.4})$$

with $p \approx 0.1 \text{ N/mm}^2$ the air pressure and $d = 1 \text{ mm}$ the thickness of the window. The cyclic thermal stress due to the rapid heating is proportional to the instantaneous temperature rise

$$\sigma_{cyc} \approx \frac{1}{2} \alpha E \Delta T_{inst}, \quad (\text{C.5})$$

with $\alpha = 18 \cdot 10^{-6}/\text{K}$ the coefficient of linear expansion and $E = 130 \text{ kN/mm}^2$ the modulus of elasticity. In the Goodman diagram the limiting line is obtained by connecting σ_{UTS} at the abscissa with σ_E at the ordinate. It divides unsafe operation conditions (above the line) from safe ones (below).

As shown in Fig. C.1 the equilibrium temperature is below 200°C for rms-beam size between 2-5 mm for 10 Hz repetition rate⁶. Both values, the ultimate tensile strength and the endurance limit are reduced to about 80% at the equilibrium temperature of 200°C [108]. The working points (σ_m, σ_{cyc}) for different beam sizes are plotted in the Goodman stress diagram in Fig. C.2(a). Already rms-beam radius of about 2 mm are close to the limiting line and lead to a critical operation. Usually a safety factor f is introduced, which is defined as the maximum value required to multiply on the working point (σ_m, σ_{cyc}) before crossing the limiting line. It can be calculated by

$$f = \frac{1}{\frac{\sigma_m}{\sigma_{UTS}} + \frac{\sigma_{cyc}}{\sigma_E}} \quad (\text{C.6})$$

and is plotted in Fig. C.2(b). The dependence of f between 4-5 mm rms-beam size is weak and results at edge of the exit window in a safety factor at 10 Hz of about 1.7.

The standard safety factor f for pressure chambers is 3.5. If no personal safety aspects have to be considered, usually a safety factor f between 2 and 3 for technical components is assumed to take into account material imperfections due to the fabrication process. Thus, the operation at 10 Hz repetition rate is critical and requires at least a well controlled beam incidence at the center of the exit window. Rms-beam sizes below 2 mm have a high probability to destroy the exit window.

C.1 Beam optics for long macropulse operation

In the previous section, the requirements on the beam cross-section for a safe long macropulse operation have been derived to avoid damages of the exit window. The calculations are based on the assumption that the beam is completely transmitted through

⁶At 1 Hz operation it has been assumed that the equilibrium temperature is close to the cooling water temperature of $T_{edge} = 30^\circ\text{C}$.

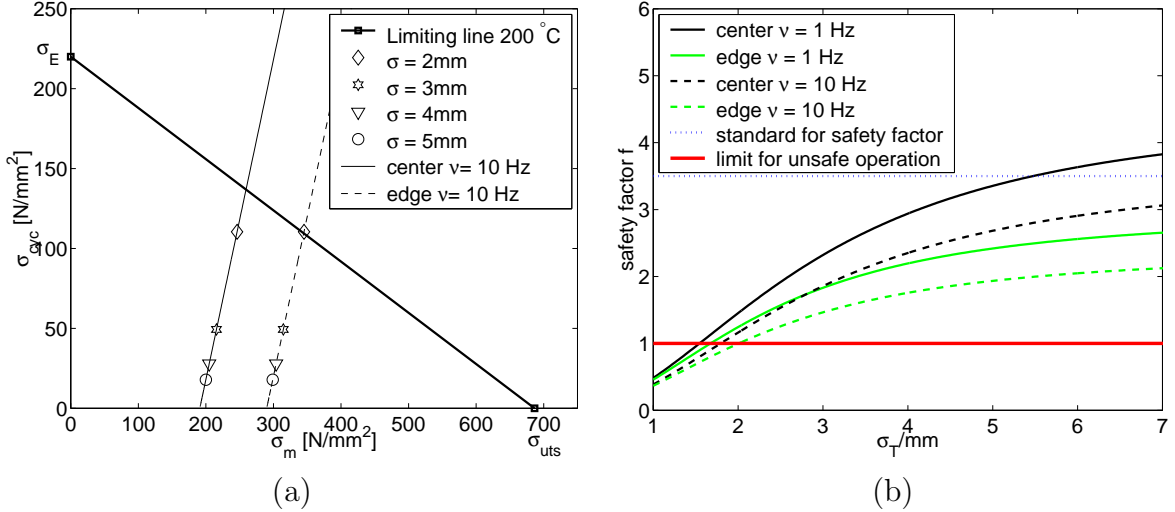


Figure C.2: (a) Goodman stress diagram for the CuCo0.5Be exit window. The working points correspond to the static stress caused by air pressure (solid line for midpoint of the window and the dashed line for maximum static pressure) and the thermal cyclic stress induced by the TTF beams of different rms-beam sizes. The limiting line is for a working temperature of 200°C. (b) safety factor f for the exit window of beam operation at 1 Hz and 10 Hz as a function of the rms-beam size. A safety factor $f = 1$ corresponds to the limit of stable operation. The dashed and dotted curves show the reduction of f when the beam incidents on the exit window at a point of maximum static pressure.

the exit window and is not lost at any other beamline device upstream. Thus the beam optics for safe operation have to fulfill the following conditions:

1. the beam cross-section has to be sufficiently large at the exit window and
2. the entire beam has to penetrate through the window.

Since the cross-section is proportional to the product of the horizontal and the vertical variances

$$\sigma_x = \sqrt{\beta_x \epsilon_x + \left(D_x \frac{\sigma_p}{p_0} \right)^2} \quad \text{and} \quad \sigma_y = \sqrt{\beta_y \epsilon_y}, \quad (\text{C.7})$$

with p_0 the momentum of the beam and $\epsilon_{x,y}$ the horizontal and vertical emittance. The first condition calls for large β -functions and a large dispersion D_x . The second condition

$$b \geq \sqrt{x_{exit}^2 + y_{exit}^2} \quad (\text{C.8})$$

with x_{exit} and y_{exit} the beam offsets at the exit window can be expressed in terms of $\beta_{x,y}$ and D_x by

$$x_{exit} = \sqrt{\frac{\beta_x}{\beta_{0,x}}} (\cos \psi_x + \alpha_{x,0} \sin \psi_x) \cdot x_0 + \sqrt{\beta_x \beta_{0,x}} \sin \psi_x \cdot x'_0 + D_x \cdot \frac{\delta p}{p} \quad (\text{C.9})$$

$$y_{exit} = \sqrt{\frac{\beta_y}{\beta_{0,y}}} (\cos \psi_y + \alpha_{y,0} \sin \psi_y) \cdot y_0 + \sqrt{\beta_y \beta_{0,y}} \sin \psi_y \cdot y'_0, \quad (\text{C.10})$$

which connects the beam centroid $(x_0, x'_0, y_0, y'_0, \delta p/p)$ at a given point upstream of the beamline with the beam centroid at the exit window. With increasing $\beta_{x,y}$ and D_x the 5-dimensional phase space volume $(x_0, x'_0, y_0, y'_0, \delta p/p)$ following Eq. C.8 decreases. Thus it is preferable to choose moderate values for (β_x, β_y, D_x) to satisfy both conditions.

Initial conditions for (β_0, α_0) :

The Twiss parameters (β, α) at the exit of the linac are determined by the initial values (β_0, α_0) at a given point upstream in the linac and the transfer matrix between this point and the exit window. The possible values for (β_0, α_0) are limited by beamline apertures. The smallest aperture system is in the collimator section. The beam loss detection system at the collimator section inhibits long macropulse operation at losses of about 0.1%. It can be assumed that rms-beam sizes

$$3 \cdot \sigma_{x,y} \leq r_{spoiler} \quad (\text{C.11})$$

in both planes and at both spoilers are required to permits macropulse operation. From the conditions in Eq. C.11 a low-limit cross-section at the exit window can be determined (worst case study). To design an appropriated optics for the experimental areas EXP1 and EXP3 the initial Twiss parameters are used with the highest transmission probability through the collimator section (see section 1.2.4).

Quadrupoles:

The number of quadrupoles which can potentially cause a damage of the exit window at long macropulse operation by improper settings should be minimized. Since the range of the initial conditions is restricted by the spoilers in the collimator section, only the quadrupoles at the experimental area EXP1 and EXP3 have to be considered. For an accurate energy measurement it is preferable to choose vanishing quadrupole gradients for Q4 and Q5 (see Fig. B.7). The optics using the remaining 4 quadrupoles (Q1-Q3 and Q6) has to demonstrate that a safe beam operation is achievable. Furthermore, the optics should be suitable for energy spread measurements of the beam at the screen in EXP3 which are regularly performed. Under this conditions various different optics have been studied.

Apertures at EXP1 & EXP3:

The apertures in the experimental areas limit the possible design of an optics by means of beam losses for too large β -functions. Since no beam loss monitor could be installed in the 3 m long drift space in front of the exit window the apertures in EXP1 and EXP3 can be used to prevent a dangerous beam transport to the beam dump. The devices should stay in the shadow region of the collimator spoilers to avoid additional beam losses and interruptions by the beam loss detection system which controls the losses in the experimental areas. The important beamline components and its geometry are listed in Table C.1. To define areas in horizontal and vertical phase space the beamline upstream and downstream of the devices have to be considered in the analysis.

Device	Geometry	Aperture	Photomultiplier
Slow wire scanner	cylindrical	$d = 35$ mm	PM1EXP1
Dipole vacuum chamber	rectangular	$d_y = 35$ mm	PM1EXP3
Toroid T8	cylindrical	$d = 75$ mm	PM2EXP3

Table C.1: Geometry and the apertures at EXP1 and EXP3. The devices are protected by beam loss monitors (names are given at last row).

Dispersion and minimum beam energy spread:

The most likely accident during beam operation is a sudden change in the beam energy. This might not been detected by the beam loss monitors in the straight linac sections. The last photomultiplier PM2EXP3 at the dispersive section equipped with an aluminum cathode detects beam losses induced at the toroid T8, the smallest aperture at this section. The diameter of the exit window and the dispersion at T8 ($D_{toroid} = -1.25$ m) determines an upper limit for the exceptable dispersion at the exit window

$$|D_{exit}| \leq \frac{b_{exit}}{b_{toroid}} |D_{toroid}| = 2 \text{ m.} \quad (\text{C.12})$$

For larger dispersion the beam can fail the exit window in case of an energy deviation. To fulfill Eq. C.12 the quadrupole Q6 must focus the beam in the horizontal plane. If the beam is focused too much in the horizontal plane the beam can fail the exit window in vertical direction. Therefore, the dispersion has been chosen to be $D_{exit} = -2$ m.

The minimum rms-energy spread of a bunch for on-crest acceleration was measured to be $\sigma_E = 100$ keV. The energy spread of a beam cannot be smaller than the energy spread of a single bunch. The minimum rms-beam size at a beam energy of 230 MeV for a vanishing β_x is

$$\sigma_x^{min} = D_{exit} \cdot \frac{\sigma_p}{p} \approx 0.9 \text{ mm.} \quad (\text{C.13})$$

Design β -function:

The β -function for the horizontal and the vertical plane has been chosen to be $\beta_x = 600$ m and $\beta_y = 1600$ m. The development of the optical functions is shown in Fig. C.3. Due to the focusing of quadrupole Q6 at the exit of the dispersive section an elliptical beam (ratio $\sigma_y/\sigma_x \approx 1.6$) at the exit window is preferable. The smallest normalized emittance for 4 nC bunch charge measured at the injector was about $\epsilon_x^N \approx \epsilon_y^N \approx 15 \mu\text{m}$. It results in a beam cross-section of

$$\sigma_x \cdot \sigma_y = 32.8 \text{ mm}^2 \quad (\text{C.14})$$

at the exit window. For a beam transmission through the center of the exit window the safety factor at 1 Hz operation is 3.5 and reduces to 2.5 if the beam incident on its edge. An optics appropriate for a beam energy spread measurement is plotted by the dashed curves in Fig. C.3. Vertically, the beam fits to the screen while the contribution of the horizontal rms-beam size to the energy spread measurement is 20 keV or $\Delta E/E = 10^{-4}$.

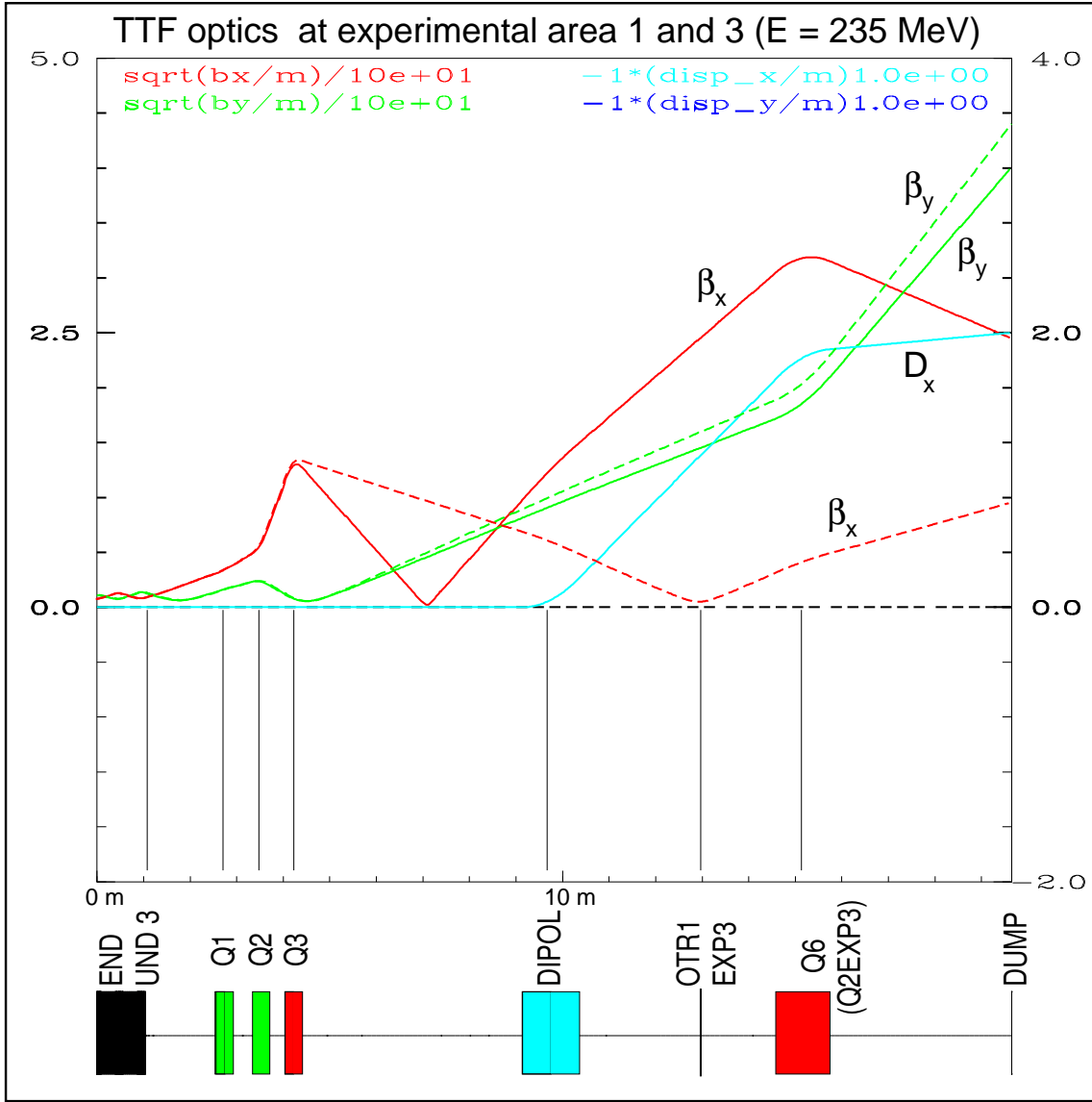


Figure C.3: Design optics at section EXP1 and EXP3. To protect the exit window in the long pulse operation mode, the Twiss parameters at the exit window are $\beta_x = 600$ m, $\beta_y = 1600$ m and $D_x = -2$ m (solid lines). The optics shown with the dashed lines can be used for energy spread measurements of the beam at the screen in EXP3 ($\beta_x = 0.28$ m, $\beta_y = 256$ m). The gradient of quadrupole Q3 has to be changed by 20% only to switch from the optics required for long macropulse operation to the optics suitable for energy spread measurements.

To switch from one optics to the other the current of Q3 has to be lowered by 20% only.

Beam transport and phase space acceptance:

To analyze the properties of the beam transport through the experimental section the relevant apertures listed in Table C.1 are imaged in the phase space at the exit window. The horizontal phase space is shown in Fig. C.4. The area labeled by “spoilers” shows the phase space acceptance of the collimator section (see Sec. 1.2.3). The phase space acceptance of the collimator is inside the exit window indicated by vertical lines (labeled by “exit window”) and has no overlap to the aperture of the slow wire scanner (labeled

by “wire”). The toroid T8, however, cuts the acceptance of the collimator by about 20%. Thus beam losses might be produced at the toroid T8 in presence of a large beam halo, a beam mismatch or a beam displacement in the collimator section. To remove the overlap between the collimator acceptance and the toroid T8 the horizontal beam size has to be further reduced at the exit window. A reduction of the horizontal beam size is in conflict to the vertical phase space where similar difficulties with the dipole vacuum chamber occur. It is also in conflict to the safety aspects of the exit window, as discussed below. The above optics is a compromise between the requirements of beam transport in the horizontal and the vertical plane. Beam losses detected at T8 indicate an improper beam

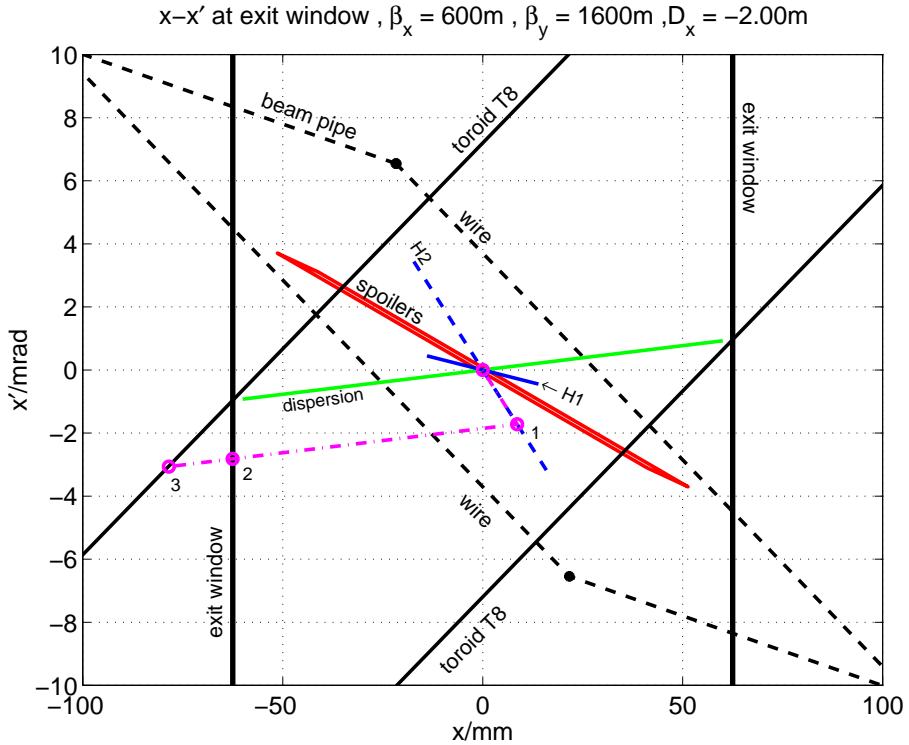


Figure C.4: Vacuum chamber apertures in the horizontal phase space at the exit window. The lines label with spoilers, wire (dashed) and toroid T8 are protected by the beam loss detection system. The shift of the beam centroid in the phase space by the steerers H1 or H2 or caused by an energy deviation are added to the plot.

operation at the linac.

The apertures upstream of the dipole shown in Fig. C.4 shift if the beam energy differs from the energy for which the dipole current has been adjusted. These apertures follow the solid line labeled by “dispersion”, while the apertures downstream of the dipole are not effected. The length of the line corresponds to $\pm 3\%$ energy deviation (or $\pm 3\%$ variation of the dipole current). For larger energy deviation beam losses at T8 occur which can be detected by PM2EXP3. Thus, a sudden energy change of the beam does not cause a horizontal offset larger than the diameter of the exit window without interrupting the beam by the active beam loss detection system. However, this holds only if the beam is centered in the collimator section.

The steerer H1 and H2 moves the phase space acceptance of the collimator (see lines labeled with “H1” and “H2”). The movement by H2 is large than for H1 and can produce beam losses at the toroid T8.

In general, a combination of the steerers and the dispersion which moves the collimator acceptance has to be considered to exclude the possibility that the beam misses the exit window. It turned out, that in the present set-up of the beamline it is extremely difficult, may be impossible, to design an optics such that beam losses in the drift space before the exit window are prevented if combinations between steerers, orbit displacements and energy offsets are considered. One likely, but avoidable situation is drawn by the dashed-dotted curve in Fig. C.4. The beam centered at the collimator section is deflected by H2 to the point 1. If now the dipole current is 3.5% to small (or the beam energy 3.5% to high) the beam would hit the edge of the exit window without producing any detectable beam losses at the toroid T8 (point 2). If the dipole current is further decreased by about 0.8% the interlock system would interrupt the beam operation (point 3). Such cases can be avoided by a careful monitoring of the beam positions and applying an orbit correction to the beam before the long macropulse operation starts.

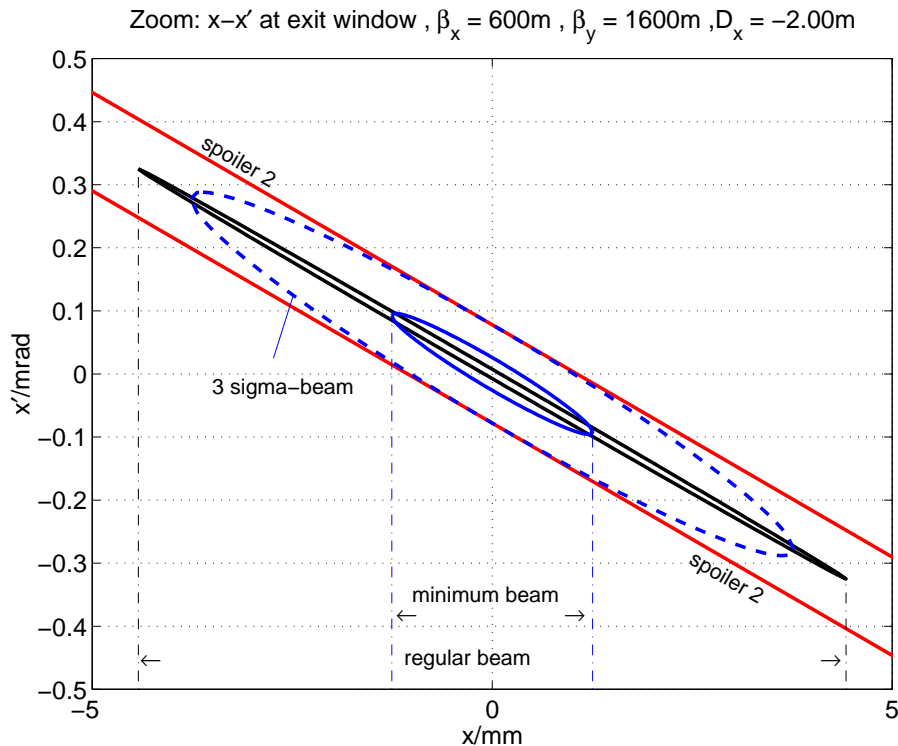


Figure C.5: Zoom by a factor 20 of the plot shown in Fig. C.4. The phase space ellipse of a beam at design optics (nominal beam) and of a beam that producing the minimum possible horizontal beam size at the exit window is shown. As observable from the 3σ -beam (9 times larger phase space) and the aperture of the spoiler the interlock is permitting such beam mismatch at the collimator section.

Due to the absence of dispersion the vertical phase space is less complex. By a proper choice for the gradient of Q6 (Q2EXP3) it can be guaranteed that the interlock system also protects the beam pipe close to the exit window.

To analyze the properties of the beam cross-sections the horizontal phase space plotted in Fig. C.4 is zoom by a factor 20 and shown in Fig. C.5. The phase space ellipse of a beam injected into the collimator with design Twiss parameters and of a beam which produces the minimum horizontal beam size at the exit window (worst case) are shown. In this plot, the enlargement of the beam sizes due to dispersion is not take into account. According to Eq. C.7 it adds quadratically to the rms-beam size obtained for a mono-energetic beam.

As shown by the 3σ -beam (dashed curve) the beam loss detection system permits the beam transport through the collimator section. The minimum rms-beam size for the design optics in the horizontal plane is 1.25 mm without dispersion and 1.6 mm with dispersion (at 100 keV energy spread) and in the vertical plane it is 1.63 mm. If both, the horizontal and the vertical approaches their minimum beam sizes, which is expected to be very unlikely, the limit for unsafe operation of the CuBe-exit window at a linac repetition rate of 1 Hz is reached.

Sensitivity of the optics:

The design optics must be robust against imperfections which might occur during beam operation. In order to estimate the sensitivity of the beam cross-section at the exit window several parameters as the beam energy or the magnet settings of the quadrupoles at the experimental area have been varied. The results for a regular beam (proper matching into collimator) and the worst case cross-section are summarized in Fig. C.6. The energy of the beam has been varied by $\pm 7.5\%$ without a major difference of the rms-beam size, while quadrupole settings towards smaller gradients produce smaller beam sizes at the exit of the linac. Particular the combination of a synchronous change of Q2 and Q3 reduces the beam cross-section by a factor of 2 at 10% smaller gradients.

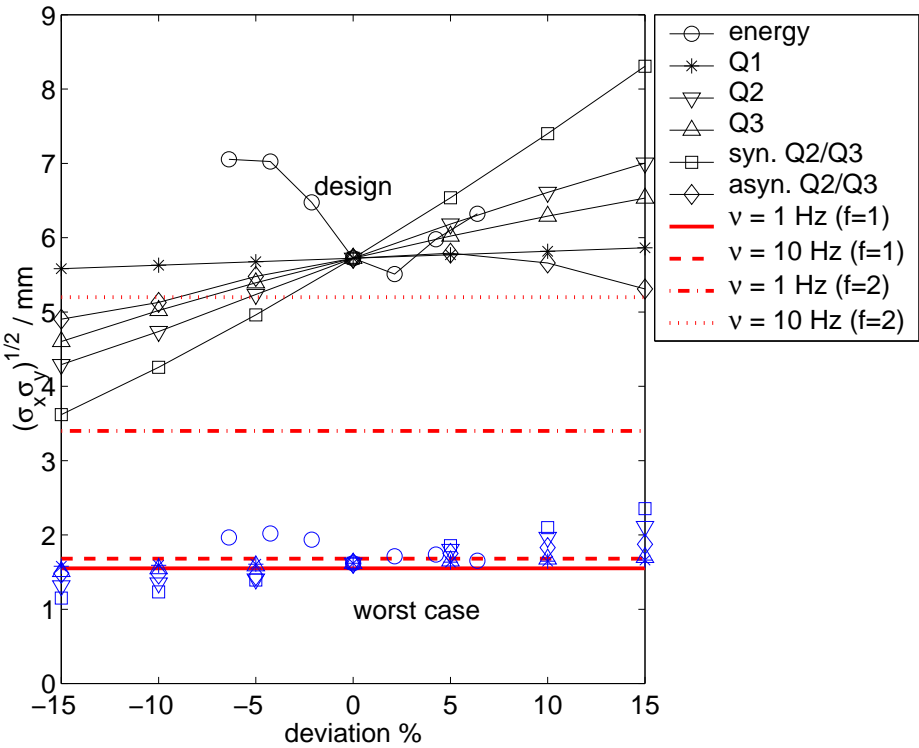


Figure C.6: Variation of the regular beam size at the exit window versus the energy deviation or deviations of quadrupole gradients (Q1-Q3). Squares and diamonds are used for combination of Q2 and Q3. The grey (blue) symbols show the results of the worst case estimate which could appear if the beam has a mis-match into the collimator section.

The minimum possible beam sizes calculated for an improper matching of the beam into the collimator are added to the plot in Fig. C.6. At 1 Hz and 10 Hz operation the limits for a damage of the exit window with a high probability ($f = 1$) are plotted by the

horizontal solid and dashed lines. In principle, there is the possibility to adjust the linac parameter such that no interlock is activated while the beam is operated in an unstable regime. Because the minimum possible beam size is close to this limits the probability for such an adjustment is negligible small.

The horizontal dashed-dotted (1 Hz) and dotted line (10 Hz) show the recommended safety factor $f = 2$ which has been determined including beam incidence close to the edge of the exit window. At 10 Hz operation, small deviations of the quadrupoles Q1 to Q3 can already reduce the beam size to a value below $f = 2$ where the beam operation is critical.

Quadrupole values at 235 MeV:

The k-values, the gradients and the currents of the quadrupoles in the experimental area are listed in Table C.2. The optics discussed above has been successfully used for the long macropulse operation at full beam currents in spring 2001 without any failures or major difficulties.

Name	k-value [m ⁻²]	gradient [T/m]	currents [A]
Q1	0.720	-0.564	-7.53
Q2	4.364	-3.421	-47.76
Q3	-3.573	2.801	39.30
Q4	≈ 0	≈ 0	-1.20
Q5 (Q1EXP3)	≈ 0	≈ 0	-0.50
Q6 (Q2EXP3)	-0.148	0.116	1.29

Table C.2: Quadrupole settings for long macropulse operation of the design optics calculated for a beam energy of 235 MeV.

Bibliography

- [1] Technical design report. Technical Report TESLA 01-23, Deutsches Elektronen-Synchrotron, DESY, March 2001.
- [2] M. Tigner. A Possible Apparatus for Electron Clashing-Beam Experiments. *Nuovo Cimento*, 37, 1965.
- [3] A. M. Kondratenko, E. L. Saldin. Generation of Coherent Radiation by a Relativistic Electron Beam in an Ondulator. *Part. Accelerators*, 10, 1990.
- [4] R. Bonifacio, C. Pellegrini, L. M. Narducci. Collective Instabilities and High-Gain Regime in a Free Electron Laser. *Opt. Commun.* **50**, 6, 1994.
- [5] Tesla Test Facility Linac - Design Report. Technical Report TESLA-FEL 95-01, Deutsches Elektronen-Synchrotron, DESY, March 1995.
- [6] TTF logbook 8 p.274 ff. H. Schlarb, A. Liepe, S. Schreiber, analyzed by P.Piot (13 January 2000).
- [7] Particle Data Group. *The European Physical Journal C*, volume 15. Societa Italiana di Fisica, Springer-Verlag 2000, 2000.
- [8] H. Wiedemann. *Particle Accelerator Physics*. Number 1. Springer-Verlag, New York Berlin Heidelberg, 1 edition, 1993.
- [9] W. P. Swanson. Radiological Safety Aspects of the Operation of Electron Linear Accelerators. Technical Report Series No.188, International Atomic Energy Agency (IAEA), February 1979.
- [10] A. Leuschner, H. Schlarb. Simulation and Measurement of Neutron Dose behind the Shielding of the TTF1 collimator section. Technical report, Deutsches Elektronen-Synchrotron, DESY, 2001. Laboratory Note DESY D3-117.
- [11] A. Fassò, A. Ferrari, J. Ranft, and P.R. Sala. New developments in FLUKA modeling of hadronic and EM interactions. *Workshop on Simulating Accelerator Radiation Environments SARE-3*, 1997.
- [12] A. Ferrari, T. Rancati, and P.R. Sala. FLUKA applications in high energy problems: from LHC to ICARUS and atmospheric showers. *Workshop on Simulating Accelerator Radiation Environments SARE-3*, 1997.
- [13] H. Wiedemann. *Particle Accelerator Physics*. Number 2. Springer-Verlag, New York Berlin Heidelberg, 2 edition, 1999.

- [14] J. Andruszkow et al. First Observation of Self-Amplified Spontaneous Emission in a Free-Electron Laser at 109 nm Wavelength. Technical Report DESY 00-066, Deutsches Elektronen-Synchrotron, DESY, May 2000.
- [15] J.S. Fraser, R.L. Sheffield and E.R. Gray. A new High-Brightness Electron Injector for Free Electron Lasers drive by RF Linacs. *Nuclear Instruments and Methods in Physics Research Section A*, 250:71–76, 1986.
- [16] B. E. Carlsten. New Photoelectric Injector Design for the Los Alamos National Laboratory XUV FEL Accelerator. *Nuclear Instruments and Methods in Physics Research Section A*, 285:313–319, 1989.
- [17] Eric R. Colby. Design, Construction and Testing of a Radiofrequency Electron Photoinjector for the Next Generation Linear Collider. Technical Report PhD Thesis, University of California Los Angeles (UCLA), 1997.
- [18] Jean-Paul Carneiro. Etude expérimentale du photo-injecteur de Fermilab. Technical Report PhD Thesis, Universite Paris XI UFR Scientifique D'Orsay, May 2001.
- [19] D. Sertore, S. Schreiber, K. Zapfe, D. Hubert and P. Michelato. Dark current at TTFL rf-gun. *Proceedings of the 22th international FEL Conference 2000, North Carolina*, August 2000.
- [20] E. Colby. A high Carge, high Duty Factor RF Photoinjector for the next Generation Linear Collider. *Proc. of the Linac Conference 1998*, 1998.
- [21] S. Schreiber. Performance Status of the RF-gun based Injector of the TESLA Test Facility Linac. *Proceedings of the EPAC00*, pages 309–311, 2000.
- [22] I. Will, A. Liero, S. Schreiber and W. Sandner. The TTF Photocathode Laser. *Proc. of the 21th international FEL conference 1999, Hamburg*, 1999.
- [23] Composants Quartz & Electronique, F-92391 Villeneuve-la-Garenne Cedex, France.
- [24] S. Schreiber, I. Will, D. Sertore, A. Liero and W. Sandner. Running Experience with the Laser System for the RF Gun based Injector at the TESLA Test Facility linac. *Nuclear Instruments and Methods in Physics Research Section A*, 445:427–431, 2000.
- [25] S. Schreiber for the TESLA Collaboration. The RF-Gun based Injector for the TeslaTest Facility Linac. *Proceedings of the Particle Accelerator Conference 1999, New York*, pages 1462–1464, 1999.
- [26] Ph. Piot, S. Schreiber, D. Sertore, K. Floettmann, A. Cianchi, L. Catani. Emittance Measurements at the TTF-Photoinjector. *Proceedings of the Particle Accelerator Conference 2001, Chicago*, 2001.
- [27] S. Schreiber and M. Ferrario. Private communication.
- [28] K. Honkavaara, Ph. Piot, S. Schreiber, D. Sertore. Bunch Length Measurements at the TESLA Test Facility using a Streak Camera. *Proceedings of the Particle Accelerator Conference 2001, Chicago*, 2001.

- [29] Kwang-Je Kim. RF and Space-Charge Effects in Laser-Driven Rf Electron Guns. *Nuclear Instruments and Methods in Physics Research Section A*, 275:201–218, 1989.
- [30] M. Ferrario, K. Flöttmann, B. Grigoryan, T. Limberg and P. Piot. Conceptual Design of the XFEL Photoinjector. Technical Report TESLA-FEL 01-03, Deutsches Elektronen-Synchrotron, DESY, 2001.
- [31] Bruce E. Carlsten. Space-Charge-Induced Emittance Compensation in High-Brightness Photoinjectors. *Particle Accelerators*, 41:27–65, 1994.
- [32] K. Flöttmann. Astra user manual. Technical report, Deutsches Elektronen-Synchrotron, DESY. www.desy.de/~mpyflo/Astra_documentation.
- [33] H. Schlarb. Diagnostic Tools for Ultra-Low Emittance and Ultra-Short Electron Bunches. *Proceedings of EPAC 2000, Vienna, Austria*, pages 187–191, 2000.
- [34] R.H. Fowler, L. Nordheim. Electrons in intense electric fields. *Proc. Roy. Soc. London, A-119*, page 173, 1928.
- [35] G.A. Loew and J.W. Wang. Field Emission and RF Breakdown in Copper Linac Structures. Technical Report SLAC-PUB-5059, SLAC, August 1989.
- [36] K. Flöttmann et al. Dark Current Emission from RF Electron Gun. Technical Report to be published, Deutsches Elektronen-Synchrotron, DESY, 2001.
- [37] W. Hartung et al. Studies of Photo-Emission and Field Emission in an RF Photoinjector with a High Quantum Efficiency Photo-Cathode. *Proceedings of the Particle Accelerator Conference 2001, Chicago*, 2001.
- [38] M. Geitz. Investigation of the Transverse and Longitudinal Beam Parameters at the TESLA Test Facility Linac. Technical Report DESY-THESIS 1999-033, Deutsches Elektronen-Synchrotron, DESY, November 1999.
- [39] N. Baboi. Studies on Higher Order Modes in Accelerating Structures for Linear Colliders. Technical Report DESY-THESIS 2001 (to be published), Deutsches Elektronen-Synchrotron, DESY, 2001.
- [40] B. Faatz, J. Feldhaus, J. Krzywinski, E.L. Saldin and E.A. Schneidmiller. Regenerative FEL Amplifier at the DESY TESLA Test Facility as a Full Coherent VUV Laser. Technical Report TESLA-FEL 97-07, Deutsches Elektronen-Synchrotron, DESY, 1997.
- [41] M. Hüning, P. Piot, H. Schlarb. Observation of Longitudinal Phase Space Fragmentation at the TESLA Test Facility Free-Electron Laser. Technical Report TESLA-FEL 00-05F, Deutsches Elektronen-Synchrotron, DESY, 2000.
- [42] R. Talman. Noval Relativistic Effect Important in Accelerators. *Physical Review Letters*, 14:1429–1432, 1986.
- [43] E.P. Lee. Cancellation of the Centrifugal Space-Charge Forces. *Particle Accelerators*, 25:241–251, 1990.

- [44] Ya.S. Derbenev, J. Rossbach, E.L. Saldin and V.D. Shiltsev. Microbunch Radiative Tail-Head Interaction. Technical Report TESLA-FEL 97-05, Deutsches Elektronen-Synchrotron, DESY, September 1995.
- [45] Ya.S. Derbenev and V.D. Shiltsev. Transverse Effects of Microbunch Radiative Interaction. Technical Report SLAC-PUB-7181, SLAC, Standfort, June 1996.
- [46] E. Saldin, E. Schneidmiller, M. Yurkov. On the coherent radiation of an electron bunch moving in an arc of a cicle. Technical Report TESLA-FEL 96-14, Deutsches Elektronen-Synchrotron, DESY, 1996.
- [47] M. Dohlus and T. Limberg. Emittance growth due to wake fields on curved bunch trajectories. *Nuclear Instruments and Methods in Physics Research Section A*, 393:494–499, 1997.
- [48] M. Dohlus, A. Kabel, T. Limberg. Design Consequences of Coherent Synchrotron Radiation Beam Dynamic Effects on the TTF-FEL Bunch Compression System. Technical Report TESLA-FEL 97-06, Deutsches Elektronen-Synchrotron, DESY, 1997.
- [49] M. Dohlus, A. Kabel, T. Limberg. Uncorrelated Emittance Growth in the TTF-FEL Bunch Compression Section due to Coherent Synchrotron Radiation and Space Charge Effects. *Proceedings of EPAC98*, 1998.
- [50] M. Dohlus, A. Kabel and T. Limberg. Optimal Beam Optics in the TTF-FEL Bunch Compression Section: Minimizing the Emittance Growth. *Proceedings of the 1999 Particle Accelerator Conference, New York*, pages 1650–1652, 1999.
- [51] T. Limberg, P. Piot, E.A. Schneidmiller. An Analysis of Longitudinal Phase Space Fragmentation at the TESLA Test Facility. Technical Report TESLA-FEL 00-05G, Deutsches Elektronen-Synchrotron, DESY, 2000.
- [52] A. Kabel, M. Dohlus and T. Limberg. Using TraFiC⁴ to calculate and minimize emittance growth due to coherent synchrotron radiation. *Nuclear Instruments and Methods in Physics Research Section A*, 455:185–189, 2000.
- [53] P. Emma, R. Brinkmann. Emittance Dilution through Coherent Energy Spread Generation in Bending Systems. *Proceedings of the 1997 Particle Accelerator Conference, Vancouver*, pages 1679–1681, 1997.
- [54] A. Loulergue, A. Mosnier. A simple-Chicane for the final Bunch Compressor of TTF-FEL. *Proceedings of EPAC00*, pages 752–754, 2000.
- [55] TTF logbook 18 p. 39 and p. 79.
- [56] B. Faatz, J. Pflueger. Magnet sorting for the ttf-fel undulator using simulated annealing. Technical Report TESLA-FEL 99-02, Deutsches Elektronen-Synchrotron, DESY, February 1999.
- [57] J. Pflueger, P. Gippner, A. Swiderski, T. Vielitz. Magnetic characterization of the Undulator for the VUV-FEL at the TESLA Test Facility. *Proc. of the 21th international FEL conference 1999, Hamburg*, 1999.

[58] K. Wittenburg and H. Schultz. A Proposal for Using Wire-Scanners at the LINAC Test Facilities. Technical Report TESLA 94-15, Deutsches Elektronen-Synchrotron, DESY, 1994.

[59] U. Hahn, J. Pflueger and G. Schmidt. Concept of electron beam diagnostic for the VUV SASE FEL at the TESLA Test Facility (TTF FEL) at DESY. *Nuclear Instruments and Methods in Physics Research Section A*, 429:279–280, 1999.

[60] Sergei Striganov, G. Schmidt and K. Wittenburg. Estimation of the signal from the wire scanner in the TTF. Technical Report TESLA 99-08, Deutsches Elektronen-Synchrotron, DESY, April 1999.

[61] G. Schmidt. Private communication, DESY, 1998.

[62] J. Pflueger. Private communication, DESY, 2001.

[63] B. Faatz and P. Pflueger. Private communication, DESY, 2000.

[64] W. Brefeld, P. Castro, T. Limberg and H. Schlarb. Beam optics for the ttf linac. internal note.

[65] P. Colomp, T. Oddolaye and P. Elleaume. Demagnetization of Permanent Magents to 180 MeV Electron Beam. Technical Report ESRF/MARCH-ID/93-09, European Synchrotron Radiation Facility, ESRF, March 1993.

[66] S. Okuda, K. Ohashi and N. Kobayashi. Effects of electron-beam and γ -ray irradiation on the magnetic flux of Nd-Fe-B and Sm-Co permanent magnets. *Nuclear Instruments and Methods in Physics Research Section B*, 94:227–230, 1994.

[67] T. Ikeda and S. Okuda. Magnetic flux loss of the permanent magnets used for the wigglers of FELs by irradiation with high-energy electrons or X-rays. *Nuclear Instruments and Methods in Physics Research Section A*, 407:439–442, 1998.

[68] H. B. Luna, X.K. Maruyama, N.J. Colella, J.S. Hobbs, R. S. Hornady, B. Kulke and J.V. Palomar. Bremsstrahlung radiation effect in rare earth permanent magnets. *Nuclear Instruments and Methods in Physics Research Section A*, 285:349–354, 1989.

[69] M. Talvitie, O-P. Kahkonen, S. Makinen, H. Rajainmaki, M. Manninen and V. Lindross. Magnetic-Flux Loss in Nd-Fe-Be Magnets Irradiated with 20 MeV Protons. *Journal of Magnetization and Magnetic Material*, 102:323, 1991.

[70] R.D. Brown and J.R. Cost. Radiation-Induced Changes in Magnetic Properties of Nd-Fe-B Permanent Magnets. *IEEE Transactions on Magnetics*, 25(4):3117–3120, 1989.

[71] E.R. Moog, P.K. Hartog, E.J. Semones, and P.K. Job. Radiation Doses to Insertion Devices at the Advanced Photon Source. *10th U.S. nat. conf. synchr. rad. instr., AIP conf. proc.*, 417:219–223, 1997.

[72] T. Bizen, T. Tanaka, Y. Asano, D.E. Kim, J.S. Bak, H.S. Lee, and H. Kitamura. Demagnetization of undulator magnets irradiated with high energy electrons. *Nuclear Instruments and Methods in Physics Research Section A*, 467-468:185–189, 2001.

- [73] Walter R. Nelsen, Hideo Hirayama, Davied W.O. Rogers. The EGS4 Code System. Technical Report SLAC-265, Stanford Linear Accelerator Center, December 1985.
- [74] J. Alderman et al. Radiation-Induced Demagnetization of Nd-Fe-B Permanent Magnets. Technical Report LS-290, Advanced Photon Source, Argonne National Laboratory, November 2000.
- [75] M. Rüter. Temperature rise in the TTF spoilers phase I, calculated with ANSI.
- [76] The NLC Design Group. Zeroth-Order Design Report for the NLC. Technical Report SLAC-474, SLAC, 1996.
- [77] Conceptual Design of a 500 GeV e^+e^- -Linear Collider with Integrated X-ray Laser Facility. Technical Report DESY 1997-048, Deutsches Elektronen-Synchrotron, DESY, May 1997.
- [78] The SASE scan procedure has been implemented by P. Castro.
- [79] TTF: DIff Orbit reference values; Fri Aug 10 08:08:20 2001.
- [80] L. Palumbo, V.G. Vaccaro and M. Zobov. Wake Fields and Impedance. Technical Report LNF-94/041(P), Laboratori Nationali di Frascati, September 1994.
- [81] W.K.H. Panofsky and W.A. Wenzel. Some Consideration Concerning the Transverse Deflection of Charge Particles in Radio-Frequency Fields. *Rev. Sci. Instrum.*, 27:947, 1956.
- [82] A. W. Chao. *Physics of Collective Beam Instabilities in High Energy Accelerator*. New York, John Wiley & Sons, Inc., 1993.
- [83] H. Schlarb. Resistive Wall Wake Fields. Technical Report TESLA 97-22, Deutsches Elektronen-Synchrotron, DESY, November 1997.
- [84] K. Yokoya. Impedance of Slowly Tapered Structures. Technical Report CERN SL/90-88 (AP), KEK Japan, July 1990.
- [85] S.A. Heifets. Diffractive model of the high-frequency impedance. *Physical Review D*, 40(9):3097–3106, 1989.
- [86] L. Palumbo. Analytical Calculation of the Impedance of a Discontinuity. *Particle Accelerators*, 25:201–216, 1990.
- [87] E. Gianfelice and L. Palumbo. Dipole Impedance of a Conducting Cylindrical Pipe with a Discontinuous Cross Section. *IEEE Transaction of Nuclear Science*, 37:1084–1089, 1990.
- [88] Yong Ho Chin. User’s Guide for ABCI, Version 8.7. Technical Report CERN SL/94-02, European Organization for Nuclear Research, February 1994.
- [89] A. Piwinski. Wake Fields and Ohmic Losses in round vacuum chambers. Technical Report DESY HERA 92-11, Deutsches Elektronen-Synchrotron, DESY, May 1992.

[90] O.Henry and O.Napoly. The Resistive Pipe Wake Potentials for Short Bunches. *Particle Accelerators*, 35:235–247, 1991.

[91] Karl L.F. Bane. The Short Range Resistive Wall Wakefields. Technical Report SLAC-AP-87, Stanford Linear Accelerator Center, 1991.

[92] K. Yokoya. Resistive Wall Impedance of Beam Pipes of General Cross Section. *Particle Accelerators*, 41:221–248, 1993.

[93] A. Novokhatski, A. Mosnier. Wakefields of Short Bunches in the Canal Covered with thin Dielectric Layer. *Proceedings of the 1997 Particle Accelerator Conference, Vancouver, Canada*, pages 1661–1663, 1997.

[94] M. Timm. Wake Fields of Short Ultra-Relativistic Electron Bunches. *Der Andere Verlag, ISB N 3-935316-11-9*, 2098.

[95] A. Novokhatski, M. Timm, T. Weiland and H. Schlarb. A proposal for the Surface Roughness Wake Field Measurement at the Tesla Test Facility. *Proceedings of the 1999 Particle Accelerator Conference, New York*, pages 2879–2881, 1999.

[96] M. Hüning, H. Schlarb and M. Timm. Experimental set to measure the wake fields excited by a rough surface. *Nuclear Instruments and Methods in Physics Research Section A*, 445:362–364, 2000.

[97] M. Hüning and P. Schmueser. Experimental investigation of wake fields excited by a rough surface. *Proceedings of the 23th international FEL Conference, Darmstadt, (to be published)*, 2001.

[98] M. Hüning. Private communication, August 2001.

[99] C. Stolzenburg. Untersuchungen zur entstehung von dunkelstrom in supraleitenden beschleunigungsstrukturen. Technical Report DESY-THESIS 1996, Deutsches Elektronen-Synchrotron, DESY, 1996.

[100] L. Cacciotti, P. Patteri and F. Tazzioli. The new front end module of the ttf stripline bpm detector with single bunch response. Technical Report TESLA 98-18, INFN Frascati, July 1998.

[101] Data collected by P. Castro.

[102] M. Wendt. Private communication.

[103] M. Liepe, S.N. Simrock. Adaptive feed forward for digital rf control system at the tesla test facility. *Proceedings of the 6th EPAC98, Stockholm*, 2098.

[104] M. Hüning. Private communication, January 2001.

[105] Brush Wellmann GmbH. Private communication, July 96.

[106] M.Abramowitz and I.A.Stegun. *Handbook of Mathematical Functions*. Number 55. Department of Commerce, 2 edition, 1964. pp.358-364.

- [107] M. Seidel. An exit window for the tesla test facility. Technical Report TESLA 95-18, Deutsches Elektronen-Synchrotron, DESY, August 1995.
- [108] K. Zapfe. Private communication, DESY, April 2001.
- [109] *Taschenbuch fur den Maschinenbau/ DUBBEL*. W. Beitz and K.-H. Grote, Springer, 20 edition, 2001.

Acknowledgements

I want to thank DESY for the opportunity to work on the interesting field of accelerator physics. During this thesis I got all the technical and the financial support to finish successfully my Ph.D. thesis.

I like to thank Prof. Dr. Schmüser for his effort and patience in advising my Ph.D. thesis. He supported the formation of this thesis by fruitful discussions and constructive ideas.

I grateful thank to Dr. J. Rossbach for placing confidence in my work to manage the collimator project successfully and for his support during the design, the construction and the commissioning of the various system components.

I always found help on the theory of accelerator physics by asking R. Brinkmann and the discussions with him on the collimator issus were always very helpful.

At Saclay, I like to thank C. Magne, B. Phung, M. Lalo and M. Jablonka for the excellent work, the engagement and the cooperation concerning the beam position and the dark current monitors implemented in the collimator section. Specially at the beginning of TTF phase I the linac operation would have been impossible without their support. Also, for the important work on the beam current monitors in the linac and the beam interlock system I would like to thank J. Fuesselier and M. Loung.

I like to thank M. Rueter, A. Sass and M. Siemens for the cooperative work in designing the collimator section.

Special thanks to the vacuum group MVP, K. Zapfe, H-P. Wedekind, D. Ahrendt, A. Wagner, M. Schwalger and Mr. Huber who die last year. Particular during the construction phase of the collimators, Mr. Huber was a great help and because of his profound knowledge about mechanics, materials, cleaning procedures and vacuum systems I had the possibility to gain many experiences on practical and technical subjects.

I would to thank G. Schmidt for the fruitful cooperation and the coordination during installation of the collimator, the undulator and the reconstruction of the experiment area I. Also I like to thank J. Prenting and his survey group for the alignment of the collimator components.

My work had many aspects and covered numerical and analytic calculations as well as the exciting experience to commission and operated the TTF linac. Special thank to S.

Schreiber who introduces me to the TTF injector and the laser system, to S. Simrock for the discussion on low level rf systems and how to deal with klystrons and modulators, K. Rehlich and O. Hensler for the support from the TTF control system and electrons components required to setup up the active beam loss protection system and M. Stark, M. Loung and A. Liero for supporting the integration into the beam inhibit system of the TTF linac.

For the realization of the active beam loss system I would like to thank K. Wittenburg, I. Kroupchenkov and H. Schultz for their support in electrons and detectors.

I want to thank Siggi Schreiber, Stephan Simrock, Markus Tischer, Christopher Gerd, Rasmus Ischebeck, Kirsten Zapfe, Bart Faatz and Nick Walker, who have read my manuscript and helped me to eliminated any error or doubtful statements both in content and in English language.

I finally like to thank my girlfriend A. Swiderski for her moral support, the understanding for being up working many whole nights and weekends and the fruitful discussion to find the inner structure of this thesis and the logical order of arguments.